The chemical and magnetic structural characterisation of magneto-resistive devices using x-ray techniques

Buchanan, James David Ralph

The Chemical and Magnetic Structural Characterisation of Magneto-Resistive Devices using X-Ray Techniques

by

James David Ralph Buchanan

A thesis submitted in partial fulfilment of the requirements for the degree of Doctor of Philosophy

The University of Durham

2003

Declaration

I hereby declare that the work contained in this thesis is my own and has not been submitted previously for any other degree. The work of collaborators is acknowledged as appropriate. In particular, I would like to acknowledge that all magneto-resistance measurements made in *Chapter 3* were performed by W.F. Egelhoff Jr, P.J. Chen, L. Gan and C.J. Powell from the National Institute for Science and Technology (NIST). The MOKE M-H loops and magneto-transport measurements in *Chapter 4* were taken by N.D. Hughes and R.J. Hicken, University of Exeter, and J.S.Moodera from Massachusetts Institute of Technology (MIT). Similarly, the M-H loops in *Chapter 6* were recorded by C.H. Marrows from the University of Leeds. The Kramers-Kronig transforms shown in *Chapter 7* were performed by N. Telling (using his software), Daresbury SRS.

The samples studied in this thesis were obtained from the following sources:

Chapter 3: W.F. Egelhoff Jr.
National Institute of Science and Technology (NIST), U.S.A.

Chapter 4: N.D. Hughes and R.J. Hicken, University of Exeter, U.K.
J.S. Moodera, Massachusetts Institute of Technology (MIT), U.S.A.

Chapter 5: W.F. Egelhoff Jr., J. Chen, L. Gan and C.J. Powell
National Institute of Science and Technology (NIST), U.S.A.

Chapter 6: C.H. Marrows, and B.J. Hickey, University of Leeds, U.K.

Acknowledgements

I would now like to take the opportunity to thank the many people who have helped me over the past few years with their encouragement, advice and friendship.

First and foremost I'd like to graciously thank Brian Tanner for his guidance and excellent supervision during my studies at Durham (and for spotting nearly **all** my split infinitives!).

Thanks must also go to a number of collaborators who I have been privileged enough to work with. Special thanks go to Bill Egelhoff for his inspirational enthusiasm and advice, and some of his fellow colleagues; J. Chen, L. Gan and C.J. Powell from NIST, for their continuous supply of samples.

I would like to acknowledge from the University of Leeds: Brian Hickey, Chris Marrows, Alex Cole, Paul Steadman, Aidan Hindmarch and Lisa Michez. My deepest thanks go to them for their support and collaboration during my time at Durham.

I would like to thank Norman Hughes and Rob Hicken from the University of Exeter, and Jagadeesh Moodera from MIT, for their excellent tunnel junctions and helpful discussions.

I must also express my gratitude to all of the station scientists who have been of tremendous help during our trips to the ESRF, Daresbury and ISIS. From XMaS, I'd like to thank Simon Brown, Paul Thompson, David Paul and Danny Mannix. From Daresbury, thanks go to Mark Roper, John Purton, Tarnjit Johal, Chiu Tang and Steve Thompson. And from ISIS (CRISP): Sean Langridge, Rob Dalgleish and Sam Foster.

I'd also like to thank everyone else who has been helpful through discussion or email during the course of my studies: Neil Telling, Ivan Schuller, Mark Goorsky, Amanda Petford-Long, Dennis Leung, Matt Wormington, Helen Laidler and Pascale Dean.

Thanks are also expressed to EPSRC for funding me over the last three years.

From Durham I would like to acknowledge a number of people, without whom the last three years would not have been so enjoyable. My thanks go to Tom Hase (for his

continued support whether in Durham or Hong-Kong), Amir Rozatian, Kathryn Kelly, Brian Fulthorpe, Xiao Shan Wu, Peter Hatton, Phil Spencer, Neil Parkinson, Tom Beale, Stuart Wilkins, Mohammed Ghazi, Ian Terry, Sean Giblin, Dan Read and Gwyn Ashcroft. I'd also like to thank Mike Pennington who has been head of department during my time here and the departmental support staff: Penny Carse, Joanne Devlin, Claire Davies, Mike Lee, Vicki Dobby, Pauline Russell, Wayne Dobby, Ian Manfren, Matt Carrick, Dave Stockdale, Andy Hunter, and Pat for the daily supply of tea and biscuits! Special credit also goes to *"he who dares"* John Dobson.

Finally, I would like to thank my friends and family for their wonderful support and encouragement during my time in Durham. Thanks go to Lynda, Mervyn and Rachel, my parents John and Jean, and my brother Robert. A special thank you to my wife Liz, for her love and support.

Abstract

The academic and industrial interest in magnetic data storage has been fuelled by the information age. The number of applications for magnetic thin-films has increased rapidly, along with the popularity of using X-ray techniques as a tool by which to characterise them. Structural characterisation is a key process to their development and understanding, correlating chemical and magnetic structure to magneto-transport.

In this thesis a number of magneto-resistive devices are studied, including spin valves, magnetic tunnel junctions and magnetic multilayers.

The credence of using grazing incidence X-ray techniques for characterisation is initially demonstrated by accounting for variations in MR from nominally identical spin-valves, through observing subtle fluctuations in the pinning NiO layer thickness. The study of magnetic tunnel junctions has revealed discrepancies in barrier thickness as measured by X-ray reflectivity and through fits to the I-V profile using Simmons' model. This demonstrates localised tunnelling and the inaccuracy of I-V modelling in determining average barrier thickness. Specular reflectivity and diffuse analysis have also determined a far larger than expected level of intermixing across Al bilayer interfaces with Al on X and X on Al, where X are transition metals from groups 3,4 and 5 of the periodic table.

AF coupled multilayers are studied using polarised neutron reflectivity, the results of which have been compared directly with the relatively new technique: resonant soft X-ray magnetic scattering (SoXMaS). Specular and diffuse scattering studies reveal striking discrepancies between the two techniques, due to differences between the relative magnetic to chemical cross sections. Simulations further demonstrate SoXMaS and its sensitivity to magnetic structure. Finally, reflectivity data from Co/Cu Bragg peaks are used to calculate the refractive index of Co across the Co L_{III} and L_{II} edge under different magnetisation orientations.

List of Publications

The work described in these chapters has appeared in the following publications:

Chapter 4:

Determination of the thickness of Al2O3 barriers in magnetic tunnel junctions
Buchanan JDR, Hase TPA, Tanner BK, Hughes ND, Hicken RJ
APPLIED PHYSICS LETTERS
81 (4): 751-753 JULY 22 2002
Selected Highlight in the Virtual Journal
of Nanoscale Science and Technology
Vol 6 Pg 5 JULY 2002

Chapter 5:

Intermixing of aluminum-magnetic transition-metal bilayers
Buchanan JDR, Hase TPA, Tanner BK, Chen PJ, Gan L, Powell CJ, Egelhoff WF
JOURNAL OF APPLIED PHYSICS
93 (10): 8044-8046 Part 3 MAY 15 2003

Anomalously large intermixing in aluminum-transition-metal bilayers
Buchanan JDR, Hase TPA, Tanner BK, Chen PJ, Gan L, Powell CJ, Egelhoff WF
PHYSICAL REVIEW B
66 (10): art. no. 104427 SEPTEMBER 1 2002

Chapter 6:

Resonant magnetic x-ray and neutron diffuse studies of transition metal multilayers
Hase TPA, Buchanan JDR, Tanner BK, Langridge S,
Dalgliesh RM, Foster S, Marrows CH, Hickey BJ
JOURNAL OF APPLIED PHYSICS
93 (10): 6510-6512 Part 2 MAY 15 2003

Comparison of Polarised Neutron and Soft X-ray Resonant Magnetic Scattering from Transition Metal Multilayers
Buchanan JDR, Hase TPA, Tanner BK, Langridge S,
Dalgliesh RM, Foster S, Marrows CH, Hickey BJ
Submitted to PHYSICAL REVIEW B

Contents

Chapter 1

Introduction

1.1 Aims

Magneto-Resistive (MR) devices have been an important area of study for many years, not only in academic institutions but in industrial development as well. Research has led to their continued application as magnetic sensors, such as the read heads found in computer hard disks.

The aim of this research is two fold. The first concerns the correlation between MR and chemical structure, as characterised using grazing incident X-ray techniques. The use of X-ray reflectivity (both specular and diffuse studies) has increased in popularity over the last 20 years as a method by which to study thin films and multilayers. Although the technique does not provide a direct image of the sample structure, like many of its complementary techniques, it does have the advantage of providing a non-destructive, global statistical characterisation. With this technique many important structural parameters, including layer thickness, interface width (intermixing and topological roughness), crystallinity, grain size as well as both in- and out-of-plane correlation lengths, can be measured.

The second aim focuses on the development of these techniques, with respect to using X-rays in the characterisation of magnetic structure, defining magnetic parameters analogous to the chemical structural components described above.

The MR devices used in the study take a variety of forms, including spin-valves, magnetic tunnel junctions and magnetic multilayers. The samples presented here were prepared as part of a number of collaborations and not produced at the University of Durham.

1.2 Thesis Outline

The following chapter will introduce the reader to the theoretical and experimental aspects of X-ray characterisation, using kinematical theory to examine X-ray interactions with matter, as well as single and multilayered devices. Reciprocal space is introduced, including the basic scanning methods used throughout this work. Fractal models are used to describe roughness, with the Born wave and distorted wave Born approximations used to model the effect of roughness on X-ray scattering. Some additional X-ray techniques are also discussed, with a look at the different X-rays sources and experimental facilities used during the course of this study. The chapter also examines the magneto-optical Kerr effect and sputtering.

Chapter 3 investigates a series of nominally identical spin-valves and attempts to correlate the magneto-resistance changes to subtle structural variations. This chapter also offers the reader an introduction to some of the experimental procedures outlined theoretically in *Chapter 2*.

Chapter 4 examines a different form of MR device, the so-called magnetic tunnel junction. The investigation focuses particularly on the barrier and the effect of oxidation on layer thickness. It compares results obtained from X-ray analysis with those determined from magneto-transport measurements.

Magnetic tunnel junctions are also the motivation behind *Chapter 5*, which is concerned with the initial aluminium deposition prior to oxidation. In this chapter we report an unexpected amount of intermixing within aluminium-transition metal bilayers. The results are then discussed with regard to in-plane grain size as determined from grazing incidence in-plane X-ray diffraction.

Chapter 6 is concerned with a relatively new technique which (through resonant tuning to the appropriate spin-degenerate energy level) provides X-rays with indirect magnetic sensitivity. This novel technique, still in its infancy, is compared with the more established technique of Polarised Neutron Reflectivity using a series of anti-ferromagnetically coupled multilayers. The scattering from both methods are compared in the specular and diffuse regime.

The penultimate chapter expands on the work presented in *Chapter 6* with a series of computer simulations to model reflectivity at magnetic resonance. The effect of moment orientation and different forms of magnetic disorder are simulated and discussed. The later part of the chapter determines the complex refractive index of cobalt at resonance by looking at the energy dependence of a charge/ferromagnetic Bragg peak across the Co L_{III} and L_{II} edges.

Finally *Chapter 8* reviews some of the important conclusions taken from this study and discusses some of the future work which would be valuable to this research field.

Chapter 2

Theory and Experimental Techniques

2.1 Introduction

X-rays were discovered over a hundred years ago by Wilhelm Röntgen [1], at the University of Wurzburg in Germany. Their potential as a structural probe was quickly realised with the first medical experiments conducted just a year later in 1896. Crystal diffraction was later observed in 1912 by Friedrich and Knipping, which was interpreted by W.L. Bragg (1913) [2] in terms of a continuous spectrum according to his well known law:

$$n\lambda=2d\sin\theta$$

Equation 2.1

Total external reflection was observed by Compton in 1923 [3] for crown glass at λ=1.279Å, indicating that n<1. This then led to the first successful reflectivity experiment from a multilayered mirror in 1940.

Although the most common experimental geometry for X-rays is diffraction, the majority of this chapter will focus on grazing incidence scattering techniques and the theoretical arguments behind them. Special attention is paid to Grazing Incidence X-Ray Reflectivity (GIXR), a technique used throughout this thesis.

The first section introduces the reader to Kinematical theory (*Section 2.2*) with the scattering of X-rays from both free electrons and complete atoms. The idea of reciprocal space is presented in *Section 2.3*, followed by a look at the interaction of X-rays at a surface or interface. This is then followed by discussion to illustrate the different scan

types within a grazing incident geometry. Specular reflectivity is discussed in *Section 2.6*, followed by *Section 2.7* which concerns diffuse scatter and introduces the reader to the Born wave approximation and subsequently the distorted wave Born approximation. Some additional X-ray techniques are then described, including resonant scattering (*Section 2.8.1*), fluorescence (*Section 2.8.2*) and diffraction (*Section 2.8.3*), both in grazing incidence and high angle geometries. A description of the X-ray sources (both laboratory based and available at synchrotron facilities) follows in *Section 2.9*. Finally, MOKE is discussed in *Section 2.10*, followed by a description concerning the basic sputtering growth technique (*Section 2.11*) used to fabricate all of the samples presented in this thesis.

2.2 Kinematical Theory

The interaction of X-rays with matter occurs whenever the incident X-ray experiences a scattering potential. It can occur via one of three ways; absorption, refraction or scattering. These interactions can be approached from a classical or quantum mechanical standpoint. In this section the classical formalism is applied, assuming all interactions to be elastic. To include inelastic scattering a quantum mechanical approach is required and the reader is referred to work by Kuriyama [4, 5].

Under the kinematical regime we make the following assumptions:

- The intensity of the beam is the same throughout the crystal.
- The scattered intensity is small.
- All waves are considered in the far-field regime.
- Scattered waves from different atoms are parallel with identical wavevectors.

2.2.1 Interaction with a Single Electron

A charged particle, such as an electron, is forced into oscillations through the electromagnetic interaction with X-rays. If the incident beam is a plane wave then dipole oscillations cause the electron to re-radiate X-rays of the same form with a π-

phase shift. This elastic scattering process, known as Thomson scattering [6], has a radiated electric field at a point **r**, written in the following form:

$$E_{rad}(\mathbf{r},t) = -\left(\frac{e^2}{mc^2}\right)\left(\frac{1}{\mathbf{r}}\right)E_o \exp[2\pi i(\mathbf{k}\cdot\mathbf{r} - \omega t)]$$

Equation 2.2

where E_o is the amplitude of the incident electric wave. (e^2/mc^2) is defined as the Thomson scattering length r_o (=2.82×10^{-13}Å) and represents the scattering power of the free electron. The preceding minus sign is due to the π-phase difference. For the derivation of *Equation 2.2* the reader is referred to *Appendix A.* In terms of intensity, for an incident beam I_o, the scattering intensity I_s is written as [7]:

$$I_s = I_o r_o^2\left(\frac{P}{\mathbf{r}^2}\right) \qquad P = \begin{cases} 1 & \text{for } \sigma \text{ polarisation} \\ \cos^2 2\theta & \text{for } \pi \text{ polarisation} \end{cases}$$

Equation 2.3

The factor P, depends on the polarisation of the incident beam with respect to the observation point **r**, where σ denotes beam polarisation in the plane normal to the observation point and π represents the polarisation in the same plane as **r**.

2.2.2 Interaction with a Single Atom

With all scattering techniques the magnitude of the scattered radiation is defined by the atomic scattering factor f, which itself is defined as the ratio of scattered amplitude for an atom in comparison to a single free electron. f can be written as a Fourier transform of the electron density [8-10]:

$$f = \int_v \rho(r)\exp[2\pi i\mathbf{q}\cdot\mathbf{r}]\ dV$$

Equation 2.4

where **q** is the scattering wavevector defined by the incident $\mathbf{k_o}$, and exiting wavevectors **k**, through $\mathbf{q} = \mathbf{k_o} - \mathbf{k}$.

Atoms are multiple electron systems, spread over what is a relatively large volume, therefore the atom with its atomic number Z, can no longer be viewed as a single point

and must be seen as a spatial charge distribution ρ, integrated over a volume element dV:

$$Z = \int_{V} \rho(r) dV$$

Equation 2.5

Since the radiation is scattered from different points in space it will cause a phase distribution. This has been illustrated below in *Figure 2.1*. As a result of this phase distribution a factor proportional to $\sin 2\theta / \lambda$ (dependent upon the atom) must be introduced to the scattering factor in order to account for the path difference.

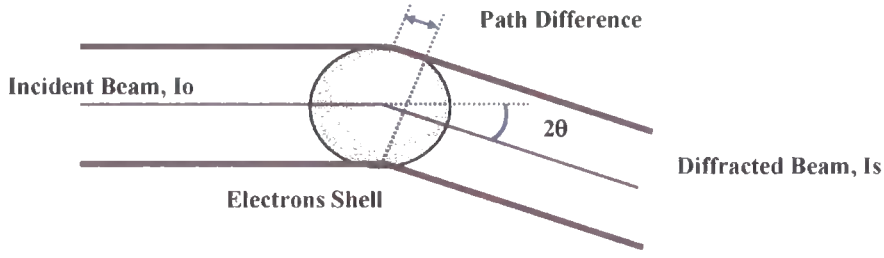

Figure 2.1: *Phase distribution caused by the path difference in the scattered beam.*

This simple picture describes the atomic structure factor for X-ray interaction away from the absorption edge i.e. scattering from free electrons within the atom. However at the absorption edge, resonance effects cause the phase change on scattering to deviate from π since the electrons are no longer free, see *Appendix A*. The scattering factor given in *Equation 2.4* is therefore no longer correct and must be modified to include dispersion and absorption effects:

$$f = f_0 + f' + if''$$

Equation 2.6

Although the majority of X-ray scattering is done away from the absorption edges where f'' is small and in most cases ignored ($f \approx f_0 + f'$), it is sometimes advantageous to exploit the tunability of synchrotron radiation and tune to an absorption edge. This is known as Resonant X-ray scattering and will be discussed further with these additional scattering factors in *Section 2.8.1*.

2.3 Reciprocal Space

It has already been shown that X-ray scattering is proportional to the Fourier transform of the charge distribution (*Equation 2.4*) and so it is therefore convenient to view scattering in Fourier, or reciprocal space. Any periodic function, such as the electronic structure in a crystal lattice, is thus represented in reciprocal space by a single point. This is general for all spatial frequencies with the direction of periodicity in real space corresponding to the point position in reciprocal space.

The three primitive lattice vectors $\mathbf{a}_1$, $\mathbf{a}_2$ and $\mathbf{a}_3$ used in real space are related, via the following equations, to the reciprocal lattice vectors $\mathbf{b}_1$, $\mathbf{b}_2$ and $\mathbf{b}_3$ [11, 12]:

$$b_1 = \frac{a_2 \times a_3}{a_1 \cdot a_2 \times a_3} \qquad b_2 = \frac{a_3 \times a_1}{a_1 \cdot a_2 \times a_3} \qquad b_3 = \frac{a_1 \times a_2}{a_1 \cdot a_2 \times a_3}$$

Equation 2.7

We can also visualise the transform between real and reciprocal space in terms of scattering using the following figure. The vector map is known as a Ewald sphere, its locus represents all of the possible scattering vectors.

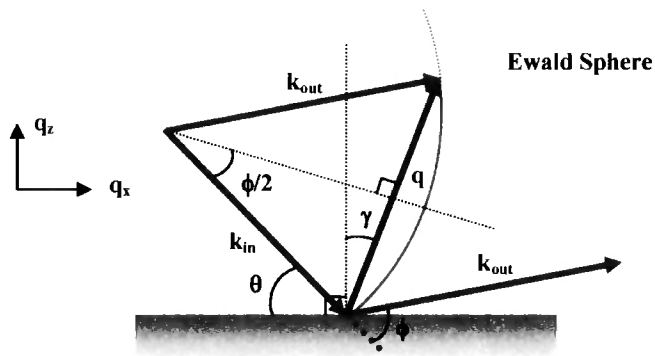

Figure 2.2: *Ewald sphere construction.*

The incident wavevector $\mathbf{k}_{in}$ defines the incoming wave, at an angle θ to the sample's surface. After scattering through an angle ϕ the exiting beam is defined with the wavevector $\mathbf{k}_{out}$. In elastic scattering the magnitude of these wavevectors are equal and so:

$$|\mathbf{k}_{in}| = |\mathbf{k}_{out}| = |\mathbf{k}| = 2\pi/\lambda$$

Equation 2.8

Therefore **q** the scattering vector, defined as $\mathbf{k}_{out}-\mathbf{k}_{in}$, is given by:

$$\mathbf{q} = \left(4\pi/\lambda\right)\sin\left(\phi/2\right)$$

Equation 2.9

The scattering vector given in *Equation 2.9* and the Ewald sphere shown in *Figure 2.2* is a simplified 2D expression. Complete 3D scattering vector matrix expressions, to include horizontal scattering, are given in *Appendix B*.

2.4 The Interaction of X-rays at a Surface or Interface

As the electromagnetic radiation propagates from one medium to the next its behaviour is governed by Maxwell's equations, with boundary conditions that require matching components of magnetic and electric field across the interface. In this section the propagation (i.e. refraction, reflection and transmission) of X-rays through a medium of varying refractive index is discussed. Snell's law is introduced to describe a single interface, followed by Fresnel's law to examine a more complex layered structure and finally Parratt's recursive formalism to model a multilayered system.

The refractive index n, for any medium is described in terms of its dispersion δ, and absorption β:

$$n = 1 - \delta - i\beta$$

Equation 2.10

where at X-ray energies:

$$\delta = \frac{N_A}{2\pi} r_0 \lambda^2 \sum_j \frac{\rho_j}{A_j}\left(Z_j + f_j'\right)$$

Equation 2.11

$$\beta = \frac{N_A}{2\pi} r_0 \lambda^2 \sum_j \frac{\rho_j}{A_j} f_j''$$

Equation 2.12

N_A is Avogadro's number, r_o is the Thomson scattering length and λ is the wavelength, ρ_j and A_j represent the density and atomic weight respectively for the j^{th} element. f' and

f'' are the so-called anomalous correction terms introduced earlier (see *Equation 2.6*) to the normal atomic scattering factor f_o.

From *Equation 2.10* it is clear that X-rays incident from free space interact with materials which are optically less dense, i.e. a refractive index of less than one. Consequentially there exists a critical angle, below which, the incident beam undergoes total external reflection from the surface. Only above this angle will the X-rays begin to penetrate deep inside the bulk of the sample.

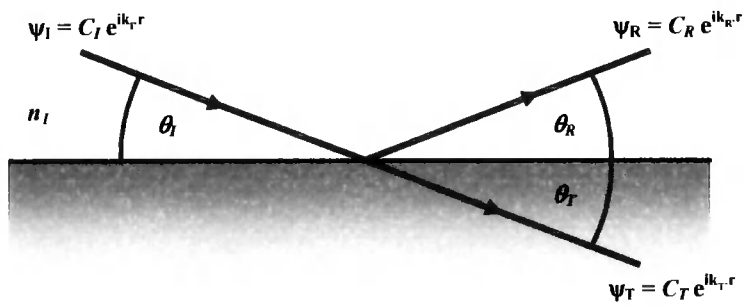

Figure 2.3: *Incident, reflected and transmitted beams from a surface layer.*

Figure 2.3 shows the basic surface interaction, assuming the X-ray beams are characterized by plane waves, $\psi = Ce^{i\mathbf{k}\cdot\mathbf{r}}$, where C and $\mathbf{k}$ are the wave amplitude and vector respectively. Imposing boundary conditions require that the wave amplitude and its derivative are continuous across the interface, such that:

$$C_I + C_R = C_T$$

Equation 2.13

$$C_I \mathbf{k_I} + C_R \mathbf{k_R} = C_T \mathbf{k_T}$$

Equation 2.14

Assuming the wavevectors are related to the wavenumber via the refractive index such that: $n_1\mathbf{k} = |\mathbf{k_I}| = |\mathbf{k_R}|$ and $n_2\mathbf{k} = |\mathbf{k_T}|$, we can consider wavevector components both parallel and perpendicular to the surface:

$$(C_I + C_R)\, n_1\mathbf{k} \cos\theta_I = C_T\, n_2\mathbf{k} \cos\theta_T$$

Equation 2.15

$$(C_I - C_R)\, n_1\mathbf{k} \sin\theta_I = C_T\, n_2\mathbf{k} \sin\theta_T$$

Equation 2.16

Snell's law is therefore derivable using *Equation 2.13* and *Equation 2.15*:

$$n_1 \cos\theta_I = n_2 \cos\theta_T$$

Equation 2.17

At the critical angle the transmitted wave can be considered to be travelling along the interface at $\theta_T = 0°$ and so by assuming the incident radiation comes from a vacuum (n_1=1) the critical angle θ_c, is defined from:

$$\cos\theta_c = n_2$$

Equation 2.18

Using the small angle approximation and through assuming a negligible amount of absorption ($\beta = 0$):

$$\theta_c = \sqrt{2\delta}$$

Equation 2.19

For incident angles below θ_c there is total external reflection with only an evanescent wave present within the sample. Due to the low penetration depth (dependent on the surface electron density and X-ray energy) of the evanescent field, total external reflection techniques gain surface sensitivity. Grazing incidence X-ray fluorescence (GIXF) and grazing incidence X-ray diffraction (GIXD) exploit this phenomenon and will be discussed further in *Section 2.8.2* and *Section 2.8.3.2* respectively.

For angles greater than θ_c, the X-rays penetrate deep into the bulk of the sample with their intensity decreasing exponentially at a rate governed by the absorption coefficient β. The transmission and reflection coefficients across a layer can be found easily through combining *Equation 2.13* with the continuity equation perpendicular to the interface seen in *Equation 2.16*:

$$\frac{C_I - C_R}{C_I + C_R} = n\frac{\sin\theta_T}{\sin\theta_I}$$

Equation 2.20

In this equation, medium 1 has been taken as a vacuum, and n_2 has been re-denoted by n. By assuming the small angle approximation, a form of the Fresnel transmission and reflection coefficients are derived as:

$$r = \frac{C_R}{C_I} = \frac{\theta_I - n\theta_T}{\theta_I + n\theta_T} \qquad t = \frac{C_T}{C_I} = \frac{2\theta_I}{\theta_I + n\theta_T}$$

Equation 2.21

2.4.1 Reflectivity from a Homogeneous Layer

We are now ready to consider the case of X-ray reflectivity from a single layer. An incident beam, from a vacuum of n=1 (medium 0) reflects off a single layer (medium 1) of finite thickness which is grown on what will be modelled as an infinite substrate (medium 2). For the structure shown in *Figure 2.4* there exists (in contrast to the infinite layer discussed earlier) an infinite number of possible reflections.

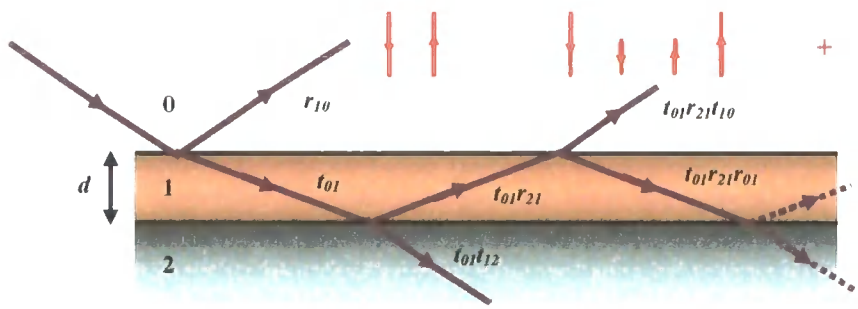

Figure 2.4: *Reflection and transmission from a single layer of finite thickness* ***d****.*

The red arrows depict the out-of-plane wavevector components and demonstrate the total reflectivity as the sum of all possible reflections written in terms of the transmission and reflection coefficients:

$$r_{Total} = r_{01} + t_{01}r_{21}t_{10}p^2 + t_{01}r_{21}^2 r_{01}t_{10}p^4 + \ldots$$
$$r_{Total} = r_{01} + t_{01}t_{10}r_{21}p^2 \sum_{m=0}^{\infty}(r_{21}r_{01}p^2)^m$$

Equation 2.22

In adding the waves together it is necessary to include the phase factor; $p^2 = e^{iqd}$, where **q** ($=2\mathbf{k}_1\sin\theta_i$) is the scattering wavevector introduced earlier and **d** is the layer thickness. *Equation 2.22* is simply a geometric series that may be summed to give:

$$r_{Total} = r_{10} + t_{01}t_{10}r_{21}p^2\frac{1}{1-r_{01}r_{21}p^2}$$

Equation 2.23

This expression is then simplified with the Fresnel equations (*Equation 2.21*):

$$r_{Total} = \frac{r_{10} + r_{21}p^2}{1 + r_{10}r_{21}p^2}$$

Equation 2.24

2.4.2 Reflectivity from a Multi-Layered System

Throughout this work, the samples studied contain more than one layer including bilayers and more complicated structures, such as spin valves and tunnel junctions which are composed of a minimum of 3 layers, but often many more. One useful group of materials is known as multilayers, in which a series of layers is repeated in sequence, in some cases up to 100 repeats. Parratt's recursive theorem [13] is used to describe such systems.

Parratt's theorem considers N layers grown on top of an infinitely thick substrate. Each layer has a thickness d_j and can be described by $n_j = 1 - \delta_j + i\beta_j$. From *Figure 2.4* it is seen that the out-of-plane wavevector components in the j^{th} layer can be described in terms of the total wavevector $\mathbf{k_j} = n_j\mathbf{k}$, and the in-plane x-component which is conserved throughout the layer such that $k_{x,j} = k_x$ for all j. Therefore from $k_z^2 = \mathbf{k}^2 - k_x^2$:

$$k_{z,j}^2 = (1 - \delta_j + i\beta_j)^2\mathbf{k}^2 - k_x^2 \approx k_z^2 - 2\delta_j\mathbf{k}^2 + i2\beta_j\mathbf{k}^2$$

Equation 2.25

and from $\mathbf{q_j}=2\mathbf{k_j}\sin\theta_{t,j} = 2\,k_{z,j}$ the wavevector transfer is:

$$\mathbf{q}_j = \sqrt{\mathbf{q}^2 - 8k^2\delta_j + i8k^2\beta_j}$$

Equation 2.26

The first step in calculating the complete reflectivity from the multilayer is to evaluate the reflectivity from the substrate interface within the N^{th} layer. Since there are no multiple reflections to consider here, the reflectivity is simply the Fresnel reflective coefficient (*Equation 2.21*), which is rewritten as:

$$r_{N,\infty} = \frac{q_N - q_\infty}{q_N + q_\infty}$$

Equation 2.27

On the other hand the expression for reflectivity from the interface between the N^{th} and $(N\text{-}1)^{th}$ layer, must allow for multiple reflections and so *Equation 2.24* is used:

$$r_{N-1,N} = \frac{r_{N-1,N} + r_{N,\infty} p_N^{\,2}}{1 + r_{N-1,N} r_{N,\infty} p_N^{\,2}}$$

Equation 2.28

where $p_N^{\,2} = e^{id_N q_N}$ and d_N is the thickness of the N^{th} layer. The reflectivity from the next interface can be calculated in a similar way and so on recursively to the top surface interface.

2.5 Scan Types

In discussing the various scan types in reciprocal space it is useful to separate the scattering vectors into their in-plane (q_x) and out-of-plane (q_z) components. An additional angle γ, defined in *Figure 2.2* as $\gamma = \theta_I - (\phi/2)$, allows q_x and q_z to be described as:

$$q_x = \left(4\pi/\lambda\right)\sin\left(\phi/2\right)\sin\gamma \qquad q_z = \left(4\pi/\lambda\right)\sin\left(\phi/2\right)\cos\gamma$$

Equation 2.29

A further dimension q_y, is of course present and can be used to describe the in-plane scattering, perpendicular to the scattering plane. This scattering vector requires an additional axis as described in *Appendix B*. There are primarily three basic grazing incident scanning techniques used throughout this thesis; specular, longitudinal diffuse (off-specular) and transverse diffuse (rocking curve).

In the specular condition the angle of incidence matches the angle of reflectivity; $\theta_I = \theta_R = \phi/2$ and so $\gamma = 0$. Consequentially the q_x term disappears with only an out-of-plane

scattering q_z component remaining. In such a scan, the sample and detector are coupled such that $\theta_i = \phi / 2$ and so the specular condition is maintained while varying the magnitude of q_z. Hence reciprocal space is probed solely as a function of q_z, see *Figure 2.5*:

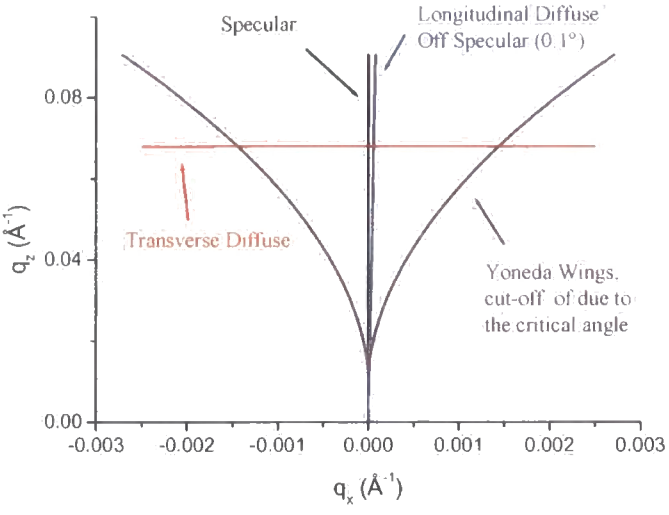

Figure 2.5: *Scan types in reciprocal space.*

Just off the specular condition the diffuse scatter can also be measured as a function of q_z. By initially off-setting the sample angle and performing a coupled scan (similar to the specular scan described earlier) a straight line in reciprocal space at a small angular off-set to the specular scan is probed, see *Figure 2.5*. This diffuse scan is known as a longitudinal diffuse or off-specular scan, used to examine the degree of vertical correlation and to obtain the true specular profile by subtracting it from the specular profile. The angular off-set should be large enough to leave the specular ridge, but small enough as to provide a reasonable estimation of diffuse scatter at q_x=0.

The in-plane diffuse scatter can also be measured, this time as a function of q_x. Here the detector angle and thus scattering angle is fixed, with only the sample being scanned from 0 to ϕ. An observation limit at the so-called Yoneda wings is evident from these scans, due to the critical angle, see *Figure 2.5*. Although the term cos γ in *Equation 2.29* does provide a slight variation to the out-of-plane component, it is low and can be neglected at small angles. Therefore transverse diffuse scans are considered as explicit functions of q_x at fixed q_z.

2.6 Specular Reflectivity

Analysis of the specular reflectivity profile allows one to measure parameters such as near surface electron density, average layer thickness and the average interface width. Since the scattering geometry for specular reflectivity has a purely out-of-plane scattering vector, only parameters normal to the surface can be measured.

The near surface electron density can be determined from the position of the critical angle, θ_c. This is evident from *Equation 2.11* and *Equation 2.19* and shown in the specular profiles simulated in *Figure 2.6* for two single layers of Au and Al of infinite thickness. At an incident angle greater than that of the critical angle, the X-rays begin to penetrate into the bulk of the sample resulting in a decrease in reflected intensity. For angles above approximately twice the critical angle, the reflected intensity for a perfectly smooth system falls as θ^{-4}, this is known as the Debye-Porod Law [14], at lower angles there are small deviations due to refraction effects. The intensity of the specular reflectivity decreases at a much sharper rate when roughness is present at any of the interfaces, as demonstrated in *Figure 2.6* with a variation in surface roughness of 0 Å, 3 Å and 6 Å. Roughness at the interface will cause the X-rays to scatter away from the specular condition into the diffuse scatter, see *Section 2.7*.

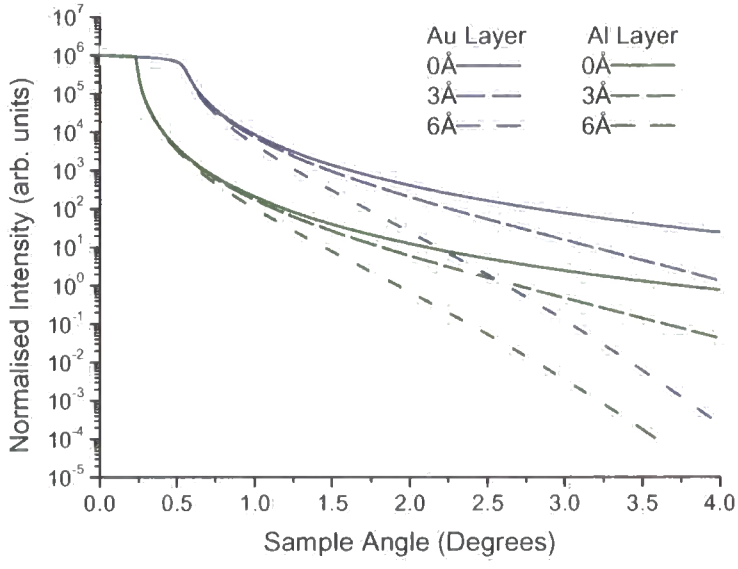

Figure 2.6: *Simulated specular profile for infinitely thick layers of Au and Al with 0 Å, 3 Å and 6 Å of surface roughness.*

The introduction of layers onto a substrate was explored theoretically in *Section 2.4.2*. The phase term in *Equation 2.28* causes interference effects between X-rays reflected from the top and bottom surface interface. This interference leads to a set of fringes called Kiessig fringes [6] with a periodicity determined by the layer thickness through Bragg's law:

$$d = \frac{\lambda}{2\Delta\theta}$$

Equation 2.30

with the period $\Delta\theta$ in radians, under the small angle approximation. Due to refraction effects this approximation should only be used at angles greater than twice that of the critical angle. The Kiessig fringes are clearly visible in the specular profiles simulated in *Figure 2.7* for a 100Å thick layer of Au and Al (with no roughness) grown on SiO_2. The greater contrast in scattering factors, due to the difference in electron density between the layers, results in a set of more defined interference fringes for the Au on SiO_2 sample.

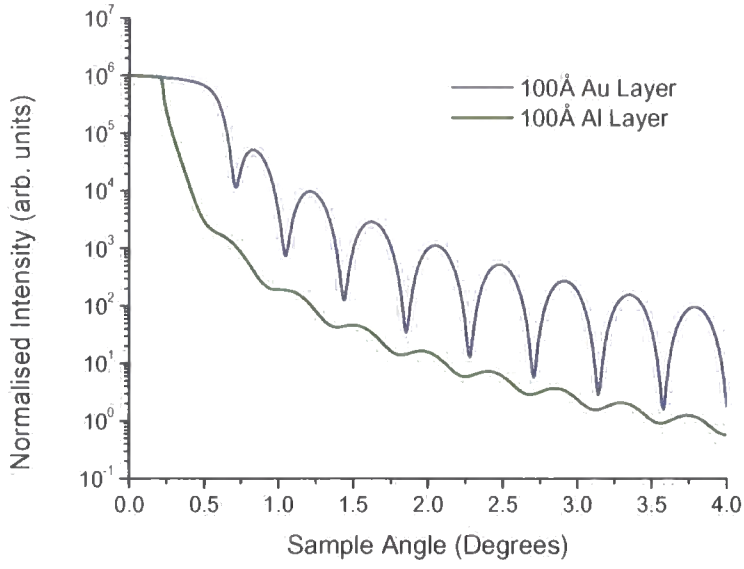

Figure 2.7: *Simulated specular profile for 100Å single layers of Au and Al.*

For systems with more than a single layer, the combination of interference fringes from all of the interfaces can result in a more complex specular profile with multiple periodicities. For multilayered systems there exists an enhanced periodicity corresponding to the repeating bilayer thickness. At the correct scattering vector the

bilayer thickness *d* will give rise to constructive interference and Bragg peaks. The intensity and sharpness depends on factors such as the number of bilayers, variation in the bilayer thickness and interface width.

The majority of the specular profiles presented in this work were fitted using *Refs Mercury* from *Bede Scientific*. This software simulates the reflectivity profile using Parratt's recursive theorem, as described in *Section 2.4.2*, according to a model structure [15]. The effect of interface width is described below in *Section 2.7* and modelled according to a Gaussian error function, clearly demonstrated in *Section 5.5.1*. Fits to experimental data are achieved by modifying the model parameters using a genetic algorithm [16] as described in *Appendix C*.

The determination of errors on these fits is exceptionally problematic due to the nature of fitting multi-variable problems and the uncertainty associated with cost space. The uncertainty of one variable is greatly affected by the uncertainty of another and therefore errors have been estimated according to the deviation in the accuracy of the fit associated with each respective parameter change.

2.7 Diffuse Scatter

Diffuse scatter originates from disorder within the sample and in-particular from roughness at the interface. So, in order to quantify the diffuse scatter, it is essential to have an accurate model with which to characterise quantitatively the morphology of an arbitrary interface. One of the problems the model must overcome is the fact that any morphology (including thin film interfaces) can appear to be quite different depending on the length scale by which we observe them. For example, the face of a coin may appear relatively smooth to the eye, however, under a microscope it looks much rougher. To allow for this, interfaces and surfaces are described according to a self-affine fractal model [17, 18]. Although fractal surfaces look the same independent of observation length scale, the self-affine objects are invariant under anisotropic scale transformations i.e. they have dimension dependent rescaling behaviour.

However, before going into this model in more detail it is necessary to describe the differential cross-section for the diffuse scatter. This can be achieved with the Born wave approximation, which uses Fermi's Golden Rule with a scattering potential V(r).

2.7.1 Born Wave Approximation

In the Born wave approximation the incident and scattered waves are assumed to be plane waves and the potential is taken to be totally homogenous within the medium; defined as $V = \mathbf{k_o}^2 (1\text{-}n^2)$ where $\mathbf{k_o}$ is the wavevector and n the refractive index. In assuming this homogeneity we are effectively ignoring any atomic structure. This approach is valid as long as the scattering is within small angles with $|\mathbf{q}|d<<1$, where $\mathbf{q}$ is our scattering vector ($=4\pi \sin\theta / \lambda$) and d is the length scale for any inhomogeneity within the sample. The potential outside the sample is defined as zero.

The differential cross section, using the Born Approximation, for a system of volume V is [18]:

$$\frac{d\sigma}{d\Omega} = N^2 r_o^{\,2} \int_V dr \int_V \exp[-i\mathbf{q}.(\mathbf{r}-\mathbf{r}')dr'$$

Equation 2.31

N is the number density of the scattering particles and r_o is the Thomson scattering length of the electron (in neutrons r_o is the coherent scattering length of the nuclei). These volume integrals may then be transferred into surface integrals using Stoke's theorem [19]:

$$\frac{d\sigma}{d\Omega} = \frac{N^2 r_o^{\,2}}{q_z^2} \iint_{S_o} dxdy \iint_{S_o} \exp\left(-iq_z[z(x,y)-z(x',y')]\right)\exp\left(-i[q_x(x-x')+q_y(y-y')]\right)dx'dy'$$

Equation 2.32

where S_o is the surface of the x-y interface plane and $z(x,y)$ is the height of the surface above the plane at the coordinates (x,y). The crucial assumption made here is in the use of a Gaussian random variable to describe a height difference function between arbitrary points on the surface, thus:

$$< [\, z(x',y') - z(x,y)\,]^2 > = g\,(X,Y)$$

Equation 2.33

where the relative coordinates $(X,Y) = (x' - x, y' - y)$. With this assumption we can write the scattering cross section for an illuminated area (L_xL_y) on the surface interface as:

$$\frac{d\sigma}{d\Omega} = \frac{N^2 {r_o}^2}{q_z^2} L_x L_y \iint_{S_o} \exp\left[-\frac{1}{2} q_z^2 g(X,Y)\right] \exp\left(-i\left[q_x X + q_y Y\right]\right) dX dY$$

Equation 2.34

It is now possible to obtain an expression for $S(\mathbf{q})$, the cross section per unit area surface (divided by $N^2 {r_o}^2$), for any given model describing $g(X,Y)$. For a perfectly smooth surface $g(X,Y) = 0$, thus:

$$S(\mathbf{q}) = \frac{1}{q_z^2} \iint_{S_o} dX dY \exp\left(-i\left[q_x X + q_y Y\right]\right) = \frac{4\pi^2}{q_z^2} \delta(q_x)\delta(q_y)$$

Equation 2.35

The delta functions contain the condition for specular scattering and the q_z dependence (squared since intensity is proportional to the square of the cross-section) accounts for the θ^4 drop off in intensity, the so-called Debye-Porod law.

Of course the interface is never perfectly smooth and so we now turn to a mathematical description of the self-affine fractal model introduced earlier.

2.7.2 The Self-Affine Fractal Model and Correlation Function

The concept of using a fractal description for the height difference function was first proposed by Sinha *et al.* [18]. In this case roughness is replaced by an exponent which accounts for the way in which roughness *changes* when observed on different length scales. The height difference function is therefore given the following form: $g(X,Y) = A(X,Y)^h$ with the texture of the interface or surface being described by the fractal exponent, h.

In this model $g(X,Y)$ tends to infinity with increasing distance (X,Y) and so a cut off point must be introduced to saturate the roughness.

$$g(X,Y) = 2\sigma^2 \left(1 - \exp\left[-\left(\frac{(X,Y)}{\xi}\right)^{2h}\right]\right)$$

Equation 2.36

Here σ is r.m.s. roughness, ξ is a correlation length (which will be discussed shortly) and h is the fractal parameter introduced earlier. This self-affine height difference function does not increase exponentially as seen in the purely fractal model, but rather

approaches $2\sigma^2$ as (X,Y) goes to infinity.

In scattering experiments instead of using a height difference function it is sometimes easier to consider a height to height correlation function, which describes the association between one point on the surface compared to another separated by a defined distance. The height to height correlation function is defined as follows:

$$C(X,Y) = \sigma^2 - \tfrac{1}{2} g(X,Y)$$

Equation 2.37

and thus from *Equation 2.36*:

$$C(X,Y) = \sigma^2 \exp\left[-\left(\frac{(X,Y)}{\xi}\right)^{2h}\right]$$

Equation 2.38

The choice of height to height correlation function is subject to debate and other mathematical forms have been suggested [20-24]. All interface structures studied in this thesis have been modelled using the height to height correlation function presented by Sinha *et al.* [18] and shown in *Equation 2.38*. This function, together with the height difference function, is represented graphically in *Figure 2.8*:

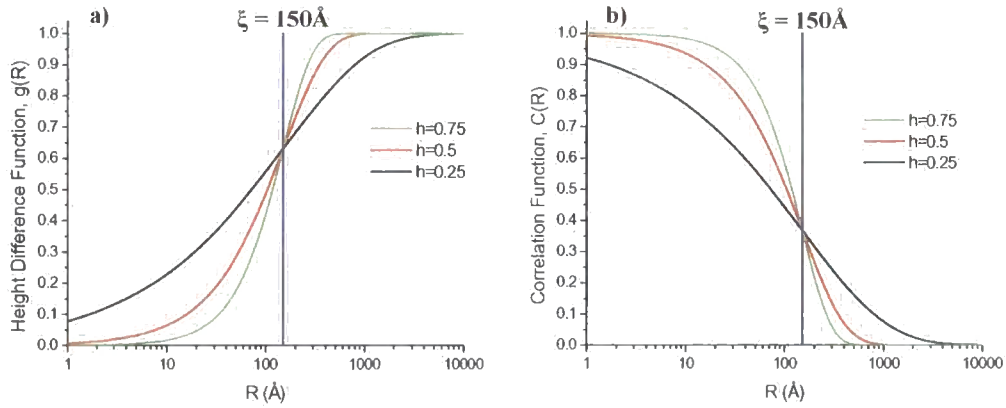

Figure 2.8:a) *Height difference function and* ***b)*** *height-height correlation function to describe the in-plane roughness as a function of R.*

The correlation length ξ, is a common point for models that use a different fractal parameter and represents the length scale at which the correlation between points has fallen to a value of 1/e. In effect, it defines the area over which the surface is fractal. For

more information concerning its transform between reciprocal and real space, see *Appendix D.*

From *Equation 2.37*, the differential cross section in *Equation 2.34* can now be rewritten as:

$$\frac{d\sigma}{d\Omega} = \frac{N^2 b^2}{q_z^2} L_x L_y \exp\left[-q_z^2\sigma^2\right] \iint_{S_o} dXdY \exp\left[q_z^2 C(X,Y)\right] \exp\left[-i(q_x X + q_y Y)\right]$$

Equation 2.39

and then recalculated to the differential cross section per unit area surface [18]:

$$S(\mathbf{q}) = \frac{1}{q_z^2} \exp\left[-q_z^2\sigma^2\right] \iint_{S_o} dXdY \exp\left[q_z^2 C(X,Y)\right] \exp\left[-i(q_x X + q_y Y)\right]$$

Equation 2.40

By substituting $F(q_z,(X,Y))=(\exp(q_z^2 C(X,Y))-1)$ it is possible to split the equation above into the separate specular and diffuse components ($S(\mathbf{q})=S_{spec}(\mathbf{q})+S_{diffuse}(\mathbf{q})$):

$$S_{spec}(\mathbf{q}) = \frac{4\pi^2}{q_z^2} \delta(q_x)\delta(q_y) \exp\left(-q_z^2\sigma^2\right)$$

Equation 2.41

$$S_{diffuse}(\mathbf{q}) = \frac{2\pi}{q_z^2} \exp\left(-q_z^2\sigma^2\right) \int_0^\infty RF(q_z,(X,Y)) J_o(q_{x,y}(X,Y)) dXdY$$

Equation 2.42

where J_o is a Bessel function of the first kind. By comparing *Equation 2.41* with *Equation 2.35* it is apparent that roughness on the specular profile is incorporated through the exponential factor, $\exp(-q_z^2\sigma^2)$, known as the Debye-Waller factor. This factor was used to simulate roughness in the specular reflectivity profiles shown in *Figure 2.6. Section 5.3.1* also makes use of this factor (with conservation arguments) to find an expression for average roughness as a function of integrated specular and diffuse scatter intensity.

Although *Equation 2.41* and *Equation 2.42* provide a reasonable approximation at high **q**, they fail to model the specular and diffuse scatter at small angles, particularly around the critical angle. The Born approximation assumes a weak interaction and therefore the reflectivity must also be small. It also fails to account for multiple

scattering events which can occur within the sample; these problems are overcome by using the distorted wave Born approximation.

2.7.3 Distorted Wave Born Approximation

In the Born approximation we assumed the surface to be a perturbation, acting on the incident plane wave. The distorted wave Born approximation (DWBA) takes the standard Born approximation a step further and was first applied to specular and diffuse scatter by Sinha *et al.* [18]. It calculates an exact solution for the wave equation at the surface and it is the interface disorder, not the surface, which acts as the perturbation. The scattering potential is thus split into two parts: V_1 representing the undisturbed system and V_2 the perturbed disturbance to it. The transmission probability is therefore given by:

$$T_{1\to 2} = \langle \tilde{\psi}_2 | V_1 | \phi_1 \rangle + \langle \tilde{\psi}_2 | V_2 | \psi_1 \rangle$$

Equation 2.43

ϕ_1 is the incident plane wave, governed by the ideal wave equation and scattered by the potential V_1. ψ_1 is an eigenstate produced by Fresnel theory which is also reflected and transmitted at the interface according to the perturbation V_2. These form waves $\tilde{\psi}_2$, known as time reversed eigenstates. The theory behind the DWBA is given in much greater detail in [18], but the expression for specular scatter, in terms of the Fresnel coefficients F_l^R, and using Gaussian statistics to represent the roughness, is given below:

$$\left|R(\mathbf{k})\right|^2 = F_l^R \exp(-q_z q_z' \sigma^2)$$

Equation 2.44

where σ is the roughness, q_z and $q_z^{'}$ are the wavevectors reflected off the surface and within the medium respectively. The similarity with the Born approximation and *Equation 2.41* is clear and this result also agrees with calculations performed by Névot and Croce [25] using a different method.

The DWBA predicts experimental results very well in the small scattering vector regime, close to the critical angle. However it diverges for higher scattering vectors where it over predicts scattering. In this regime the Born approximation is more valid.

Using second order perturbation theory, de Boer [26] showed that both solutions are just the limiting cases of a more general (but complex) form of the specular component.

Analogous to *Equation 2.34* derived within the BA, the differential cross section for the diffuse scatter is given below:

$$\left(\frac{d\sigma}{d\Omega}\right) = L_x L_y \frac{\left|\mathbf{k}_o{}^2(1-n)^2\right|^2}{16\pi^2} |T(\mathbf{k}_1)|^2 |T(\mathbf{k}_2)|^2 S(q_t)$$

Equation 2.45

$|T(\mathbf{k}_i)|$ are the Fresnel coefficients for the incident (i=1) and scattered (i=2) waves (missing from *Equation 2.34* for the BA), which allow scattering near the critical angle to be modelled accurately. $S(\mathbf{q})$ is defined elsewhere [18] and contains the height difference function as described in *Section 2.7.2*. In general the solution to the Fourier transform for $S(\mathbf{q})$ does not have any analytical solution and so it must be calculated numerically, a method which is computationally expensive. Wormington [27] developed a method based on a series of look-up tables; this software can be used to simulate diffuse scatter and has been used to do so in *Chapter 4*.

2.8 Additional X-ray Techniques

2.8.1 Resonant X-ray Scattering

In *Section 2.2.2* the classical Thomson atomic scattering factor was introduced to quantify the scattered radiation from a charge distribution. Although the scattering factor was later expanded to include anomalous dispersion correction terms, these were neglected since the discussion assumed X-ray energies away from the absorption edges. In such a regime the classical model of a free electron cloud is an adequate description since the Thomson form factor is real. However, to include the correction terms and the necessary imaginary component required for absorption, it is necessary to revise this simple model. The most obvious step is to account for the fact that electrons are not free but rather bound in atoms. Indeed both dispersion and absorption corrections are dominated by the tightly bound inner electrons and are described in the next section,

where even a simple oscillatory model is sufficient to present the scattering factor in the following form:

$$f(\mathbf{q},\omega) = f_0(\mathbf{q}) + f'(\omega) + if''(\omega)$$

Equation 2.46

Due to the spatial confinement of the inner electrons there is no appreciable **q** dependence and so f' and f'' are denoted as functions of X-ray energy only.

2.8.1.1 Oscillatory Model

The first model to be discussed is the forced charged oscillator where we consider the classical description of an electron bound in an atom. This description is widely publicised and here we follow the work of James [11] and Als-Nielsen *et al.* [6].

Assuming the incident X-ray beam has its electric field polarized in the x-plane: $\mathbf{E_{in}} = \hat{\mathbf{x}} E_o e^{-i\omega t}$, the equation of motion for an electron driven by this field is:

$$\ddot{\mathbf{x}} + \Gamma\dot{\mathbf{x}} + \omega_s^2\mathbf{x} = -\left(\frac{eE_0}{m}\right)e^{-i\omega t}$$

Equation 2.47

where ω_s is the resonant frequency of the oscillating electron, Γ is the damping constant and $\Gamma\dot{\mathbf{x}}$ represents the velocity dependent energy dissipation. The solution to this equation is $\mathbf{x}(t) = \mathbf{x_0}e^{-i\omega t}$, and so reveals the amplitude of the forced electron oscillations as:

$$\mathbf{x}_o = -\left(\frac{eE_o}{m}\right)\frac{1}{(\omega_s^2 - \omega^2 - i\omega\Gamma)}$$

Equation 2.48

The radiated field strength at a distance r and t is given by $\hat{x}(t-(r/c))$ and so by modifying *Equation 2.2*:

$$E_{rad}(r,t) = -\frac{mr_o}{er}\ddot{\mathbf{x}}\left(t - r/c\right)$$

Equation 2.49

and thus:

$$\frac{E_{rad}(r,t)}{E_{in}} = -\frac{r_o}{r}\frac{\omega^2}{(\omega^2-\omega_s^2-i\omega\Gamma)}e^{ikr}$$

Equation 2.50

Since the atomic scattering factor f_S, is defined as the amplitude of the outgoing wave, it can be written in terms of the Thomson scattering length r_o, for a single electron, as:

$$f_s = \frac{\omega^2}{(\omega^2-\omega_s^2+i\omega\Gamma)}$$

Equation 2.51

If this is then re-written into the form of *Equation 2.46*, we have:

$$f = f_o + \frac{\omega_s^2(\omega^2-\omega_s^2)}{(\omega^2-\omega_s^2)^2+(\omega\Gamma)^2} - \frac{i\omega_s^2\omega\Gamma}{(\omega^2-\omega_s^2)^2+(\omega\Gamma)^2}$$

Equation 2.52

The frequency dispersion corrections have been modelled in *Figure 2.9* for a single electron oscillator model. In this model $\Gamma = 0.1\omega_s$.

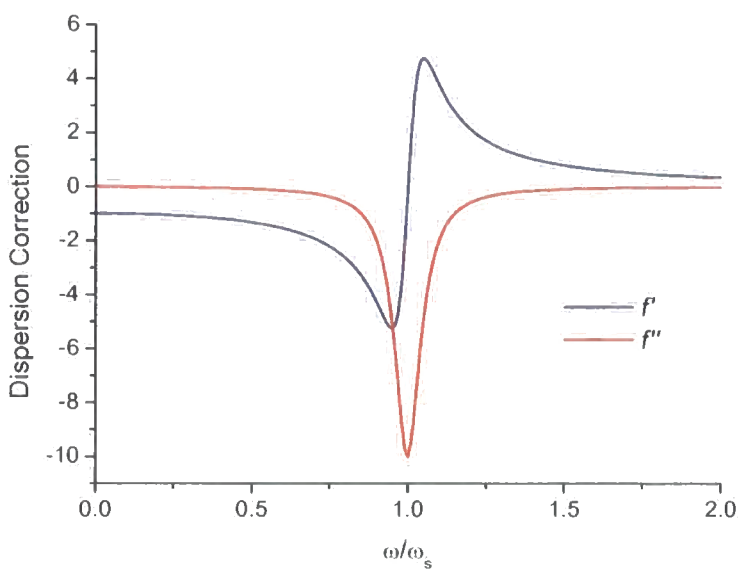

Figure 2.9: *The real f', and imaginary f'', parts of the dispersion corrections as a function of frequency ω relative to the resonant frequency ω_s, calculated using the single oscillatory model.*

From *Equation 2.12* it is clear that the imaginary part of the atomic scattering length is proportional to the absorption coefficient β. Therefore the absorption cross section can also be expressed in terms of the incident X-ray frequency ω:

$$\sigma_s(\omega) = 4\pi r_o c \frac{\omega_s^2 \Gamma}{(\omega^2 - \omega_s^2)^2 + (\omega\Gamma)^2}$$

Equation 2.53

The damping constant is small in comparison with the resonant frequency and so the effective absorption cross-section is defined as a delta function.

$$\sigma_s(\omega) = 2\pi^2 r_o c \delta(\omega - \omega_s)$$

Equation 2.54

If only a single discrete state existed this model would be a satisfactory description. However, there is a continuum of excited free states. Above the absorption edge the electron can be excited into any one of these states, each with a different characteristic frequency ω_s. The system can therefore be modelled as an assembly of oscillations and so the absorption cross section in *Equation 2.54* is generalised to:

$$\sigma_s(\omega) = 2\pi^2 r_o c \sum_s g(\omega_s)\delta(\omega - \omega_s)$$

Equation 2.55

where $g(\omega_s)$ is the relative weight of each transition.

2.8.1.2 A Quantum Mechanical Description

This section will now introduce quantum mechanics as a tool for understanding resonant scattering and thus some of the possibilities and applications this technique can offer.

In deriving the absorption cross-section the key quantity to define is the transition probability *W*. Using first-order perturbation theory:

$$W = \frac{2\pi}{\hbar} \left| \langle f | H_I | i \rangle \right|^2 \rho(E_f)$$

Equation 2.56

The Hamiltonian H_I, describes the interaction between the X-ray photon and the electron between its initial $|i>$ and final $|f>$ state. If the electron spin is neglected, H_I is given by:

$$H_I = \frac{e\mathbf{A}\cdot\mathbf{p}}{m} + \frac{e^2A^2}{2m}$$

Equation 2.57

The vector potential **A** describing the photon field is linear in the photon annihilation and creation operators and so the first term in the Hamiltonian indicates the possibility of a photon either being destroyed or created. This is photoelectric absorption shown in *Figure 2.10a).*

The Hamiltonian's second term is quadratic in **A** and therefore allows for the possibility of a photon being destroyed followed by a photon being created while leaving the electron in its initial state. This describes Thomson scattering as shown in *Figure 2.10b).*

In order to describe resonant scattering one must turn to second order perturbation theory:

$$W = \frac{2\pi}{\hbar}\left|\langle f|H_I|i\rangle + \sum_{n=1}^{\infty}\frac{\langle f|H_I|n\rangle\langle n|H_I|i\rangle}{E_i - E_n}\right|^2 \rho(E_f).$$

Equation 2.58

From the second term in *Equation 2.58* we see that scattering is possible via an intermediate state. The incident photon is first destroyed exciting the electron to an intermediate state $|n>$, the electron subsequently decays producing a scattered photon. Again this process has been displayed graphically in *Figure 2.10c).*

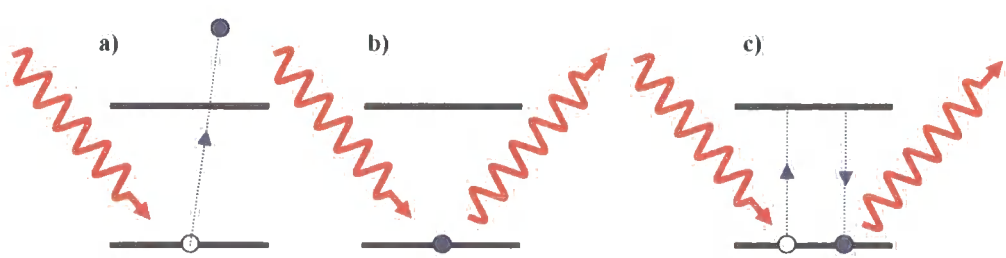

Figure 2.10: a) *Absorption,* ***b)*** *scattering and* ***c)*** *resonant mechanisms.*

Resonant scattering is effectively a probe of the intermediate atomic states. Due to the denominator in *Equation 2.58*, resonance occurs whenever the incident photon energy matches the transition energy. The allowed transitions are governed by quantum mechanical selection rules which infer that electric dipole transitions dominate and by the Pauli exclusion principle, require that only unoccupied states are allowed as possible transitions states.

This model, in addition to the previous damped oscillatory model, demonstrates the resonance dependence on the atomic level structure. Resonant scattering techniques are therefore element sensitive and, with the tunability of the synchrotron sources, can be exploited for scattering enhancement from a specific element. This can dramatically enhance the scattering contrast between layers and is known as resonant X-ray scattering.

At energies away from the absorption edge, dispersion is negligible and so the difference in scattering cross section is simply related, via a Fourier transform, to the difference between the electron densities. In the case of Co and Cu (or Fe) this is less than 1 % which results in low scattering contrast between layers leaving X-ray scattering techniques insensitive to the interface structure. This is a serious problem in analyzing many popular layered systems (as we shall see in *Chapter 3*).

Another application is found through the different influences which can affect these resonant intermediate states. For example, they may be split through magnetic interactions and so therefore X-ray scattering techniques can be applied to the study of magnetic order. Soft X-ray magnetic anomalous scattering is a relatively new field of study both experimentally and theoretically, and will be discussed in much greater detail in *Chapter 6* and *Chapter 7*.

2.8.2 X-ray Fluorescence

Thus far we have mainly been concerned with X-ray scattering. However it is absorption which is of importance in X-ray Fluorescence. Fluorescence will occur whenever the incident radiation is of sufficient energy to excite electrons to higher energy states. The subsequent atomic decay can cause fluorescence to be non-radiative

with Auger emission, in which the energy from the electron decay into the 1s state is used to excite an electron from another s-shell. While Auger emission remains linear with atomic number, fluorescence is proportional to the atomic number to the fourth power. The emitted photon has an energy equivalent to the difference between the two binding energies from the corresponding states. Therefore because each element has a distinctive set of energy levels, the energy of the photon emitted has an identifying signature unique to that particular element. Castaing's approximation [28] makes the assumption that fluorescence peak intensity is proportional to element concentration and so we have a non-destructive technique capable of measuring quantitatively the elemental composition within a sample. An example of a fluorescence spectrum is shown in *Section 3.7.2*, used to determine the relative amounts of Co and Cu within a series of spin-valves. Since this technique is fast and relatively simple, it is popular in many field applications and within industry for production control.

A powerful application to XRF is called grazing incidence X-ray fluorescence (GIXF), which combines the element identification with depth sensitivity using a grazing incident X-ray beam. For further information related to GIXF the reader is referred to [29, 30].

2.8.3 Introduction to X-ray Diffraction

Diffraction techniques are capable of measuring several important crystallographic parameters. One of the most important applications in the context of thin metallic films concerns the study of epitaxial quality, determined by the shape and distribution of the diffraction peaks within reciprocal space. For example, consider a simple double layered material with each layer possessing different d-spacings. A diffraction pattern will contain two diffraction peaks, one for each periodicity, with the separation of the peaks being dependent on the difference in the d-spacing. If there is any kind of angular tilt between the layer's crystal planes, then the diffraction peaks will be off-set with respect to each other in q_x, with the angle between the peaks in reciprocal space equal to the angle between the planes. If the crystals have a mosaic (i.e. composed of regions of flat crystallites at small angles to each other) the diffraction peaks broaden in q_x.

Although we have only discussed single crystal diffraction, powder diffraction is far more common. A typical powdered structure will consist of a large number of small crystallites which are randomly orientated with respect to each other. These polycrystalline samples will then produce reflections from all of the individual *hkl* planes suitably orientated within the sample. A complete powder diffraction pattern can be used to determine the crystal lattice dimensions and the presence of microstructure effects, such as lattice misorientation, domain or grain size and strain.

One of the primary causes of peak broadening originates from the finite size of the diffracting material. Size effects can arise from domain or grain structure; their affect on the peak broadening is given by the Scherrer equation:

$$\Delta_{SIZE}(2\theta) = \frac{\kappa\lambda}{D\cos(\theta_B)}$$

Equation 2.59

where $\Delta(2\theta)$ is the FWHM of the diffraction peak (in radians) and θ_B is the peak position, λ is the wavelength, κ is a constant that depends on the peak shape profile and D is the grain size. The peak width can also increase due to strain on the lattice within the crystal or powder, according to the differential of Bragg's law:

$$\Delta_{STRAIN}(2\theta) = 2\varepsilon \tan(\theta_B)$$

Equation 2.60

where $\Delta(2\theta)$ is the FWHM of the diffraction peak (in radians), θ_B is the peak position and ε is the micro-strain dispersion.

Thin film polycrystalline structures are studied using diffraction in *Chapter 5* with particular focus on the strain and grain size. Williamson-Hall plots are introduced as a method by which to differentiate between strain and grain size, both of which increase peak width. They are discussed further with examples in *Section 5.6.3.1.*

2.8.3.1 High Angle X-ray Diffraction (HXRD)

High angle diffraction scans are the most common form of diffraction experiment. They consist of coupled $\theta/2\theta$ scans, similar to the low angle reflectivity scans described in *Section 2.6*. Like specular scans the scattering vector has a purely out-of-plane component, giving diffraction from planes parallel to the surface. The high angle geometry allows determination of repeater units on a scale much smaller in comparison to, for example, layer thickness. For a more detailed description of HXRD the reader is referred to the following publications [6, 8, 31].

2.8.3.2 Grazing Incidence In-Plane X-ray Diffraction (GIIXD)

Below the critical angle, grazing incident diffraction gains sensitivity due to the limited penetration depth of the evanescent wave. The detector and sample are scanned in a ratio of 2 to 1 in the plane of the sample, and so the in-plane scattering vector gives diffraction from planes perpendicular to the surface. The scan geometry for GIIXD can be seen below in *Figure 2.11*:

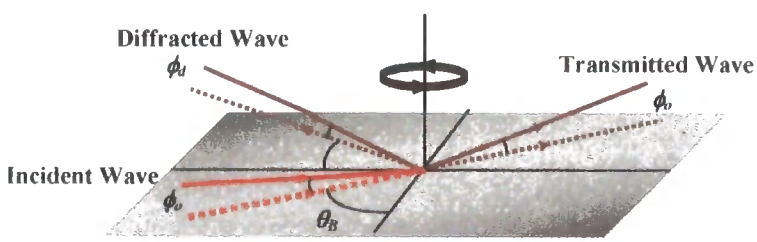

Figure 2.11: *Scanning geometry used for GIIXD.*

GIIXD can therefore be used to investigate the in-plane crystallographic structure, again determining factors such as texture, grain size and strain. This method is used and discussed is much greater detail in *Section 5.6.3.1*.

2.9 X-ray Sources and Facilities

2.9.1 Electron Impact Devices

The standard X-ray tube in use today has changed very little since its development in 1912. W.D. Coolidge [3] from General Electric Research Laboratories in New York had used a filament to accelerate electrons into a water-cooled metal anode.

The main limitation with this device was the efficiency with which the target anode could be kept cool. Although water was used initially, it was realised that the cooling efficiency could be improved further by rotating the anode. However the technical difficulties in building a vacuum-sealed high frequency rotating shaft kept the rotating anode source at bay until the 1960s.

Electron impact devices produce X-ray spectra with two distinctive components. The first of which is known as *bremsstrahlung* radiation (from the German for braking), which consists of a continuous spectrum due to the deceleration (due to inelastic scattering) of the electrons through the anode target [6]. The second component is a set of sharp lines, their energies specifically dependent on the composition of the target anode. The impact of an electron can remove one of the atomic electrons from the lower shell, the resulting vacancy will then cause the relaxation of an electron from a higher shell and thus fluorescence radiation with a characteristic energy due to the energy difference between the shells. For experimental purposes the emitted radiation has to be monochromated, usually to one of the atomic emission lines where the intensity is several orders of magnitude greater than the *bremsstrahlung*.

2.9.1.1 GXR1 Reflectometer

Many of the measurements presented here have been made with the *Bede GXR1* reflectometer. This equipment uses a 2.2 kW Cu X-ray tube as a source. A channel-cut Si (111) double-bounce crystal monochromates the X-rays to the K_β emission line. Slits then collimate the beam to a height of ~100 μm and an adjustable width. The sample table and detector are mounted on cradles, which are controlled by stepper motors. Additional motors, necessary for alignment, are controlled in the same way.

The detector used on the GXR1 is a *Bede EDRa* scintillation detector [32] capable of a high dynamic range with a high photon flux and low background. This detector, based on the scintillation material yttrium aluminate is appropriate for use in the energy range 5-40 keV. For a single X-ray photon absorbed, the scintillator emits a light pulse. The signal is then amplified via electronics with an output in counts per second. A typical saturation rate of approximately 750,000 c.p.s. is given with a dead time of only τ=390 ns. Dead time corrections can be made with *Equation 2.61*:

$$R_{MEASURED} = R_{REAL} \exp(-R_{REAL}\tau)$$

Equation 2.61

2.9.2 Synchrotron Sources

In the early 1970s it was realised that the emitted radiation from accelerating charged particles in synchrotrons and storage rings would make better X-ray sources in comparison to the earlier lab sources previously discussed. Although these rings were initially built for high-energy nuclear experiments, there are now facilities all over the world constructed explicitly for the production of X-rays. The development of synchrotron radiation facilities has marked a significant turning point in the use of X-ray techniques. With a broader energy spectrum, combined with greater beam quality and a huge increase in flux, synchrotron radiation allows for a range of experiments that have previously been impossible.

All synchrotron facilities share the same basic characteristics; a linear accelerator injects charged particles into a booster ring where they are further accelerated into a main storage ring. Electrons in the storage rings are kept in a stable orbit by means of a series of bending magnets (Lorentz force) located around the ring [3, 33]. The strength of the bending magnets is dependent on the energy of the electrons and the radius of the ring.

As the electron beam travels round the main storage ring energy will be lost and in order to compensate, radio frequency, r.f. cavities have been introduced. These devices are tuned to the revolution frequency (typically a few MHz) restoring energy to the beam.

The actual radiation is produced at the bending magnets, and at insertion devices such as wigglers or undulators located in the straight parts of the ring. Insertion devices are a series of magnets, which alternate the magnetic field as experienced by the electrons. This results in the beam oscillating rather than travelling in a straight line. In a wiggler the radiation from each 'wiggle' is simply added to give an overall intensity but undulators are designed such that radiation emitted from one electron oscillation is in phase with the other oscillations. The emitted radiation is therefore coherent. For information concerning insertion devices and other X-ray sources the reader is referred to [3, 6].

2.9.2.1 Station 2.3, Daresbury SRS, U.K.

The Daresbury Synchrotron Radiation Source (SRS) facility consists of a 2 GeV electron storage ring serving 36 stations. Although station 2.3 was originally designed for powder diffraction it can be used for single crystal diffraction as well as low angle reflectivity experiments. The beamline includes two high accuracy encoded circles, which are under independent servo-control. Vertical and rotational motors are also available and are required for sample alignment.

The station is positioned 15 metres from a 1.2 Tesla bending magnet. The wavelengths available range from 0.5 to 2.5 Å, reaching a maximum intensity at 1.3 Å. The white X-ray beam is monochromated using a double bounce Si (111) channel-cut crystal, the crystal being water cooled to maintain a constant temperature of 303±0.1 K. After monochromation the beam has a vertical divergence of approximately 0.5 mrads. It is important to note that the X-ray beam does suffer some contamination at longer wavelengths since the two monochromator reflections are not offset for harmonic suppression. This results in a strong contamination due to the Si (333) reflection at $\lambda/3$.

In order to account for the beam decaying, there is a beam monitor just after the post-monochromator slits. The final data can then be normalised to the monitor.

The figure below shows the complete set-up for station 2.3. Beam-defining slits are found before and after the monochromator to ensure the position of the beam remains constant with wavelength and beam decay. There are two sets of slits on the detector arm, the anti-scatter and analyser slits. These slits define the instrument resolution; reflectivity measurements use a typical slit height of 300 μm.

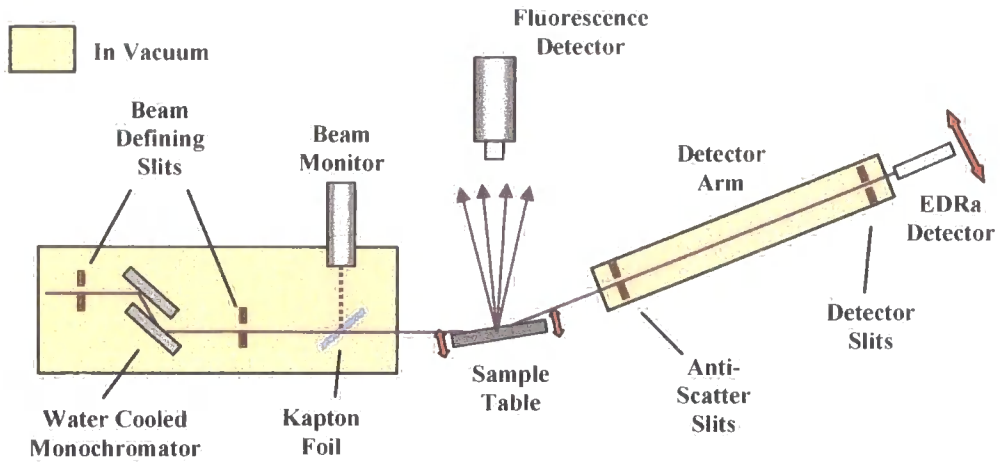

Figure 2.12: *Set-up for Station 2.3, Daresbury SRS.*

To reduce air-scatter as much as possible, the bulk of the line is kept under vacuum. In soft X-ray beamlines (such as 5U1, see *Section 6.3*) it is essential to have the whole line, including the sample stage, in vacuum. The EDRa detector used at this station is similar to the detector described earlier for the GXR1.

2.9.2.2 X-ray Magnetic Scattering (XMaS) Beamline - BM28, ESRF, France

The XMaS beamline at BM28 is located on the European Synchrotron Radiation Facility (ESRF), a 3rd generation synchrotron facility with 40 beamlines. The main storage ring has a circumference of 850 metres and the booster operates at 6 GeV. This provides a far wider range of wavelength with greater intensity and higher brilliance at higher energies compared with the Daresbury SRS.

The XMaS beamline was designed for magnetic and high-resolution experiments. The optics monochromate and focus the X-ray beam with an energy range between 3 and 1 keV. A two crystal Si (111) monochromator is, in combination with a toroidal focussing mirror, used to condition the beam. A flux of 10^{12} c.p.s. is possible with a horizontal and vertical divergence of 0.16 ° and 0.01 ° respectively.

A 4-circle, 11-axis *Huber* diffractometer allows for a wide range of experiments. The four encoded circles provide high precision in the vertical and horizontal plane. The vertical axes allow reflectivity and high-angle diffraction experiments, and the

horizontal axes allow for grazing incidence diffraction. A photo of the diffractometer can be seen in *Figure 2.13*:

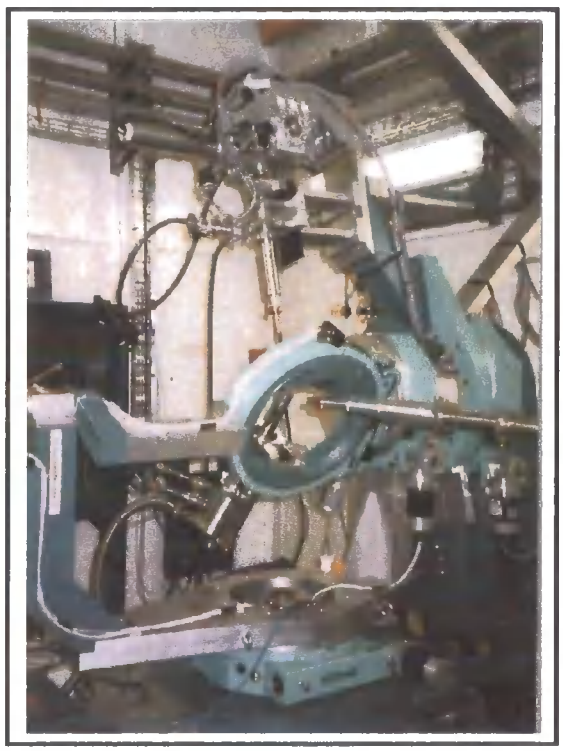

Figure 2.13: *The 11-axis Huber diffractometer at XMaS (BM28) at the ESRF.*

2.10 Magneto-Optical Kerr Effect (MOKE)

The magnetic optical Kerr effect (MOKE) is used as a magnetic characterisation technique, measuring magnetisation - field (M-H) loops or even imaging magnetic domain structure. This technique, based on the Kerr effect, involves a rotation of linearly polarised light dependent on the magnitude and direction of magnetisation. The linearly polarised light incident on the sample is usually from a He/Ne laser and the reflected light is then analysed through a crossed polarizer orientated at 90 ° to the incident beam-defining polarizer. The intensity detected by the photodiode then defines the rotation in polarisation.

One of the problems with MOKE is that the angle of rotation is usually very small and so there is little contrast between the adjacent domains. In addition, due to the

relatively low penetration depth of the incident light, this technique is only surface sensitive to approximately 200 Å.

There are 3 different types of MOKE measurements; polar, longitudinal and transverse depending on the relative orientation of the magnetisation with respect to the beam and the plane of the surface. In the polar Kerr effect the magnetisation is orientated perpendicular to the surface and although the rotation in this configuration is at a maximum the demagnetizing energy favours magnetisation in the surface plane and so without sufficient anisotropy this method can not be used. The more common measurements are made with the magnetisation vector being parallel to the plane of the sample and either parallel (longitudinal) or perpendicular (transverse) to the incident beam. The combination of vector magnetometry with spatial resolution allows the surface magnetic structure to be mapped, building up an image of the domain structure [34] and magnetic anisotropy [35].

2.11 Sputtering

During the sputtering process, target atoms are ejected from a target material due to the bombardment of energetic ions or high-speed atoms. This process has been illustrated in *Figure 2.14*:

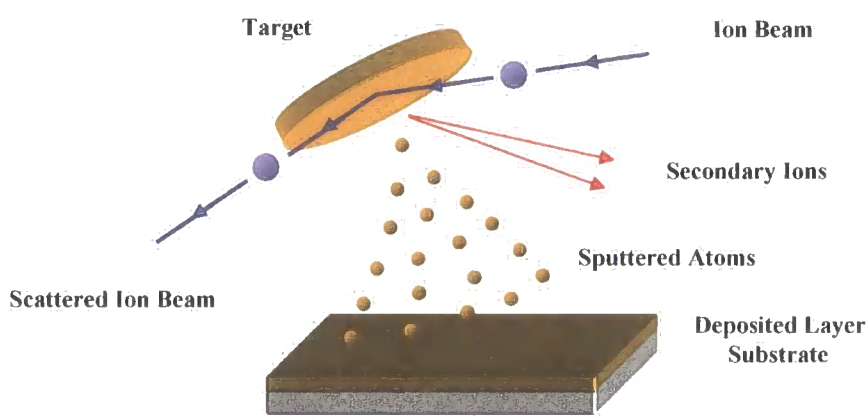

Figure 2.14: *Schematic of the basic sputtering deposition process.*

Sputtering has a threshold energy; if the energy of the incoming ion or atom is too small then sputtering will never occur. This threshold is the atomic binding energy, which depends on the sputtered material and in most cases is in the order of a few eV. It

is related to the heat of sublimation, as sputtering is after all the change of state from solid to gas.

The sputter yield, defined as the number of atoms sputtered per incident ion, determines the rate at which the film is being deposited. For incident ions of energy around 1 keV, the sputtering yield is in the order of unity. The angle of incidence for the ions or high-speed atoms is also a crucial factor in determining the sputter yield and can be varied to alter the rate of deposition. Not all materials have the same angular dependence, and so when combined with the variation in binding energy, the task of depositing alloys to precise ratios becomes a complex and skilled procedure.

Usually the sputtering chamber is in an argon atmosphere, the pressure influencing the yield. The surface temperature of deposition can also affect the morphology of the deposited film. In some cases these growth factors are varied to induce roughness and sample defects. By varying the incident flux, roughness can be induced across a surface. In general, sputtered layers usually have high values for the fractal parameter h ($\approx 0.6 - 1$). The sputtering process can also be used to remove surface roughness due to erosion effects. If the sputtered ions are incident at oblique angles then roughness features on the surface are removed, resulting in a general smoothing over the surface.

For a more detailed description concerning sputtering [36] and the specifics involved in growing thin films, the reader is referred to Roy *et al.* [37].

2.12 References for Chapter 2

1. W. Rontgen (1896) "*Uber ein neue Art von Strahlen (About a new Type of Rays)*" Nature **53** pg. 274.

2. L. Bragg (1975) "*The Development of X-ray Analysis*" Dover Publications Inc.

3. A.G. Michette and C.J. Buckley (1993) "*X-ray Science and Technology*" Institute of Physics Publishing.

4. M. Kuriyama (1969) "*The Dynamical Scattering Amplitude of an Imperfect Crystal*" Acta. Cryst. **A25** pg. 56.

5. M. Kuriyama (1972) "*The Dynamical Scattering Amplitude of an Imperfect Crystal. II. A Relation Between Takagi's Dynamical Equation and a More Exact Dynamical Equation*" Acta. Cryst. **A28** pg. 588.

6. J. Als-Nielson and D. McMorrow (2001) "*Elements of Modern X-Ray Physics*" Wiley.

7. B.H. Bransden and C.J. Joachain (1983) "*Physics and Atoms and Molecules*" Longman Group Limited.

8. A. Guinier (1994) "*X-ray Diffraction in Crystals, Imperfect Crystals and Amorphous Bodies*" Dover Pub.

9. W.H. Zachariesen (1994) "*Theory of X-ray Diffraction in Crystals*" Dover Publications.

10. C. Kittel (1986) "*Introduction to Solid State Physics*" 6th Edition, Wiley & Sons.

11. R.W. James (1948) "*The Optical Principles of the Diffraction of X-rays*" G. Bell and Sons Ltd.

12. E. Hecht (2002) "*Optics*" 4th Edition, Addison Wesley.

13. L.G. Parratt (1954) "*Surface Studies of Solids by Total Refection of X-Rays*" Phys. Rev. **95** pg. 359-369.

14. H.D. Bale and P.W. Schmidt (1984) "*Small Angle X-ray Scattering Investigation of Submicroscopic Porosity with Fractal Properties*" Phys. Rev. Lett. **53** pg. 596-599.

15. I. Pape, T.P.A. Hase, B.K. Tanner, and M. Wormington (1998) "*Analysis of grazing incidence X-ray diffuse scatter from Co-Cu multilayers*" Physica B. **253** pg. 278-289.

16. M. Wormington (1999) "*Characterisation of structures from X-ray scattering data using genetic algoritms*" Philos T Roy Soc A **357** pg. 2827-2848.

17. H.E. Stanley and A.-L. Barabasi (1995) "*Fractal Concepts in Surface Growth*" Cambridge University Press.

18. S.K. Sinha, E.B. Sirota, S. Garoff, and H.B. Stanley (1988) "*X-ray and neutron scattering from rough surfaces*" Phys. Rev. B **38** (4) pg. 2297-2311.

19. P. Bruno and C. Chappert (1991) "*Oscillatory coupling between ferromagnetic layers separated by a nonmagnetic metal spacer*" Phys. Rev. Lett. **67** pg. 1602-1605.

20. R. Stommer, J. Grenzer, J. Fischer, and U. Pietsch (1995) "*X-ray diffuse scattering in Langmuir-Blodgett multilayers prepared from fatty acid salts*" J. Phys D: Appl Phys **28** pg. A216-A219.

21. G. Palasantzas and J. Krim (1993) "*Effect of the form of the height-height correlation function on diffuse x-ray scattering from a self-affine surface*" Phys. Rev. B **48** (5) pg. 2873-2877.

22. G. Palasantzas (1994) "*Finite-size effects on self-affine fractal surfaces due to domains*" Phys. Rev. B **49** (15) pg. 10544-10547.

23. G. Palasantzas (1993) "*Roughness spectrum and surface width of self-affine fractal surfaces via the K-correlation model*" Phys. Rev. B **48** (19) pg. 14472-14478.

24. A. Gibaud, N. Cowlam, G. Vignaud, and T. Richardson (1995) "*Evidence of Self-Affine Rough Interfaces in a Langmuir-Blodgett Film from X-Ray Reflectometry*" Phys. Rev. Lett. **74** (16) pg. 3205-3208.

25. L. Nevot and P. Croce (1980) "*Caracterisation des surfaces par reflexion rasante de de rayons X. Application a l'etude du polissage verres silicates.*" Revue Phys. Appl. **15** (761-779) pg.

26. D.K.G. de Boer (1994) "*Influence of the roughness profile on the specular reflectivity of x-rays and neutrons*" Phys. Rev. B **49** (9) pg. 5817-5820.

27. M. Wormington *PhD Thesis,* University of Warwick.

28. K. Durose (2000) "*Solid State Analytical Techniques - Lecture Notes (Durham)*" pg.

29. T.P.A. Hase, B.K. Tanner, P.A. Ryan, C.H. Marrows, and B.J. Hickey (1998) "*Determination of the Copper Layer Thickness in Spin Valves by Grazing Incidence X-ray Fluoresence*" IEEE Trans. Magn. **34** pg. 831-833.

30. K.N. Stoev and K. Sakurai (1999) "*Review of grazing incidence x-ray spectrometry and reflectometry*" Spectrochim. Acta. B **54** (1) pg. 41-82.

31. B.E. Warren (1990) "*X-ray Diffraction*" Dover Pub.

32. S. Cockerton and B.K. Tanner (1995) "*A New High Dynamic Range X-ray Detector*" Advances in X-Ray Analysis **38** pg. 371-376.

33. N.W. Ashcroft and N.D. Mermin (1976) "*Solid State Physics*" Saunders College Publishing.

34. H. Niedoba, B. Mirecki, M. Jackson, S. Jordan, S. Thompson, J.S.S. Whiting, P. Djemia, F. Garnot, P. Moch, T.P.A. Hase, I. Pape, and B.K. Tanner (1996) "*Magnetization Process and Magnetic Properties of Co/Cr/Co Trilayers*" Phys. Stat. Sol. A **158** (1) pg. 259-264.

35. S.M. Jordan and C. Prados (1997) "*New technique to measure magnteic anisotropy using the vectorial magneto-optic Kerr effect*" J. Magn. Magn. Mater. **172** (1-2) pg. 69-73.

36. C.H. Marrows (1997) *PhD Thesis,* University of Leeds.

37. R.A. Roy and R. Messier (1984) "*Preparation-physical structure relations in SIC sputtered films*" J. Vac. Sci. Technol **A2** pg. 312-315.

Chapter 3

A Detailed Characterisation of GMR Spin-Valves

3.1 Introduction

This chapter will introduce the reader to some of the experimental procedures outlined theoretically in *Chapter 2*. During the course of this study an important set of Magneto-Resistive (MR) devices called spin-valves are structurally characterised. The concept and theory behind MR devices are explained with particular emphasis on Giant Magneto-Resistance (GMR). Spin-valves and GMR multilayers are then described in great detail, with a literature summary to assess some of the difficulties involved in their development, a research field driven by the magnetic recording industry.

In this study, a series of nominally identical sputtered spin-valves have been analysed with the aim of explaining the reasons for varied GMR by attempting to correlate this variation to structural differences. The power and application of X-ray techniques as a non-destructive characterisation tool is thus demonstrated. *Section 3.7* describes the various experimental procedures including specular, off-specular longitudinal diffuse, transverse diffuse and fluorescence. These data are then used to model a suitable structure for each of the spin-valves. Finally a NiO layer is analysed directly, using the same characterisation techniques, to assess it as a potential factor for explaining the variation in GMR.

3.2 Introduction to GMR

The MR effect arises from changes to the resistance of a device through the application of an external magnetic field. Although there are different forms of MR,

GMR is of interest here since the changes in resistance are much larger than those found in normal materials. The definition of MR is:

$$MR = \frac{\rho_s - \rho_o}{\rho_o} = \frac{\Delta\rho}{\rho_o}$$

Equation 3.1

where ρ_o and ρ_s are the resistances of the material in zero and saturating fields respectively.

Baibich *et al.* [1] and Binasch *et al.* [2] simultaneously discovered GMR in 1988 when they observed that the resistance of anti-ferromagnetically (AF) coupled Fe/Cr systems reduced by a factor of two upon the application of a strong external saturating field, sufficient to re-orientate the Fe magnetic layers to a parallel alignment. The normal Anisotropic Magneto-Resistance (AMR) found in such multilayers was insufficient to explain the magnitude of the observed MR and so the effect was correctly attributed to spin-dependent scattering in the coupled magnetic layers and the subsequent difference in device resistance with the layer magnetisation aligned parallel or anti-parallel.

The initial AF interlayer exchange coupling responsible for GMR was discovered two years earlier, by Grunberg *et al.* [3], who had observed anomalous coupling between the Fe layers in a series of Fe/Cr/Fe trilayers. It was found that for a certain Cr spacer layer thickness the Fe layers would couple anti-ferromagnetically. In 1990, Parkin *et al.* [4] demonstrated that this AF coupling, and thus GMR, was not restricted to Fe/Cr systems, but was also found in Co/Cr and Co/Ru multilayers. It was also shown to follow (with GMR) an oscillatory pattern as a function of the non-magnetic spacer layer thickness. There have been many attempts to explain theoretically the oscillatory exchange coupling, with the Ruderman-Kittel-Kasuya-Yosida (RKKY) type interaction being the most favoured [5, 6]. This type of exchange couples moments over relatively large distances and is the dominant exchange interaction where there is no direct overlap between the coupled magnetic electrons. It thus acts through an intermediary, which in the case of multilayers or spinvalves is found in the conduction electrons from the non-magnetic metal spacer layer. The exchange oscillates from positive to negative, and therefore, depending on the separation between the ions or magnetic layers, may result in ferro or anti-ferromagnetic coupling.

3.2.1 Spin-Dependent Scattering

The GMR effect is explained through spin-dependent scattering, a phenomenon determined by the density of states at the Fermi energy. In the case of transition metals the important electron scattering occurs in and between the 4s and 3d bands. In ferromagnetic materials the 3d band structure is exchange split by $\pm\mu_o J$, (where J is the exchange integral). This has been illustrated below in *Figure 3.1* for the basic trilayer system with layer magnetisation both *a)* anti-parallel and *b)* parallel:

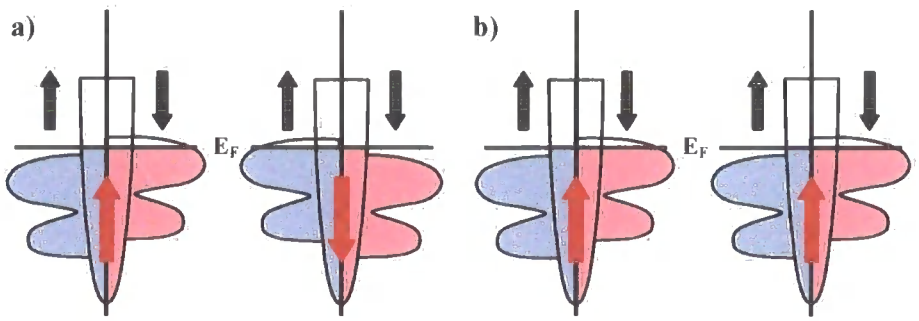

Figure 3.1: *Spin dependent electron energy diagram (s and d bands for spin majority and minority electrons) for each electrode under* ***a)*** *anti-parallel and* ***b)*** *parallel alignment.*

We can now start to visualise the current passing through the device in terms of two channels with spin-up and spin-down electrons. In accordance with Fermi's golden rule, the scattering rates are proportional to the density of states at the state being scattered into (in this case the Fermi level in the 3d-band). These are of course different for electrons of different spin. For spin majority electrons, whose spins are aligned parallel to the magnetisation vector, the electron d-band is at a lower energy and occupied. It is therefore impossible to scatter from the s-band into this d-band due to the unavailability of states, and hence within this spin channel there is a negligible amount of scattering and so minimal resistance. On the other hand, the spin minority electrons have free d-states above the Fermi surface into which they can scatter and so the resistance is much higher. This has been demonstrated below in *Figure 3.2* for the trilayer system under anti-parallel and parallel alignment:

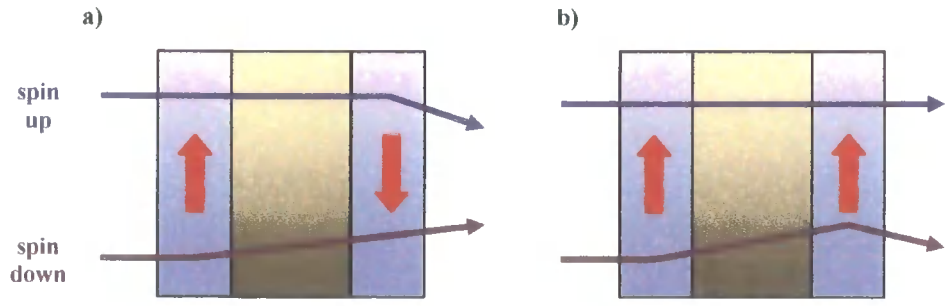

Figure 3.2: *Spin dependent scattering for spin up and spin down electrons for* ***a)*** *anti-parallel and* ***b)*** *parallel alignment.*

This depiction is now reviewed using a simple resistor model.

3.2.2 Resistor Model

When the ferromagnetic layers are aligned antiferromagnetically the scattering and hence the resistance is greater. This can be represented using a basic resistor circuit model as shown below in *Figure 3.3*:

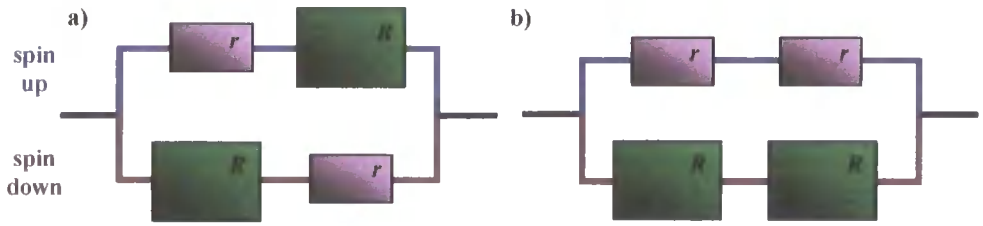

Figure 3.3: *Resistor Circuit Model illustrating how Spin dependent scattering affects resistance for* ***a)*** *anti-ferromagnetic and* ***b)*** *ferromagnetic coupling.*

Here, r represents the resistance for the electrons with spins parallel to the ferro-magnetisation and hence low scattering, where R is the resistance for the spins aligned anti-parallel with high scattering. By adding the resistance in series and parallel it is possible to calculate the overall resistance for the complete system with the ferromagnetic layers coupled ferro and anti-ferromagnetically:

$$\rho_{ap} = \frac{1}{r+R} + \frac{1}{R+r} = \frac{2}{R+r}$$

Equation 3.2

$$\rho_p = \frac{1}{r+r} + \frac{1}{R+R} = \frac{2(r+R)}{(r+r)(R+R)}$$

Equation 3.3

The careful engineering of these devices (with particular emphasis on the non-magnetic spacer layer) will produce two magnetic layers initially coupled anti-ferromagnetically under no applied field. When a sufficient field is applied to overcome this coupling, the orientation of the moments in one of the magnetic layers will "switch" and thus induce parallel ferromagnetic alignment between the two magnetic layers. There is a significant difference in resistance under this moment orientation change and so from the resistor model and the definition of GMR defined earlier in *Equation 3.1*, the GMR can be written as:

$$GMR = \frac{\rho_{ap} - \rho_p}{\rho_{ap}} = 1 - \frac{(r+R)^2}{4rR}$$

Equation 3.4

3.3 Spin-Valves and Magnetic Multilayers

Although the important trilayer system describes the essence of the basic spin-valve, much of the earlier GMR work concentrated on magnetic multilayers. Magnetic multilayers are basically a series of bilayers which have been repeated. The basic bilayer includes a ferromagnetic layer, for example Co, whose thickness is small and on the order of the mean free path of the electron, followed by a non-magnetic spacer layer like Cu. The chemical and magnetic structure of magnetic multilayers such as these have been investigated in *Chapter 6* using soft X-ray scattering and neutron reflectivity.

By varying the thickness of the non-magnetic spacer layer it is possible, as discussed earlier, to change the coupling of the surrounding magnetic layers. However, for extremely thin spacer layers, possible pin-hole formation allows the two layers to be coupled directly and cause ferromagnetic alignment between the magnetic layers. As the thickness of the spacer layer increases the coupling oscillates from ferromagnetic to anti-ferromagnetic alignment. In the case of the Co/Cu multilayer, the 1st order AF coupling is found with a spacer layer thickness of approximately 10 Å. At intermediate values, the coupling can also become bi-quadratic with the moments aligned at 90 ° to each other [7], instead of the ideal 180 °.

It is relatively easy to observe high values of GMR (up to 80 % at room temperature) in magnetic multilayers, however, they have the disadvantage of requiring large fields to overcome the strong exchange coupling between the large number of ferromagnetic layers. For example the Fe/Cr multilayer, grown at the first AF coupling peak, has an extremely large exchange coupling requiring a field in excess of several Tesla to saturate completely the film. This obviously restricts the possible usefulness of these systems in any device application. To maximise the GMR it is important to have first order AF alignment and although the AF magnetic structure is not as well defined with the spacer grown to the second order AF coupling peak, it is sometimes a desirable alternative since the weaker exchange coupling requires a smaller field to switch and saturate the layers into ferromagnetic alignment.

The most effective solution has required the redesigning of the structure to decouple the ferromagnetic layers and remove the strong exchange energy. Here we introduce the so-called spin-valve, based on the fundamental trilayer device described in the previous section. It consists of two ferromagnetic layers separated by a non-magnetic spacer layer. The thickness of the non-magnetic spacer layer is sufficient for the magnetic layers to be decoupled. It is also important to make the coercive field (i.e. the field require to re-orientate or 'switch' the layer moments) different for each layer. This can be achieved using different materials for the two ferromagnetic layers, but is often done by 'pinning' one of the ferromagnetic layers by exchange bias to another magnetic layer. In order to maximise this exchange bias across the interface the pinning layer is usually antiferromagnetic and depending on the specific antiferromagnet used, is either grown below the bottom FM layer or above the top FM layer. In addition, it is sometimes desirable to deposit extra FM layers at the interface to reduce interdiffusion problems and increase the spin polarisation [8], this is called an engineered spin-valve. Although there are variations, the three basic spin-valves have been illustrated below in *Figure 3.4*:

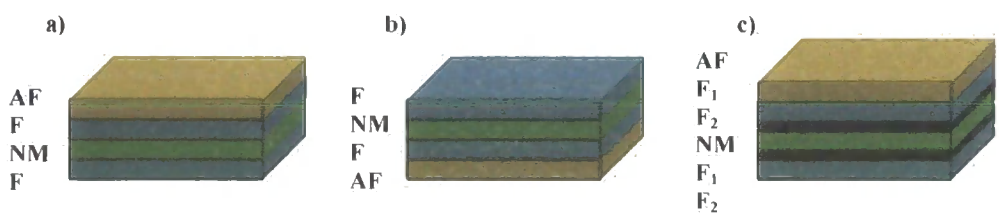

Figure 3.4: *The three basic spin-valves:* ***a)*** *Top Spin-valve* ***b)*** *Bottom Spin-valve and* ***c)*** *An Engineered Spin-valve.*

The magnetisation loop for a spin-valve takes on a step-like function. The unpinned free ferromagnetic layer will switch direction when an external field greater than its coercive field is applied. In the case of a soft magnetic material such as permalloy ($Ni_{81}Fe_{19}$) the coercivity is extremely small with only 20-40 Oe required to switch the resistance from a low to a high state. This is the level of magnetic sensitivity required to read computer disks and such systems are now incorporated into the latest generation of hard disk read-heads. The pinned ferromagnetic layer will only flip direction if the external field exceeds that of the exchange biasing field from the pinning layer. This field is much greater than the coercive field required to flip the free magnetic layer. To introduce unidirectional anisotropy by exchange bias, the FM layer is brought into contact with an antiferromagnet and then cooled through the Neél temperature.

Exchange bias is of considerable importance to many technological applications. It was first discovered in 1956 by Meiklejohn and Bean [9] who observed its characteristic shift in the centre of the magnetic hysteresis loop. Despite its importance, a complete theoretical understanding of the phenomenon has not been reached. For more information the reader is referred to Kiwi's review [10].

3.4 Literature Summary

As we have seen from the previous section, the origins of GMR are well understood. However, there are still a number of issues which remain as yet unsolved, such as the influence of texture, roughness and the reason for different deposition techniques yielding completely different, and often contradictory, results. The difficult problem of relating GMR to chemical and magnetic structure is nothing new and has been an intense area of research since its discovery in 1988 [1, 2], but why is it such a difficult problem and why is it so hard to investigate?

The vital areas of study are those structural features which give rise to any form of electron scattering and depending on the form of scattering (spin-dependent or independent), relate it to GMR. However, correlating any single structural feature to GMR is complicated since scattering mechanisms will occur throughout the sample. For example, experimentally correlating GMR from spin-dependent scattering with interfacial properties is impossible if spin-dependent scattering is also apparent within

the bulk of the sample. Furthermore, any attempt to change a single property will certainly affect other structural aspects, for example, induced changes to the interface properties can also lead to pin-hole formation and so direct magnetic coupling between the magnetic layers. This will consequently reduce the anti-ferromagnetic order between the magnetic layers and hence reduce the GMR.

In much of the literature the focus has been restricted to the study of interface structure, particularly at the magnetic / non-magnetic boundary. Many groups have argued this is the most important structural component to control in order to produce samples with good GMR. It is important for two reasons; firstly roughness at the interface can cause increased spin-dependent or independent scattering, and secondly, samples with a layer thickness comparable to the interface roughness can result in layers with a different 'effective' thickness (a characteristic shared with the magnetic tunnel junctions studied in *Chapter 4*). However, to describe an interface in terms of simply 'roughness' is insufficient. An interface should also include components of intermixing as well as the topological roughness (a distinction made clear in *Chapter 5*) and where possible, the roughness should be modelled to describe its morphology. The entirety of the work presented in this thesis has used Sinha's fractal model [11] to describe the interface, see *Section 2.7.2*.

Scattering from the bulk is also important, for example, in 3d ferromagnetic films the bulk scattering is normally spin-dependent. If the asymmetries in bulk and interface spin dependence are opposite, this can lead to GMR varying in a complex manner due to the interference between the two contributions [12].

One important example addresses the need to understand the different origins of electron scattering and looks at the differences between Fe/Cr and Co/Cu multilayers. Studies [13] show that interface spin-dependent scattering is the dominant scattering mechanism in Fe/Cr multilayers, apparent with increased GMR as a result of increased interface width. This is due to the creation of a virtual bound *d*-state at the Fermi level through the diffusion of Cr in Fe. Cu into Co produces no such bound state and so the effect is just an increase in spin-independent scattering, thus reducing GMR. The spin-dependent scattering in Co/Cu multilayers comes from the bulk, a theory which is supported from the observation [14] that GMR increases with Co layer thickness, as the ratio in bulk to interface scattering increases.

There are of course various methods available to change the interface and/or crystallographic structure within GMR devices, some of the more common methods employed are now reviewed.

3.4.1 Annealing

The process of annealing can form a vital part of crystal manufacture. Through careful control of the annealing temperature and time, this practice can be significant in reducing defects and impurities. In addition, annealing can be used to alter interface structure and several growers [15-17] have used this to induce roughness in Co/Cu samples. The annealing allows for a greater atomic mobility at the interface with the diffusion of Cu atoms into the Co layer. The resultant increase in interface width brought about a rise in the amount of spin-independent scatter and a lowering of GMR.

The same experiments have also been performed on Fe/Cr samples, but with quite different results. Some groups [18, 19] have found that annealing reduced GMR and Rensing *et al.* [12] observed both MR enhancement and suppression but claimed the structural effects were too subtle to be detected by X-ray techniques. Despite this confusion, the majority of published work [13, 20, 21] finds a clear enhancement with annealing and it is now generally accepted that greater interface roughness increases GMR. This confirms spin-dependent scattering at the Fe/Cr interface, a hypothesis confirmed theoretically [22] in which GMR was found to be greater in samples with a higher roughness amplitude and lower in-plane correlation length. Schad *et al.* [20] claimed they could exclusively study the affect of Fe/Cr interface scatter, by arguing their samples had a negligible amount of bulk scatter due to epitaxial growth of ultra clean materials on suitable substrates. They found GMR increased with lower in-plane correlation lengths and increased interface roughness, confirming the theoretical predictions described earlier.

3.4.2 Growth Parameters and Buffers

Perhaps one of the more popular methods of varying the roughness in multilayers and spin-valves is to change the growth parameters. An increased argon gas pressure

was used in the sputtering of Co/Cu multilayers [23] to increase roughness, resulting once again in increased resistance and reduced GMR. However, it should be noted that changing the pressure can also influence texture, an important factor (as discussed in *Section 3.4.4*) in determining spin-dependent and independent scattering.

Observations with Fe/Cr multilayers [13] have also noted an increase in interface roughness with increasing pressure, an effect also shared through reducing the Fe target power and thus decreasing the quality of the interface. Both modifications to the growth procedure increased GMR. Paul *et al.* [24] induced uncorrelated roughness through irradiating their samples with 200 MeV Ag ions. These samples were then compared directly to those which had not been irradiated, finding that GMR decreased with roughness and concluding the uncorrelated component of roughness had a much larger affect on MR. A diagrammatically representation of correlated and uncorrelated interface structures is given in *Figure 4.9*.

The deposition technique is of course another crucial factor, with a strong dependence between the film properties and the sample manufacturing technique. Reiss *et al.* [25] compared NiFe/Cu multilayers grown by sputtering and evaporation techniques. Samples prepared using sputtering exhibited a much higher GMR, attributed to structural differences consistent with strong AF coupling and good multilayer structure. TEM measurements indicate the evaporated films are 10 times rougher than the sputtered ones, a roughness comparable to the thickness of the spacer layer.

Another method [12] which allows for alterations to the structural parameters, is in changing the properties of the buffer layer (an initial seed layer on which is subsequentially grown the device). Takeda *et al.* [26] varied the interface roughness by growing the samples on different buffer layers; they found an increased GMR as a result of increased magnetic disorder at the Fe/Cr interface.

However, changing the buffer has a far wider influence on the structure than just changing the interface roughness. The buffer can affect grain size and crystallographic texture, as well as interface morphology. It should also be noted that the presence of a buffer layer with low resistance can cause current shunting through the buffer layer, affecting GMR.

3.4.3 Contaminants and Surfactants

In order to probe scattering at the interface, several groups have investigated the affect on GMR by introducing contaminants at the interface during the growth process. This will affect both the magnetic and chemical interfaces. Bouzianne *et al.* [27] introduced Zr into the Co/Cu system to find a decrease in GMR, which according to X-ray reflectivity measurements, was the result of a reduction in interface quality. Wellock *et al.* [28] performed a very similar experiment with Au. They concluded the Au only roughened the interface, reducing GMR as a result of a drop in spin-dependent scattering at the interface since the Au did not affect the resistance. This contradicts a lot of the previous findings and makes for an interesting comparison with results obtained using annealing to roughen the interface. Hall *et al.* [16] attributed a drop in GMR to increased resistance. This demonstrates that although roughness can be introduced using different techniques the resultant structure and affect on MR is not necessarily the same.

Dieny *et al.* [29] modified the roughness in Fe/Cr multilayers by introducing impurities at the interface and found, in contradiction to the majority of published work, a decrease in GMR. However, it should be noted that the introduction of impurities to the Cr layer affected its thickness and so they failed to keep the exchange coupling between the magnetic layers constant, a key parameter in defining the magnitude of GMR.

Egelhoff *et al.* [30] described a method by which they were able to increase GMR. They discovered the Co/Cu spinvalves with the greatest MR were not always produced in the best vacuum. The presence of oxygen during the growth process, acts as a surfactant that suppresses defects, reducing roughness and spin-independent scattering at the interface.

3.4.4 Crystal Structure and Grains

The crystallographic texture is also very important, for example it can affect magneto-crystalline anisotropy, that of hcp Co is almost an order of magnitude greater than that of fcc Co. There are many contradictory results concerning the crystallinity of the Co layer, although it is now believed that as Co grows on Cu (111) it forms an fcc

structure for the first few monolayers and then, with increasing thickness, develops into a hexagonal structure.

In sputtered samples there is a great deal of disorder within the crystal structure, with a powdered structure being more common than not. The affect of grain size is therefore also important since scattering can occur at the grain boundary. In general, the resistivity is inversely proportional to the grain size, with spherical grains producing greater GMR [31, 32].

3.4.5 Future Work

The ability to understand the relationship between interfacial structure and the transport properties responsible for GMR is limited by the difficulty inherent to structural analysis and crystal growth. Complete analysis should include a full characterisation of the interface structure and its properties. To date, nearly all the work has centred on the characterisation and correlation of the chemical structure, in particular the role of the interface. However, an equally important study is to examine with more detail the magnetic structure. As we shall see from *Chapter 6* and *Chapter 7* the magnetic and chemical structure and associated disorder are not necessarily the same.

3.5 Experimental Details

As we have seen in *Section 3.4*, there are a number of issues relating GMR to device structure which are as yet unsolved. The bottom spin-valves studied here have been grown with a nominally identical structure under very strictly controlled conditions and so the reason for variation in GMR is unclear. It may be speculated that it is related to very subtle changes in structure and it is the aim of the present work to deduce these structural changes.

The series of spin-valves will be characterised using X-ray techniques. The specular reflectivity, as described in *Section 2.6*, will provide averaged out-of-plane information such as the layer thickness and interface roughness. These parameters are obtained

through fits to the experimental data using models simulated with the *Bede* Mercury code as described in *Section 2.6*.

Unfortunately a disadvantage with this technique is noted in the similarity between scattering factors for Cu and Co at the X-ray energies used in this experiment. This means it is not possible to distinguish between those layers and their respective interfaces. To resolve between the two elements, in the spin-valve trilayer, it would be advantageous to use resonant X-ray scattering by tuning to either the Cu or Co edge, see *Section 2.8.1*. However, in this laboratory based study, the average layer thickness of the electrodes and spacer layer has been deduced by measuring the relative element concentrations using X-ray fluorescence, see *Section 2.8.2*. In this we are using Castaing's approximation [33], allowing an equal cross-section and absorption rate for each of the elements, thus presuming fluorescence intensity is proportional to the element concentration.

3.6 The Samples

The spin-valves used in this study were made at the National Institute of Standards and Technology (NIST) in the U.S.A. They were all grown at room temperature by D.C. magnetron sputtering (at 2 mTorr) on a 3000 Å substrate of a silicon thermal oxide on Si, with a single 500 Å layer of nickel oxide, cleaved into approximately 1 cm^2 squares. All depositions were at normal incidence with a magnetron power of 200 W at 350 V.

The NiO layer is antiferromagnetically ordered at room temperature and acts as the pinning layer, like those discussed in *Section 3.3*. In general the GMR in such spin-valves follow a linear increase with layer thickness, levelling off at approximately 400-500 Å. The top and bottom ferromagnetic layers are composed of Co, 25 Å and 30 Å respectively. The Cu spacer layer is 21 Å thick. Therefore the overall structure of these bottom spin-valves are: SiO_2 / NiO (500 Å) / Co (25 Å) / Cu (21 Å) / Co (30 Å).

In our initial study seven spin-valves were grown, which for our purposes here will be labelled A-G. Each has a nominally identical layered structure but exhibit a different GMR. Magneto-transport measurements were made at NIST at room temperature using a 4-point probe dc mode in a vacuum chamber connected to the deposition chamber. The GMR values are tabulated below in *Table 3.1*:

Label	A	B	C	D	E	F	G
GMR(%)	6±0.1	8.9±0.1	9.1±0.1	10±0.1	10.6±0.1	12±0.1	13.7±0.1

Table 3.1: *GMR values obtained for all 7 spin-valves studied.*

3.7 Results

3.7.1 Structural Characterisation using GIXR

The first step in characterising these spin-valves was to perform a specular $\theta/2\theta$ scan, where the motors are scanned with the detector angle fixed at twice the sample angle. This maintains the condition that the angle of X-ray incidence equals the angle of the exiting X-rays detected, the so-called specular condition. In reciprocal space the scattering vector has no in-plane component and so proceeds in q_z along the specular ridge. The true specular profile is obtained by subtracting the off-specular scan from the specular scan. The off-specular is very similar to the $\theta/2\theta$ specular scan with an initial offset in sample angle of typically 0.1 °, sufficient to be off the specular ridge (the width of which is determined by the instrument resolution) and thus measure of the forward diffuse scatter. Its subtraction from the specular data removes any forward or longitudinal diffuse scatter from the specular signal. The true specular profile will provide average in-plane information as a function of depth, such as layer thickness and interface width.

Measurements were taken on the *Bede GXR1* reflectometer in the Durham laboratory as described in *Section 2.9.1.1.* The Cu target tube and double-bounce Si monochromator provides the Cu K_β emission, at a wavelength of λ=1.393 Å. A typical $\theta/2\theta$ specular scan, corrected for the effect of forward diffuse scatter, is shown below in *Figure 3.5* for spin-valve D:

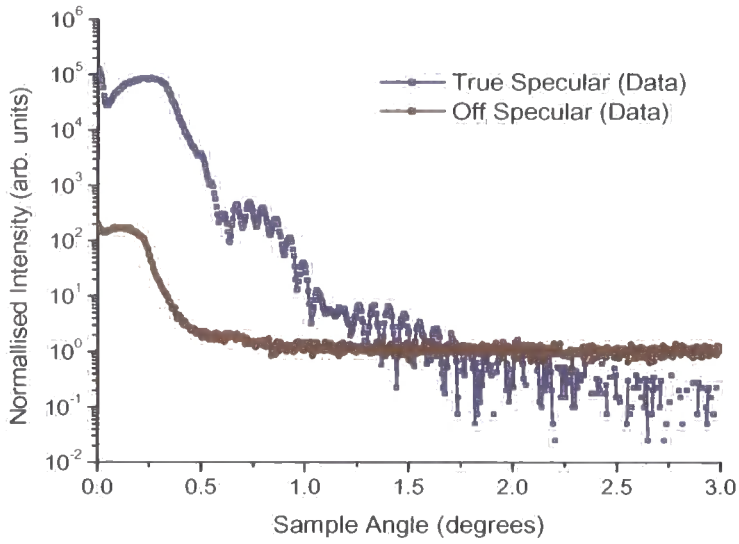

Figure 3.5: *Specular θ/2θ scan (blue) corrected for the effect of forward diffuse scatter, by subtracting the longitudinal off-specular diffuse scatter (brown), on spin-valve D with nominal structure SiO_2/NiO(500 Å)/Co (25 Å)/Cu (21 Å)/Co (30 Å) and a GMR value of 10 %.*

The multi-periodic Kiessig fringes observed in this reflectivity profile are a result of the interference from X-rays reflecting off interfaces within the sample structure. Their respective frequencies are inversely proportional to the layer thickness (via Bragg's Law) and their definition related to both the relative scattering factors from the surrounding layers and the interface width between the layers. The higher frequency fringes are due to interference from the bottom NiO pinning layer, and the lower frequency fringes come from the thinner Co-Cu-Co trilayer sandwich.

Parameters, such as the layer thickness and interface width, are obtained through fitting the specular data with the *Bede* Mercury code as described in *Section 2.6*. The fit obtained is shown below in *Figure 3.6* with the corresponding parameters used for that fit in the table opposite. The interface width refers to the surface interface for each respective layer, for example, the SiO_2 interface width of 4.5±1 Å refers to the interface between the SiO_2 and the NiO layer.

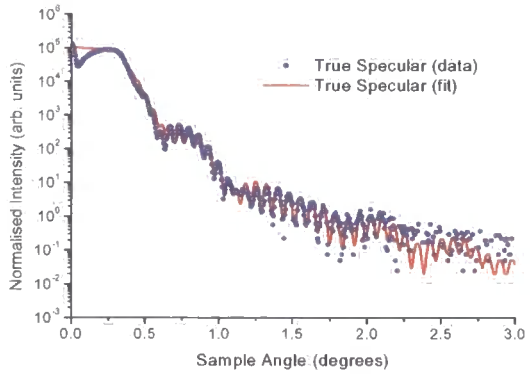

Layer	Thickness (Å)	Interface Width (Å)
Co Oxide	8.6±5	7.5±1
Co-Cu-Co	69.3±5	4.8±1
NiO	499±5	1.7±1
SiO_2	-	4.5±1

Figure 3.6 and Table 3.2: *Fits to true specular profile, for spin-valve D, shown in Figure 3.5 with the parameters used for that model fit given in the table.*

The parameters obtained from this fit are an average out-of-plane measurement, across the sample. The specular (with corresponding fit) and off-specular scans have been repeated for all spin-valves, fits for the remaining six spin-valves can be seen in *Figure 3.7*. Note that at this energy it is not possible to separate the Co-Cu-Co layers.

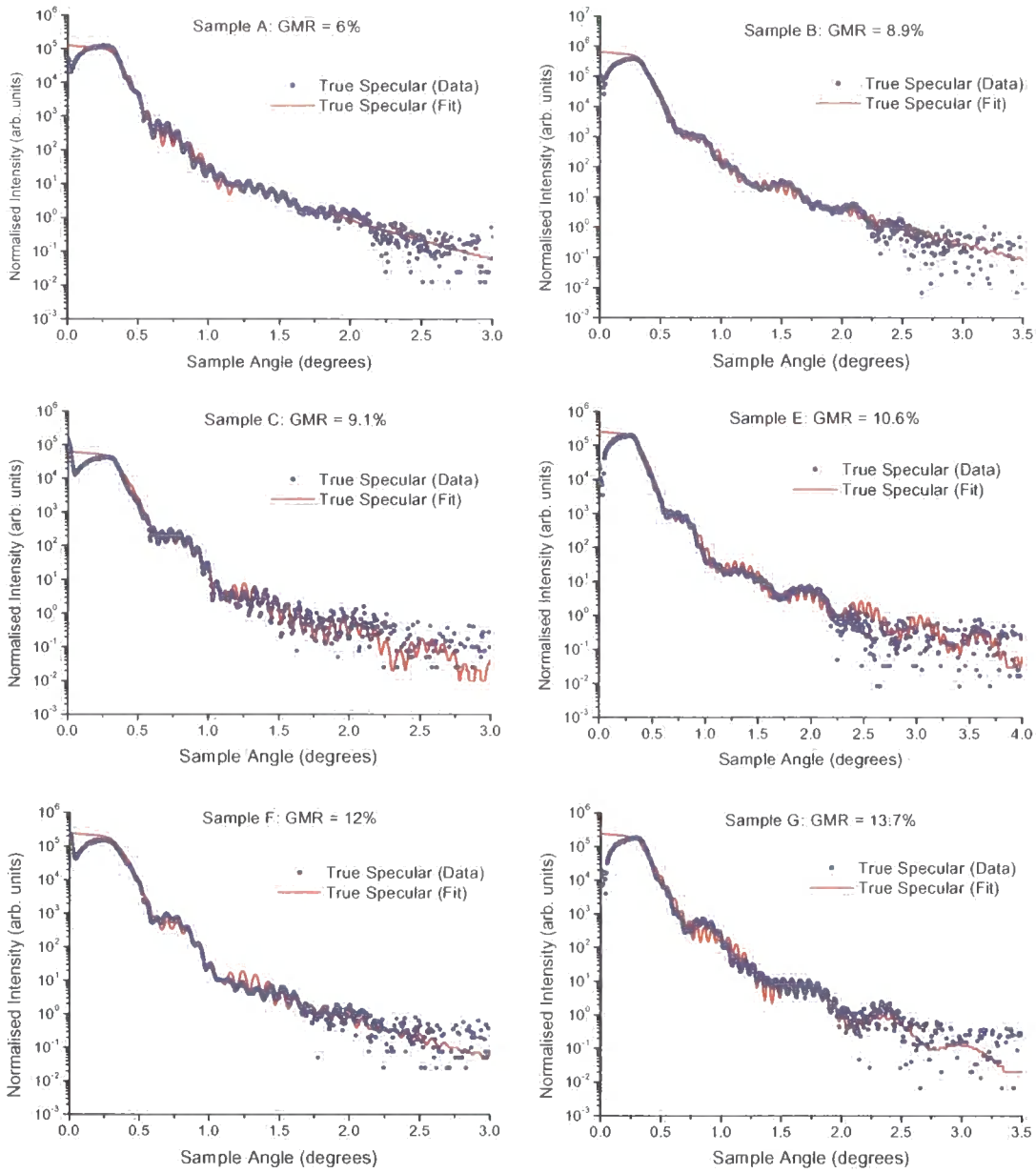

Figure 3.7: *Fitting the true specular profile for all of the spin-valves studied with the GMR as indicated.*

It is the primary objective of this study to correlate the parameters obtained from these fits to the GMR measured for each sample respectively. *Table 3.3* summarises the thickness of the NiO pinning layer, the Co-Cu-Co trilayer and the Co Oxide layer and their variation between each spin-valve.

Label	GMR (%)	Layer Thickness (Å)		
		NiO	Co-Cu-Co	Co Oxide
A	6±0.1	397±5	74±3	12±2
B	8.9±0.1	412±5	72±3	6±2
C	9.1±0.1	447±5	70±3	13±2
D	10±0.1	499±5	69±3	9±2
E	10.6±0.1	490±5	72±3	7±2
F	12±0.1	519±5	67±3	13±2
G	13.7±0.1	515±5	69±3	6±2

Table 3.3: *Layer thicknesses obtained from the fits shown in Figure 3.7.*

The deposited trilayer sandwich, consisting of two Co magnetic electrodes and the Cu spacer layer, remains consistent for all samples with an average thickness of 70.42 Å and a standard deviation of 2.34 Å. This demonstrates good control and reproducibility in the sputtering technique and even though there are small variations between the samples they show no correlation with the GMR. It is of course conceivable to expect variations in the individual electrode and spacer layer thickness, these values are of importance (as discovered in *Section 3.4*) and although these parameters can not be measured directly using GIXR they will be investigated further in the following section using X-ray fluorescence.

Without the use of a capping layer it is difficult to control surface oxidation, but it can be of great importance, however, in this spin-valve set there appears to be little correlation between the oxide layer thickness and GMR.

On the other hand, there is a surprisingly large variation in the NiO thickness. This layer has not been produced with the same sputtering process used in making the Co and Cu layers, but rather purchased as an initial wafer of SiO_2/NiO and cut for subsequent deposition. The NiO layer is AF and forms the pinning layer used to increase the coercivity of the lower Co layer, thus allowing the switching process between the magnetic layers to take place. Any variation in exchange bias between the pinning and pinned layer will strongly affect the GMR. The correlation between the NiO thickness and GMR is evident from *Table 3.3* and shown graphically below in *Figure 3.8*:

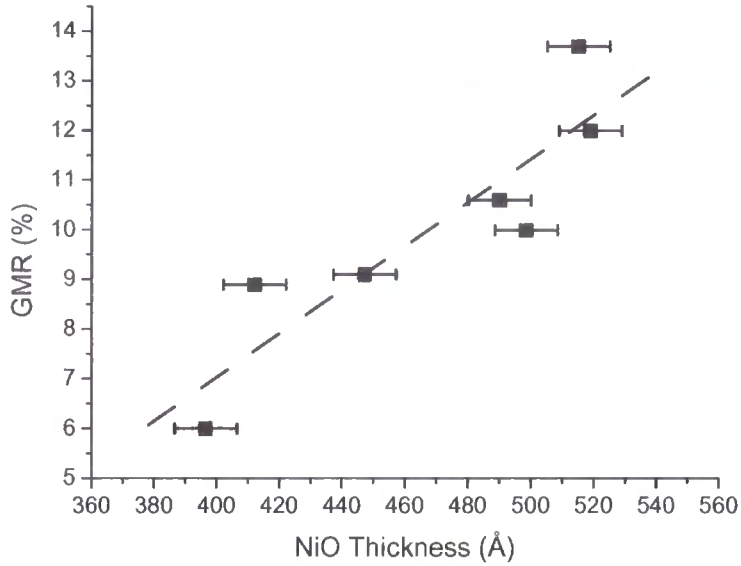

Figure 3.8: *Correlation between GMR and the spin-valve NiO thickness (with the dashed line to show a linear fit with an R-squared value of 0.8).*

The figure clearly shows a variation in NiO thickness from under 400 Å up to almost 520 Å, with a general increase in GMR with increasing NiO thickness.

It is also important (as we have seen from some of the examples discussed in *Section 3.4*) to examine the interface width and attempt to ascertain if roughness or interdiffusion has any bearing on the GMR or indeed explain the variation in NiO thickness. The table below summarises the interface widths determined from the fits shown in *Figure 3.6* and *Figure 3.7*.

Label	GMR (%)	Interface Width (Å)			
		SiO_2	NiO	Co-Cu-Co	Co Oxide
A	6±0.1	10.7±3	5.7±2	2.9±1	11.4±4
B	8.9±0.1	7.9±2	6±2	4.5±2	11.1±4
C	9.1±0.1	8.2±2	1.9±1	4.1±2	6.8±3
D	10±0.1	4.5±1	1.7±1	4.8±2	7.5±3
E	10.6±0.1	3.8±1	1±0.4	1±0.2	9.4±3
F	12±0.1	2.8±1	4.6±2	5.7±3	9.1±2
G	13.7±0.1	2.8±1	2.5±1	3.4±1	6.3±2

Table 3.4: *Interface widths obtained from the fits shown in Figure 3.6 and Figure 3.7.*

The NiO/trilayer, trilayer/oxide and top oxide interfaces widths show no clear correlation with the magnitude of GMR. On the other hand there is a systematic variation in the interface width between the silicon substrate and the NiO pinning layer, as illustrated below in *Figure 3.9:*

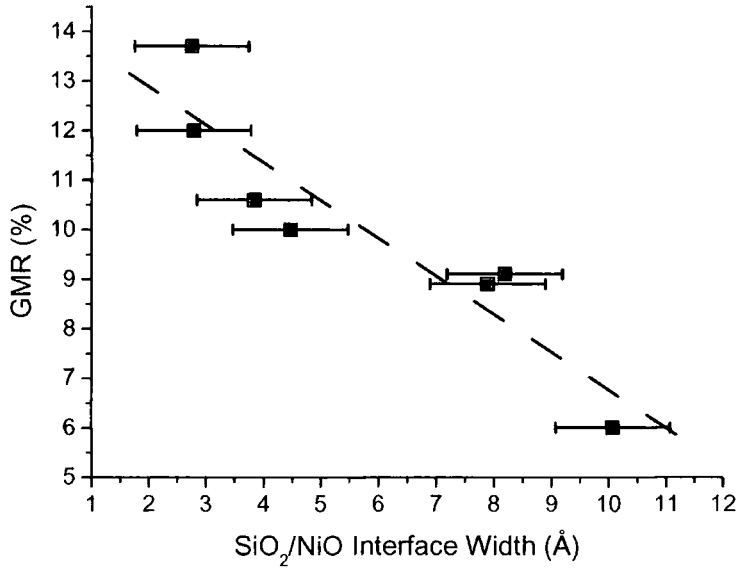

Figure 3.9: *Correlation between the SiO_2/NiO interface width and GMR (with the dashed line to show a linear fit with an R-squared value of 0.89).*

This discovery, combined with the observed variation in NiO thickness, might suggest some sort of diffusion or alloying process between the SiO_2 and NiO during the production of these wafers. Clearly any diffusion or alloying will greatly shape the chemical and magnetic structural properties of the NiO layer and again affect the exchange bias between the pinning and pinned layer. In order to determine whether this interface width is largely due to roughness or intermixing, it was necessary to perform a series of transverse diffuse scans.

Transverse diffuse scans or 'rocking curves' are performed with a fixed detector position 2θ; the sample angle θ is then scanned from 0 through to 2θ. As described in *Section 2.5*, this probes reciprocal space along the q_x direction, providing in-plane structural information. Using an appropriate model, such as Sinha's self-affine fractal description presented in *Section 2.7.2*, the transverse diffuse scattering profile can describe the interface morphology including parameters such as roughness σ, correlation length ξ, and the fractal parameter h. Within the Born approximation (*Section 2.7.1*) it is

also possible, by simply integrating the diffuse and specular scatter, to differentiate the interface width into its constituent components of roughness and intermixing. The theory behind these calculations are described in much greater detail in *Section 5.3.1*. A typical transverse diffuse scan is shown below for spin valve B, with a fixed 2θ position of 1.63 °. The x-axis has been given in θ as well as q_x.

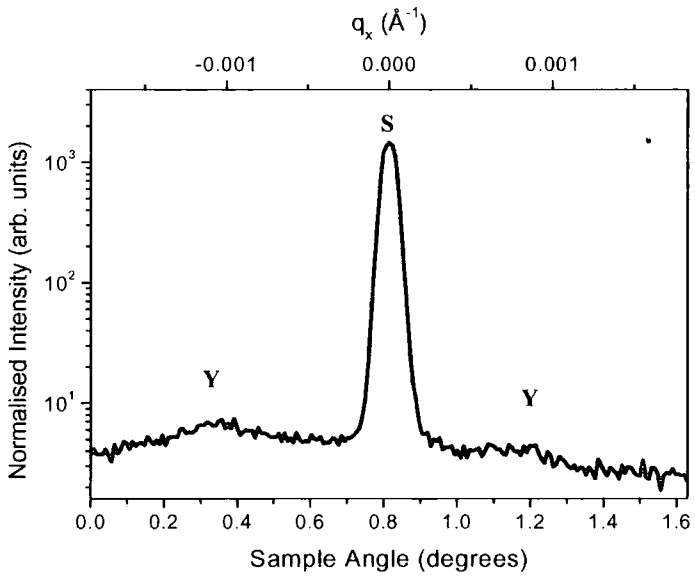

Figure 3.10: *Transverse Diffuse scan taken for spin valve B, a GMR value of 8.9 %.*

This figure also demonstrates the key features common to transverse diffuse scans. The peak (**S**) at q_x=0 is the specular ridge as a result of out-of-plane scatter. The surrounding scatter is all diffuse as a result of roughness from within the sample, its intensity is proportional to the magnitude of that roughness with a shape corresponding to the roughness correlation. The symmetrical peaks (**Y**) on either side are the so-called Yoneda wings and represent the cut-off in observation due to the critical angle, as described in *Section 2.5*.

Within the Born approximation average roughness values for each spin-valve have been calculated and are presented below in *Table 3.5*. It should be noted the diffuse scatter comes from each interface and so this form of analysis provides an average result for interface roughness.

Label	A	B	C	D	E	F	G
GMR(%) ±0.1	6	8.9	9.1	10	10.6	12	13.7
Born Roughness, σ (Å)	3.3±1	2.7±1	3.9±1	3.7±1	2.9±1	3.4±1	2.9±1

Table 3.5: *Average roughness for each spin-valve as calculated from Born analysis.*

Analysis from the diffuse scatter finds no correlation in average interface roughness with GMR. The next section leaves the area of reflectivity to determine the precise elemental concentrations of the spin-valve using X-ray fluorescence.

3.7.2 Fluorescence Measurements

Fluorescence measurements were made using a *Bede Microsource* with a rhodium target. The *Microsource* is in principle, similar to a basic electron impact X-ray tube, as described in *Section 2.9.1*. However in this source, the electrons are focussed onto the target material with a series of magnetic coils. This has the advantage of providing a very small and bright beam spot, comparable to that produced by a rotating anode. The X-rays are monochromated to reduce background bremsstrahlung using two Cr layer filters each 10 μm in thickness. The fluorescence spectrum for spin-valve F is shown below, with the Co, Ni and Cu peaks identified.

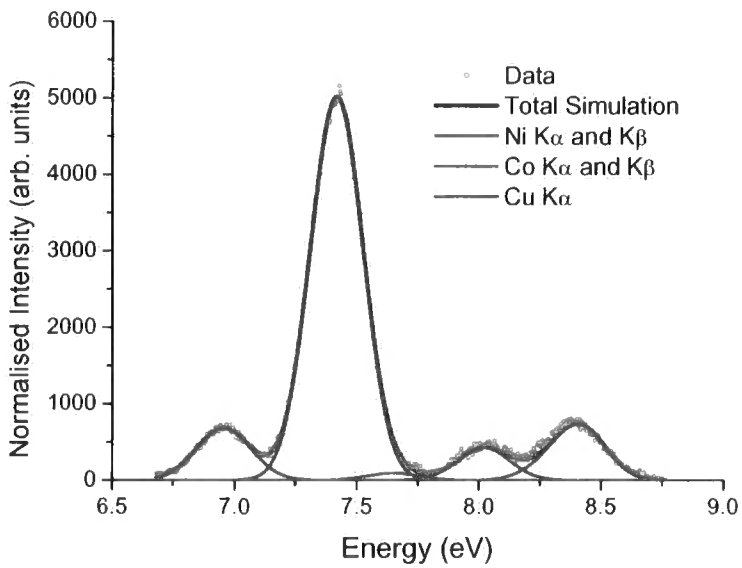

Figure 3.11: *Fluorescence of spin-valve F, with a GMR value of 12 %.*

By fitting this spectrum (also shown), the relative element concentrations within the sample are obtained. The fitting software (written by the author) is designed specifically for fluorescence spectra, maintaining the appropriate ratios between K_α and K_β emissions (usually around 1 in 7). The fitting algorithm employs a simple downhill fitting method.

Fluorescence spectra for each spin-valve remain almost identical, concentration results (as a percentage) from each fit are presented below in *Table 3.6*:

Spin-Valve	GMR (%)	Concentration (%)		
		Ni	Co	Cu
A	6±0.1	79.1±2	14.2±1	6.7±1
B	8.9±0.1	81.1±2	13.1±1	5.9±1
C	9.1±0.1	79.8±2	13.7±1	6.5±1
D	10±0.1	78.7±2	14.2±1	7.1±1
E	10.6±0.1	80.6±2	12.4±1	7.0±1
F	12±0.1	81.5±2	11.5±1	6.9±1
G	13.7±0.1	80.3±2	12.5±1	7.1±1

Table 3.6: *Spin-valve element concentrations determined from XRF spectra.*

Results indicate that a consistent amount of each element is being deposited during the growth process, for each spin-valve respectively. This suggests good control in the sputtering process and confirms the results present in *Section 3.7.1*. Any slight variation holds no correlation with the GMR. It is however interesting to note a constant amount of Ni between samples, it again indicates (combined with the variation in NiO layer thickness) a degree of intermixing or alloying with the SiO_2 substrate.

Based upon the measured thickness of the Co-Cu-Co trilayer and the relative amounts of Co and Cu, it is possible to calculate the spacer layer thickness. An average value (close to the nominal structure) of 24.0 Å was obtained with a low standard deviation of 1.42 Å.

3.8 The NiO Wafer

To summarise the results in *Section 3.7*, we find the thickness of the NiO pinning layer and substrate to NiO interface width are the only structural parameters which showed any kind of correlation with GMR. The thickness of the NiO layer increased with GMR and this was accompanied by an increase in the interface width between the

SiO_2 and the NiO, suggesting some intermixing or alloying between the two layers. This is confirmed in the XRF results which indicate a consistent amount of Ni within each of the samples. The intermixing of SiO_2 with the NiO layer will undoubtly affect the magnetic AF structure reducing the pinning or exchange bias with the lower magnetic Co layer thus reducing GMR.

As previously mentioned, the NiO wafer grown on SiO_2 was purchased separately and not part of the sputtering process that appears to be consistent and well controlled throughout the entire spin-valve series. To test the quality and uniformity of these NiO wafers, a similar wafer has been studied using the same characterisation techniques.

3.8.1 Characterisation

Specular reflectivity scans were performed to find the layer thickness and interface width. Transverse diffuse scans were then used to determine the degree of intermixing between the SiO_2 and NiO layer, and fluorescence spectra taken to determine the relative amounts of Ni across the surface. Example reflectivity (showing the specular with fit) and fluorescence data taken from the centre of the wafer are shown below in *Figure 3.12*:

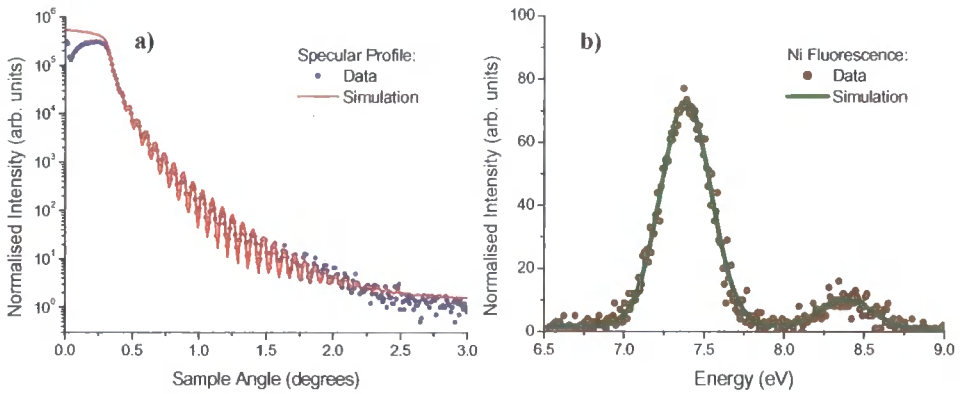

Figure 3.12: a) *Reflectivity and* ***b)*** *fluorescence data obtained from the centre of the NiO wafer.*

These scans were repeated at 39 different target points, allowing a spatial distribution in layer thickness and interface width to be mapped across the NiO wafer. The target points were placed 1 cm apart in both x and y and have been shown in the figure below together with the top (surface) interface width and bottom (SiO_2\NiO) intermixing, as

well as the NiO layer thickness. The gaps in the map were filled in by triangular interpolation.

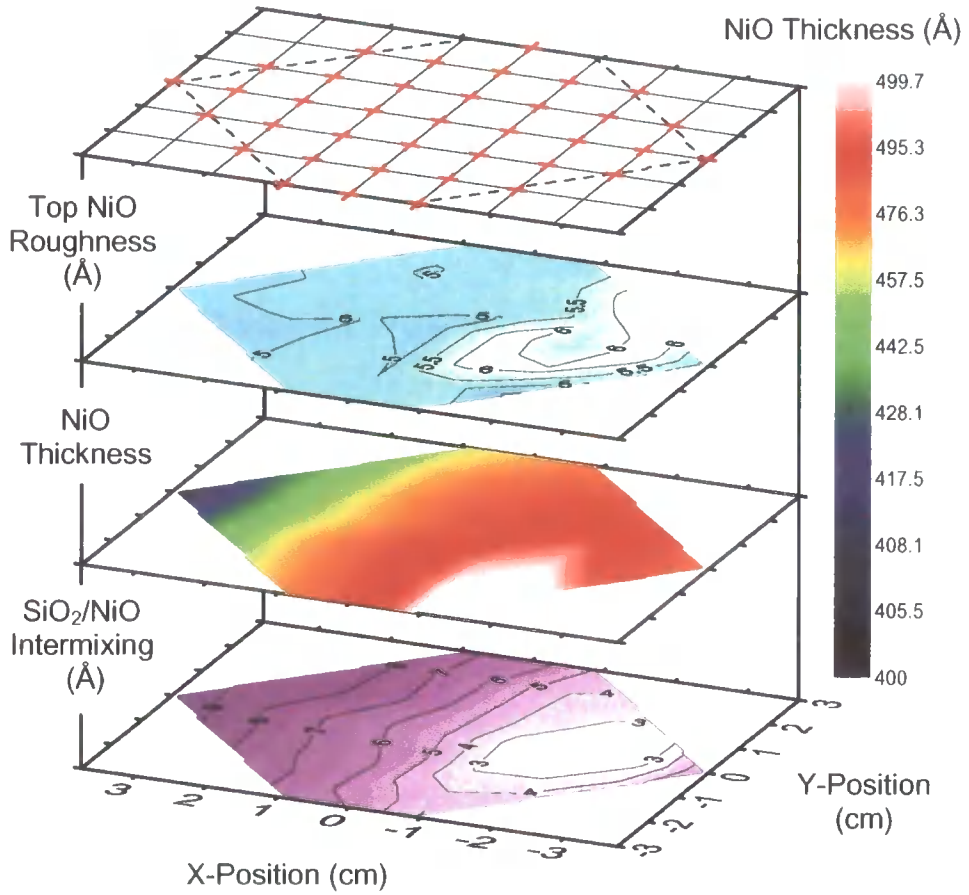

Figure 3.13: *Reflectivity data taken from the NiO wafer, including surface roughness, layer thickness and SiO_2/NiO intermixing lengths calculated from the transverse diffuse data.*

Spatial resolution perpendicular to the beam was simply set by the horizontal slit size, configured in this case at 5 mm. Parallel to the beam, the resolution was dependent on the vertical beam height, detector slits and of course the beam footprint i.e. the angle of incidence. If a parallel beam is assumed then an estimated resolution of 1 cm is calculated through angular considerations. To improve resolution, measurements were conducted twice with the wafer at 90 ° to its original orientation, average values were then taken.

The figure shows a large and an approximately linear variation in NiO thickness across the wafer, ranging from 400 Å to 500 Å. Although the top interface width

remains relatively constant the bottom intermixing varies with the NiO thickness above. A higher level of interface width is associated with a thinner layer thickness.

In the XRF experiments the resolution was set by the size of the beam and position of the detector with respect to the sample surface. Slits confined the beam to 5 mm × 5 mm and the detector was placed 1 cm from the sample surface resulting in an estimated spatial resolution of ~1 cm. The spectra collected (normalised with time) found no variation in Ni intensity across the wafer (consistent with the results obtained for the individual spin-valves in *Section 3.7.2*) and so the variations in NiO layer thickness are attributed to intermixing with the substrate.

The results obtained from the NiO wafer confirm the conclusion made concerning the spin-valves and suggest that variations in GMR are without a doubt the result of inconsistencies in the pinning layer thickness.

3.8.2 Additional Spin-Valves

To double check this result, an additional set of spin-valves were grown on the **same** NiO wafer studied in this section. The wafer was cut carefully and samples were sputtered as described in *Section 3.6* with the following nominal structure:

$$SiO_2\backslash NiO\backslash Co(25\ Å)\backslash Cu(25\ Å)\backslash Co(25\ Å)$$

The NiO thicknesses are known from the map shown in *Figure* 3.13. Once grown, magneto-transport measurements were made to determine the GMR, the values obtained have an error of ±0.1 and have been presented below in *Figure 3.14*:

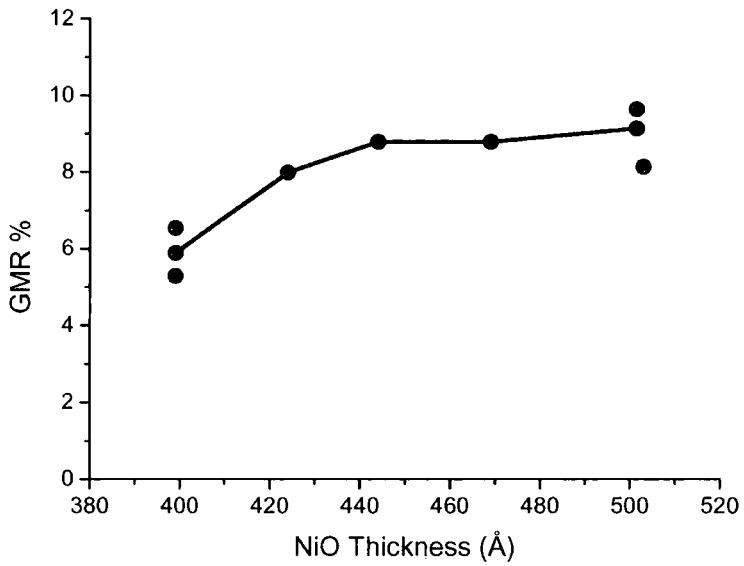

Figure 3.14: *GMR determined from spin-valves grown with nominal structure Co(25 Å)\Cu(25 Å)\Co(25 Å), on top of the NiO layer of varying thickness.*

This figure is comparable to *Figure 3.8*, and confirms the previous findings; a decrease in the NiO pinning layer thickness is causing a reduction in GMR.

3.9 Discussion and Conclusion

In this chapter the reader has been introduced to some of the important X-ray techniques through the study of an important type of GMR device known as the spin-valve. A series of nominally identical sputtered spin-valves, with differing MR, were studied in an attempt to correlate this variation in MR with differences in device structure.

Average out-of-plane structural measurements were made through a series of specular and longitudinal diffuse off-specular scans, with the true specular profile fitted to obtain the model structure. The parameters obtained for each of the spin-valves were consistent in layer thickness and close to nominal. There was however a correlation between the NiO layer thickness and GMR, with a steady increase in GMR with layer thickness. This observation appeared to also correlate with a decrease in interface width between the NiO layer and SiO_2 substrate. All other interface widths showed no

correlation, including the average roughness as calculated from transverse diffuse scans made across the specular ridge in q_x.

Fluorescence spectra were also taken to discern between elements from the Co-Cu-Co trilayer and check that the element concentrations remain constant between spin-valves. In assuming Castaing's approximation we find all concentrations are consistent within the nominal structure, and in particular the Co and Cu elements found within the trilayer. Ni concentrations also remain constant between samples, which suggests intermixing or alloying between the NiO and SiO_2 since the NiO layer thickness varied. This hypothesis is confirmed when we examined the change and correlation in interface width between the layers.

To examine the NiO layer in more detail, a similar NiO wafer to that used in the production of these spin-valves, was examined using the same characterisation techniques. Results confirm not only a variation in NiO thickness of up to 100 Å, but also a variation in intermixing length (determined from the transverse diffuse scans under the Born approximation) between the NiO and the SiO_2 substrate. Although this reveals a strong correlation with NiO layer thickness, the interface width is insufficient to explain the degree of variation in pinning layer thickness. The evidence suggests that up to 100 Å of Ni is missing from the pinning layer, however fluorescence results support a consist amount of Ni within the sample and so it is believed that the Ni must migrate into the SiO_2 layer and possibly as far as the Si layer underneath. This could be due to the SiO_2 not being fully oxidised, it is well known that Si and Ni intermix very strongly. If the Ni is spread evenly within the substrate, the scattering cross-section remains largely unaffected and therefore we are insensitive to this migration with X-ray techniques. The NiO layer is AF ordered and forms the pinning layer for the lower Co ferromagnetic layer. Any disruption to the AF structure will decrease the strength of the exchange bias and reduce the magnetic pinning, thus affecting the magnetic and magneto-transport properties.

By studying a series of GMR spin-valves, variations in GMR have been attributed to changes in NiO pinning layer thickness as a result of intermixing with the lower SiO_2 substrate. This chapter has demonstrated the power of grazing incident X-ray techniques and X-ray Fluorescence as a non-destructive characterisation tool. The reader has also been introduced to an important type of MR device and the concept of correlating structural changes to magneto-transport properties.

3.10 References for Chapter 3

1. M.N. Baibich, J.M. Broto, A. Fert, F. Nguyen Van Dau, F. Petroff, P. Eitenne, G. Creuzet, A. Friederich, and J. Chazelas (1988) "*Giant Magnetoresistance of (001)Fe/(001)Cr Magnetic Superlattices*" Phys. Rev. Lett. **61** (21) pg. 2472-2475.

2. G. Binasch, P. Grunberg, F. Saurenbach, and W. Zinn (1989) "*Enhanced magnetoresistance in layered magnetic structures with antiferromagnetic interlayer exchange*" Phys. Rev. B **39** (7) pg. 4828-4830.

3. P. Grünberg, R. Schreiber, Y. Pang, M.B. Brodsky, and H. Sowers (1986) "*Layered Magnetic Structures: Evidence for Antiferromagnetic Coupling of Fe Layers across Cr Interlayers*" Phys. Rev. Lett. **57** pg. 2442-2445.

4. S.S.P. Parkin, N. More, and K.P. Roche (1990) "*Oscillations in Exchange Coupling and Magnetoresistance in Metallic Superlattice Structures: Co/Ru, Co/Cr, and Fe/Cr*" Phys. Rev. Lett. **64** pg. 2304-2307.

5. P. Bruno and C. Chappert (1992) "*Ruderman-Kittel theory of oscillatory interlayer exchange coupling*" Phys. Rev. B **46** pg. 261-270.

6. P. Bruno and C. Chappert (1991) "*Oscillatory coupling between ferromagnetic layers separated by a nonmagnetic metal spacer*" Phys. Rev. Lett. **67** pg. 1602-1605.

7. T.P.A. Hase, I. Pape, D.E. Read, B.K. Tanner, H. Durr, E. Dudzik, G. van der Laan, C.H. Marrows, and B.J. Hickey (2000) "*Soft x-ray magnetic scattering evidence for biquadratic coupling in Co/Cu multilayers*" Phys. Rev. B **61** (22) pg. 15331.

8. B. Heinrich and J.A.C. Bland (1994) "*Ultrathin Magnetic Structures II*" Springer-Verlag.

9. W.H. Meiklejohn and C.P. Bean (1956) "*New Magnetic Anisotropy*" Phys. Rev. **102** pg. 1413-1414.

10. M. Kiwi (2001) "*Exchange Bias Theory*" J. Magn. Magn. Mater. **234** (3) pg. 584-595.

11. S.K. Sinha, E.B. Sirota, S. Garoff, and H.B. Stanley (1988) "*X-ray and neutron scattering from rough surfaces*" Phys. Rev. B **38** (4) pg. 2297-2311.

12. N.M. Rensing and B.M. Clemens (1993) "*Magnetic Ultrathin Films: Multilayers and Surfaces, Interfaces and Characterization*" Mat. Res. Soc. Symp. Proc. **313** pg. 197.

13. E.E. Fullerton, D.M. Kelly, J. Guimpel, I.K. Schuller, and Y. Bruynseraede (1992) "*Roughness and Giant Magnetoresistance in Fe/Cr Superlattices*" Phys. Rev. Lett. **68** (6) pg. 859-862.

14. S.S.P. Parkin, R. Bhadra, and K.P. Roche (1991) "*Oscillatory magnetic exchange coupling through thin copper layers*" Phys. Rev. Lett. **66** pg. 2152-2155.

15. A. Wawro, L.T. Baczewski, R. Kalinowski, M. Aleszkiewicz, and J. Rauuszkiewicz (1997) "*Interfacial roughness and magnetoresistance in Co/Cu multilayers*" Thin Solid Films **306** (2) pg. 326-330.

16. M.J. Hall, B.J. Hickey, M.A. Howson, C. Hammond, M.J. Walker, D.G. Wright, D. Greig, and N. Wiser (1992) "*Interface scattering and the giant magnetoresistance of MBE - grown Co/Cu superlattices*" J. Phys. Cons. Matter **4** pg. 495-502.

17. M. Suzuki and Y. Taga (1995) "*Role of interfacial roughness in the giant magnetoresistance in Co/Cu superlattices*" Phys. Rev. B **52** pg. 361-365.

18. N.M. Rensing, A.P. Payne, and B.M. Clemens (1993) "*The effect of roughness on the magnetoresistance of Fe/Cr multilayers*" J. Magn. Magn. Mater. **121** pg. 436-439.

19. S.S.P. Parkin and B.R. York (1993) "*Influence of deposition temperature on giant magnetoresistance of Fe/Cr multilayers*" Appl. Phys. Lett. **62** pg. 1842.

20. R. Schad, P. Belien, G. Verbanck, V.V. Moshchalkov, Y. Bruynseraede, H.E. Fischer, S. Lefebvre, and M. Bessiere (1999) "*Giant magnetoresistance dependence on the laterial correlation length of the interface roughness in magnetic superlattices*" Phys. Rev. B **59** (2) pg. 1242-1248.

21. F. Petroff, A. Barthelemy, A. Hamzic, A. Fert, P. Etienne, S. Lequien, and G. Creuzet (1991) "*Magnetoresistance of Fe/Cr superlattices*" J. Magn. Magn. Mater. **93** pg. 95-100.

22. J. Barnas and Y. Bruynseraede (1996) "*Influence of the quantum size effect and interface roughness on the giant magnetoresistance in ultrathin magnetic layered structures*" J. Magn. Magn. Mater. **156** (1-3) pg. 287-288.

23. J. Ben Youssef, K. Bouziane, O. Koshkina, H. LeGall, M. ElHarfaoui, M. ElYamani, J.M. Desvignes, and A. Fert (1997) "*Correlation of GMR with texture and interfacial roughness in optimized rf sputtering deposited Co/Cu multilayers*" J. Magn. Magn. Mater. **165** (1-3) pg. 288-291.

24. A. Paul, A. Gupta, S.M. Chaudhari, and D.M. Phase (2001) "*Effect of Interface Structure correlation on magnetoresistance of Fe/Cr multilayers.*" Vacuum **60** pg. 401-405.

25. G. Reiss, T. Lucinski, L. Van Loyen, D. Elefant, H. Brückl, N. Mattern, R. R., and W. Ernst (1998) "*Presence and absence of antiferromagnetic coupling and giant magnetoresistance in sputtered and evaporated permalloy/copper multilayers*" J. Magn. Magn. Mater. **184** (3) pg. 281-288.

26. M. Takeda, Y. Endoh, A. Kamijo, and J. Mizuki (1995) "*Interfacial roughness and the giant magnetoresistance effect of Fe/Cr multilayers*" Physica B **213** (1-4) pg. 248-250.

27. K. Bouzianne, J. Ben Youssef, M. El Harfaoui, O. Koshkina, H. Le Gall, J.M. Desvignes, M. El Yamani, and A. Fert (1997) "*Comparative study of giant magnetoresistance in CoZr/Cu and Co/Cu multilayers*" J. Magn. Magn. Mater. **165** pg. 284-287.

28. K.P. Wellock, B.J. Hickey, D. Greig, M.J. Walker, J. Xu, and N. Wiser (1994) "*The effect of Au impurities at the interfaces on the magnetoresistance of MBE - grown Co/Cu multilayers*" J. Appl. Phys. **75** (10) pg. 7055-7057.

29. B. Dieny, V.S. Speriosu, S. Metin, S.S.P. Parkin, B.A. Gurney, P. Baumgart, and D.R. Wilhoit (1991) "*Magnetotransport properties of magnetically soft spin-valve structures*" J. Appl. Phys. **69** pg. 4774-4779.

30. W.F. Egelhoff, P.J. Chen, C.J. Powell, M.D. Stiles, R.D. McMichael, J.H. Judy, K. Takano, and A.E. Berkowitz (1997) "*Oxygen as a surfactant in the growth of giant magnetoresistance spin valves*" J. Appl. Phys. **82** (12) pg. 6142-6152.

31. W.J. Song and R. Yang (2000) "*Giant magnetoresistance in magnetic granular systems*" Physica B. **279** (1-3) pg. 181-184.

32. R. Yang and W.J. Song (1998) "*The shape and size dependence of giant magnetoresistance in magnetic granular films*" Phys. Lett. A. **244** (1-3) pg. 139-143.

33. K. Durose (2000) "*Solid State Analytical Techniques - Lecture Notes (Durham)*" pg.

Chapter 4

The Structural Characterisation of Al_2O_3 Barriers within Magnetic Tunnel Junctions

4.1 Introduction

Magnetic Tunnel Junctions (MTJs) under a small applied magnetic field, display room temperature magneto-resistance values which are in general far higher than the GMR spinvalves examined earlier in *Chapter 3*. A MTJ consists of two ferromagnetic (FM) layers separated by a thin insulating barrier layer. The spin polarised tunnelling across this barrier is determined by the relative orientation of magnetic moments in each of the FM layers. Switching with applied field is usually achieved by using FM layers with different magnetic coercivities or through magnetically pinning one of the FM layers by exchange bias with an anti-ferromagnetic (AF) layer. It is the change in relative orientation of moments between the FM layers that leads to a change in tunnelling probability and resistance; the so-called magnetic-tunnelling effect and Tunnelling Magneto-Resistance (TMR).

MTJs date back to as far as the 70s; however their MR properties were too small to be of any practical application and so it is only in recent years that they been accepted as a viable candidate for magnetic memory storage [1] and read head technology [2].

Tedrow, Meservey and *Fulde* first discovered spin polarised tunnelling in thin superconducting aluminium films [3]. Further development resulted in the observation of this effect in ferromagnetic films [4-7] suggesting the possibility of a magnetic field dependence in tunnelling behaviour. The tunnel junctions that followed [8-11] were grown using NiO, AlN, AlON and Al_2O_3 barriers, between Ni, NiFe and Co ferromagnetic layers. Although these trilayer junctions confirmed spin-dependent

tunnelling, their TMR values were only a few percent at 4.2 K and only a fraction of a percent at room temperature.

Presently, many of the problems leading to low values of TMR seen in the early MTJs have been solved. Currently values greater than 10 % (even as high as 20 % [12]) are consistently reproducible at room temperature. The predominant reason for increased TMR is due to the significant improvements made to the fabrication techniques, considerably reducing the interface roughness as well as other structural defects. The structure of the barrier is of key importance since defects will greatly affect tunnelling and thus the MR response. Al_2O_3 insulating barriers, such as those studied here, are usually grown through the plasma oxidation of an initially deposited Al layer. The barriers have been known to contain defects, some natural [13] and others artificially grown [14, 15] to investigate their affect on MR. Factors such as roughness [16] and chemical homogeneity [17] have been investigated. The specifics of barrier oxidation have also been studied [18, 19], a process which is very important in the optimisation of TMR; uncontrolled oxidation can lead to pinholes and other regions of high conductivity within the barrier or unwanted oxidation of the lower ferromagnetic layer.

In this chapter the effects of oxidising Al barriers are investigated, correlating values for TMR with characterised structure by two different techniques. An introduction to MTJs follows, through Julliere's model, followed by a more fundamental quantum mechanical approach. A brief section compares GMR spin valves and multilayers with TMR tunnel junctions, after which the samples are described and their magnetic and magneto-transport measurements presented. The magneto-transport measurements provide the current – voltage (I-V) relationship (or conductance dI/dV) and using a modified version of the Simmons' model [20] the barrier widths are determined. These results are compared with a more direct structural characterisation technique, namely GIXR. A large discrepancy between the results obtained with these techniques has been found and suggests localised tunnelling across a barrier of varying thickness. This hypothesis is confirmed by a lack of conformal roughness as inferred from the diffuse scatter and through a series of computer simulations that model the tunnelling across an arbitrary barrier.

4.2 Theory of Magnetic Tunnel Junctions and TMR

4.2.1 Julliere's Model

Julliere [21] first observed TMR in a Co/Ge/Fe junction at 4.2 K; a 14 % change in tunnelling conductance was measured with the application of a magnetic field. This reduced to less than 1 % when a bias of a few mV was applied to the junction. He explained his results with a simple model based on the probability of tunnelling for both spin states within each FM electrode. In this model $n\uparrow$ and $n\downarrow$ represent the probability of tunnelling for spin majority and spin minority electrons respectively. The spin majority electrons are defined as the electrons whose magnetic moment is in the same direction as the magnetic field (and spin minority in the opposite direction). The overall tunnelling conductance will be proportional to the combined probabilities from both spin channels, as illustrated in *Figure 4.1*. Therefore the resistivities (inversely proportional to the conductance) can be deduced for both parallel (R_p) and anti-parallel (R_{ap}) alignment between the FM layers labelled 1 and 2 respectively.

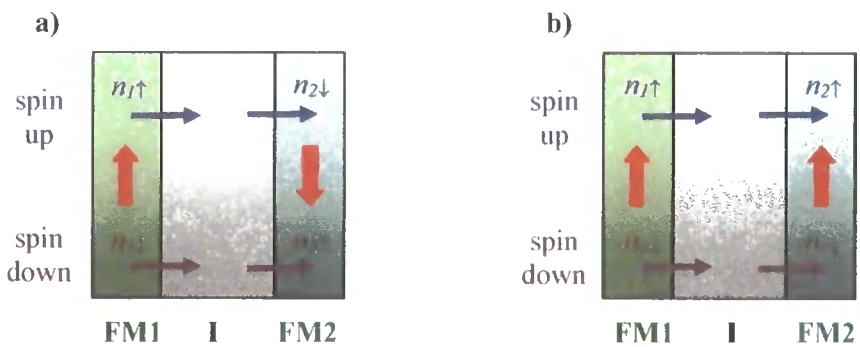

Figure 4.1: *Julliere's spin polarisation model to calculate the total resistance within magnetic tunnel junctions* ***a)*** R_{ap} *anti-parallel and* ***b)*** R_p *parallel alignment.*

If the possibility of spin-flip tunnelling is ignored, n_{ap} and n_p can be found by summing the probability contribution from each channel:

$$n_{ap} = n_{1\uparrow} n_{2\downarrow} + n_{1\downarrow} n_{2\uparrow} \qquad n_p = n_{1\uparrow} n_{2\uparrow} + n_{1\downarrow} n_{2\downarrow}$$

Equation 4.1

Since the conductance is proportional to the tunnelling probability, $\sigma \propto n$, therefore $R \propto n^{-1}$:

$$R_{ap} \alpha (n_{1\uparrow} n_{2\downarrow} + n_{1\downarrow} n_{2\uparrow})^{-1} \qquad R_p \alpha (n_{1\uparrow} n_{2\uparrow} + n_{1\downarrow} n_{2\downarrow})^{-1}$$

Equation 4.2

The TMR can then be calculated in terms of the respective tunnelling probabilities:

$$TMR = \frac{\Delta R}{R} = \frac{R_{ap} - R_p}{R_{ap}} = 1 - \frac{n_{1\uparrow} n_{2\downarrow} + n_{1\downarrow} n_{2\uparrow}}{n_{1\uparrow} n_{2\uparrow} + n_{1\downarrow} n_{2\downarrow}}$$

Equation 4.3

From the definition of electron polarisation $P = (n\uparrow - n\downarrow) / (n\uparrow + n\downarrow)$, the TMR can be rewritten as:

$$TMR = \frac{2P_1P_2}{(1+P_1P_2)}$$

Equation 4.4

The TMR values obtained with this model are much higher than those observed experimentally. This is due to the model assuming a perfect case; it fails to account for limiting factors such as domain walls, scattering from the interface and bulk. It is also reasonable to expect small variations in the electronic structure of the barrier, interface and FM layers, to play a key role in the magneto-resistance. The possibilities of direct coupling between the magnetic layers, surface degradation and other defects have also been ignored. *Julliere's* model therefore provides an upper limit in estimating TMR.

Although other theories and adaptations to *Julliere's* model have been proposed in order to explained FM/I/FM tunnelling [22-30] with more accuracy, none to date have been entirely satisfactory. For example, issues of TMR magnitude, temperature and bias dependence have not been completely explained.

4.2.2 Quantum Mechanics of Spin Dependent Tunnelling

The physical mechanism behind the spin degenerate tunnelling probabilities, and hence TMR, is a difference in the density of states [31] between the ferromagnetic materials at the Fermi surface. The tunnelling probability is proportional to the number of available tunnelling electrons, as well as the number of final states allowed below the Fermi energy level. The application of a field (due to the interaction with the spin magnetic moments) will split the quasi-particle density of states into spin-up and spin-down components. The energies are therefore displaced from their original value by

$\pm\mu_o J$, where J is the exchange integral [32]. It is this displacement in energy around the Fermi energy level, illustrated in *Figure 4.2*, which allows electrons of either spin direction to be selected from the electrons tunnelling i.e. spin polarisation.

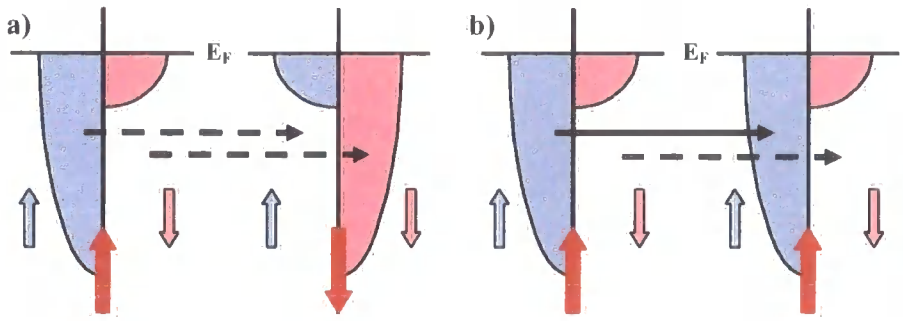

Figure 4.2: *Spin dependent electron tunnelling energy diagram for* ***a)*** *anti-parallel and* ***b)*** *parallel alignment.*

Assuming a perfect barrier, electrons can only tunnel into an empty state of the same spin and so consequentially there is a higher tunnelling current (lower R) in the parallel alignment in comparison to the anti-parallel state, and thus MR.

An appropriate model to describe tunnelling through a potential barrier will be discussed in detail in *Section 4.7.1*.

4.2.3 Comparing GMR to TMR

It is helpful at this point to contrast some of the aspects of TMR with GMR. The GMR spin valves studied in *Chapter 3* are one particular category of GMR device, they are essentially a trilayer consisting of two magnetic layers with a non-magnetic spacer. MTJs are similar in that they contain the same type of magnetic electrodes, but with an insulating or semi-conducting layer in-place of the non-magnetic spacer. Like spinvalves their resistance depends on the relative orientation of the magnetic moments between the two ferromagnetic layers and, like spinvalves, this dependence can be engineered accordingly e.g. magnetic pinning. However, the devices are primarily different in their origin of magneto-resistance. While GMR samples can be studied with current-in-plane (CIP) and current-perpendicular to-plane (CPP), the only geometry of interest for tunnel junctions is CPP. This will of course fundamentally affect the magneto-transport properties and the device design, for example, tunnel junctions can only use metallic pinning layers.

For comparable MR values, the resistance of MTJs is much higher in comparison to GMR devices and therefore the voltage required for MTJs is much higher. On the other hand, the current is much smaller promoting the use of GMR spin valves or multilayer structures preferentially for devices that are current driven.

The factors which govern the magnitude of TMR and GMR are quite different, for CPP the conduction is controlled by regions that limit the current. In MTJs these are primarily the insulating spacer layer and the spacer / electrode interface. In GMR no particular region stands out as an area of primary resistance, as discussed in *Section 3.4*, and so the current is controlled by the electronic structure and scattering centres situated throughout the device. Although the spin dependence, responsible for GMR, originates from the electronic structure and scattering, these factors are not relevant for TMR.

In MTJs the MR is controlled by spin-dependent conduction at the barrier / electrode interface, in other words, controlled by the number of available states for tunnelling. This explains the differing temperature dependence observed in TMR and GMR devices. The resistance of multilayers and spin valves increases with greater temperature due to increased scattering, however in MTJs there is a drop in resistance as more states are made available for tunnelling with increased energy. The addition of spin-dependence in the barrier band structure can also affect TMR, although to date most barriers are non-magnetic and so MR is governed purely by the interface. The electrode / insulator interface is also important due to the high electron reflectivity; this causes the electron to spend a larger period of time in the interface region. As discussed in *Section 3.4* the short screening lengths, found within metallic electrodes, result in a density of states (DOS) that are very localised. This means the DOS (and its spin polarisation) at the interface could be quite different to that of the bulk. In addition, the DOS also depend on the crystallographic orientation of the surface or interface. Therefore the bonding of orbitals in the insulator with those in the magnetic layer is of key importance to TMR, since they determine the DOS at the Fermi level and its dependence on spin. The role of the interface is important, but in no way as decisive for GMR as for TMR.

4.3 The Samples

The MTJs used in this study were deposited by d.c. magnetron sputtering (see *Section 2.11*) by Norman Hughes at the University of Exeter. A series of tunnel junctions were grown, through a shadow mask, onto a silicon (100) substrate that had previously been coated with rf sputtered aluminium oxide buffer layer. Successive layers of cobalt, aluminium and permalloy ($Ni_{81}Fe_{19}$) were subsequentially deposited with a nominal thickness of 90 Å, 14 Å and 110 Å respectively. The initial base pressure was $1x10^{-7}$ Torr with the sputtering being conducted in an argon atmosphere of 5 mTorr.

The Al deposition rate was determined with a Dektak profilometer revealing a rate of 6.7(±0.1) $Å s^{-1}$. In order to obtain a standard Al layer thickness of 14 Å, the samples were exposed to the Al source for 2.1 s via a timed shutter. To oxidise the aluminium, 100 mTorr of oxygen was introduced to the chamber immediately after the precursor Al layer was deposited. The chamber was then pumped down again to regain base pressure before the permalloy layer was deposited.

A quartz crystal oscillator system recorded continuously the deposition rate showing a consistency in the $Ni_{81}Fe_{19}$ and Co layer thickness for all the samples to within ±5 %. Although the crystal monitors were insufficiently sensitive to determine the thickness and errors of the Al layers, the reproducibility of the results obtained for the $Ni_{81}Fe_{19}$ and Co layer thickness implied consistency for each of the Al layers to within ±5 %.

A sample series of 21 tunnel junctions were grown with a variation in the Al oxidation time of 1, 3 and 5 minutes. In addition, a number of control samples were grown which were left unoxidised. The nominal structure for each sample is Si(100) / 250 Å Al_2O_3 / 90(±5) Å Co / 14(±0.7) Å Al (oxidised) barrier / 110(±6) Å $Ni_{81}Fe_{19}$.

As well as the tunnel junctions grown at Exeter, a series of samples were grown by Jagadeesh Moodera at the Massachusetts Institute of Technology. Although these samples possessed no TMR, they have been included due to some interesting structural changes observed to the barrier with oxidation and annealing, which explain the absent TMR and confirm effects seen in the Exeter samples.

The MIT samples include the basic Co / Al_2O_3 / NiFe trilayer structure, with an additional Al capping layer, but without the Al_2O_3 buffer. They were grown at a base

pressure of $1x10^{-7}$ Torr on a SiO_2 substrate cooled to 80 K. After growing an initial Co layer, Al was deposited whereupon the sample was split into two sections. One half was exposed to glow discharge oxidation for 100 seconds while the other side remained unoxidised. The sample was split in this way to ensure the only variable in the sample growth was its barrier oxidation. The top ferromagnetic permalloy layer was grown under magnetic field with a final Al capping layer on top of that. Finally, a series of oxidised samples were annealed at 200 °C for 30 minutes. For comparison, two sample sets were grown with a nominal barrier thickness of 12 Å and 16 Å. The complete nominal structure for these samples is: SiO_2 / 80 Å Co / X Å Al (oxidised) barrier / 60 Å $Ni_{81}Fe_{19}$ / 10 Å Al where X = 12 and 16.

4.4 Magnetic Measurements

In order to determine the magnetic properties of the tunnel junctions, M-H loops were measured using MOKE (see *Section 2.10*) at the University of Exeter. The magnetisation was measured over a 360 ° rotation of applied field and a selection of the M-H loops can be seen in *Figure 4.3*:

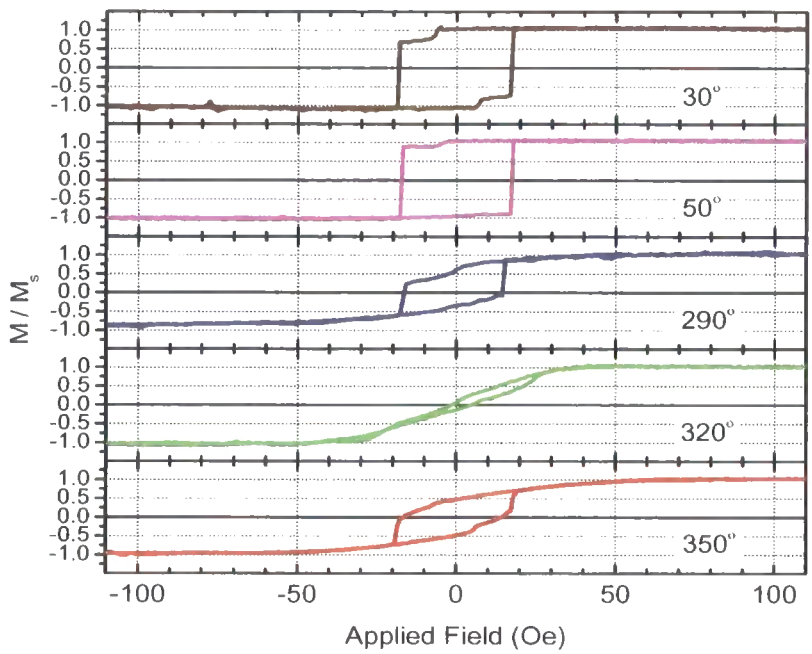

Figure 4.3: *A series of M-H loops measured at different field orientations using MOKE (courtesy of Dr Norman Hughes).*

The M-H loop at 30 ° clearly shows the magnetic reorientation of the individual ferromagnetic layers, with the soft NiFe layer switching under a small applied field, followed by the Co layer at saturating field strength. The ferromagnetic layers have a coercive field strength of ~5.5 Oe and ~17 Oe for the NiFe and Co layers respectively. The easy axis is easily identified at 50 °.

4.5 Magneto-Resistance Measurements

A 4-point d.c. measurement was performed to evaluate the magneto-transport properties and MR response, an example of which can be seen in *Figure 4.4*. The TMR values were calculated using *Equation 4.3*.

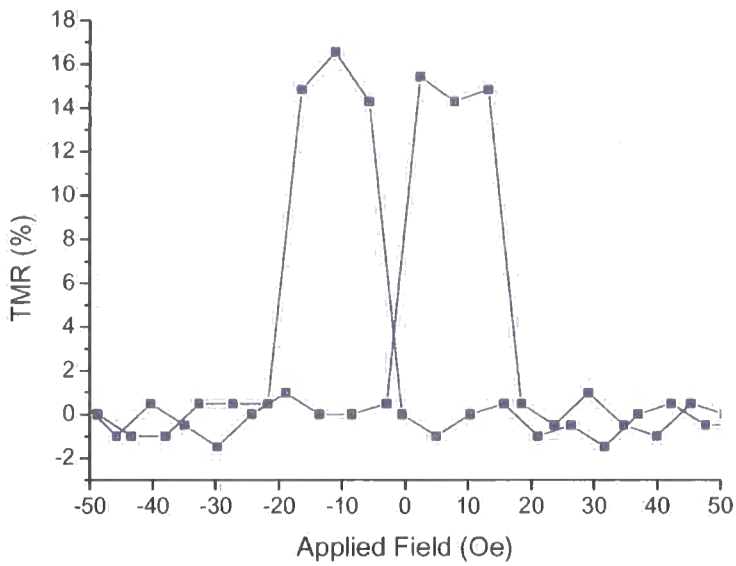

Figure 4.4: *Magnetoresistance as a function of applied field for a typical tunnel junction at a field orientation of 50 ° to produce maximum MR (courtesy of Dr Norman Hughes).*

The applied field initially flips the magnetic moments in the top NiFe layer, inducing anti-parallel alignment between the two ferromagnetic layers. This increases the overall resistance and hence a step increase in the junction's MR. As the field strength increases further it is great enough to re-orientate the bottom Co layer, as well the top, sending the

junction back into a state of parallel alignment and reducing the resistance back to its original value.

4.6 Aluminium Oxidation

One of the first objectives was to determine the relationship between the MR and the amount of time the Al barrier was subjected to oxidation. The results have been presented in *Figure 4.5*:

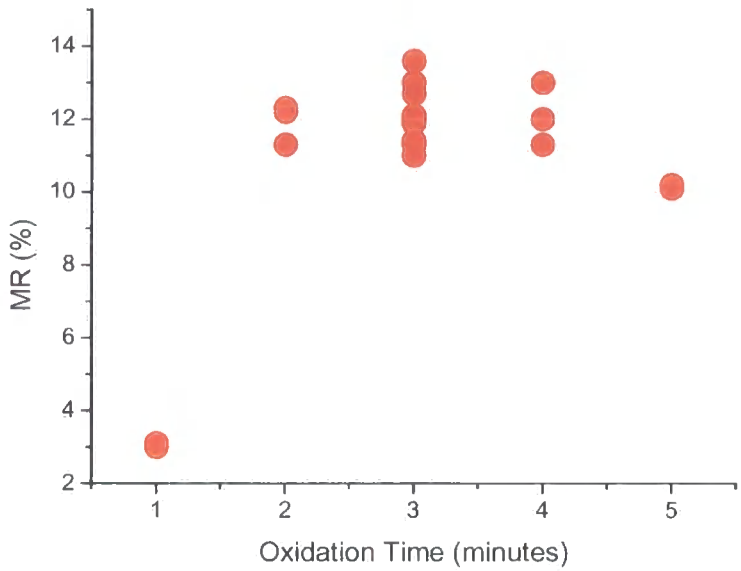

Figure 4.5: *The variation in magneto-resistance with individual magnetic tunnel junctions as a function of aluminium barrier oxidation time (courtesy of Dr Norman Hughes).*

The results show a peak in the MR, indicating an optimum oxidation period of approximately 3 minutes for a 14 Å thick Al layer. A smaller oxidation period leads to samples with lower MR, this is probably due to portions of the Al layer being unoxidised. This could lead to pinhole formation, as well as the presence of other high conductivity regions within the barrier layer. Greater oxidation times can not only oxidise the Al barrier, but the bottom ferromagnetic layer underneath, reducing the MR. The oxidation will not only affect the ferromagnetic properties of the layer, but the interface structure as well, a crucial parameter in TMR.

Ideally one could directly examine the amount of Al layer oxidised during the growth process, although GIXR provides excellent contrast between the barrier and the surrounding magnetic layers, providing clear information on the barrier's structure, this technique is not well suited to determining the degree of layer oxidation. Throughout this work we have presumed Al oxidation in the Al_2O_3 phase, an assumption observed throughout the literature. The difference between scattering factors for Al and Al_2O_3 is too small to assess the oxidation with any accuracy. This has been demonstrated in *Figure 4.6* in which an identical tunnel junction has been simulated with an Al and Al_2O_3 barrier.

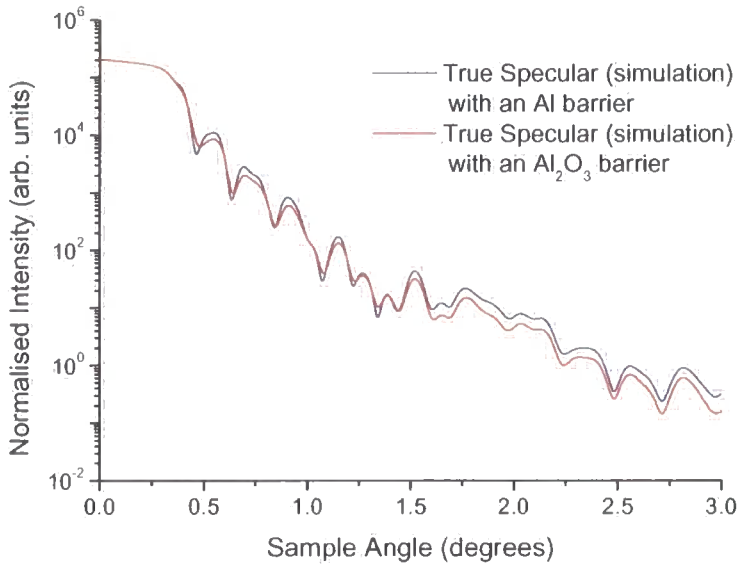

Figure 4.6: *Simulated specular profiles for 2 similar tunnel junctions with Al (blue) and Al_2O_3 (red) barriers demonstrating the impracticalities of using GIXR as a technique to determine the extent of layer oxidation.*

The simulations presented here clearly show the inability of GIXR in determining the degree of layer oxidation. Any differences in the specular profile can be simply lost through minor differences in the sample interface roughness.

4.7 Current – Voltage (I-V) Characterisation

In addition to examining the tunnel junction MR, a 4-point d.c. measurement was also performed in order to evaluate the current density as a function of bias voltage. It

was then possible, with the theoretical arguments of Simmons' and Hartman, to fit the non linear I-V curve and determine values such as the barrier height and width.

4.7.1 Simmons' Model

In this section the Simmons' Model is introduced to describe the current flow through a single barrier of a generalised shape. The formula derived here follows the original derivation made by John Simmons' [20] in 1963 and describes the current – voltage relationship for a tunnel junction. To derive this model, some simplifying assumptions have been made. First of all, the potential barrier has been considered in a single dimension with the current flowing solely in the x-direction.

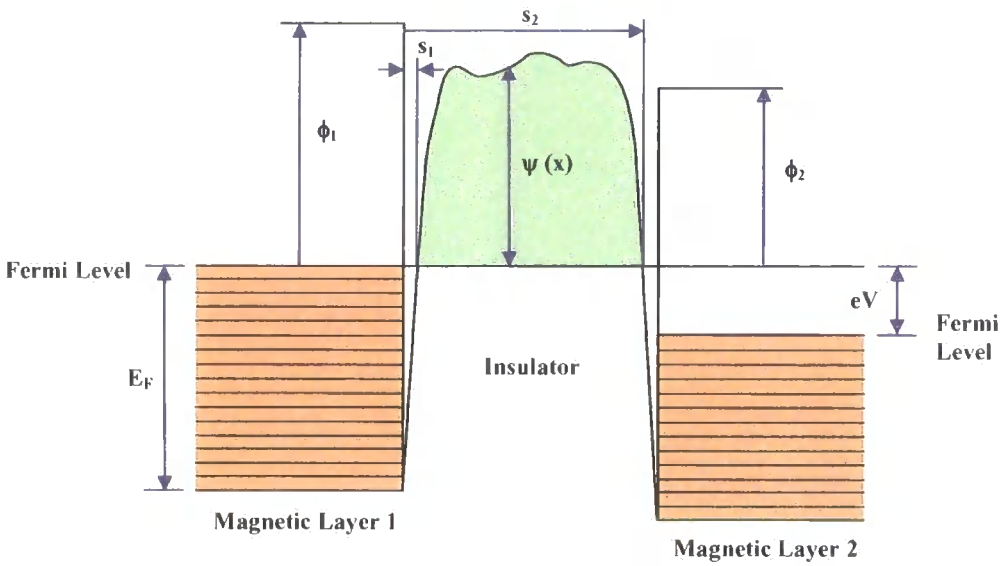

Figure 4.7: *MTJ energy diagram showing a general potential barrier between the two magnetic layers.*

The tunnel junction, as an energy diagram, has been illustrated in *Figure 4.7*. Equilibrium conditions require that the insulator energy gap is above the Fermi level for the two magnetic layers. As a result, the insulator introduces a potential barrier restricting the flow of electrons. Current can only flow past this barrier if either the electrons have sufficient thermal energy to surmount the barrier or if the barrier is thin enough to allow quantum tunnelling. Low temperatures have been assumed, thus through neglecting thermal electrons, all current flow is accounted for with tunnelling.

First of all let us consider the number of electrons flowing from ferromagnetic layer 1 to layer 2. This will be dependent on the number of electrons in layer 1 and their energy distribution:

$$N_{1\to 2} = \int_0^{v_{max}} D(E_x) v_x n(v_x) dv_x = \frac{1}{m} \int_0^{E_{max}} D(E_x) n(v_x) dE_x$$

Equation 4.5

$n(v_x)dv_x$ is the number of electrons per unit volume with a velocity between v_x and dv_x, E_{max} ($= \frac{1}{2} m v_{max}^2$) is the maximum energy of the electrons. $D(E_x)$ is the probability of an electron penetrating the barrier, a factor dependent upon the barrier height function, thickness and of course the energy of the incident electron. If an isotropic velocity distribution is assumed then the number of electrons (expressed in polar coordinates) between the usual infinite limits is given by:

$$n(v_x) = \frac{4\pi m^3}{h^3} \int_0^{\infty} f(E) dE_r$$

Equation 4.6

where $f(E)$ is the Fermi-Dirac distribution. Through substituting *Equation 4.6* into *Equation 4.5*:

$$N_{1\to 2} = \frac{4\pi m^2}{h^3} \int_0^{E_{max}} D(E_x) dE_x \int_0^{\infty} f(E) dE_r$$

Equation 4.7

And so in a similar way the number of electrons tunnelling from layer 2 into layer 1 is:

$$N_{2\to 1} = \frac{4\pi m^2}{h^3} \int_0^{E_{max}} D(E_x) dE_x \int_0^{\infty} f(E + eV) dE_r$$

Equation 4.8

The net flow $N = N_{1\to 2} - N_{2\to 1}$ and thus the current density becomes:

$$J = \int_0^{E_{max}} D(E_x) \gamma dE_x$$

Equation 4.9

where $\gamma = \gamma_1 - \gamma_2$, and:

$$\gamma_1 = \frac{4\pi m^2 e}{h^3} \int_0^{\infty} f(E) dE_r \qquad \gamma_2 = \frac{4\pi m^2 e}{h^3} \int_0^{\infty} f(E + eV) dE_r$$

Equation 4.10

The tunnelling probability function $D(E_x)$, is given by the WKB approximation, in which a slowly varying potential $E_F + \psi(x)$, is assumed:

$$D(E_x) = \exp\left[-\frac{4\pi}{h}\sqrt{2m}\int_{s_1}^{s_2}(E_F + \psi(x) - E_x)^{1/2}dx\right]$$

Equation 4.11

After integration:

$$D(E_x) \approx \exp\left[-A(E_F + \overline{\psi} - E_x)^{1/2}\right]$$

Equation 4.12

where $A \propto \Delta s$ $(=s_2 - s_1)$ and $\overline{\psi}$ is the mean height of the barrier above E_F as defined in *Figure 4.7* and so given by the following equation:

$$\overline{\psi} = \frac{1}{\Delta s}\int_{s_1}^{s_2}\psi(x)dx$$

Equation 4.13

For the barrier system depicted in *Figure 4.7*, γ (defined in *Equation 4.10*) has been evaluated at 0 K:

$$\gamma = \left\{ \begin{array}{cc} (4\pi me/h^3)(eV) & 0 < E_x < E_F - eV \\ (4\pi me/h^3)(E_F - E_x) & E_F - eV < E_x < E_F \\ 0 & E_x > E_F \end{array} \right\}$$

Equation 4.14

Substituting *Equation 4.12* and *Equation 4.14* into *Equation 4.9* yields:

$$J = \frac{4\pi me}{h^3}\left\{eV\int_0^{E_F - eV}\exp\left[-A(E_F + \overline{\psi} - E_x)^{1/2}\right]dE_x + \int_{E_F - eV}^{E_F}(E_F - E_x)\exp\left[-A(E_F + \overline{\psi} - E_x)^{1/2}\right]dE_x\right\}$$

Equation 4.15

After a lot of integration, for which the reader is referred to [20], the current density can be expressed as:

$$J = J_o\{\overline{\psi}\exp(-A\overline{\psi}^{1/2}) - (\overline{\psi} + eV)\exp(-A(\overline{\psi} + eV)^{1/2})\}$$

Equation 4.16

where $J_o = e/2\pi h(\beta\Delta s)^2$ and β is a correction factor. The general form of *Equation 4.16* means it can be applied to any shape of potential barrier assuming the mean height is known. The current-voltage characteristic profile can be measured and with *Equation*

4.16 the barrier height and width determined. *Equation 4.16* has been numerically evaluated below with J in units of Acm^{-2}, ψ in V with s_1 and s_2 in Å units.

$$J = \left[\frac{6.2\times10^{10}}{(\beta\Delta s)^2}\right]\{\overline{\psi}\exp(-1.025\beta\Delta s\overline{\psi}^{1/2}) - (\overline{\psi}+V)\exp(-1.025\beta\Delta s(\overline{\psi}+V)^{1/2})\}$$

Equation 4.17

Although the general formula derived in *Equation 4.16* is a good approximation to the current – voltage relationship, in this study a more accurate form of the derivation was used. Based on Simmons' model, and extended [33-35] with the work of Hartman, some of the factors neglected through assumptions made in the earlier approximation were included. The affect of differing work functions for each of the magnetic layers has been considered resulting in a trapezoidal barrier shape. The theory of image potential, which reduces the potential barrier by rounding off the edges and reducing the thickness, has also been included. This introduces a hyperbolic function resulting in an elliptical integral which can only be solved numerically. Finally, the theory has been extended for use at room temperature. For more details the reader is referred to [36].

4.7.2 Determination of Barrier Widths

Fits to the I(V) data were taken in a bias voltage range of ±700 mV and have been shown in *Figure 4.8*. Both the current density and conductance are shown here with the corresponding fit. Bias destruction tests have revealed a mean breakdown voltage of 1.1 V.

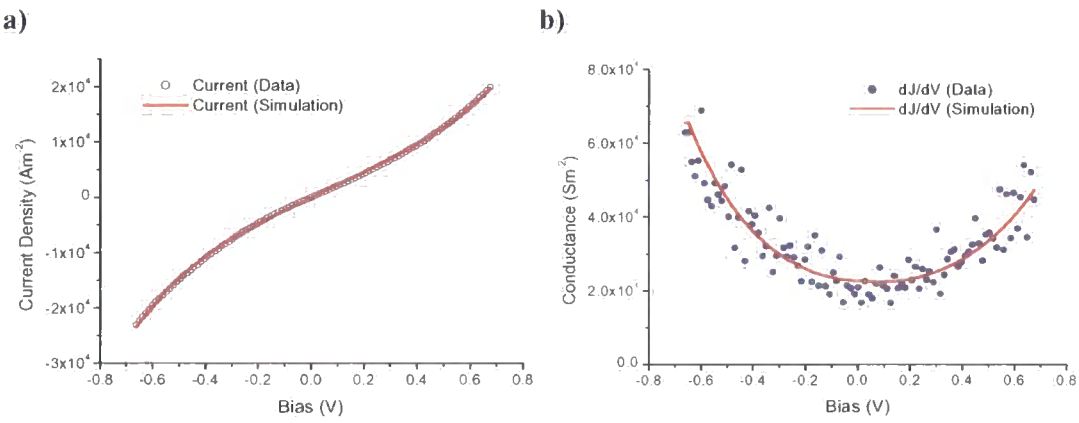

Figure 4.8: *The* ***a)*** *current density and* ***b)*** *conductance as a function of applied voltage fitted with Simmons' model (courtesy of Dr Norman Hughes).*

By assuming a homogeneous Al_2O_3 insulating layer, fits have been made to the current density profile. The mean barrier widths determined for all the tunnel junctions have been tabulated along with the average MR values in *Table 4.1*:

Sample Oxidation	I(V) Thickness (Å)	MR (%)
1 minute	12.1±0.1	3.1±0.05
3 minute	13.2±0.3	12.1±0.8
5 minute	16.4±0.1	10.2±0.05

Table 4.1: *Measured barrier thickness using I(V) Simmons' modelling and MR for samples with varied oxidation periods.*

The widths obtained from fitting the magneto-transport tunnelling data are in good agreement with the nominal structure, with a slight increase in barrier width with oxidation time. In order to directly compare the transport measurements GIXR has been used for structural characterisation.

4.8 Structural Characterisation using GIXR

As previously mentioned, GIXR is ideally suited to the study of magnetic tunnel junctions due to a large difference in the scattering factors between Al (or Al_2O_3) and the surrounding ferromagnetic layers. This results in excellent contrast between the layers, providing clear information on the barrier's structure.

Measurements were taken on the *Bede GXR1* reflectometer in the Durham laboratory as described in *Section 2.9.1.1*, and at station 2.3 at the Daresbury SRS, see *Section 2.9.2.1*. The true specular profile provides average in-plane information as a function of depth, such as layer thickness and interface width. These parameters are obtained through fitting the specular data using the *Bede* Mercury code as described in *Section 2.6*. The diffuse scatter provides information on the nature of the interface morphologies and reveals correlation or conformality in roughness between the layers.

The concept of out-of-plane correlation has been demonstrated below where we find two multilayered systems featuring *a)* correlated and *b)* uncorrelated roughness between the layer interfaces. The former consists of a roughness profile which is repeated exactly onto the other interfaces whereas the uncorrelated interfaces show no inter-dependence

and are therefore statistically random. In reality, systems exhibit partially correlated roughness, as shown in *c)*, a mixture between the extreme forms of roughness.

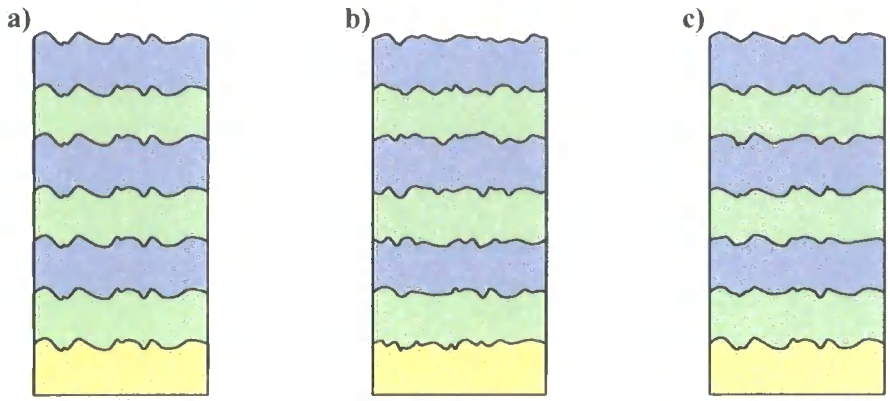

Figure 4.9: *Different forms of roughness in a multilayer system:* ***a)*** *totally correlated,* ***b)*** *totally uncorrelated and* ***c)*** *partially correlated.*

In order to make a direct comparison with the results presented in *Section 4.7.2*, the samples oxidised for 1, 3 and 5 minutes were characterised. The specular reflectivity profiles with their corresponding fits, together with the structural parameters used in modelling the fit, are shown in *Figure 4.10* and *Table 4.2:*

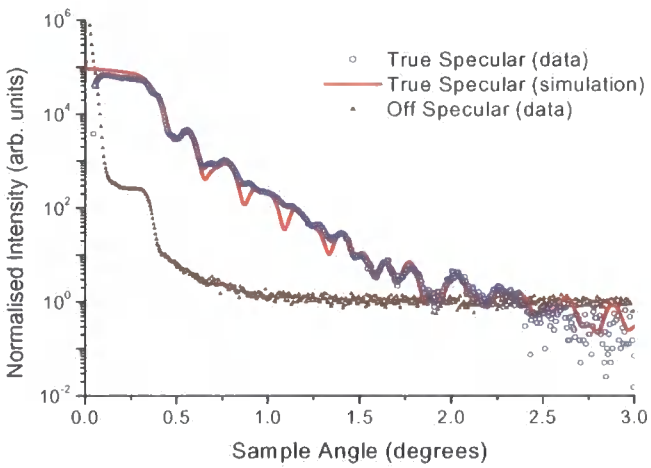

1 minute oxidation period:

Layer	Thickness (Å)	Roughness (Å)
Oxide	8.9±2	1.9±0.5
NiFe	148±5	1.0±0.5
Al_2O_3	24.2±1	2.2±0.5
Co	131±5	4.6±0.5
Al_2O_3	250±5	2.3±0.5
Si	-	6.9±0.5

Figure 4.10a and Table 4.2a: *True Specular (data and fit) and off-specular profile for a MTJ with a 1 minute barrier oxidation period.*

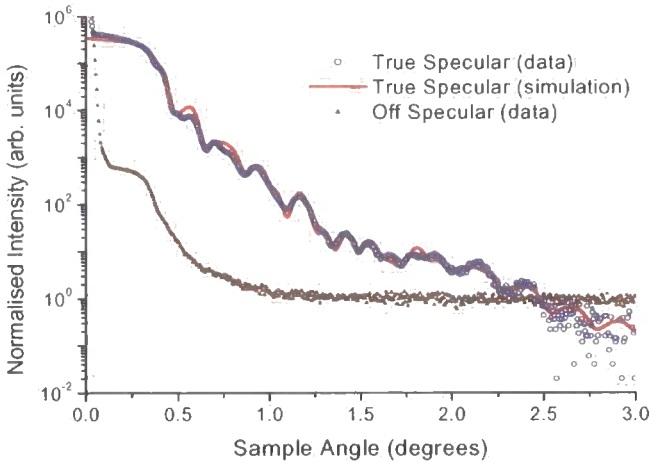

3 minute oxidation period:

Layer	Thickness (Å)	Roughness (Å)
Oxide	3.5±2	5.9±0.5
NiFe	151±5	11.5±0.5
Al_2O_3	28.1±1	2.7±0.5
Co	125±5	5.5±0.5
Al_2O_3	248±5	4.6±0.5
Si	-	6.3±0.5

***Figure 4.10b and Table 4.2b**: True Specular (data and fit) and off-specular profile for a MTJ with a 3 minute barrier oxidation period.*

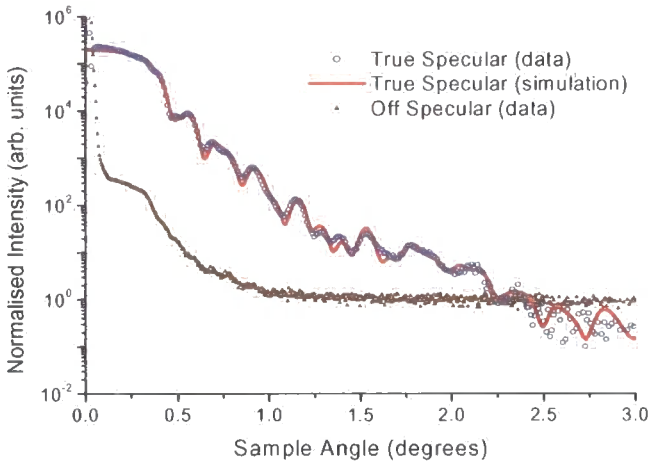

5 minute oxidation period:

Layer	Thickness (Å)	Roughness (Å)
Oxide	3.1±2	6.8±0.5
NiFe	153±5	2.1±0.5
Al_2O_3	31.2±1	2.3±0.5
Co	124±5	4.5±0.5
Al_2O_3	239±5	3.4±0.5
Si	-	6.5±0.5

***Figure 4.10c and Table 4.2c:** True Specular (data and fit) and off-specular profile for a MTJ with a 5 minute barrier oxidation period.*

The metallic layer thickness and roughness values were found to be similar for all the samples, demonstrating consistency and good control throughout the sputtering process. The true specular data has been corrected for the effect of forward diffuse off-specular scatter (as described in *Section 2.5*), which has also been shown in the figure.

An unoxidised control sample was also characterised, the specular reflectivity profile with the fitted structural parameters are shown in the figure and table below:

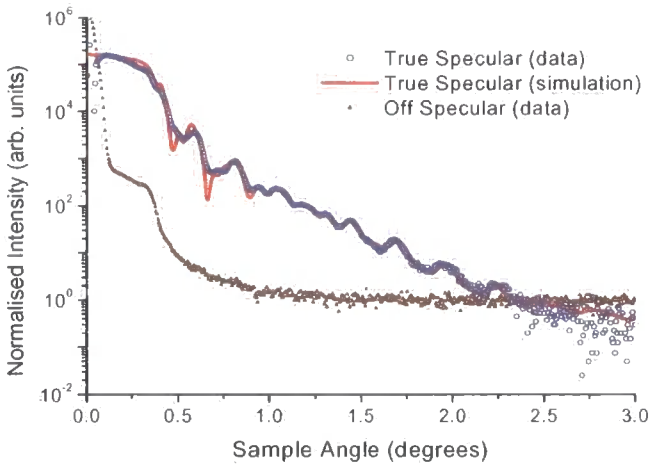

No Oxidation:

Layer	Thickness (Å)	Roughness (Å)
Oxide	3.4±2	7.8±0.5
NiFe	151±5	4.1±0.5
Al	16.1±1	7.9±0.5
Co	134±5	5.3±0.5
Al_2O_3	253±5	4.9±0.5
Si	-	6.9±0.5

Figure 4.10d and Table 4.2d: *True Specular (data and fit) and off-specular profile for a MTJ with no oxidation.*

Immediately a disparity in the barrier thickness is noted. Although some increase in layer thickness would be expected through the oxidation process, it is surprising to find almost a factor of 2 increase. In theory it might be possible to calculate the expansion from relative Al densities between pure Al and the Al oxide. However the amorphous Al oxide has no well defined lattice structure, this makes such calculations very difficult.

Another interesting observation has been made through comparing values for the interface width between the Co / Al_2O_3 interface and the Co / Al interface. The sample with the Al left unoxidised has an interface width of 8 ± 1 Å. This is consistent with the results obtained in *Chapter 5*, see *Table 5.9*. In oxidising the Al layer there is a reduction in interface width, between the Co and the barrier, to about 4.5 Å. This suggests the oxidation of the Al layer produce a migration of Al atoms out of the Co layer.

One further and important observation is seen in the longitudinal diffuse scatter shown on these figures. The absence of Kiessig fringes in the off specular diffuse indicates almost no conformality between the roughness of the top and bottom surface, and suggests non-conformal roughness across the barrier.

The in-plane correlation length has also been examined with a series of transverse diffuse scans, in q_x. These were made at an energy of 780 eV at station 5U1 at the Daresbury SRS, see *Section 6.3*. The soft energy provides access to a greater range in

reciprocal space, as described in *Section 6.6.2*, allowing length scales down to 300 Å to be probed. The transverse diffuse scans are shown below in *Figure 4.11:*

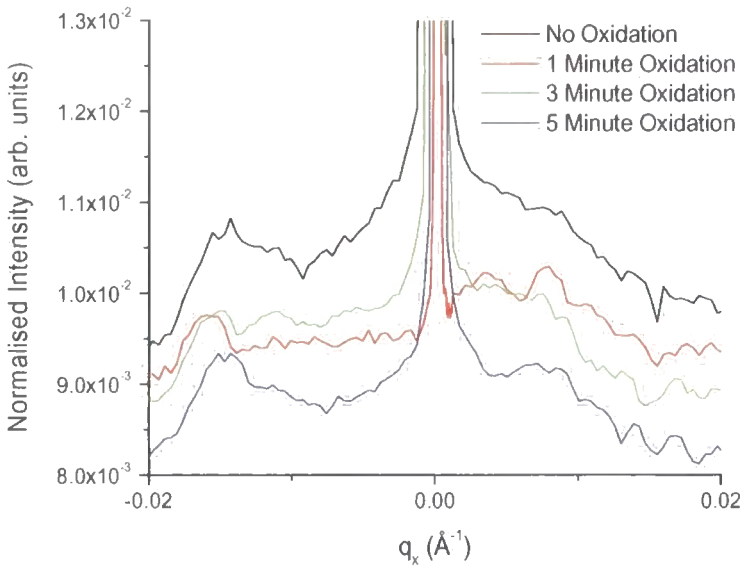

Figure 4.11: *Transverse Diffuse scans to determine the in-plane correlation lengths, ξ.*

By measuring the FWHM and using the theory presented in *Appendix D*, in-plane correlation lengths were obtained. Each of the samples have very low correlation lengths; for the unoxidised and 5 minute oxidised sample $\xi = 330 \pm 20$ Å and for the 1 and 3 minute oxidised samples $\xi < 300$ Å. This indicates, in conjunction with the absence of any out-of-plane correlation, a considerable variation in the barrier thickness due to roughness.

The additional set of samples grown at MIT were also analysed using GIXR. The profiles shown in *Figure 4.12* are those for the sample set prepared with a 12 Å Al thickness; unoxidised, oxidised and oxidised annealed:

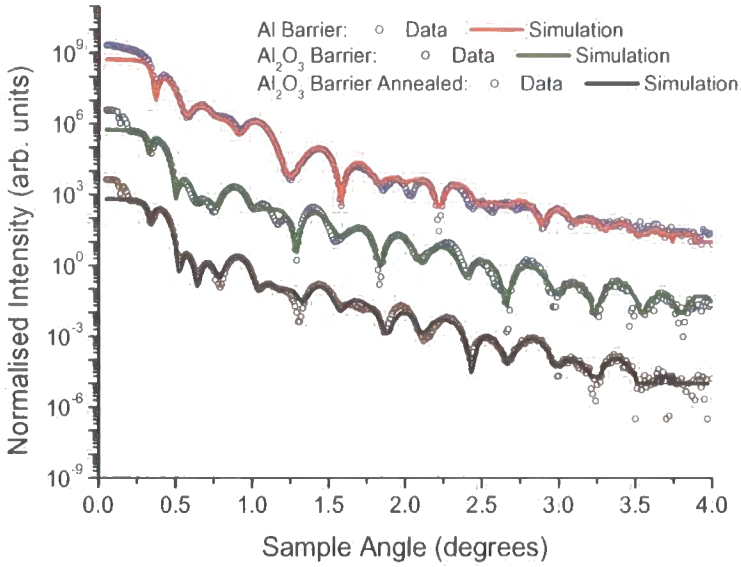

Figure 4.12: *True Specular (data and fit) and off-specular profile for a MTJ with a nominal Al thickness of 12 Å.*

Excellent fits to the reflectivity profiles provide thicknesses for the Co and NiFe layers which are consistent between all samples and comparable with the nominal structure. However the Al and Al_2O_3 barriers are much thicker than anticipated, their values and respective roughness on either side has been given in the table below:

	Nominal	Al only	Al_2O_3	Al_2O_3 annealed
Top Roughness (Å)	-	5.1±0.5	4.1±0.5	4.6±0.5
Thickness (Å)	12±1	19.5±1	71.2±2	90.1±2
Bottom Roughness (Å)	-	6.2±0.5	3.2±0.5	3.3±0.5

Table 4.3: *Barrier properties obtained from the fits seen in Figure 4.12 for a tunnel junction with a nominal thickness of 12 Å.*

For comparison, a further set has been characterised; these samples have a nominal Al thickness of 16 Å. Once again parameters associated with the Co and NiFe layers are consistent with each other and their nominal values, however, the Al and Al_2O_3 barriers are much thicker than nominal.

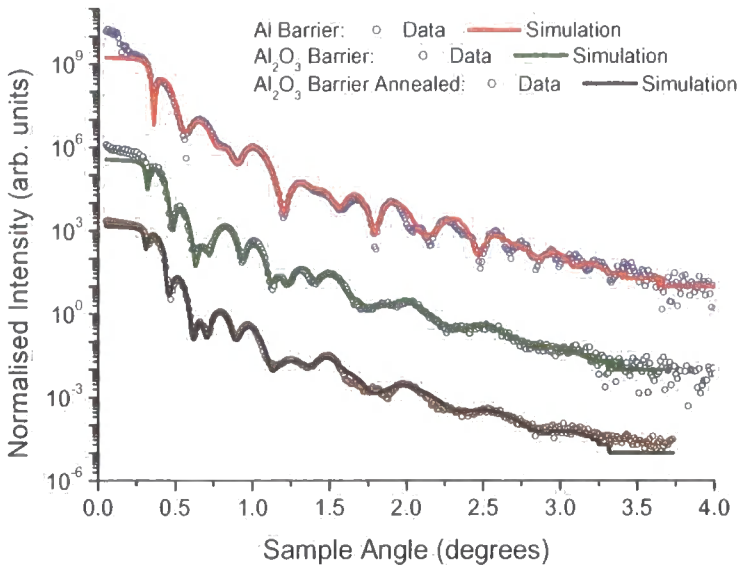

Figure 4.13: *True Specular (data and fit) and off-specular profile for a MTJ with a nominal Al thickness of 16 Å.*

	Nominal	Al only	Al_2O_3	Al_2O_3 annealed
Top Roughness (Å)	-	5.5 ± 0.5	3.5 ± 0.5	13.3 ± 0.5
Thickness (Å)	16 ± 1	24.2 ± 1	76.4 ± 2	91.3 ± 2
Bottom Roughness (Å)	-	5.2 ± 0.5	9.2 ± 0.5	3.6 ± 0.5

Table 4.4: *Barrier properties obtained from the fits seen in Figure 4.13 for a tunnel junction with a nominal thickness of 16 Å.*

Although the Al layers are thicker than nominal, the important result is seen in the thickness of the barrier after oxidation. The large increase is far greater than expected and confirms the effect seen in the earlier MTJs grown at Exeter. Annealing had very little affect to the overall structure, although a slight further increase to the barrier thickness is noted.

It now becomes clear as to why no MR was seen in these samples. The larger than nominal Al layers, combined with the oxidation expansion, has resulted in barriers which are too thick for any substantial tunnelling to occur between the magnetic layers. The thickness of the barrier is very important, if the barrier is too thick tunnelling disappears, however as you reduce the barrier thickness there is an increased probability of pinhole formation.

4.9 Comparing Barrier Widths

Both GIXR and I(V) measurements agree that oxidation has the affect of monotonically increasing the barrier thickness. *Figure 4.14* and *Table 4.5* below show this increase in thickness with oxidation and, in addition, the contrast between the results obtained from the two individual techniques.

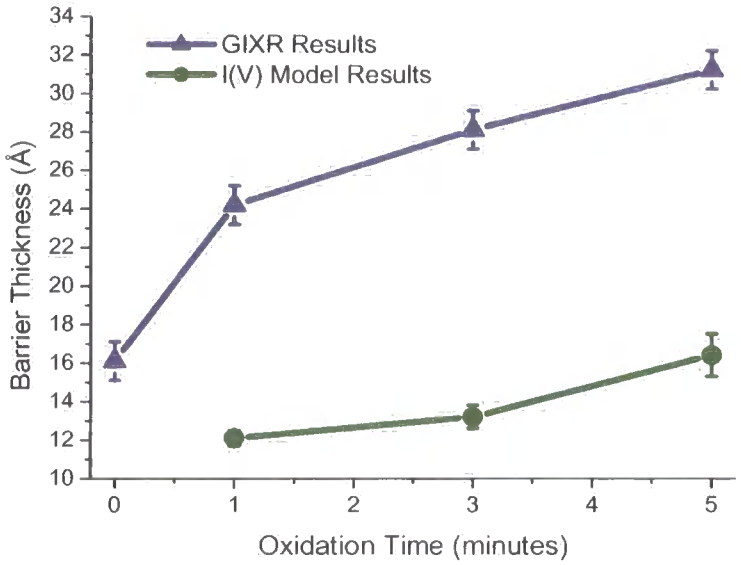

Figure 4.14: *A measure of barrier thickness as a function of oxidation time using i) GIXR and ii) Simmons' modelling.*

Sample oxidation	Thickness (Å)			Ratio of GIXR & I(V) thickness	MR (%)
	Nominal	GIXR	I(V)		
None	14	16.1	-	-	-
1 minute	14	24.2	12.1	2.1	3.1
3 minute	14	28.1	13.2	2.1	12.1
5 minute	14	31.2	16.4	1.9	10.2

Table 4.5: *Measured barrier thickness for different oxidation times using i) GIXR and ii) I(V) Simmons' modelling.*

In comparing the results obtained from GIXR with the I(V) modelling a large discrepancy in barrier thickness is noted. The Al_2O_3 layer thickness as 'seen' by the X-

ray reflectivity is, in all cases, much greater than the original thickness of the Al layer and roughly twice that of the value determined from the I(V) modelling. This result is not an artefact of the GIXR modelling process since the Al thickness of the unoxidised control sample yielded a value of 16.1(±1) Å, a value which is in excellent agreement with the results obtained from the Dektak profilometer calibration. In addition, the high contrast available (with X-ray techniques) between the barrier and the surrounding layers promotes confidence, with the sensitivity to the barrier width being so high that even a small change to barrier thickness results in a drastically different reflectivity profile. This has been demonstrated in *Figure 4.15*, where an extra 5 Å has been introduced to the Al_2O_3 barrier thickness.

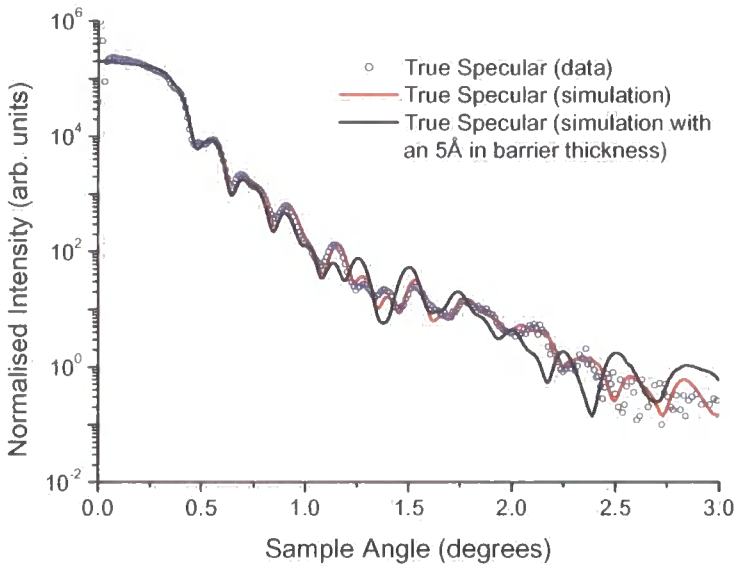

Figure 4.15: *True Specular data and 2 simulations with a 5 Å difference in Al_2O_3 barrier thickness, demonstrating the sensitivity of GIXR to barrier thickness.*

Confident both experimental results are free from random error, the forward discussion will address the validity of both techniques in the structural characterisation of magnetic tunnel junctions and attempt to answer the reason for the unexpected discrepancy.

4.10 Discussion

The values obtained for the metallic layer thickness and roughness using GIXR were found to be very similar for all of the samples. This demonstrated good control during the growth process and in particular, good controlled growth of the Al layer. Through investigating the affect of glow discharge oxidation time, MR measurements revealed a peak in TMR associated with a 3 minute oxidation period. Reduced MR with under-oxidation can be attributed to portions of the barrier being left unoxidised, this can result in pinhole formation and the presence of other high conductive regions reducing the tunnelling and hence TMR. Over-oxidising can lead to the oxidation of the lower Co layer, affecting the interface as well as the magnetic structure. Co oxide is anti-ferromagnetic which will affect the magnetic interface and the ferromagnetic Co layer underneath. Indeed, recent results obtained by the author (in collaboration with Alex Cole from the University of Leeds) suggest over-oxidation of the barrier can cause exchange bias pinning from the pseudo AF CoO layer. This will affect spin polarisation, tunnelling and the TMR.

An important observation noted a substantial increase in barrier thickness with oxidation, which was far greater than expected. No explanation for such an increase has been found, although this result has been confirmed in two sample sets from different laboratories. It is not an artefact of the modelling process since measurements of the unoxidised Al layers revealed (in both sample sets) much smaller values, closer to nominal. The difference in scattering values between the (Al, Al_2O_3 or any other form of Al oxidation) barrier and the magnetic (Co or NiFe) layers is sufficient to produce a high level of sensitivity such that changing the barrier thickness by as little as 5 Å results in a dramatically different reflectivity profile as seen in *Figure 4.15*.

Although the GIXR evidence for increased barrier thickness with oxidation is convincing, the I(V) fitting contradicts these findings revealing values much closer to those nominally expected and therefore explains some of the confusion surrounding this subject. In applying the Simmons' model we have assumed homogenous Al oxidation in an Al_2O_3 phase, a necessary assumption when calculating the barrier potential. The 'characteristic' or 'effective' tunnelling thickness obtained from the Simmons' model does not match with the average thickness obtained with the direct structural

characterisation. A phenomenon explained by localised tunnelling in areas at which the barrier thickness is near a minimum, perhaps as a result of general fluctuations in the barrier thickness or through more specific localised defects. If this is the case I(V) modelling will always measure the lowest thickness values for the barrier compared with the average values obtained with GIXR. The hypothesis has been illustrated below in *Figure 4.16*:

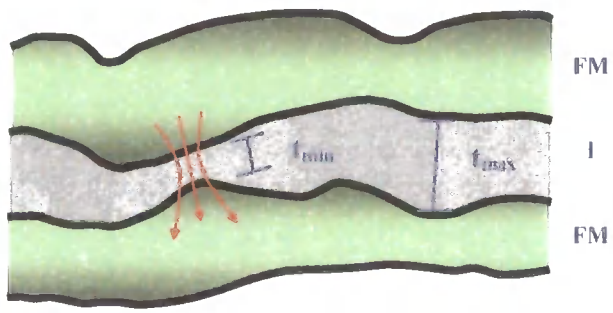

Figure 4.16: *Illustrating a barrier with varied barrier thickness and the tunnelling across the narrowest point.*

Localised tunnelling has also been seen by Da Costa *et al.* [16] who used an atomic force microscope equipped with a conducting tip to compare topographical information with current flow. Their results showed large local variation in the tunnelling current which was attributed to small changes in barrier thickness and so confirmed that the total conductance is dominated by contributions from localised sites.

The diffuse scatter data obtained confirmed these ideas; an absence of Kiessig fringes in the longitudinal off-specular scans show that there is almost zero conformality in roughness between the layers, and most importantly, between the barrier interfaces indicating a variation in the barrier thickness. The transverse diffuse scans revealed very small in-plane correlation lengths of approximately 300 Å, this suggests further variation in barrier width as a result of roughness.

Localised tunnelling should come as no great surprise since the tunnelling probability holds an exponential dependence with barrier thickness, see *Equation 4.16*. Therefore, the tunnelling would be localised to a length scale similar to the in-plane length scale seen in the roughness. In order to confirm these results, a series of computer tunnelling

simulations follow, using model interface structures. These demonstrate the degree to which localised tunnelling occurs due to imperfections at the interface.

4.11 Tunnel Current Simulations

4.11.1 Model

In order to examine the hypothesis discussed in the previous section, a series of computer models was designed to simulate the tunnelling across an insulating barrier. The code begins by simulating the barrier interface, using a statistical self-affine fractal model with the standard correlation function as described with *Equation 2.38* in *Section 2.7.2*. The chosen roughness σ, fractal parameter h, and correlation length ξ, correspond to 5 Å, 0.8 and 300 Å respectively. Once each interface (on either side of the barrier) has been constructed (to Angstrom resolution, both in and out-of-plane), the software maps the tunnelling current from points along each interface across the barrier. This is done using the basic Simmons' Model as outlined in *Section 4.7.1*, using *Equation 4.17*:

$$J = \left[\frac{6.2\times10^{10}}{(\beta\Delta s)^2}\right]\left\{\bar{\psi}\exp(-1.025\beta\Delta s\bar{\psi}^{1/2}) - (\bar{\psi}+V)\exp(-1.025\beta\Delta s(\bar{\psi}+V)^{1/2})\right\}$$

Equation 4.17

The barrier height and applied voltage were chosen at 30 V and 0.6 V respectively. The distance across the barrier, Δs, was calculated from the relative point positions on each interface. Once this has been completed for each point relative to every other point on the opposite interface (with a step size of 1 Å), the model sums up the current position and magnitude across the barrier. The entire procedure as been outlined in the following diagram:

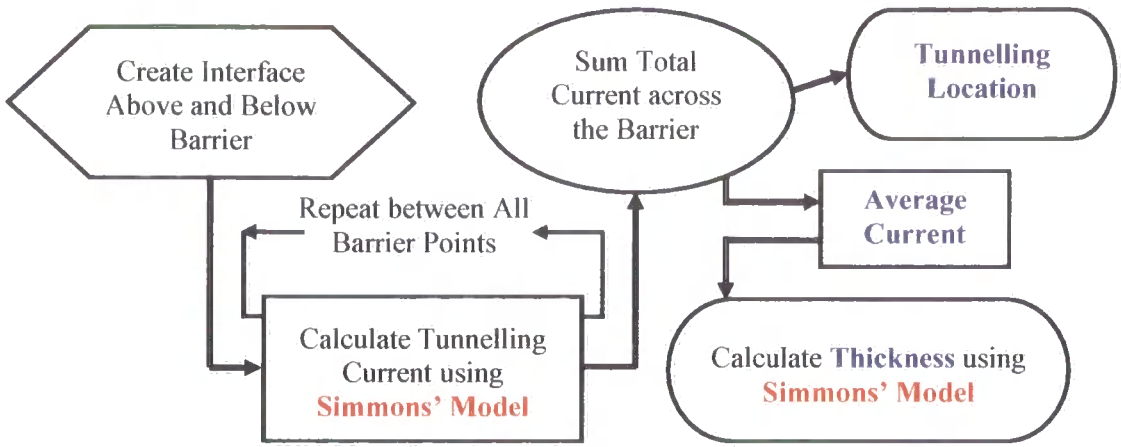

Figure 4.17: *Flow diagram to outline the basic procedure used in the tunnelling simulation.*

The simulations will provide information on the average current tunnelling through the barrier as well as the localisation (if any) of that tunnelling. It is also possible, with the average current, to re-evaluate the barrier thickness by putting the tunnelling current back into Simmons' model. The procedure effectively predicts the experimental thickness result for this model system by repeating the I(V) Simmons' analysis in *Section 4.7.2*. Finally the result can then be compared (as done experimentally) with the average barrier thickness.

4.11.2 Results

The first set of simulations have the average barrier thickness set to 28 Å, the thickness value obtained experimentally for the optimal magnetic tunnel junction oxidised for 3 minutes. The figure below shows the tunnelling across the model barrier on a *a*) linear and *b*) log scale:

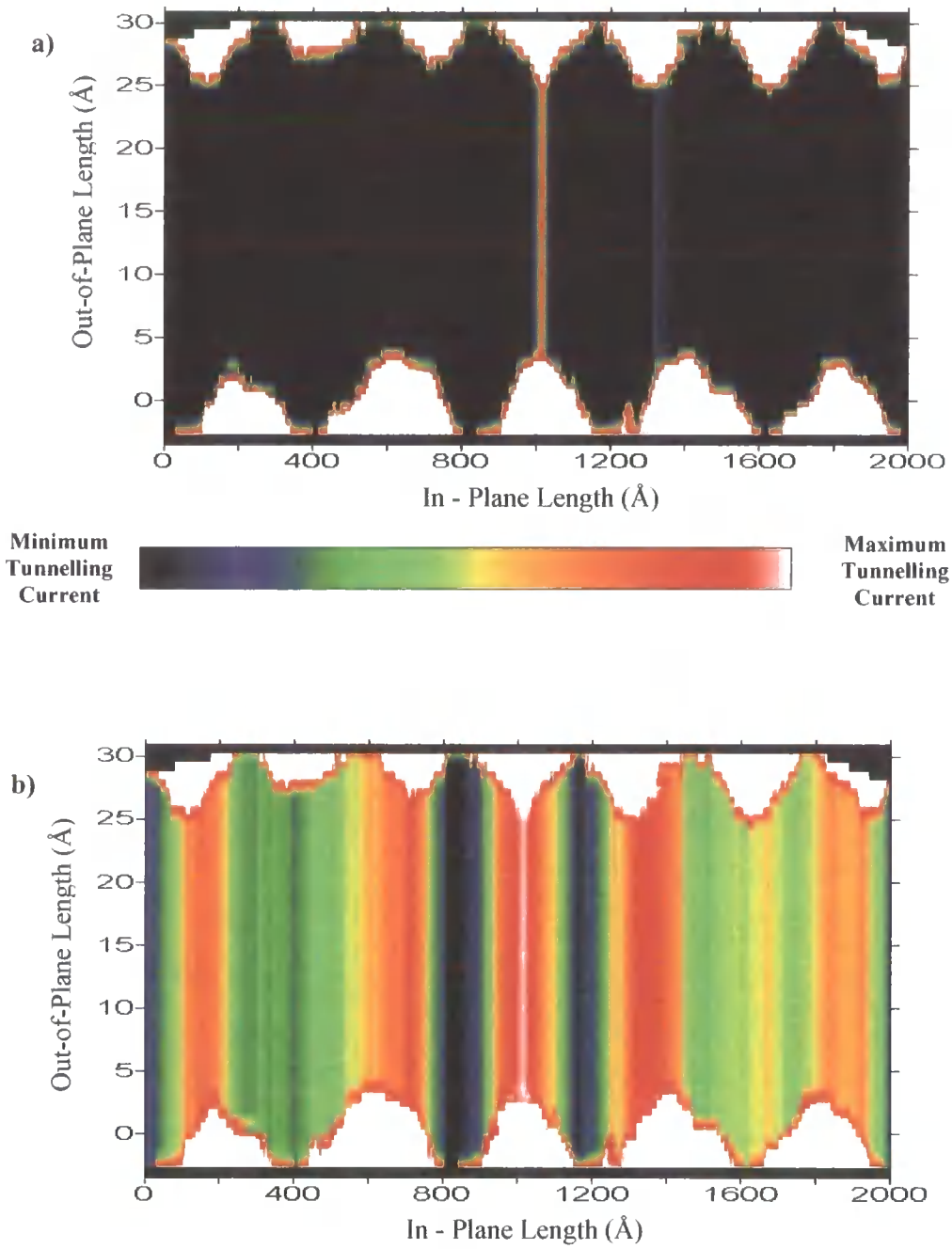

Figure 4.18: *Tunnelling current simulation across a 28 Å barrier with the tunnelling current shown on a* ***a)*** *linear and* ***b)*** *log scale.*

The linear scale plot reveals a surprising degree of localised tunnelling. The coloured key bar illustrates the range of current from a maximum arbitrary value (white) to zero (black). This observation supports the earlier discussions which inferred a large degree of localised tunnelling which, as previously mentioned, should not be too surprising due

to the tunnelling current's exponential dependence with barrier thickness. The log scale demonstrates there is a smaller contribution to tunnelling across the rest of the barrier.

By re-substituting the total barrier current back into the Simmons' model we obtain a much smaller barrier thickness; only 22 Å in comparison to the average barrier thickness of 28 Å. This simulated model confirms the inaccuracy of using I(V) fits to find the barrier thickness in real systems and confirms the findings presented in the previous sections.

To expand on this, additional simulations were made with the average barrier thickness values varying from 20 Å to 40 Å. The corresponding thickness, as measurable with I(V) fits using the Simmons' model, have been calculated and displayed comparatively in the following figure:

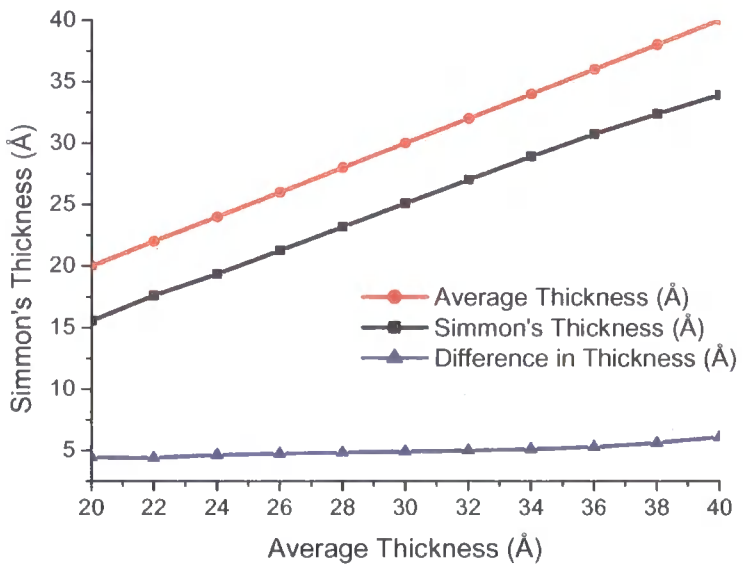

Figure 4.19: *Figure to show the discrepancy between average thickness and the thickness obtained with Simmons' model.*

This shows an increase in the Simmons' barrier thickness with increasing average barrier thickness, as well as the clear difference between the two. Note the similarity between this figure and the one obtained experimentally with increased oxidation times shown in *Figure 4.15*.

Although these simulations confirm the reasons given for the discrepancy between the two experimental thicknesses, they do not account for the magnitude in difference. However, the model assumes two perfect fractal interface structures defined by the

correlation function. A real system contains defects and as made clear in *Figure 4.18*, the tunnelling is extremely sensitive to barrier thickness fluctuations from any interface morphological changes. The presence of a defect to narrow the barrier will have a large affect on the current, but more precisely, affect the maximum fraction of total current at any one place across the barrier i.e. the magnitude of localised tunnelling. Such a scenario has been simulated and presented in the following figure. The average barrier thickness has been set to 28 Å, with a defect introduced to reduce the barrier thickness as measured from the Simmons' model from 22 Å down to 16 Å, the same value recorded experimentally.

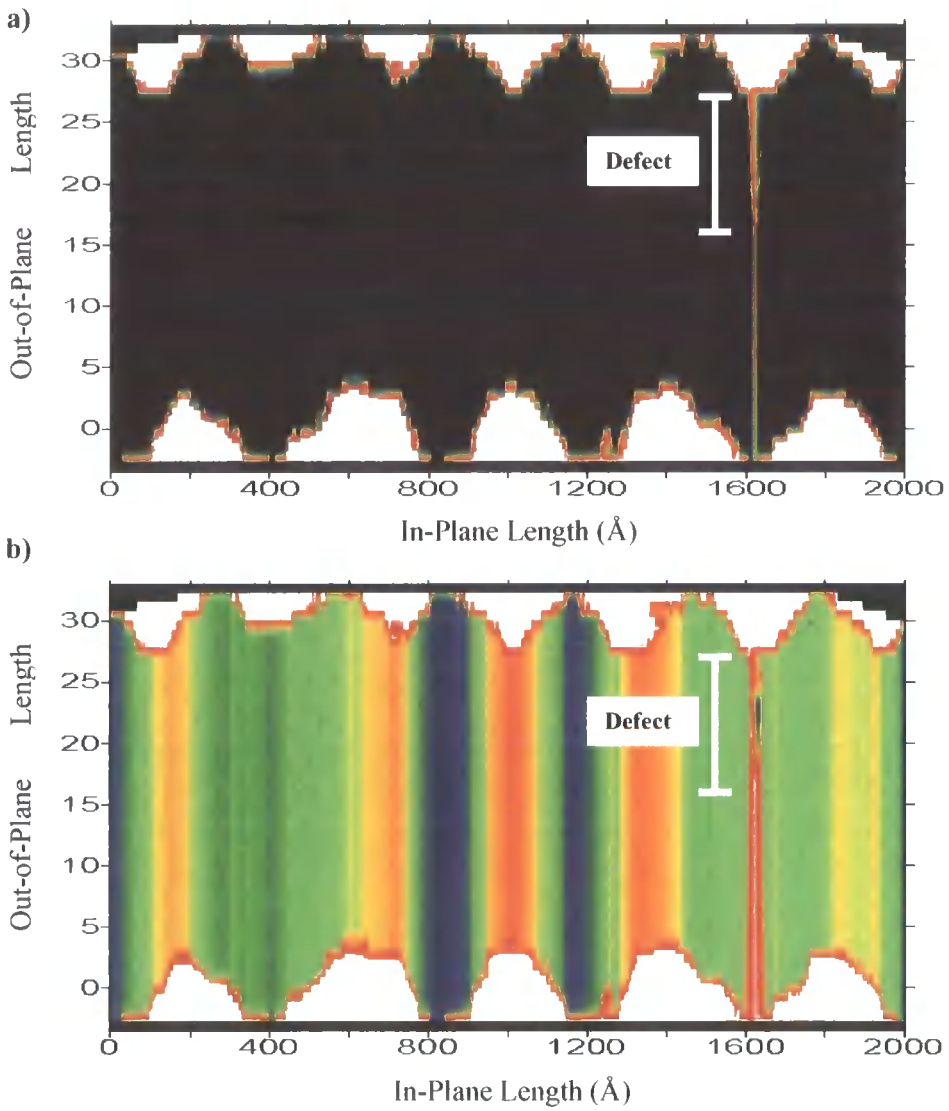

Figure 4.20: *Tunnelling current simulation across a 28 Å barrier with the introduction of a defect to reduce the thickness, as recorded from the Simmons' model, down to 16 Å.*

It is more than likely that such a defect would occur (probably more than once) somewhere across the barrier. It is also feasible that the deposition of the Al barrier across the lower magnetic layer was slightly uneven, this would result in regional variations across the sample (on a much longer length scale) in barrier thickness.

Such defects are responsible for the lower values recorded from the Simmons' model and yet are undetectable using GIXR which is only sensitive to the **average** barrier thickness across the whole sample.

4.12 Conclusions

The initial aims of this chapter were to investigate and optimise the magneto-resistance through varying the Al oxidation during the growth process and attempt to correlate that optimisation with structural differences, using two contrasting characterisation techniques. The magneto-transport properties were examined through a current – voltage relationship and through fitting this tunnelling current to the Simmons' model, a barrier width was extrapolated and compared directly with fits to GIXR data. A total of 21 tunnel junctions were grown, with varying oxidation periods of 1, 3 and 5 minutes and in addition some samples were grown without any oxidation to the Al barrier. A second set of samples were grown in a different laboratory to study and confirm the affect of oxidation on the barrier's structure.

In this study of MTJs it was found, with an initial Al barrier thickness of approximately 15 Å, that an oxidation time of 3 minutes produced sputtered junctions with the highest MR values (~12.1 %). Through examining possible correlation with the barrier structure, a monotonic increase in barrier thickness was recorded as a function of oxidation time. However, the barrier thickness as measured by the GIXR was almost twice that obtained by fitting the non-linear current–voltage to the Simmons' model. This indicated a substantial increase in barrier thickness by almost a factor of two upon oxidation.

The discrepancy between the two techniques can not be understood fully through any inhomogeneity in barrier oxidation, but rather explained in that tunnelling is in fact localised to specific regions across the barrier, where the thickness is at a minimum and thus providing a far higher probability of tunnelling. These regions can occur because of defects and other fluctuations due to non-conformal roughness, which is evident from

an absence of Kiessig fringes in the longitudinal off-specular scan and from the low correlation lengths (~300 Å) obtained from the transverse diffuse scans.

This hypothesis is confirmed with a series of tunnelling simulations. The tunnelling current between two interfaces (created under the standard correlation function) is calculated using the Simmons' model. The simulations not only show localised tunnelling but allow evaluation of (from the average current) the tunnelling thickness as measured from fits to the current-voltage profile with the Simmons' model. Simulation results confirm the average thickness is always greater than the Simmons' thickness. With the introduction of a defect, this effect is even more pronounced and could account for the discrepancy recorded experimentally.

It has been shown that current-voltage modelling is an inaccurate method for the absolute determination of barrier thickness. Due to fluctuations in barrier thickness, the method actually records a 'characteristic' or 'effective' barrier thickness as determined from the tunnelling electrons. The exponential dependence of the tunnelling probabilities results in strong localisation of tunnelling across the narrowest sections in the barrier and so using current-voltage modelling as a characterisation tool simply measures the minimum barrier thickness. Grazing incidence X-ray reflectivity barrier thickness measurements are always greater since this technique measures the average barrier thickness. Confusion surrounding the determination of barrier thickness could also be attributed to the substantial increase in thickness observed upon oxidation. Throughout this study we have seen the barrier thickness almost double during oxidation, from a value which is comparable to that measured from fitting the current-voltage profile.

4.13 References for Chapter 4

1. S.S.P. Parkin, K.P. Roche, M.G. Samant, P.M. Rice, R.B. Beyers, R.E. Scheuerlein, E.J. O'Sullivan, S.L. Brown, J. Bucchigano, D.W. Abraham, Yu Lu, M. Rooks, P.L. Trouilloud, R.A. Wanner, and W.J. Gallagher (1999) "*Exchange-biased magnetic tunnel junctions and application to nonvolatile magnetic random access memory (invited)*" J. Appl. Phys. **85** pg. 5828-5833.

2. W.J. Gallagher, S.S.P. Parkin, Y. Lu, X.P. Bian, A. Marley, K.P. Roche, R.A. Altman, S.A. Rishton, C. Jahnes, T.M. Shaw, and G. Xiao (1997) "*Microstructured magnetic tunnel junctions*" J. Appl. Phys. **81** pg. 3741-3746.

3. R. Meservey, P.M. Tedrow, and P. Fulde (1970) "*Magnetic Field Splitting of the Quasiparticle States in Superconducting Aluminum Films*" Phys. Rev. Lett. **25** pg. 1270-1272.

4. R. Meservey and P.M. Tedrow (1972) "*Spin Polarization of Tunneling Electrons from Films of Fe, Co, Ni and Gd*" Solid State Commun. **11** pg. 333-336.

5. P.M. Tedrow and R. Meservey (1971) "*Spin-Dependent Tunneling into Ferromagnetic Nickel*" Phys. Rev. Lett. **26** pg. 192-195.

6. G. Busch, M. Campagna, and H.C. Siegmann (1971) "*Spin-Polarized Photoelectrons from Fe, Co, and Ni*" Phys. Rev. B **4** pg. 746-750.

7. P.M. Tedrow and R. Meservey (1973) "*Spin Polarization of Electrons Tunneling from Films of Fe, Co, Ni, and Gd*" Phys. Rev. B **7** pg. 318-326.

8. P. LeClair, J.S. Moodera, and R. Meservey (1994) "*Ferromagnetic-ferromagnetic tunneling and the spin filter affect*" J. Appl. Phys. **76** (10) pg. 6546-6548.

9. J. Nowak and J. Rauluszkiewicz (1992) "*Spin dependent electron tunneling between ferromagnetic films*" J. Magn. Magn. Mater. **109** pg. 79-90.

10. T. Miyazaki, T. Yaoi, and S. Ishio (1991) "*Large magnetoresistance effect in 82Ni-Fe/Al-Al_2O_3/Co magnetic tunneling junction*" J. Magn. Magn. Mater. **98** pg. L7-L9.

11. S. Maekawa and U. Gafvert (1982) "*Electron Tunneling between Ferromagnetic Films*" IEEE Trans. Magn. **18** pg. 707-708.

12. J.S. Moodera, J. Nowak, and R.J.M. van de Veerdonk (1998) "*Interface Magnetism and Spin Wave Scattering in Ferromagnet-Insulator-Ferromagnet Tunnel Junctions*" Phys. Rev. Lett. **80** (13) pg. 2941-2944.

13. C. He Shang, J. Nowak, R. Jansen, and J.S. Moodera (1998) "*Temperature dependence of magnetoresistance and surface magnetization in ferromagnetic tunnel junctions*" Phys. Rev. B **58** pg. R2917-R2920.

14. R. Jansen and J.S. Moodera (1998) "*Influence of barrier impurities on the magnetoresistance in ferromagnetic tunnel junctions*" J. Appl. Phys. **83** pg. 6682-6684.

15. E.Y. Tsymbal and D.G. Pettifor (1999) "*The influence of impurities within the barrier on tunneling magnetoresistance*" J. Appl. Phys. **85** (8) pg. 5801-5803.

16. V. Da Costa, F. Bardou, C. Béal, Y. Henry, J.P. Bucher, and O. K. (1998) "*Nanometric cartography of tunnel current in metal–oxide junctions*" J. Appl. Phys. **83** pg. 6703-6705.

17. R.C. Sousa, J.J. Sun, V. Soares, P.P. Freitas, A. Kling, M.F. da Silva, and J.C. Soares (1998) "*Large tunneling magnetoresistance enhancement by thermal anneal*" Appl. Phys. Lett. **73** pg. 3288-3290.

18. J.S. Moodera, E.F. Gallagher, K. Robinson, and J. Nowak (1997) "*Optimum tunnel barrier in ferromagnetic–insulator–ferromagnetic tunneling structures*" Appl. Phys. Lett. **70** pg. 3050-3052.

19. T.E. Clark, F.B. Mancoff, S.X. Wang, M.B. Clemens, and R. Sinclair (1999) "*Study of DC plasma oxidised Al_2O_3 barriers in spin dependent tunneling junctions using high resolution transmission electron microscopy*" IEEE Trans. Magn. **35** (5) pg. 2922-2924.

20. J.G. Simmons (1963) "*Generalised Formula for the Electric Tunnel Effect between Similar Electrodes Films Seperated by a Thin Insulating Film*" J. Appl. Phys. **34** (6) pg. 1793-1803.

21. M. Julliere (1975) "*Tunneling between ferromagnetic films*" Phys. Lett. **54A** (3) pg. 225-226.

22. J.C. Slonczewski (1989) "*Conductance and exchange coupling of two ferromagnets separated by a tunneling barrier*" Phys. Rev. B **39** pg. 6995-7002.

23. J. Mathon (1997) "*Tight-binding theory of tunneling giant magnetoresistance*" Phys. Rev. B **56** pg. 11810-11819.

24. J.M. MacLaren, X.G. Zhang, and W.H. Butler (1997) "*Validity of the Julliere model of spin-dependent tunneling*" Phys. Rev. B **56** pg. 11827-11832.

25. E.Y. Tsymbal and D.G. Pett (1997) "*Modelling of spin-polarized electron tunnelling from 3d ferromagnets*" J. Phys. Condens. Matter. **9** pg. L411-L417.

26. H. Itoh, T. Ohsawa, and J. Inoue (2000) "*Magnetoresistance of Ferromagnetic Tunnel Junctions in the Double-Exchange Model*" Phys. Rev. Lett. **84** (11) pg. 2501-2504.

27. S.T. Chui (1997) "*Bias dependence in spin-polarized tunneling*" Phys. Rev. B **55** (9) pg. 5600-5603.

28. A.M. Bratkovsky (1997) "*Tunneling of electrons in conventional and half-metallic systems: Towards very large magnetoresistance*" Phys. Rev. B **56** (5) pg. 2344-2347.

29. X. Zhang, B. Li, and G. Sun (1997) "*Spin-polarized tunneling and magnetoresistance in ferromagnet/ insulator(semiconductor) single and double tunnel junctions subjected to an electric field*" Phys. Rev. B **56** (9) pg. 5484-5488.

30. J. Inoue and S. Maekawa (1996) "*Theory of tunneling magnetoresistance in granular magnetic films*" Phys. Rev. B **53** (18) pg. 11927-11929.

31. M.B. Stearns (1977) "*Simple Explanation of Tunneling Spin-Polarization of Fe, Co, Ni and its Alloys*" J. Magn. Magn. Mater. **5** pg. 167-171.

32. S. Blundell (2001) "*Magnetism in Condensed Matter*" Oxford University Press.

33. J.G. Simmons (1963) "*Electric Tunnel Effect between Dissimilar Electrodes Separated by a Thin Insulating Film*" J. Appl. Phys. **34** pg. 2581-2590.

34. J.G. Simmons (1964) "*Generalized Thermal J-V Charcateristic for the Electric Tunnel Effect*" J. Appl. Phys. **35** pg. 2655-2658.

35. T.E. Hartman "*Tunneling Through Asymmetric Barriers*" J. Appl. Phys. **35** pg. 3283-3294.

36. N. Hughes (2002) *PhD Thesis,* University of Exeter.

Chapter 5

Intermixing Studies in Aluminium Transition-Metal Bilayers

5.1 Introduction

The deposition of thin films of aluminium is an essential process in the manufacture of many important technologies. These films can be used, for example, as conductors, passivators and magnetic sensors such as the tunnel junctions examined in *Chapter 4*. The barriers used in magnetic tunnel junctions (MTJs) are often aluminium oxides and so to date a great deal of attention has been paid to the barrier evolution during the fabrication process. The standard growth process involves the initial deposition of an Al layer followed by oxidation. However, these barriers often contain defects [1-3] which can affect device efficiency. *Chapter 4* focused on barrier oxidation and the affect it has on the barrier structure (interface roughness, as well as the average and characteristic width) and thus magneto-transport. This chapter takes a step back in the fabrication process and examines the initial Al deposition.

One of the tricky aspects involved in barrier growth is the ability to oxidise the entire Al layer with no oxidisation to the lower ferromagnetic material. This goal will be exceptionally difficult to achieve if there is any initial intermixing at the interface that may occur on depositing the Al. Such was the initial motivation for this study; to determine, using grazing incidence X-ray techniques, the degree of intermixing across Al / magnetic-transition metal interfaces. However, the surprisingly large extent of intermixing observed led us to expand our study to include non-magnetic metals. This investigation presents a complete systematic study covering all transition metals from

groups 3,4 and 5 of the periodic table (with the one exception of Tc due to its radioactive nature).

The chapter begins by defining the interface morphology and discussing the important differences between intermixing and topological roughness. This is followed by a description of the experimental methods used in determining these interfacial parameters. The interface width is obtained from fits to the specular profile, and topological roughness from transverse diffuse analysis, thus allowing the intermixing to be deduced. By way of example, the data and subsequent analysis from a limited series of element bilayer sets; Pt, Mo, Ni, Fe and Co are presented. Finally *Table 5.9*, containing all 46 intermixing lengths obtained from this study, is presented on page 125.

The discussion of the results is based around the possible diffusion mechanisms which may be responsible for the intermixing. These include possible correlation with activation and cohesive energies, as well as the possibility of alloying and intermetallic formation. As grain boundary diffusion appears to be the most plausible, the in-plane grain size was measured from four element series (W, Ta, Ir and Os) using grazing incident X-ray diffraction.

5.2 Interface Morphology

At this point it is worth addressing more explicitly some of the terminology we shall need to describe the interface and its individual topological components which are of interest in this study. We shall also outline the X-ray techniques used to determine and evaluate these components quantitatively.

Figure 5.1 shows the three main interface morphological parameters. The interface width σ_T, is made up from components of topological roughness σ and intermixing Σ. Note that all of these parameters are defined and measured out-of-plane and are assumed to have an error function distribution. They relate to each other by adding in quadrature:

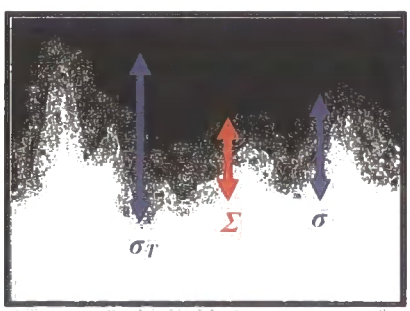

Figure 5.1: *Pictorial representation of an interface including the individual components of topological roughness and intermixing.*

$$\sigma_T^2 = \Sigma^2 + \sigma^2$$

Equation 5.1

The *average* interface width is determined by fitting the specular data and since, by definition, the scattering vector is purely out-of-plane, it is only sensitive to a measure of out-of-plane disorder (i.e. the interface width σ_T). In this geometry it is not possible to distinguish between roughness σ and intermixing Σ. In order to find the intermixing we must obtain the true topological roughness from the diffuse scatter. The diffuse scatter originates from roughness and so by using the theory which will be outlined in *Section 5.3.1* under the Born approximation, a value for the topological roughness σ is obtained. Finally, a simple calculation using *Equation 5.1* provides a measure of intermixing across the interface.

5.3 Experimental Details

The reflectivity measurements made in this chapter were performed at Station 2.3 of the Daresbury synchrotron radiation source (see *Section 2.9.2.1*) and on a *Bede GXR1* reflectometer in the Durham laboratories (see *Section 2.9.1.1*). For each of the samples, specular and longitudinal diffuse off-specular scans were taken. The specular data was then corrected for the effect of forward diffuse scatter, with the subtraction of the off-specular scatter, to provide the true specular profile as previously described in *Section 2.5*. These data are then used to determine average in-plane structural information as a function of depth, such as the layer thickness and the total interface width σ_T between the layers. The layer and interface parameters are obtained through fits using the *Bede* Mercury code as described in *Section 2.6*.

In order to differentiate the interface width into components of diffusion and roughness, transverse diffuse scans were also made, one at a Kiessig minimum and one at the maximum. Quantitative values of the interface roughness are obtained through modelling with *Bede* REFS, which uses the distorted wave Born approximation, or through following the energy conservation arguments discussed below in *Section 5.3.1*, under the Born approximation. The modelling and fitting using REFS is time-consuming and so, for the majority of transverse diffuse scans, analysis was conducted using the arguments described in the following section.

5.3.1 Estimating σ from I_{DIFF} / I_{SPEC}

Savage *et al.* [4] have demonstrated, using simple energy conservation arguments, that it is possible to determine the interface roughness from the relative ratio of integrated intensity between the specular and diffuse scatter. It has already been shown in *Section 2.7* (*Equation 2.41*) that the specular intensity is attenuated (under the Born wave model) by the so-called Debye-Waller factor:

$$I_{SPEC} = I_o \exp(-q_z^2\sigma^2)$$

Equation 5.2

Conservation arguments maintain $I_o = I_{SPEC} + I_{DIFF}$ and so:

$$I_{DIFF} = I_o - I_{SPEC} = I_o\,(1-\exp(-q_z^2\sigma^2))$$

Equation 5.3

Rearranged in terms of the ratio between the integrated diffuse and specular intensities results in the following dependence on the out-of-plane scattering vector q_z and roughness σ:

$$I_{DIFF}/I_{SPEC} = \exp(q_z^2\sigma^2) - 1$$

Equation 5.4

Thus, the topological roughness σ is found experimentally by integrating the specular and diffuse scatter, with respect to the in-plane component of the scattering vector q_x. Since the Born approximation assumes a point-like scattering nature from weak interactions, it is therefore important to only use this model for high values of q_z. This method also assumes the entire diffuse scatter is accessible within the transverse diffuse scan. However due to the cut-off observation limit in reciprocal space (see *Section 2.5*), it is only possible to probe a restrictive range of q_x. Thus *Equation 5.4* provides an underestimation to the true roughness, but nevertheless it can be used to a reasonable approximation to separate the interface width into its components of roughness and mixing.

5.4 The Samples

All of the samples used in this study were made at the National Institute of Standards and Technology (NIST) in the U.S.A. The metal bilayers were grown at room temperature by D.C. magnetron sputtering (at 2 mTorr) on substrates consisting of a silicon wafer with a thermal oxide layer of approximately 3000 Å. All depositions were at normal incidence with a magnetron power of 200 W at 350 V. In order to ensure all the atoms are thermalised, the distance between the target and substrate in the sputtering system was increased, from a typical distance of approximately 4 cm, up to 18 cm. This is equivalent to approximately 10 mean free paths in the sputtering gas pressure of 2 mTorr and so therefore producing in the region of 100 collisions with the Ar atoms and ions. This will thermalise all of the sputtered atoms before they reach the substrate.

For each transition metal X, two bilayer samples were grown: X deposited on Al and Al deposited on X. This was done for every transition metal from rows 4,5 and 6 of the periodic table with the exception of Tc. The nominal structure for the majority of these samples consisted of layers each 50 Å thick. However, for highly reactive samples with a large of amount of intermixing, layer thicknesses of 100 Å and even 200 Å were grown.

5.5 Results

This study has examined 23 elements and so over 46 separate samples, since a number of samples were duplicated to check the consistency of the growth techniques and intermixing analysis. Due to the large amount of data obtained it is impractical to present all the specular, off-specular and transverse diffuse scans here. Instead, by way of an example, the data sets for Pt and Mo have been presented as well as the initial magnetic-transition metals; Fe, Co and Ni. These samples and their respective results are in no way outstanding and are representative of the systems studied. The true specular profiles (with fits) for the remainder of elements studied have been catalogued in the *Appendix E*.

5.5.1 Platinum (Pt) Sample Set

The first sample set we shall examine is Pt. As is the case for each of the elements, two samples have been prepared; Al grown on Pt and Pt grown on Al. Here, 50 Å layers were deposited onto a SiO_2 substrate. *Figure 5.2* shows the specular profile for Al grown on Pt. High amplitude Kiessig fringes already indicate the presence of a well-structured bilayer with little disorder (including mixing) across the interface.

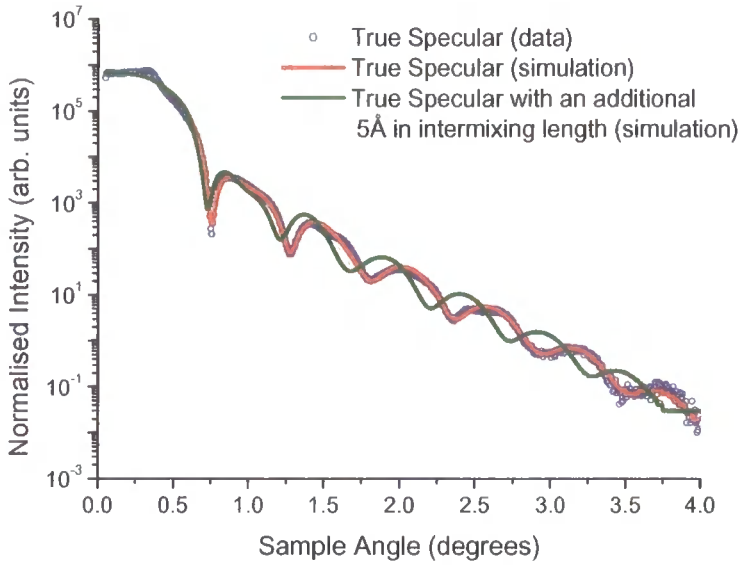

Figure 5.2: *Specular profile (corrected for the effect of forward diffuse scatter) for the bilayer with a nominal structure SiO_2/Pt(50 Å)/Al(50 Å). Simulated fit to the data (red) and an identical simulation with an additional 5 Å of interface width introduced to the model (green).*

The model used in obtaining the best fit is shown below in *Table 5.1a)*. In this, as well as some other examples, it was necessary to include an additional compound layer at the model interface. To demonstrate the sensitivity, a further simulation has been included in *Figure 5.2*, shown in green, in which an additional 5 Å has been added to the interface width.

Transverse diffuse scans were made across the minimum and maximum in the Kiessig interference fringes. *Figure 5.3* shows the diffuse data at fixed q_z across the peak of a Kiessig fringe.

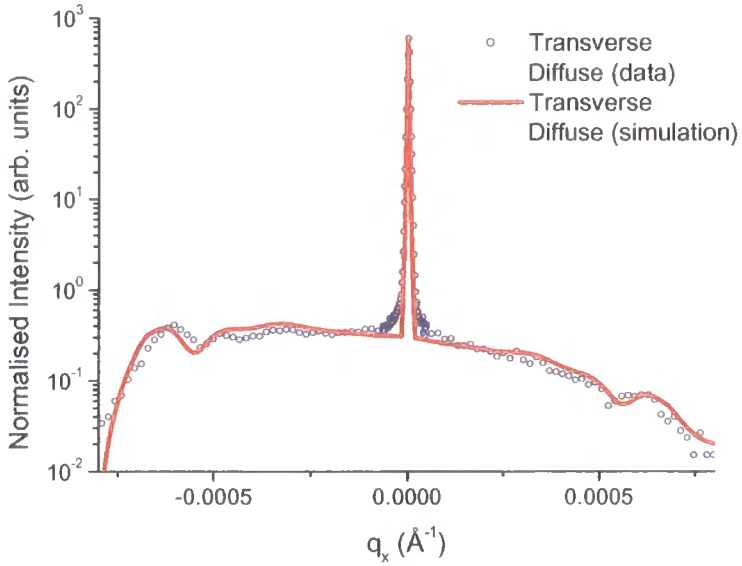

Figure 5.3: *Transverse diffuse scan and simulated fit at fixed q_z across the peak of a Kiessig fringe for SiO_2/Pt(50 Å)/Al(50 Å).*

In this case the diffuse scatter has been modelled using *Bede* REFS with the layer thicknesses and interface widths obtained from the true specular fit. This model is then expanded to allow the interface width to be resolved into the topological roughness and thus (with *Equation 5.1*) intermixing length, see *Table 5.1:*

Layer	Thickness (Å)	Interface Width σ_T (Å)	Topological Roughness σ (Å)	Intermixing Σ (Å)
AlO_2	17	7	7	-
Al	39	5	1.4	4.8
$Al_{50}Pt_{50}$	11	4	1.1	3.8
Pt	54	12	3.4	11.5
SiO_2	-	4	1.1	3.4

Table 5.1: *Modelling parameters used for the fit shown in Figure 5.2, with the calculated intermixing length for the bilayer with a nominal structure SiO_2/Pt(50 Å)/Al(50 Å).*

It is now possible to calculate the total intermixing length at the interface, which is defined as the thickness of any additional compound layer, plus, half the total intermixing at the interfaces above and below the compound layer (only half the interface intermixing length is taken since the other half is part of the compound layer). The total intermixing is therefore calculated as:

$$\frac{1}{2}(11.5\ \text{Å}) + \frac{1}{2}(3.8\ \text{Å}) + 11\ \text{Å} = 18.65\ \text{Å} \approx 19\ \text{Å}$$

In all cases the total intermixing length has been rounded to the nearest Ångstrom.

Through examining the structural model obtained, and shown in *Table 5.1*, it should be noted that the interface roughness in all cases is much smaller than the intermixing i.e. $\sigma << \Sigma$. A relatively low value for the roughness indicates good control throughout the growth process and it is the intermixing which is primarily responsible for the unusually large interface width and the breakdown in well defined interface structure. Indeed, when the intermixing Σ exceeds the topological roughness σ by greater than a factor of about 3, the contribution of the roughness to the total interface width σ_T is negligible (less than 5.5 %).

Grazing incidence X-ray reflectivity is a technique very well suited to this kind of study in that it fundamentally measures, with great sensitivity, the electron density as a function of depth. This has been illustrated below in *Figure 5.4a)* for the Al on Pt bilayer using the model structure obtained in *Table 5.1*. A derived pictorial representation has also been shown in *Figure 5.4b)*.

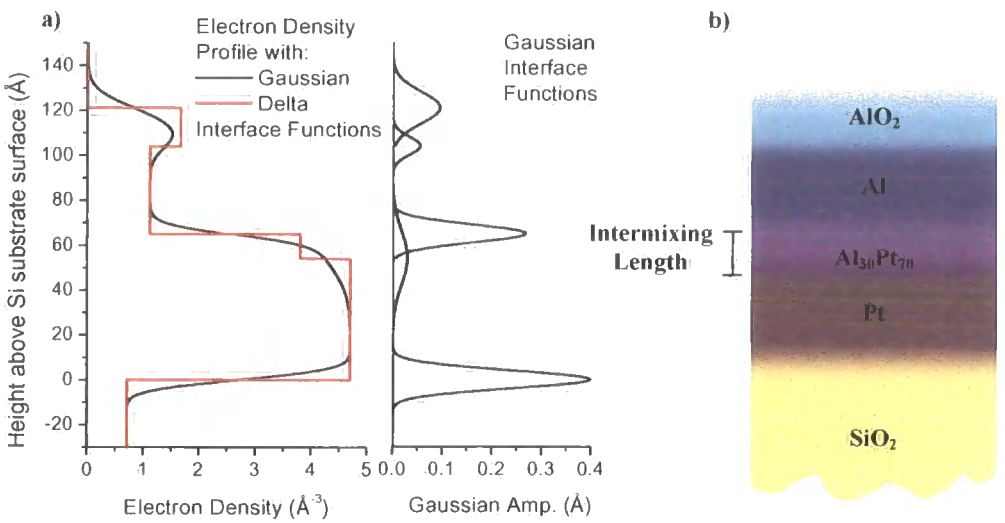

Figure 5.4: ***a)*** *Electron density profile as a function of depth through an Al on Pt bilayer, with a corresponding pictorial representation in* ***b)***.

The interface widths follow a Gaussian error function to model the transition in electron density from one layer to the next. As previously mentioned, this is often an insufficient descriptive for the interface and so compound layers (such as the one shown in the system above) are introduced. The diagram shown in *Figure 5.4b)* graphically represents (with colour) the sample with layer thicknesses and interface widths

corresponding to the depth electron density profile shown in *a)*. The intermixing length has also been shown.

The next sample is nominally identical to the sample presented above, however here the layers are grown in reverse order with 50 Å of Pt deposited on 50 Å of Al. The specular profile is shown below in *Figure 5.5*:

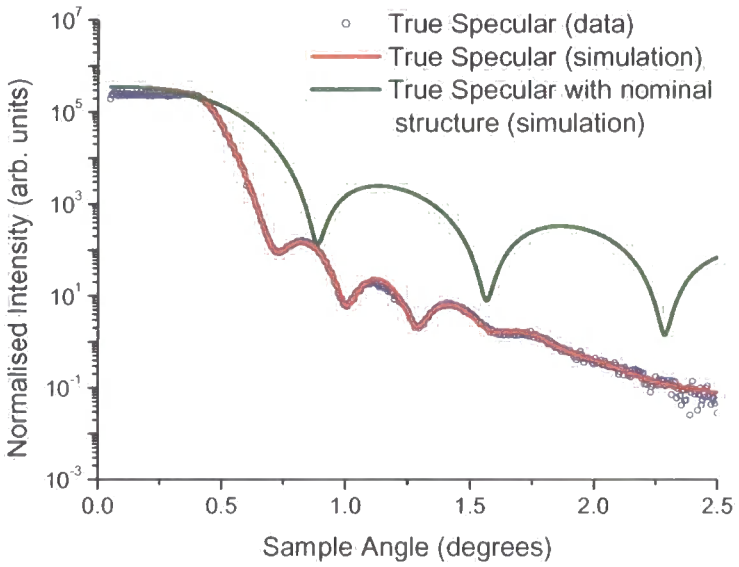

Figure 5.5: *Specular profile for the bilayer with a nominal structure SiO_2/Al(50 Å)/Pt(50 Å). Simulated fit to the data (red) and for comparison an additional simulation modelled using the nominal structure with zero interface width (green).*

If the specular profile shown here is compared with that presented in *Figure 5.2*, it is already clear without any fitting that the diminished clarity of interference features, coupled with the greater fall off in intensity with increasing angle, indicate lower structural definition with a higher interface width and intermixing length. For comparison, the specular reflectivity from a bilayer of nominal structure has been simulated and shown in green on *Figure 5.5*. The deviation from nominal structure due to intermixing is apparent from the substantial differences between the specular profiles. The structural model (layer thickness and interface width) obtained from the fit is shown in *Table 5.2*.

To resolve the interface roughness into topological roughness and intermixing, the Born approximation as been used as discussed in *Section 5.3.1*, to find the average

roughness. This is done by first integrating the components of specular and diffuse scatter as shown in the transverse diffuse scan below:

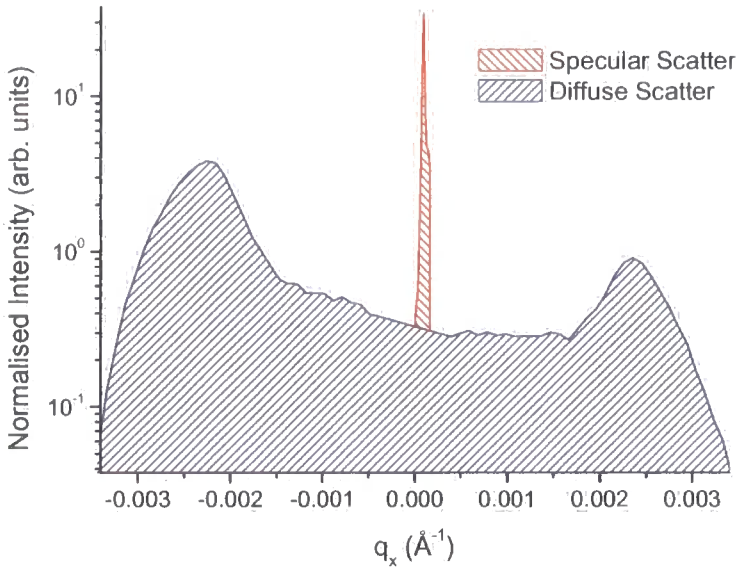

Figure 5.6: *Transverse diffuse scan across the peak of a Kiessig fringe at q_z = 0.187 Å^{-1}, integrated to find the ratio in specular to diffuse scatter.*

This transverse diffuse scan taken at q_z=0.187 Å^{-1} has an integrated intensity (normalised) of 9.1×10^{-4} for the specular and 1.37×10^{-3} for the diffuse scatter, and so using *Equation 5.4* we obtain an interface roughness of σ=3.4 Å. This was then averaged with the roughness (2.6 Å) obtained from the transverse diffuse data, taken across the minimum of a Kiessig fringe at q_z = 0.169 Å, to give an average interface topological roughness of 3.0(±0.5) Å. From *Equation 5.1* the intermixing can now be calculated and added to *Table 5.2*:

Layer	Thickness (Å)	Interface Width σ_T (Å)	Intermixing Σ (Å)
Pt Oxide	22	11	-
Pt	61	11	10.5
$Al_{20}Pt_{80}$	33	16	15.5
Al	24	9	8.4
SiO_2	-	3	0

Table 5.2: *Modelling parameters used to fit profiles shown in Figure 5.5 and the intermixing length calculated from a roughness of 3 Å for the film with nominal structure SiO_2/Al(50 Å)/Pt(50 Å).*

As before, the total intermixing is calculated from the thickness of the AlPt compound layer in addition to half the intermixing length at each interface above and below the compound layer:

$$\tfrac{1}{2}(15.5\ \text{Å}) + \tfrac{1}{2}(8.4\ \text{Å}) + 33\ \text{Å} = 44.95\ \text{Å} \approx 45\ \text{Å}$$

The interface intermixing length for Pt grown on Al is 45 Å, over twice that measured for the Al grown on Pt interface, which was found to be 19 Å. The asymmetry will be discussed further in *Section 5.7.2.*

5.5.2 Molybdenum (Mo) Sample Set

The second example of this study is the Mo sample set. The nominal structure for the two bilayers presented here are SiO_2/Mo(50 Å)/Al(50 Å) and SiO_2/Al(50 Å)/Mo(50 Å); their measured specular reflectivity is shown in *Figure 5.7a)* and *b)* respectively.

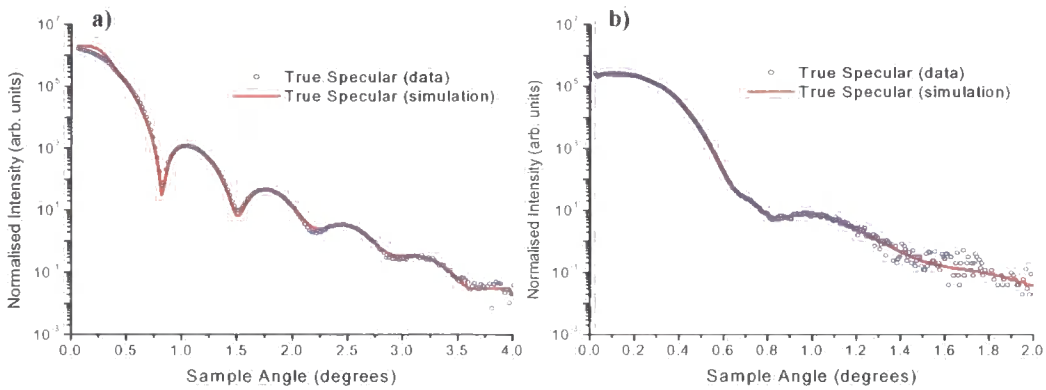

Figure 5.7: *Specular profile and simulated fit for bilayer films with nominal structures a) SiO_2/Mo(50 Å)/Al(50 Å) and b) SiO_2/Al(50 Å)/Mo(50 Å).*

Immediate inspection and comparison between the two plots suggest a variation in structural definition, with the Al grown on Mo shown in *a)* possessing a better defined interface in comparison with Mo grown on Al, see *Figure 5.7b)*. There is a similar asymmetry to that seen earlier in the Pt sample series.

The model structure used to produce the fits to the specular profiles have been displayed in *Table 5.3* along with the intermixing lengths, as calculated from the topological roughness deduced from the Born approximation. The transverse diffuse scans shown below were integrated to obtain the relative amounts of specular and diffuse scatter.

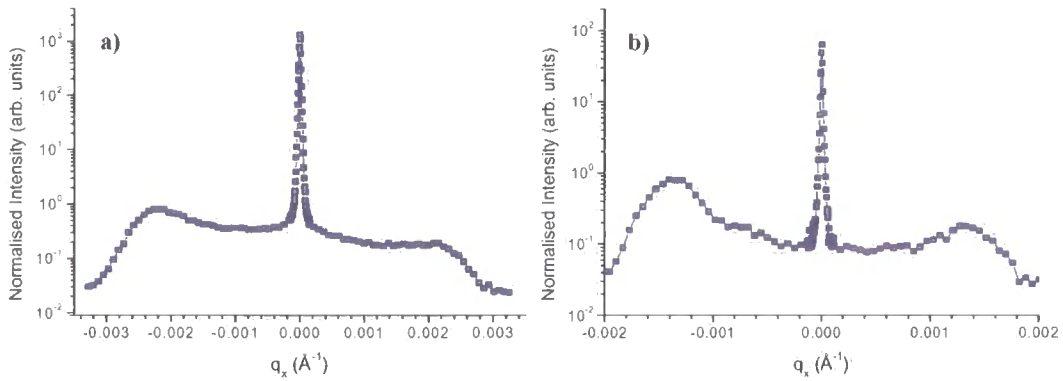

Figure 5.8: *Transverse diffuse scans to find the topological roughness for samples with nominal structure a) SiO_2/Mo(50 Å)/Al(50 Å) and b) SiO_2/Al(50 Å)/Mo(50 Å).*

Integrated intensities revealed, via *Equation 5.4*, a similar *average* roughness value of 3.2 Å and 4.1 Å for Al on Mo and Mo on Al respectively. The interface intermixing width has been extracted using *Equation 5.1*, and is presented below in *Table 5.3*:

Layer		Thickness (Å)		Interface Width σ_T (Å)		Intermixing Σ (Å)	
Al_2O_3	Mo Oxide	2	35	21	20	-	-
Al	Mo	50	33	2	26	0	25.7
-	$Al_{80}Mo_{20}$	-	22	-	16	-	15.4
Mo	Al	51	40	13	9	12.6	8
SiO_2	SiO_2	-	-	6	6	5.1	4.4

Table 5.3: *Modelling parameters used to fit the specular profiles shown in Figure 5.7 with the calculated intermixing parameter calculated from a roughness of 3.2 Å and 4.1 Å for the bilayers with nominal structures a) SiO_2/Mo(50 Å)/Al (50 Å) in black and b) SiO_2/Al(50 Å)/Mo(50 Å) in blue respectively.*

The total intermixing length for the Mo on Al interface is calculated as described above; the addition of the compound layer thickness with half the intermixing width above and below the compound layer gives a value of ½(15.4 Å) + ½(8 Å) + 22 Å = 33.7 Å ≈ 34 Å. In the case of the Al on Mo sample, no extra compound layer was necessary to model the mixing across the interface, in other words a simple error function was sufficient to describe the electron density distribution. Therefore the total intermixing length is simply described as the interface intermixing length; 12.6 Å ≈ 13 Å.

5.5.3 Magnetic Transition Metal Bilayers

The final example presents the results obtained from the magnetic transition metal bilayers: Ni, Fe and Co, the initial samples to be investigated in this study. Such samples have been included here due to their obvious technological importance.

The specular profiles for Al grown on X (where X = Ni, Fe and Co) have been shown below in *Figure 5.9*. In all cases the nominal structure is SiO_2/X(50 Å)/Al(50 Å) and so for a direct comparison between the profiles and their respective elements, they have been plotted in q_z (out-of-plane scattering vector) as apposed to the sample angle shown earlier. As well has correcting for the effect of forward diffuse scatter (as before), the normalised intensity as been multiplied by a factor of q_z^4. This accounts for the usual reduction in reflectivity, known as the Debye-Porod law (see *Section 2.6*) and allows us to visualise the further reduction as a direct consequence of interface disorder, primarily intermixing.

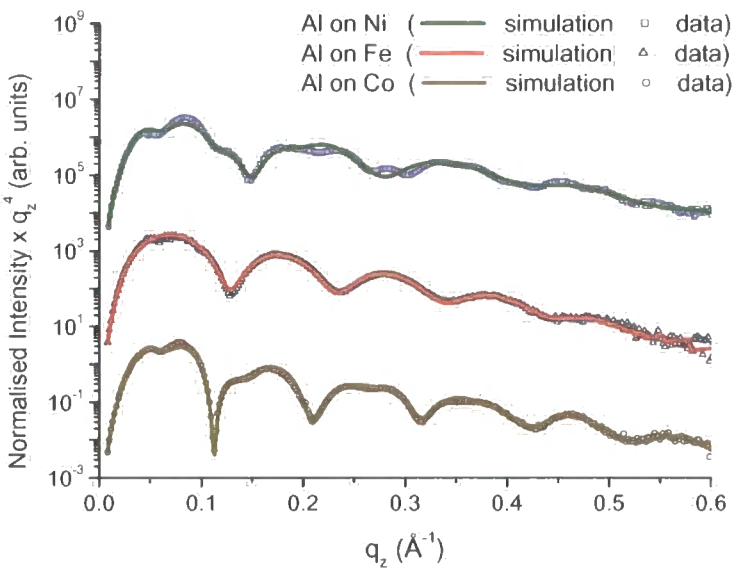

Figure 5.9: *Specular and fitted profiles from simulation for films with nominal structures: SiO_2/X(50 Å)/Al(50 Å) where X = Ni, Fe and Co.*

There is good structural definition, suggesting a low level of intermixing with Al for all these elements. Once again the specular data were fitted using the *Bede* Mercury code to obtain the layer thicknesses and interfacial widths, as seen in *Table 5.4*:

Layer	Thickness (Å)			Interface Width (Å)		
	Ni	Fe	Co	Ni	Fe	Co
Al_2O_3	31	20	21	8	6	11
Al	42	18	47	3	18	5
Al-X	12	-	2	3	-	8
X	35	38	61	3	17	4
SiO_2	-	-	-	5	3	3

Table 5.4: *Modelling parameters used for the fits in Figure 5.9 for films with nominal structure: SiO_2/Al(50 Å)/X(50 Å) where X = Ni, Fe and Co.*

The Born roughness was obtained (from the relative amounts of specular and diffuse scatter) for all three samples: 2.4 Å, 14.2 Å and 2.8 Å for Ni, Fe and Co on Al respectively. The intermixing lengths deduced where then used to calculate the complete intermixing lengths:

Fe	Co	Ni
Al on Fe	Al on Co	Al on Ni
9	**8**	**14**

Table 5.5: *The intermixing lengths (Å) for SiO_2/X/Al where X = Fe, Co and Ni.*

In a similar fashion the specular profiles for X (=Ni, Fe and Co) on Al were recorded and are displayed below in *Figure 5.10*:

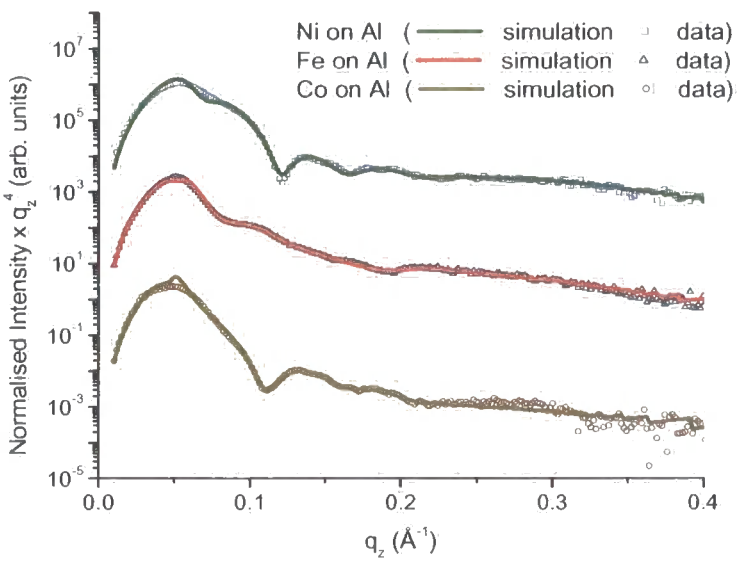

Figure 5.10: *Specular and fitted profiles from simulation for films with nominal structures: SiO_2/Al(50 Å)/X(50 Å) where X = Ni, Fe and Co.*

The magnetic transition metal bilayers show no exception to the asymmetry observed in intermixing at the interface between Al on X and X on Al. The lower degree of fringe definition and thus structural definition is apparent from a direct comparison with *Figure 5.9* and confirms the models used in obtaining fits for these profiles:

Layer	Thickness (Å)			Interface Width (Å)		
	Ni	Fe	Co	Ni	Fe	Co
X Oxide	23	18	-	22	34	-
X	48	64	21	14	10	24
Al-X	70	14	49	16	4	23
Al	19	69	41	6	12	16
SiO_2	-	-	-	2	10	4

Table 5.6:*Modelling parameters used for the fits in Figure 5.10 for films with nominal structure: SiO_2 / Al (50 Å) / X(50 Å) where X = Ni, Fe and Co.*

The Born approximation applied to the diffuse scatter provided average roughness values of 5.2 Å and 3.1 Å for the Ni, Fe on Al respectively. The Co on Al interface has a greater interface width and so in this case the transverse diffuse scatter has been modelled using the fractal model incorporated into the *Bede* Refs code. The fit to the data has been shown below in *Figure 5.11* with the modelled topological roughness and deduced intermixing lengths given in *Table 5.7*.

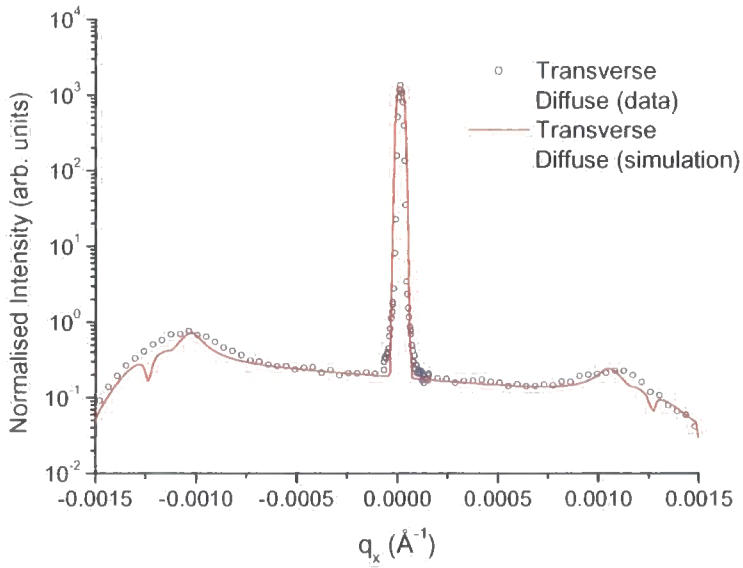

Figure 5.11: *Transverse diffuse scan and fit from simulation at fixed q_z = 0.127 $Å^{-1}$ across the peak of a Kiessig fringe for SiO_2 / Al (50 Å) / Co (50 Å).*

Layer	Topological Roughness σ (Å)	Intermixing Σ (Å)
Co	8	23
$Al_{50}Co_{50}$	8	21
Al	5	15
SiO_2	1	4

Table 5.7: *Resolved components of topological roughness σ and intermixing Σ, used to model the transverse diffuse fit in Figure 5.11 for SiO_2/Al(50 Å)/Co(50 Å).*

The total intermixing lengths for the magnetic transition metals (Ni, Fe and Co) grown on Al are:

Fe	Co	Ni
Fe on Al	Co on Al	Ni on Al
21	68	79

Table 5.8: *The intermixing lengths in Å for SiO_2 / X / Al where X = Fe, Co and Ni.*

5.5.4 The Intermixing Table

Finally the table below presents the intermixing lengths for all 46 interfaces: Al on X and X on Al where X covers the transition metals from groups 3,4 and 5 of the periodic table, with the exception of Tc.

Ti		V		Cr		Mn		Fe		Co		Ni		Cu	
Al on Ti	Ti on Al	Al on V	V on Al	Al on Cr	Cr on Al	Al on Mn	Mn on Al	Al on Fe	Fe on Al	Al on Co	Co on Al	Al on Ni	Ni on Al	Al on Cu	Cu on Al
17	50	26	94	5	33	104	151	9	21	8	68	14	79	28	168
Zr		**Nb**		**Mo**		**Tc**		**Ru**		**Rh**		**Pd**		**Ag**	
Al on Zr	Zr on Al	Al on Nb	Nb on Al	Al on Mo	Mo on Al	NOT FEASIBLE		Al on Ru	Ru on Al	Al on Rh	Rh on Al	Al on Pd	Pd on Al	Al on Ag	Ag on Al
10	51	8	36	13	34			8	52	4	47	48	56	25	45
Hf		**Ta**		**W**		**Re**		**Os**		**Ir**		**Pt**		**Au**	
Al on Hf	Hf on Al	Al on Ta	Ta on Al	Al on W	W on Al	Al on Re	Re on Al	Al on Os	Os on Al	Al on Ir	Ir on Al	Al on Pt	Pt on Al	Al on Au	Au on Al
20	44	1	9	1	35	21	86	1	71	2	54	19	45	52	63

Table 5.9: *The intermixing lengths, in Å, for transition metals (from group 3,4 and 5) grown on Al and Al grown on transition metals.*

The accuracy of the values listed in *Table 5.1* varies greatly and depends on the extent of the intermixing. The most likely cause of error comes from fitting the specular data and the accuracy of that model fit. Samples with a relatively small amount of intermixing have a well-defined layered structure, which is noted through strong interference features in the specular profile; see for example *Figure 5.2*, *Figure 5.7a)* and *Figure 5.9*. The fitting software provides models with a high degree of accuracy on such profiles, with precise values for the interface width to within ±0.5 Å, for example, the Al on Pt specular profile shown in *Figure 5.2* includes an additional 5 Å in intermixing length to demonstrate the sensitivity. Consistency is also noted with the Al on Co bilayer, shown in *Figure 5.9*, the intermixing length has been found to be 8 ± 1 Å with five independent samples grown in more than one laboratory. This demonstrates the consistency of the sputtering growth process and X-ray characterisation.

Samples with a relatively large amount of intermixing provide values with a greater degree of uncertainty. This is primarily due to the electron density model breaking down; the Gaussian function distribution inaccurately describes the interface and so there is a subsequent inability to fit the specular profile with precision, thus reducing our confidence in the model structure. A study of several Ru on Al samples gave an intermixing length of 52 ± 10 Å. The highly reactive Ag on Al system gave values of 45 and 64 Å for what are nominally identical samples.

The intermixing lengths for these sputtered polycrystalline Al bilayers, shown in *Table 5.9*, are considerably larger than expected. This study has also shown a large variation between the systems, in addition to a striking difference in mixing length between samples of Al on X, and X on Al. In all cases, the intermixing lengths for Al on X are much smaller than those measured for X on Al. In an attempt to understand these results, it is important to examine some of the possible mechanisms responsible for this mixing or diffusion.

5.6 Basic Diffusion Mechanisms

The process of diffusion plays a crucial role in many areas of material science, for example, during heat treatment the redistribution of solutes within material can produce specific microstructures. It is important to understand how this redistribution occurs and on what time scale.

In many systems, diffusion often appears to be well-ordered, with the solute atoms moving from regions of high concentration to those solute depleted, thus reducing disorder and inhomogeneity within the system. However, diffusion in a crystalline solid is more complicated with an apparent random movement of atoms within the lattice affected by compositional or binding energy differences.

The free energy changes across the system provide the driving force for the diffusion process, with the actual path of the diffusion being determined by local variations. The movement of the atoms i.e. the **kinetics** of the reaction will determine how quickly the material will reach equilibrium. The equilibrium "steady-state" condition is determined by the **thermodynamics** of the system.

The migration of atoms within a perfect crystalline structure occurs primarily via one of two mechanisms, both of which will be discussed here.

5.6.1 Interstitial Diffusion

In the first case the solute atom is small in comparison to the host atom and so can fit into the 'gaps' or interstices within the lattice. Assuming relatively low solute concentrations there are always vacant sites to move into, as illustrated below in *Figure 5.12:*

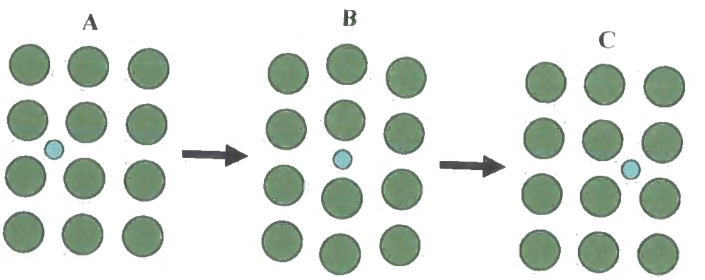

Figure 5.12: *The motion of a comparatively small solute atom migrating via interstices in the matrix lattice.*

This is certainly a conceivable case when we consider the diffusion of aluminium in any of our transition metals. Taking this simplistic view we note the aluminium atom is much smaller (1.18 Å) than even copper, the smallest transition metal, which has an atomic diameter of 1.45 Å.

In any diffusion mechanism, the atom in motion must pass through a state of high energy, an effective energy barrier for atomic motion. This has been illustrated in the figure on the right, diffusion will only occur with sufficient thermal energy to overcome the 'jump' energy. The probability of it overcoming this barrier is simply given by the Boltzmann distribution:

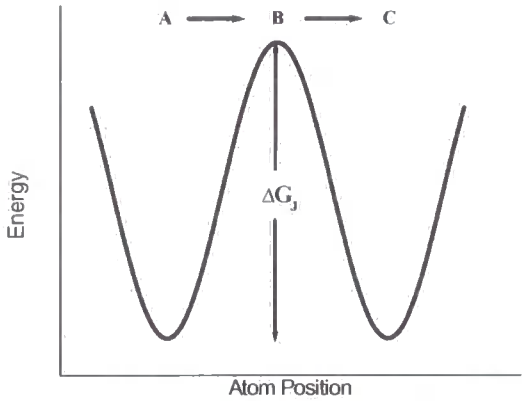

Figure 5.13: *Diagram to represent the energy considerations associated with diffusion.*

$$\exp\left(\frac{-\Delta \mathbf{G}_J}{k_B T}\right)$$

Equation 5.5

where $\Delta \mathbf{G}_J$ is the free jump energy, T is the temperature and k_B is Boltzmann's constant. If the interstitial atom has a vibration frequency υ (assuming simple harmonic motion) and z nearest neighbour sites, the jump frequency is given by:

$$\Gamma = z\upsilon \exp\left(\frac{-\Delta \mathbf{G}_J}{k_B T}\right)$$

Equation 5.6

If the free energy difference is due to a binding energy difference and entropy change then $\Delta \mathbf{G}_J = \Delta \mathbf{H}_J - T\Delta \mathbf{S}_J$. Therefore assuming diffusion rates are proportional to jump probabilities it is possible to calculate the diffusion with Arrhenius type dependence in terms of an enthalpy energy barrier:

$$D = D_O \exp\left(\frac{-\Delta \mathbf{H}_J}{k_B T}\right)$$

Equation 5.7

In this case the activation energy is equal to the enthalpy barrier for atomic migration.

5.6.2 Substitutional Diffusion

The second migration mechanism considers the situation where the solute atom is relatively large compared with the host. In this case, for motion to occur, the atom must

occupy sites on the lattice which are normally occupied by the host matrix atom which can only move if there is a vacant lattice site nearby. This situation has been illustrated below in *Figure 5.14*:

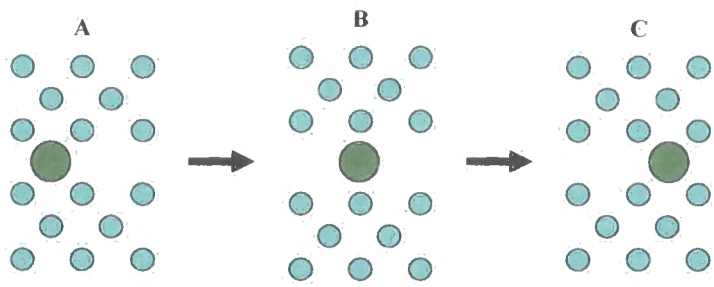

***Figure 5.14**: The motion of a comparatively large solute atom migrating via vacancies in the matrix lattice.*

In the interstitial case, atoms will always have available vacant sites and so the rate of atomic jumps across the barrier (i.e. diffusion) will depend solely on the thermal energy available. However the diffusion for substitutional atoms depends on the availability of a vacant site, as well as the probability of atomic energy jump. Let us define the fraction of sites which are occupied with a vacancy as X_V, therefore the jump frequency will be given by:

$$\Gamma = z\upsilon X_V \exp\left(\frac{-\mathbf{G}_J}{k_B T}\right)$$

Equation 5.8

The number of vacancies available is temperature dependent and is given by:

$$X_V = \exp\left(\frac{-\mathbf{G}_V}{k_B T}\right)$$

Equation 5.9

where $\mathbf{G}_V$ is the free binding energy. Through substituting *Equation 5.9* into *Equation 5.8*, and expressing it in terms of enthalpy changes:

$$D = D_0 \exp\left(\frac{-(\Delta\mathbf{H}_J + \Delta\mathbf{H}_V)}{k_B T}\right)$$

Equation 5.10

The activation energy is now therefore a sum of the enthalpy changes for atom migration and vacancy generation. This greatly reduces the rate of diffusion for substitutional atoms, compounded by the fact that the high energy barrier is

considerably greater in comparison to the interstitial diffusion, since any movement from the lattice sites is associated with high energy.

5.6.3 Grain Boundaries (A Fast Diffusion Path)

In the discussion above we have only considered a perfect crystal with a well defined lattice structure. However, the diffusion behaviour can be modified significantly by defects in the lattice, such as grain boundaries and dislocations. In these defects the atomic structure is more open with a much higher vacancy concentration, thus making it much easier for atomic migration to occur. Diffusion along a grain boundary is often called a 'fast' or 'short-circuit' diffusion path and although it can still be described by the Arrhenius equation, the activation energies are far lower compared with bulk activation energies. Therefore the diffusion coefficient for grain boundary diffusion is always higher than diffusion in the bulk and could go some way to explaining the extensive intermixing observed in many of these samples.

Harrison [5] analysed the kinetics and divided the diffusion into three cases: type-A where there is extensive lattice diffusion over a highly ordered crystal lattice structure resulting in uniformly layered growth, type-C in which lattice diffusion is negligible and diffusion is dominated by grain boundary diffusion and finally type-B which is simply a intermediate state including both forms of diffusion. Al is usually polycrystalline, with varying grain sizes, suggesting perhaps in this case type-C is a more prevalent mechanism. Of course this will depend on the cross-sectional area of the boundaries as a fraction of the total bulk area.

$$D = \frac{D_G d + D_B \delta}{d + \delta}$$

Equation 5.11

Equation 5.11 shows the total diffusion D made up from grain diffusion D_G, and fast boundary diffusion D_B, where d is the grain size and δ is the effective grain boundary thickness.

To determine whether grain boundaries are principally responsible for diffusion in our samples, we have attempted to measure the grain sizes from a number of samples using in-plane diffraction. Since we are interested in diffusion between the layers we need to determine the in-plane grain sizes, this is done using Grazing Incidence In-plane X-ray Diffraction (GIIXD).

5.6.3.1 Determining In-Plane Grain Sizes

This section presents the results from a series of GIIXD scans to obtain in-plane diffraction patterns and determine in-plane grain sizes. These experiments were performed on four sample series; Ta, W, Ir and Os at BM28 (XMaS) at the ESRF, see *Section 2.9.2.2*. Williamson-Hall plots were used to resolve the broadening of the diffraction peak into the effects of strain and grain size, although in some cases due to insufficient peaks it was necessary to perform a direct analysis using the Scherrer equation and assume a negligible amount of strain. The grain sizes obtained are fully summarised in *Table 5.10* at the end of this section.

The W series were examined first with the in-plane diffraction for the Al on W bilayer shown below in *Figure 5.15*:

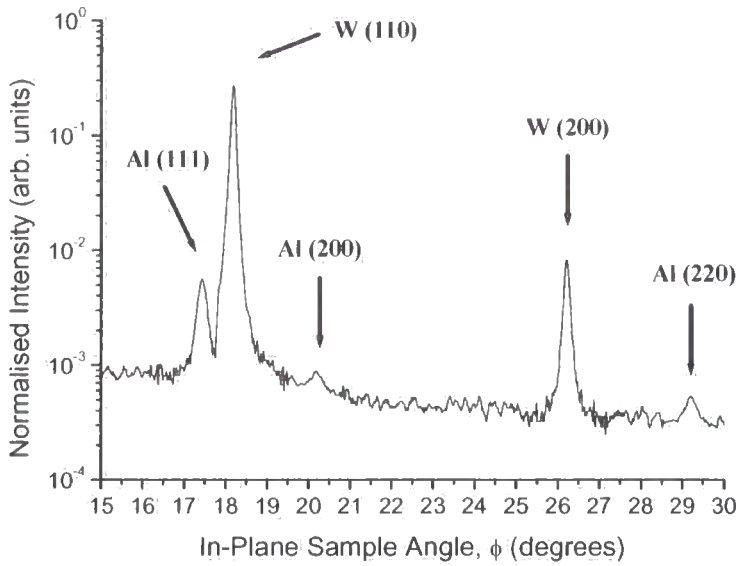

***Figure 5.15**: In-plane diffraction pattern (with peaks identified) for the Al on W bilayer.*

The diffraction pattern shows a number of peaks which arise as a result of constructive Bragg interference. The multiple peaks, each easily identifiable, confirm polycrystalline growth in both the Al and W layer.

This diffraction pattern was made with the sample set vertically at grazing incidence angle $\alpha = 0.6$ °. This angle is well above the critical angle and ensures that the X-rays are penetrating the entire sample. However, it is sometimes useful to employ the angular

dependence of the X-ray penetration depth to study parameters as a function of depth. For example, the integrated peak intensities will be proportional to the number of scattering planes. *Figure 5.16a)* and *b)* display such plots for the Al (111) and W (110) peak respectively, including the calculated (using the *Bede* REFS software) penetration depth as a function of incident angle. Through comparing *a)* and *b)* it is clear that at low angles (e.g α=0.2 °, below the critical angle) the diffraction is surface sensitive, with a peak in diffraction intensity coming from the Al surface layer. The W peak intensity only increases substantially as the grazing incidence angle α approaches the critical angle, which for this sample was noted at ~0.45 °, from the specular $\theta/2\theta$ profile (see *Appendix E*).

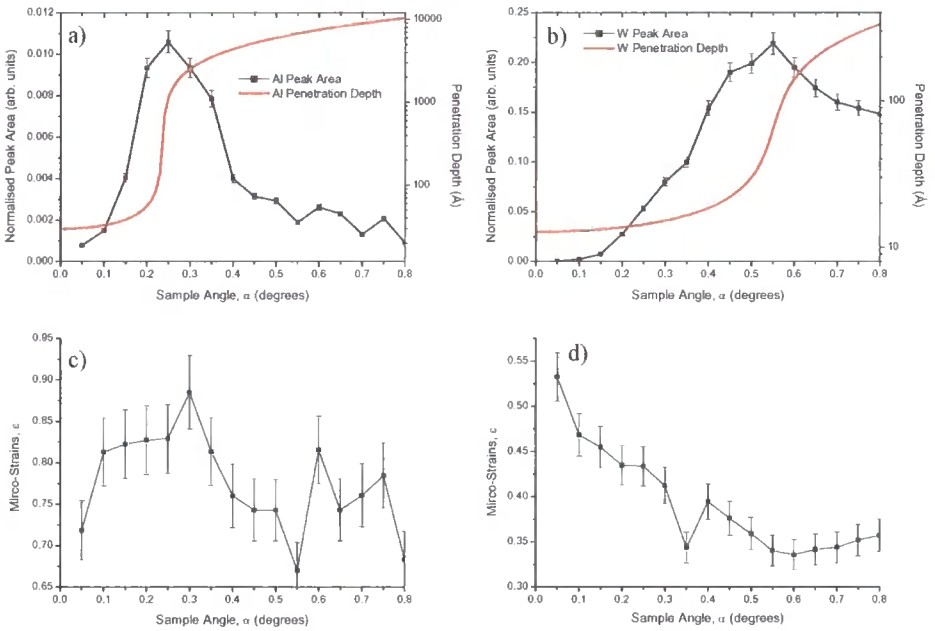

Figure 5.16: *Grazing incident diffraction for the Al on W bilayer showing the* ***a)*** *Al and* ***b)*** *W integrated peak intensities (with simulated penetration depth) and* ***c)*** *Al and* ***d)*** *W lattice strain as a function of vertical sample angle, α.*

Figure 5.16c) and *d)* show the calculated lattice strain as a function of the grazing incidence angle α. Strain will cause a variation in the *d*-spacing and consequently cause a broadening in the diffraction peak. The strain equation is presented in *Section 2.8.3* and *Equation 2.60*:

$$\Delta_{STRAIN}(2\theta) = 2\varepsilon \tan(\theta_B)$$

Equation 5.12

Where $\Delta(2\theta)$ is the FWHM of the diffraction peak (in radians), θ_B is the peak position and ε is the micro-strain. There appears to be no significant variation in lattice strain in the Al layer with depth, see *Figure 5.16c)*. On the other hand we see in *d)* for W reduced strain, or relaxation with increasing layer depth.

However, so far we have neglected any size effects from the grains; limited grain size also broadens the diffraction peak. Assuming this time a negligible amount of strain, it is possible to calculate the grain size directly from the Scherrer equation (*Equation 2.59*):

$$\Delta_{SIZE}(2\theta) = \frac{\kappa\lambda}{D\cos(\theta_B)}$$

Equation 5.13

where $\Delta(2\theta)$ is the FWHM of the diffraction peak (in radians), θ_B is the peak position, λ is the wavelength and D is the grain size. κ is a constant that depends on the peak shape profile, during the course of this study the diffraction peaks were fitted using Lorentzians with $\kappa = 1$.

For the Al on W bilayer the reduced peak width indicates increasing grain size with depth, this seems unlikely and supports the original interpretation of increased strain at the interface.

This form of analysis clearly only requires a single peak, however when multiple peaks are available, it is possible to use a Williamson-Hall plot to resolve the strain and size effects. This is possible due to the difference in angular dependence for size (*Equation 5.13*) and strain (*Equation 5.12*) on peak width. By summing these equations to provide the total peak width Δ_{TOTAL}, and then rearranging we get:

$$\Delta_{TOTAL}(2\theta)\cos(\theta_B) = 2\varepsilon \sin(\theta_B) + \frac{\lambda}{D}$$

Equation 5.14

From this equation it is clear the relationship between the width multiplied by the cosine of the Bragg angle, against the sine of the Bragg angle, should be linear. The linear relationship is represented as a line of best-fit on a Williamson-Hall plot with the

gradient being proportional to the strain and the intercept on the y-axis being inversely proportional to the grain size.

In the W series the grain size varied considerably between the two samples, with the grain size for the Al on W (for both Al and W) being much larger in comparison to the grain sizes obtained from the W on Al bilayer. Williamson-Hall plot analysis for the Al on W bilayer revealed a grain size of 537±94 Å and 776±115 Å (for the Al and W respectively), in comparison to 122±7 Å (Al) and 157±43 Å (W) for the W on Al sample. The significance of this shall be discussed further in *Section 5.7.2*. It should be noted that the grain size of 122±7 Å given for the Al, in the W on Al system, was calculated (due to there being only a single peak) using the Scherrer equation shown in *Equation 5.13*, and so represents a lower limit for the grain size. All other grain sizes were calculated using the Williamson-Hall plot, an example of which shall be given in the following Al on Os example.

Figure 5.17 presents the diffraction patterns for the Al grown on Os bilayer. Due to some of the crystallographic planes having similar *d*-spacings, it was necessary to take advantage of the surface sensitivity of GIIXD to isolate diffraction from the surface Al layer. The critical angle as noted from the specular profile was located at $\alpha_c \sim 0.52$ °.

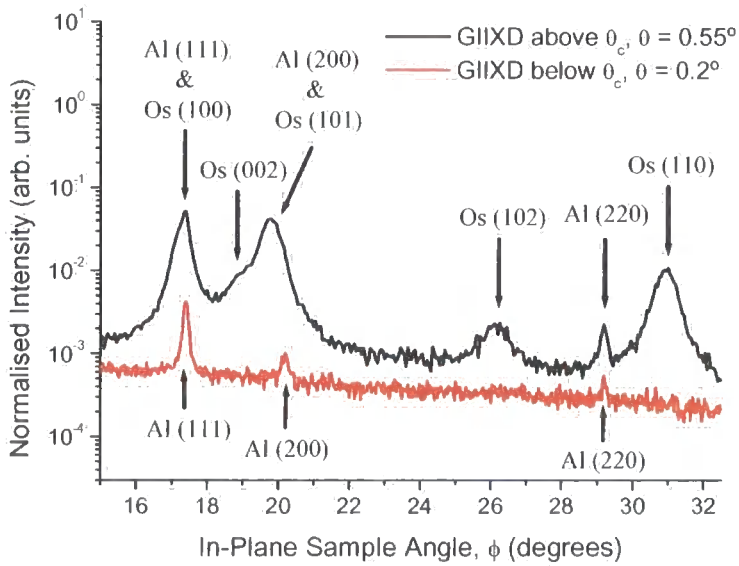

Figure 5.17: *Grazing In-plane diffraction for Al on Os, both above (black) and below (red) the critical angle.*

Williamson-Hall plots are shown below in *Figure 5.18a)* and *b)* for the Al and Os layer respectively. The Al points come from the (111), (200) and (220) reflections and the Os points originate from the (002), (102) and (110) reflections.

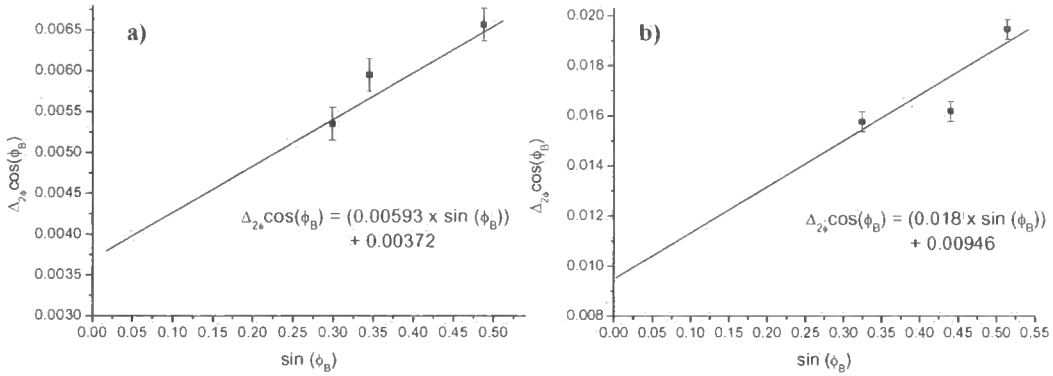

Figure 5.18: *Williamson-Hall plots to determine grain sizes in the* ***a)*** *Al and* ***b)*** *Os layers.*

The equations from the lines of best-fit have been included on the graphs, with the intercept equal to λ/D. The two plots above have provided, for the Al on Os bilayer, in-plane grain sizes of 377±48 Å and 147±53 Å for Al and Os respectively.

GIIXD measurements on the Os on Al bilayer revealed an Os grain size of 91±12 Å. However there were no detectable Al peaks with which to examine the Al grain size. The absence of Al peaks is common to the Os, Ir and Ta systems and even the single Al(111) peak identified in the W on Al diffraction pattern was extremely weak. This is not a result of absorption, since the absorption constant indicates a penetration depth of ~240 Å at this incident angle and energy. It can only be attributed to the Al being in a nano-crystalline or amorphous state. If this is the case there will be a large number of boundaries and dislocation throughout the Al layer which could account for the large and consistent asymmetry observed between bilayers grown with Al before and after the metallic layer X.

Both Ir bilayers were studied in exactly the same fashion with the Williamson-Hall plot analysis giving an Al grain size of 536±91 Å and Ir grain size of 200±54 Å for the Al grown on Ir system. Once again it was impossible to measure any Al peaks in the Ir on Al bilayer. A value of 208±65 Å was determined for the Ir grain size.

The Al on Ta system was a little more difficult to record due to the similarity in *d*-spacing between the Al(111) and the Ta(110). The in-plane diffraction pattern for this sample (measured at an incident angle of α=0.5 °) can be seen below in *Figure 5.19*:

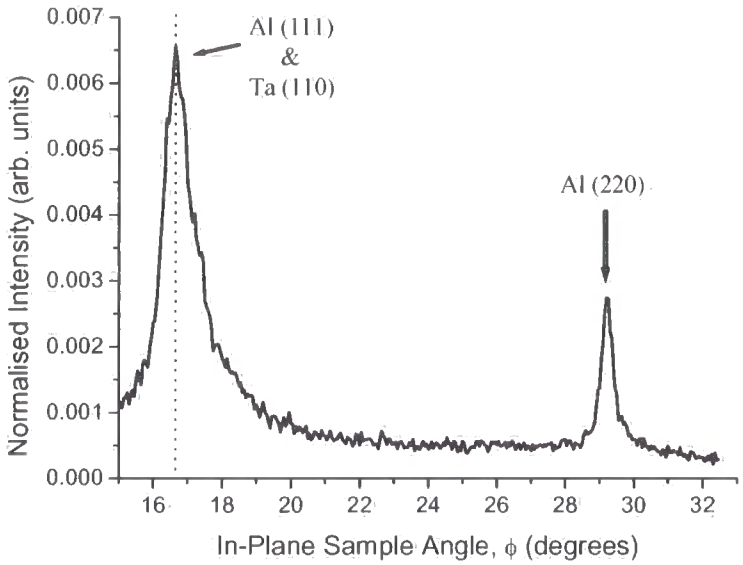

***Figure 5.19**: In-plane diffraction pattern for Al on Ta showing strain dispersion.*

The peak at a lower angle is composed of the Al(111) and Ta(110) reflections which from published *d*-spacing tables result (at this energy) in reflections at 17.3705 ° and 17.398 ° respectively. Due to this similarity in *d*-spacing there appears to be lattice matching between the layer structures which is also indicated with the asymmetric diffraction peak as a result of strain dispersion. The Al is strained to lattice match the Ta (with a slightly lower *d*-spacing) and then relaxes towards the top of the sample back to its original *d*-spacing. The lattice matching will in general form much sharper interfaces and could go some way to explaining the reason for Ta having, on average, the lowest amount of intermixing (1 Å for Al grown on Ta and 9 Å for Ta grown on Al). Using the Scherrer analysis, the width of the Al(220) peak indicated a grain size greater than 167±6 Å.

The Ta on Al system did not show the same form of strain, confirming it is indeed the Al which is strained to Ta. The in-plane diffraction pattern for this system is presented, with the corresponding Williamson-Hall plot for Ta, below in *Figure 5.20*:

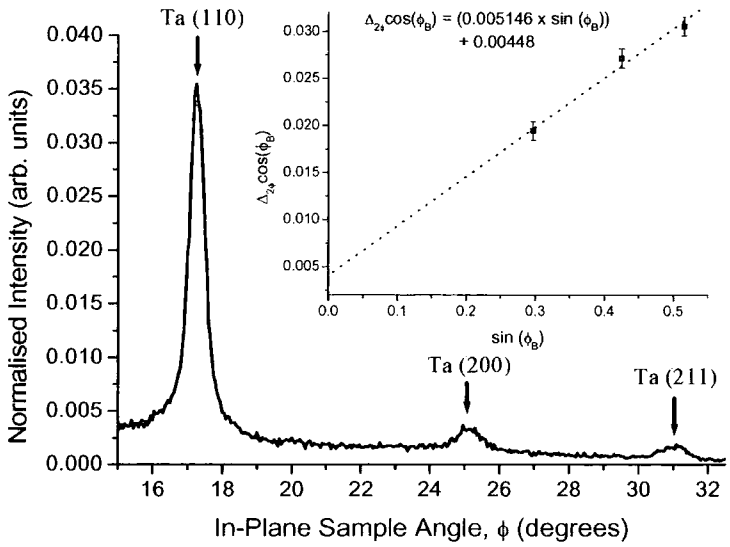

Figure 5.20: *In-plane diffraction pattern and Williamson-Hall plot (insert) used to determine the in-plane grain size of Ta in the Ta on Al bilayer.*

The grain size obtained for the Ta layer was 349±130 Å.

Table 5.10 summarises the grain sizes obtain for these four systems using in-plane diffraction and compares them with the intermixing lengths found earlier.

Al on X			X on Al		
System / Intermixing (Å)		**Grain Size (Å)**	System / Intermixing (Å)		**Grain Size (Å)**
Al on Ta	1	**>167 (±6)** ?	**Ta on Al**	9	**349 (±130)** ?
Al on W	1	**537 (±94)** **776 (±115)**	**W on Al**	35	**157 (±43)** **>122 (±7)**
Al on Ir	2	**536 (±91)** **200 (±54)**	**Ir on Al**	54	**208 (±65)** ?
Al on Os	1	**377 (±48)** **147 (±53)**	**Os on Al**	71	**91 (±12)** ?

Table 5.10: *In-plane grazing sizes as determined from GIIXD.*

There are a number of interesting and perhaps significant observations to be made from this table. The first is to note a general trend of larger grain sizes for the systems with Al grown on X, with perhaps the exception of the Ta system, however interpretation is difficult here due to broadening by strain and near lattice matching. For the X on Al systems it was difficult to observe any Al peaks indicating an amorphous or, a more probably, nano-crystalline Al structure. If this is the case there would be a large number of dislocations and boundaries in the Al structure promoting fast diffusion and the subsequent growth of layer X with smaller grain sizes. If we assume the 122 Å Al grain size measured for the W on Al system is accurate and representative for all samples with Al grown first, this would still induce smaller grain sizes for X grown on top and a higher degree of intermixing between the layers.

It is also interesting to observe the differences in the X grain size for the X grown on Al configuration and compare those to the observed intermixing lengths. A comparison between Ta on Al and Os on Al indicate the smaller the grain size the greater the degree of intermixing. The W and Ir samples agree within error, and both are intermediate to the more extreme cases of intermixing length and grain size observed in the Ta and Os samples. Such a trend supports the hypothesis discussed in *Section 5.6.3*.

5.7 Discussion

If either of the two simple diffusion models; interstitial or substitutional (as described in *Sections 5.6.1* and *5.6.2* respectively) are primarily responsible for the extent of the intermixing then the diffusion of Al into X would be governed by interstitial diffusion and X into Al by substitutional diffusion. It is feasible the diffusion observed would entail some sort of combination of these two effects, although it would be difficult to explain the asymmetric intermixing lengths. In addition, the bulk diffusion rates of the thermalised atoms cannot account for the observed intermixing lengths. Using the activation energies published in *Smithells Metals Reference Book* [6] and via the Arrhenius equation (*Equation 5.7* and *Equation 5.10*) the diffusion rate from one atomic species to another can be calculated. The bulk diffusion parameters show no correlation with the observed intermixing length and so do not predict the rate of intermixing observed at room temperature. The samples also appear to be very stable; several samples showed no noticeably change in interface structure after a year. Further

evidence to suggest bulk diffusion rates are not responsible for the measured intermixing lengths since this kind of diffusion has a relatively long timescale.

It is important to consider the possibility of the sputtering process itself contributing directly to the intermixing, although, it is unlikely since the energetic atoms produced in the sputtering process are thermalised in the system used. The target to substrate distance is usually 4 cm, but in this case it was extended to 18 cm which is equivalent to 10 mean free paths at the sputtering gas pressure. This corresponds to approximately 100 collisions with the Ar atoms and ions, which will thermalise the great majority of sputtered atoms before they reach the substrate. There is little variation in the atomic size of the atoms; the largest atomic diameter is 2.08 Å for Hf and the smallest is 1.45 Å for Cu and so to a first order approximation the mean free path is independent of element. It is believed that all atoms (even those in row 6 with a greater atomic mass) will be well thermalised after 100 collisions. Indeed, it is worth noting that on average more mixing is measured in row 4 than in row 6, even though the lighter atoms will have slightly fewer collisions. This strongly suggests that high energy impact does not account for the high level of intermixing observed.

Although there is no clear correlation with the bulk diffusion, there is a very weak correlation with the cohesive energy. The cohesive energy is defined as the energy required to separate the metallic crystal into individual atoms. The plots below in *Figure 5.21* show a general decrease in intermixing length with an increase in cohesive energy for both sample types; Al on X shown in *a)* and X on Al shown in *b)*.

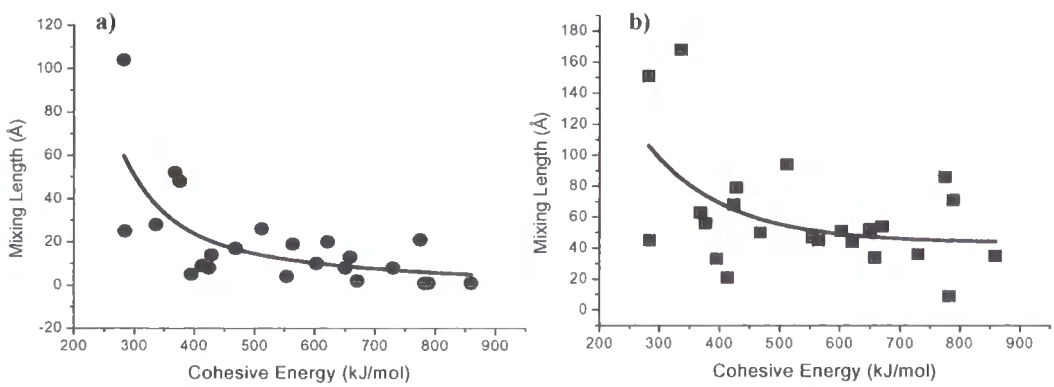

Figure 5.21: *The correlation between the intermixing length and the cohesive energy of element X in the sample set a) Al on X and b) X on Al with an exponential fit as a "guide to the eye."*

Although the activation energy is closely related to the cohesive energy, and usually of the same order, there are important distinctions to note. The activation energy is the energy required to 'put' the atom in its place, where as the cohesive energy defines the energy required to break the atom from any bond. The correlation with cohesive energy could be cited as evidence to demonstrate the independence of the sputtering kinetics from the diffusion process. It suggests the bonds or lattice structure form first during sputtering deposition and the following diffusion process is governed solely by the interstitial or substitutional atom's ability to break the cohesive bond and move through the lattice by some mechanism.

5.7.1 Alloying and Intermetallic Formation

Although each of the Al bilayer samples were grown at room temperature, the possibility of alloy formation should not be overlooked. Indeed such reactions would no doubt increase the level of intermixing with the formation of the alloy layer at the centre.

Thin film transition metal aluminides are of particular interest due to some of their important properties, such as low resistance and good adhesion to SiO_2. However, our understanding of aluminide formation is relatively poor in comparison to the silicides where a general pattern of behaviour is known. In thin film reactions it is not yet possible to predict what aluminide phase will grow initially, although it is generally believed that kinetics are responsible for the formation rather than thermodynamic driving forces [7].

The growth of aluminides in thin films can vary in uniformity, from kinetically well-defined lateral uniform growth in a layer-by-layer fashion, to irregular reactions found preferentially along grain boundaries.

Recalling the categorisation of diffusion proposed by Harrison [5] it is generally accepted that silicide formation occurs via type-A diffusion due to the fact Si is normally a single crystal structure. However, as discussed earlier, Al is usually polycrystalline promoting a more structurally irregular aluminide formation.

There is a large amount of literature which has focused on the thin film phase formation between Al and transition metals through annealing. Aspects such as initial

phase and formation temperature have been addressed. The Co/Al reaction has been thoroughly investigated with work by Howard *et al* [8] and Colgan and Mayer [9] identifying Co_2Al_9 as the initial phase with growth beginning at 50 °C. Al was identified as the most rapidly diffusing species during the initial phase formation. In a similar manner Howard *et al.* also identified, through interacting thin films of Al and Cr, Al rich $CrAl_3$ at 300 °C and 450 °C. Colgan and collaborators have also studied the interdiffusion and alloying by annealing a series of Al bilayers including, Ni/Al [10], Pt/Al [11] and Pd/Al [12]. In all cases the interdiffusion proceeded via an intermetallic formation. However the minimum reaction temperature recorded in the experiment was 300 °C for the Ni/Al bilayer, 225 °C for the Pt/Al bilayer and 250 °C for the Pd/Al bilayer. There are too many studies to describe each of them in detail and there is no single pattern to describe the initial phase formation or reaction temperature. The reaction temperature ranged from 200-250 °C for Pd_2Al_3 [12, 13] and Pt_2Al_3 [14, 15], up to 500-525 °C for WAl_{12} formation [9, 16]. It is important to note that despite the importance in considering alloy formation, all these reactions take place at an initial temperature much greater than the room temperature at which the samples were sputtered, stored and analysed. In addition, the heats of alloying taken from de Boer [17] based on the Miedema's model for 1:1 alloys show no correlation with the intermixing length.

Although alloying seems high unlikely in the series of samples studied here, it is important to understand the growth uniformity of the aluminides and relate that to the diffusion process at work. Howard *et al.* [8] observed a correlation between the melting point of compounds, growth kinetics and the subsequent interface uniformity. Low melting point compounds such as Al/Cr, Al/Ti, Al/Pt, Al/Pd and Al/Co generally had planar interfaces thus suggesting lattice diffusion. The high melting point compounds including Al/Hf, Al/Zr and Al/Ta had more irregular growth interfaces with diffusion dominant along the grain boundaries. Howard and co-workers formulated a relationship between the melting point of the compound and the growth kinetics based on lattice diffusivity decreasing with increasing compound melting point. However more recent results obtained in Al/Ta [9] and Al/Pt [11] disagree with this correlation finding the opposite growth pattern. Attempts at correlating the intermixing lengths found in this study with the compound melting point have also resulted in no clear correlation.

It would appear there is no easy rule to explain the reactions involved between Al and transition metals, perhaps due to the fact both materials tend to be polycrystalline. Colgan surmised [18] the reaction front (i.e. the interface) is usually planar although impurities and grain sizes can modify this.

5.7.2 Fast Grain Boundary Diffusion

One of the surprising results of this study has been the large extent of the intermixing observed in some of these systems. Perhaps the most likely explanation lies in the diffusion along grain boundaries, the so-called 'fast' or 'short-circuit' diffusion described in detail in *Section 5.6.3*. With this in mind a series of in-plane diffraction experiments were performed in order to determine the in-plane grain size, a parameter which should strongly determine the number of grain boundaries available and therefore the degree of interface intermixing. The results obtained have been highlighted in *Table 5.10*.

Consider the W series and the grain sizes obtained. The Al on W grain sizes for both Al and W are much larger (over 500 Å) compared with the mirror sample, W on Al, which reveals grain sizes of approximately 150 Å. This pattern is also apparent in the Os and Ir systems. It is not unusual to have a matching grain size in subsequently grown layers and it would appear that the initial deposition of Al followed by X results in much smaller grains. The Al would appear to grow in a nano-crystalline (or amorphous) state, resulting in many dislocations and boundaries, thus promoting intermixing in the subsequent growth of the metal X grown (also with small grains) on top.

With the initial deposition of X, grains grow much larger and this carries through to the surface Al layer. The larger grains result in fewer boundaries and dislocations, and therefore lower intermixing.

The difference in grain sizes certainly explains the observed asymmetry in the intermixing length between Al on X and X on Al, a phenomena which has remained consistent for each of the elements, with the X on Al bilayer always possessing a larger intermixing length at the interface in comparison to the Al on X bilayer.

This interface asymmetry was also found recently using anomalous X-ray scattering in Ni/Au multilayers by Bigault *et al.* [19] and in NiFe/Cu multilayers by Luo *et al.* [20]. However, our results disagree with the suggestion made by Bigault *et al.* who

proposed such an asymmetry in intermixing was the result of a kinetic (out-of-equilibrium) segregation driven by the growth front.

5.8 Conclusion

In this chapter we have used GIXR and GIIXD techniques to study and evaluate the intermixing across Al/X and X/Al interfaces where X represents the transition metals from row 4,5 and 6 of the periodic table (a total of 46 bilayers). The bilayers usually consist of two 50 Å layers (depending on the level of intermixing), Al and X, deposited by d.c. magnetron sputtering on to a Si substrate.

Structural interface characterisation was performed through fitting specular profiles to obtain layer thickness and interface widths. Transverse diffuse scans were used to resolve the interface width into its individual components of topological roughness and intermixing. Grazing incident X-ray techniques are very well suited to this kind of investigation in that X-rays are fundamentally effected by electron charge and so extremely sensitive to any change in electron density as a function of sample depth, making this a choice technique in any intermixing study. Fits to the specular profile were performed using the *Bede Refs Mercury* code, which employs a Gaussian error distribution to modal the interface structure. However, in some cases it was necessary to include additional compound layers.

A final table (shown on page 125, *Table 5.9*) has been constructed to present the intermixing lengths for all samples studied.

In an attempt to understand the results presented in this table, several mechanisms have been explored. Three forms of diffusion have been considered; interstitial, substitutional and fast grain boundary diffusion. To investigate the more likely case of fast diffusion along the grain boundaries, grazing incident in-plane diffraction techniques have been used to determine the in-plane grain sizes.

The measurements suggest the smaller the grain size, the greater the amount of intermixing (with perhaps the exception of the Ta system which appears to have been affected by strain due to near lattice matching, which itself may potentially be a mechanism to prevent intermixing) due to the increased frequency of dislocation and grain boundaries. The results also account for the asymmetric intermixing, with X on Al always showing a greater degree of intermixing in comparison to Al on X. The GIIXD

patterns show no (or weak) Al diffraction peaks for the X on Al bilayers. This suggests that the Al grown on silicon is either nano-crystalline (or possibly amorphous), with subsequently many dislocations and boundaries for diffusion to occur upon the deposition of X. If this is the case it supports the Harrison type-c model with diffusion being primarily a result of grain boundary diffusion with a negligible amount of lattice diffusion. Such a model explains the high level of intermixing observed.

No alternative explanation accounts fully for the extent of the intermixing and its variations with the element systems. Published activation energies for bulk diffusion, with the Arrhenius equation, permitted the determination of diffusion rates. However, calculations revealed no correlation for the observed intermixing length and so do not predict the rate of intermixing observed at room temperature.

The possibility of the sputtering process contributing directly to the intermixing was also examined. This was dismissed due to the sputtering geometry, which included a extended target to substrate distance allowing for approximately 100 collisions with the Ar atoms and ions, thus thermalising all sputtered atoms before they reach the substrate.

The independence of the sputtering process on the intermixing length was also confirmed through discovering a weak correlation with the cohesive energy. The cohesive energy defines the energy required to break the atom from its bond, suggesting a bond is initially formed on sputtering which is later broken as part of the diffusion process.

It is of course likely that no single mechanism is responsible for all the intermixing observed here in these 46 bilayers, but rather, a complex combination of mechanics which make any attempt at a global explanation exceptionally difficult. Despite this, the in-plane diffraction data does suggest grain boundary diffusion is the most prevalent force driving this intermixing. With the deviation in grain sizes observed, this mechanism not only promotes substantial intermixing but its variation as well. The results also suggest the Al grown on Si is nano-crystalline or in a amorphous state, allowing for a high level of intermixing for X on Al and thus explaining the asymmetry observed for all 26 bilayer series.

5.9 References for Chapter 5

1. E.Y. Tsymbal and D.G. Pettifor (1999) "*The influence of impurities within the barrier on tunneling magnetoresistance*" J. Appl. Phys. **85** (8) pg. 5801-5803.

2. R. Jansen and J.S. Moodera (1998) "*Influence of barrier impurities on the magnetoresistance in ferromagnetic tunnel junctions*" J. Appl. Phys. **83** pg. 6682-6684.

3. C. He Shang, J. Nowak, R. Jansen, and J.S. Moodera (1998) "*Temperature dependence of magnetoresistance and surface magnetization in ferromagnetic tunnel junctions*" Phys. Rev. B **58** pg. R2917-R2920.

4. D.E. Savage, J. Kleiner, N. Schimke, Y.H. Phang, T. Jankowski, J. Jacobs, R. Kariotis, and M.G. Legally (1991) "*Determination of roughness correlations in multilayer films for x-ray mirrors*" J. Appl. Phys. **69** (3) pg. 1411-1424.

5. L.G. Harrison (1961) "*Influence of Dislocations on Diffusion Kinetics in Solids with particular reference to the Alkali Halides*" Trans. Faraday Soc. **57** pg. 1191-1199.

6. E.A. Brandes and G.B. Brook (1992) "*Smithells Metals Reference Book*" 7th Edition, Butterworth-Heinemann.

7. R.W. Bene (1982) "*First nucleation rule for solid-state nucleation in metal-metal thin-film systems*" Appl. Phys. Lett. **41** pg. 529-531.

8. J.K. Howard, J.F. White, and P.S. Ho (1978) "*Intermetallic compounds of Al and transitions metals: Effect of electromigration in 1–2-μm-wide lines*" J. Appl. Phys. **49** (7) pg. 4083-4093.

9. E.G. Colgan and J.W. Mayer (1989) "*Thin-film reactions of Al with Co, Cr, Mo, Ta, Ti, and W*" J. Mater. Res. **4** pg. 815-820.

10. E.G. Colgan, M. Nastasi, and J.W. Mayer (1985) "*Initial phase formation and dissociation in the thin-film Ni/Al system*" J. Appl. Phys. **58** (11) pg. 4125-4129.

11. E.G. Colgan (1987) "*Phase formation and dissociation in the thin-film Pt/Al system*" J. Appl. Phys. **62** (4) pg. 1224-1231.

12. E.G. Colgan (1987) "*Phase formation and dissociation in the thin-film Pd/Al system*" J. Appl. Phys. **62** (6) pg. 2269-2274.

13. E.G. Colgan, C.-Y. Li, and J.W. Mayer (1987) "*Interfacial reaction-induced morphological instabilities in thin Al/Pt and Al/Pd films*" J. Mater. Res. **2** pg. 557-567.

14. E.G. Colgan, C.-Y. Yi, and J.W. Mayer (1987) "*Void formation in thin Al films*" Appl. Phys. Lett. **51** (6) pg. 424-426.

15. E. Ma and M.-A. Nicolet (1988) "*Pt_2Al_3 Formation on Evaporated and Large-Grained Al Substrates*" Phys. Stat. Sol. A **110** pg. 509-514.

16. G.J. van Gurp, J.L.C. Daams, A. van Oostrom, L.J.M. Augustus, and Y. Tamminga (1979) "*Aluminum-silicide reactions. I. Diffusion, compound formation, and microstructure*" J. Appl. Phys. **50** (11) pg. 6915-6922.

17. F.R. de Boer (1998) "*Cohesion in Metals*" North Holland, Amsterdam.

18. E.G. Colgan (1990) "*A review of thin-film aluminide formation*" Materials Science Reports **5** pg. 1-44.

19. T. Bigault, F. Bocquet, S. Labat, O. Thomas, and H. Renevier (2001) "*Interfacial structure in (111) Au:Ni multilayers investigated by anomalous x-ray diffraction*" Phys. Rev. B **64** pg. 125414.

20. G.M. Luo, Z.H. Mai, T.P.A. Hase, B.D. Fulthorpe, B.K. Tanner, C.H. Marrows, and B.J. Hickey (2001) "*Variable wavelength grazing incidence x-ray reflectivity measurements of structural changes on annealing Cu/NiFe multilayers*" Phys. Rev. B **64** pg. 245404.

Chapter 6

Soft X-ray Resonance Magnetic Scattering and Polarised Neutron Reflectivity from AF Coupled Magnetic Multilayers

6.1 Introduction

Determining the structural properties of any magneto-transport device, such as spin-valves, tunnel junctions or multilayers, is clearly of enormous importance to their development. Correlating the structure with growth parameters allows for advances in the fabrication techniques, and relating structure to magneto-transport properties develops a greater physical understanding of the system and highlights key characteristics required for the desired magneto-effect, such as greater magneto-resistance. Use of a wide variety of characterisation techniques, such as high-resolution transmission electron microscopy, as well as X-ray and neutron scattering, have resulted in significant progress in correlating structure with transport properties and thereby improving the efficiency of such devices.

However, most characterisation studies have concentrated purely on the chemical structure, with particular emphasis being placed on the role of the interface morphology with respect to magneto-transport. The literature is filled with studies which focus on the chemical structure; indeed this thesis has also been centred thus far on relating growth conditions and magneto-transport to chemical structure. The role of the chemical structure is important and becoming better understood, however, this is insufficient! A fuller description must include similar characterisation of the magnetic structure, a constituent relatively understudied and yet a key component in understanding factors

like spin accumulation, scattering and the magnitude of the magnetoresistance effect. Magnetic characterisation techniques must therefore be developed in order to advance a more detailed and coherent model concerning the role of magnetic structure and magnetic interface morphology within the field of thin film magnetism.

Soft X-rays are part of the electro-magnetic spectrum and are therefore sensitive to magnetic, as well as chemical, structure. For many decades the theoretical framework has been in-place to describe photon scattering from magnetic structure and although this work focused on the basic interaction, Platzman and Tzoar (1970) [1] theoretically explored the potential for fundamental investigations of magnetic materials. These ideas were later realised experimentally by de Bergevin and Brunel (1981) [2] who used X-rays to study orbital magnetic scattering in NiO crystals. Unfortunately the magnetic signal is very weak, typically 6 orders of magnitude weaker than the pure Thomson charge scatter. However, as predicted theoretically [3], Gibbs *et al.* [4] observed a 50-fold enhancement in magnetic signal on tuning to the L_{III} edge of Ho. Issacs *et al.* [5] also noted a similar enhancement in uranium actinides at the uranium M edges as a result of the split spin-orbital Fermi states due to the magnetism present.

From this work the use of X-ray techniques to study the magnetic structure of materials has developed [6, 7], propelled in part, by the availability and quality of synchrotron sources providing tuneable X-rays to probe absorption edges which show strong spin-orbit coupling. For transition metals, the appropriate resonance for magnetic sensitivity is in the 3d band (4f for the lanthanides and 5f for the actinides) found within the soft X-ray energy region, thus labelling this technique: Soft X-ray Magnetic Scattering (SoXMaS). The theory describing resonance has been discussed in *Section 2.8.1*; its application to magnetic studies will be shown in *Section 6.2.*

The value of hard X-ray reflectivity has been demonstrated throughout this thesis, with model fitting used to extract important parameters such as layer thickness and interface morphology. Modelling is possible at these energies since the scattering cross-sections are known accurately. At soft energy resonance these cross-sections (as well as the magnetic factors) are unknown, and therefore must be determined in order to simulate scattering and quantify the experimental data. To this end, the possibility of using neutrons as a comparative is explored.

Neutron scattering was recognised from an early stage as an invaluable tool due to the distinct properties of the neutron. Not only do thermal neutrons have a wavelength comparable to the interatomic distance within crystals, but also the energy required for thermal excitation. The magnetic structure of thin films are studied primarily with Polarised Neutron Reflectivity (PNR) [8] and although traditionally neutron experiments have always been constrained through limited flux, recent developments in detector design have allowed the diffuse neutron scatter to be exploited [9] in the study of magnetic disorder. The information available with neutron scattering is, in principle, complementary to that obtained with X-rays, with both techniques possessing atomic and magnetic scattering amplitudes. For this reason neutrons have been employed here as a comparable technique.

In this chapter we have studied a series of sputtered transition metal magnetic multilayers, comparing directly the specular and diffuse scatter from PNR and SoXMaS experiments, with particular emphasis on the charge and magnetic contributions in relation to their separate structural components. The reader is initially introduced to the theories governing resonant magnetic scattering and polarised neutron reflectometry with a description of the respective stations where these experiments were performed; namely 5U1 at the Daresbury SRS and CRISP at ISIS in the Rutherford Appleton Laboratories in Oxford. By way of further introduction to SoXMaS, results from some Cu/Co multilayers are given to familiarise the reader with the affects of scattering from magnetic (as well as chemical) structure.

To compare SoXMaS with PNR, in an attempt to determine the value of the unknown scattering factors (at soft-resonant energies) for magnetic materials, we have used the two techniques under similar geometries to study the Fe/Cr and Co/Ru multilayers. It is important to note that the data presented in this chapter originates from the **same** set of samples using both techniques. It is our aim to develop SoXMaS as a viable complementary technique to neutron scattering in the study and characterisation of thin magnetic structure. However, the determination of scattering factors using calibration by neutrons has proved difficult due to major discrepancies in the results obtained with these techniques. Evidence indicates substantial differences between the two techniques, in their sensitivity to chemical and magnetic structure.

6.2 Theory of Resonant Magnetic Scattering

Whenever the X-ray energy is tuned to an absorption edge, electrons within the core level are promoted to an intermediate state with a subsequent decay and photon remission. The magnetic sensitivity arises when the electron shells involved in the excited state are spin polarised i.e. with differences in the transition probability for spin-up and spin-down electrons. Magnetic X-ray scattering therefore occurs via purely electronic transitions and does not interact directly with the magnetic moment. This effect is polarisation dependent and gives rise to two fields of magnetic study; SoXMaS and Magnetic X-ray Circular Dichroism (MXCD). MXCD is sensitive to the imaginary part of the anomalous scattering amplitude and is basically the difference between absorption spectra measured for opposite signs of circular polarisation. It can measure through selection rules the spin and orbital components of element-specific and site-specific magnetic moments. MXCD is widely used in the study of ferromagnetic systems and is described in greater detail in references [10, 11].

Let us now examine the theory governing magnetic X-ray scattering in more detail. In *Section 2.8.1* it was necessary, in order to explain resonance, to elaborate on the simple electron cloud model. A basic bound state model was sufficient to introduce the anomalous scattering terms required to modify the Thomson scattering factor, see *Equation 2.46*. This factor is expanded on further, following the work of Hannon *et al.* [3], to write the total coherent elastic scattering amplitude for scattering from a magnetic ion:

$$f(\mathbf{q},\omega) = f_o(\mathbf{q}) + f'(\omega) + if''(\omega) + f_{spin}$$

Equation 6.1

where f_{spin} is the spin dependent magnetic scattering amplitude representing the interaction between the electron spin and the X-ray wave.

Away from resonance f' and f'' are terms proportional to the orbital and spin angular momentum, and provide the total non–resonant magnetic scattering amplitude as [12, 13]:

$$f_{non-res}^{(mag)} = i\left(\frac{\hbar\omega}{mc^2}\right) r_o \, f_D \, [\tfrac{1}{2}\mathbf{L}(\mathbf{q})\cdot\mathbf{A} + \mathbf{S}(\mathbf{q})\cdot\mathbf{B}]$$

Equation 6.2

where r_o is the Thomson scattering length and f_D is the Debye-Waller factor. $\mathbf{L}(\mathbf{q})$ and $\mathbf{S}(\mathbf{q})$ are the Fourier transforms of the orbital and spin magnetic densities respectively, with $\mathbf{q}$ (= $\mathbf{k}'$- $\mathbf{k}$) being the wavevector momentum transform. $\mathbf{A}$ and $\mathbf{B}$ are given in terms of the scattering vectors with respect to the incident ε, and scattered ε', polarisation vectors:

$$\mathbf{A} = 2(1-\hat{k}\cdot\hat{k}')(\hat{\varepsilon}'\times\hat{\varepsilon}) - (\hat{k}\times\hat{\varepsilon})(\hat{k}\cdot\hat{\varepsilon}') + (\hat{k}'\times\hat{\varepsilon}')(\hat{k}'\cdot\hat{\varepsilon})$$

$$\mathbf{B} = (\hat{\varepsilon}'\times\hat{\varepsilon}) + (\hat{k}'\times\hat{\varepsilon}')(\hat{k}'\cdot\hat{\varepsilon}) - (\hat{k}\times\hat{\varepsilon})(\hat{k}\cdot\hat{\varepsilon}') - (\hat{k}'\times\hat{\varepsilon}')\times(\hat{k}\times\hat{\varepsilon})$$

Equation 6.3

It is important to emphasize that although the electric and magnetic multipole transitions contribute (via f' and f'') to off-resonance scattering, the scattering is dominated by the electric multipole transitions. From *Equation 6.2* it is clear that the magnetic contribution is smaller by a factor of $(\hbar\omega/mc^2)$. For example, at X-ray energies of ~8keV the ratio in scattered intensity between the magnetic and charge contributions from a single electron is approximately 1: ($3600 \times Z^2$).

The exclusion principle dictates that only transitions to the unoccupied orbitals are allowed, which in the case of transition metals results in an exchange interaction sensitive to magnetisation of the d band. Although the quadrupole transitions are weak they can be significant [4] and their polarisation dependence has been calculated [14]. However, in this discussion the scattering amplitude is simply defined by its electric dipole resonant contribution:

$$f_{EL}(\omega) = \left(\frac{4\pi}{|\mathbf{k}|}\right) f_D \sum_{M=-L}^{L} \left[\hat{\varepsilon}'^{*}\cdot\mathbf{Y}_{LM}(\hat{\mathbf{k}}')\mathbf{Y}_{LM}^{*}(\hat{\mathbf{k}})\cdot\hat{\varepsilon}\right] F_{LM}(\omega)$$

Equation 6.4

where $\mathbf{Y}_{LM}(\hat{\mathbf{k}})$ are the vector spherical harmonics. $F_{LM}(\omega)$ is determined by the atomic properties and represents the strength of the resonance:

$$F_{LM}(\omega) = \sum_{\alpha,\eta} \frac{P_\alpha P_\alpha(\eta)\Gamma_x}{\Gamma(x(\alpha,\eta) - i)}$$

Equation 6.5

P_α is the probability of the ion existing in its initial state α and $P_\alpha(\eta)$ is the probability of transition from that state to a final excited state η. Γ_x / Γ is the ratio of partial line width of the excited state due to all forms of electric dipole radiative decay, to that of both radiative and non-radiative decay. Finally, x is the deviation from the resonance condition in units of the total half width: $x = (E_\eta - E_\alpha - \hbar\omega)/(\Gamma/2)$.

The electric dipole transitions are usually the easiest to calculate and dominate the resonant magnetic cross-section, an example of such a transition is the 2p to 3d in Co, which occurs at the L_{III} absorption edge. The vector spherical harmonics for this transition can be written as follows [14] for L = 1 and M=±1:

$$\hat{\varepsilon}'^{*}\cdot\mathbf{Y}_{1\pm1}(\hat{\mathbf{k}}')\mathbf{Y}^{*}_{1\pm1}(\hat{\mathbf{k}})\cdot\hat{\varepsilon}=\left(\frac{3}{16\pi}\right)\left[\hat{\varepsilon}'\cdot\hat{\varepsilon}\mp i(\hat{\varepsilon}'\times\hat{\varepsilon})\cdot\hat{z}_n-(\hat{\varepsilon}'\cdot\hat{z}_n)(\hat{\varepsilon}\cdot\hat{z}_n)\right]$$

Equation 6.6

And for L = 1 and M=0:

$$\hat{\varepsilon}'^{*}\cdot\mathbf{Y}_{10}(\hat{\mathbf{k}}')\mathbf{Y}^{*}_{10}(\hat{\mathbf{k}})\cdot\hat{\varepsilon}=\left(\frac{3}{8\pi}\right)\left[(\hat{\varepsilon}'\cdot\hat{z}_n)(\hat{\varepsilon}\cdot\hat{z}_n)\right]$$

Equation 6.7

where $\hat{z}_n$ is the unit vector of the magnetic moment for the nth ion. Thus combining these terms with *Equation 6.4* the dipole operator is derived:

$$f^{XRES}_{nE1}=\left[(\hat{\varepsilon}'\cdot\hat{\varepsilon})F^{(0)}-i(\hat{\varepsilon}'\times\hat{\varepsilon})\cdot\hat{z}_n\,F^{(1)}+(\hat{\varepsilon}'\cdot\hat{z}_n)(\hat{\varepsilon}\cdot\hat{z}_n)F^{(2)}\right]$$

Equation 6.8

with

$$F^{(0)}=(3/4k)[F_{11}+F_{1\text{-}1}]$$
$$F^{(1)}=(3/4k)[F_{11}-F_{1\text{-}1}]$$
$$F^{(2)}=(3/4k)[2F_{10}-F_{1\text{-}1}]$$

Equation 6.9

The first term in *Equation 6.8* contributes solely to charge scattering since it contains no magnetic dependence; it is through this term that the classical f' and f'' (anomalous dispersion corrections) enter into the resonant scattering amplitude. The second and third terms are first and second order magnetic contributions. It is worth noting that the second term is used in spectroscopic measurements such as MXCD discussed earlier.

It is convenient to rewrite the polarisation terms from *Equation 6.8* into a 2 × 2 matrix, with the polarisation states either being perpendicular σ, or parallel π, to the scattering plane. As such, the possible configurations for incident and scattered polarisation vectors are represented in the matrix as:

$$\begin{pmatrix} \sigma \rightarrow \sigma & \pi \rightarrow \sigma \\ \sigma \rightarrow \pi & \pi \rightarrow \pi \end{pmatrix}$$

Equation 6.10

This formulism was first used by de Bergevin and Brunel [2] in their derivation of the non-resonant magnetic cross-section for X-ray scattering and later adopted by Hill and McMorrow [14] in presenting the magnetic resonance exchange scattering:

$$f_{nE1}^{XRES} = F^{(0)}\begin{pmatrix} 1 & 0 \\ 0 & \hat{k}'\cdot\hat{k} \end{pmatrix} - iF^{(1)}\begin{pmatrix} 0 & \hat{k}\cdot\hat{z}_n \\ -\hat{k}'\cdot\hat{z}_n & (\hat{k}'\times\hat{k})\cdot\hat{z}_n \end{pmatrix} + \frac{F^{(2)}}{\left[1-\left(\hat{k}'\cdot\hat{k}\right)^2\right]}\times\ldots$$

$$\begin{pmatrix} \left[(\hat{k}'\times\hat{k})\cdot\hat{z}_n\right]^2 & \left[\hat{k}'\cdot\hat{z}_n - \left(\hat{k}\cdot\hat{k}'\right)\hat{k}\cdot\hat{z}_n\right](\hat{k}'\times\hat{k})\cdot\hat{z}_n \\ \left[\left(\hat{k}\cdot\hat{k}'\right)\hat{k}'\cdot\hat{z}_n - \hat{k}\cdot\hat{z}_n\right](\hat{k}'\times\hat{k})\cdot\hat{z}_n & \left(\hat{k}\cdot\hat{k}'\right)\left[\left(\hat{k}\cdot\hat{z}_n\right)^2+\left(\hat{k}'\cdot\hat{z}_n\right)^2\right]-\left[1+\left(\hat{k}\cdot\hat{k}'\right)^2\right]\left[\left(\hat{k}\cdot\hat{z}_n\right)\left(\hat{k}'\cdot\hat{z}_n\right)\right] \end{pmatrix}$$

Equation 6.11

Resolving the vectors $\hat{k}, \hat{k}'$ and $\hat{z}_n$ into their coordinate components in terms of the scattering angle θ, (as defined in the following figure for an out-of-plane scattering geometry) allows *Equation 6.11* to be re-written into a more manageable form:

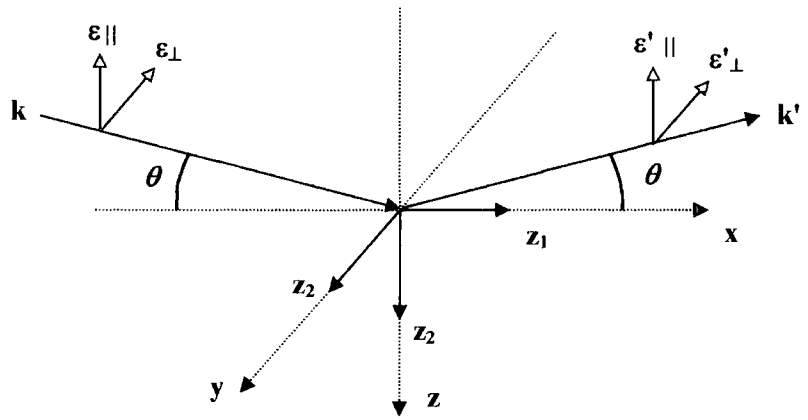

Figure 6.1: *Coordinate system used in calculating the polarisation dependence for a resonant X-ray scattering experiment.*

$$f_{nE1}^{XRES} = F^{(0)}\begin{pmatrix} 1 & 0 \\ 0 & \cos 2\theta \end{pmatrix} - iF^{(1)}\begin{pmatrix} 0 & z_1\cos\theta + z_3\sin\theta \\ z_3\sin\theta - z_1\cos\theta & -z_2\sin 2\theta \end{pmatrix}$$

$$+ F^{(2)}\begin{pmatrix} z_2^{\,2} & -z_2(z_1\sin\theta - z_3\cos\theta) \\ z_2(z_1\sin\theta + z_3\cos\theta) & -\cos^2\theta(z_1^{\,2}\tan^2\theta - z_3^{\,2}) \end{pmatrix}$$

Equation 6.12

The dependence of f_{nE1}^{XRES} on θ and moment direction z is clearly very important and although there is little change with scattering angle θ, there is a large dependence with the magnetic moment vector. Analysis presented in *Section 7.2* finds magnetic scattering is reduced to zero when moments are re-orientated in-plane and perpendicular to the incident beam, see *Figure 7.2*.

Although the theory (outlined above) is well understood, there are still a number of unsolved discrepancies. One complication arises in accounting for the change in circular polarisation at each interface due to direct coupling between horizontal and vertically polarised light. In this geometry, we are measuring both real and imaginary components of the charge and magnetic atomic scattering factors. Unlike hard X-rays, in which the anomalous terms in the scattering factors cannot be considered to be isolated, core electrons and the formalism of Cromer and Libermann cannot be used [15, 16].

In this study we have used linear σ polarisation light, which has no cross-terms due to interference and thus allowing, at the appropriate scattering vector, pure magnetic scattering and a more direct comparison with neutron reflectivity.

6.3 Station 5U1 – Daresbury SRS, U.K.

All soft energy experiments presented in this chapter were carried out on the soft X-ray spectroscopy beamline 5U1 at the Daresbury SRS, UK [17]. Unlike the bending magnetic sources previously described, the X-ray source for this station is a variable gap permanent magnetic undulator. The 10-period undulator is one metre in length, with a variable gap between 42 and 88 mm providing a fundamental energy of 60 eV with quasi-continuous harmonics to above the operating limit (~1 keV) of the monochromator. After exiting the undulator the beam is then incident upon a monochromatic system as shown in *Figure 6.2:*

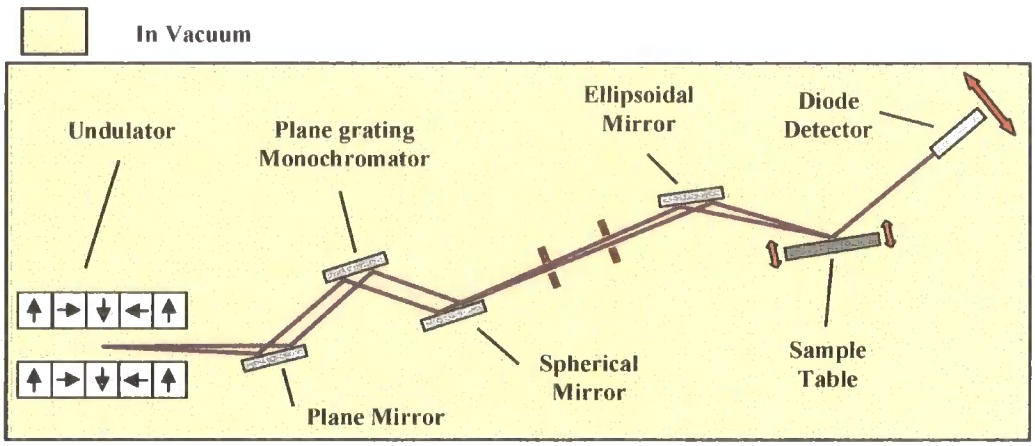

Figure 6.2: *Basic Optical Layout for 5U1 at the Daresbury SRS.*

There are four main optical elements (all coated with platinum); an initial variable angle 250 mm long plane mirror reflects the X-ray beam from the undulator onto a variable angle plane grating monochromator (PGM) with 1200 lines mm^{-1}. The monochromated beam is then focused, via a fixed spherical mirror, through a set of slits. A further ellipsoidal mirror is fixed further downstream which acts to refocus the beam onto the sample.

The energy resolution, ΔE/E, of the beam line is dependent on the energy E and defined by the monochromating grating and entrance slit size. In this series of experiments the energies used ranged between 700 and 800 eV, the slit size was 100 μm, providing an energy resolution FWHM of ~0.4 eV. The energy resolution is clearly of enormous importance when performing any resonance experiment and will of course affect any recorded experimental scattering factors.

The penetration depths of X-rays at soft energies are very small and so it is necessary to perform all reflectivity (or diffraction) experiments in vacuum. The experiments presented here were conducted using the in-vacuum two circle diffractometer available at the SRS and photographed below in *Figure 6.3*:

Figure 6.3: *In-vacuum 2 circle diffractometer installed on 5U1 at the Daresbury SRS, U.K.*

The diffractometer has two concentric circles driven by external stepper motors through differentially pumped o-ring seals. These control the sample and detector arcs. The detector is a p-i-n diode which allows X-ray detection through measuring the drain current. The current is amplified and converted to a voltage, which is then converted to a frequency proportional to the X-ray flux incident on the diode.

The sample mount includes an electro-magnet which can provide fields up to 80 mT with magnetic cooling via a liquid nitrogen sink. Unfortunately it is not possible to increase the field substantially without increasing the size of the magnet, this is impossible due to spatial constraints imposed by the size of the vacuum chamber.

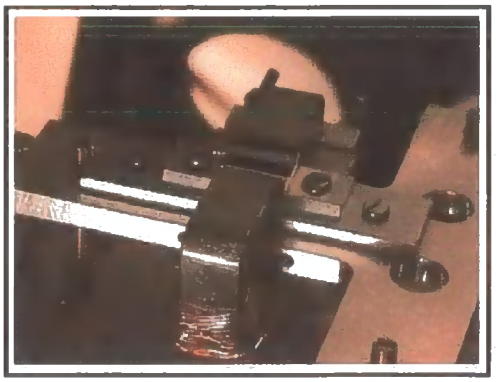

Figure 6.4: *Electro-magnet (with sample) installed on 5U1.*

Sample alignment is achieved initially with a laser on a coincident path (arranged using a Fe grating) to that of the X-ray beam and then more accurately with the X-ray beam itself.

6.4 Theory of Neutron Scattering

The mechanism behind neutron scattering is far more complex in comparison to X-ray scattering, since the neutron is not only described by its wavevector **k**, but also by its spin σ. The spin of the neutron results in a magnetic moment, which undergoes dipole-dipole interactions with magnetic moments from any unpaired electrons. However, like X-rays, neutrons will display interference effects when scattered from ordered condensed-matter systems. It is therefore possible to determine the crystallographic structure from nuclear interaction and the magnetic ordering via magnetic interactions. Another benefit of neutron scattering, which will not be discussed here, is its ability to measure dynamical processes, such as phonon and magnon interaction.

A basic description of elastic neutron scattering will now follow, comparing this technique, where possible, with X-ray scattering. Discussion will start with a basic description of neutron scattering from a single nucleus and proceed to a magnetic ion. This will then be followed by a brief discussion concerning the specifics and benefits of PNR. For a more detailed description of neutron scattering the reader is referred to reference [18].

6.4.1 Scattering from a Nucleus

There is of course a very strong interaction between neutrons and nuclei, it is after all the interaction which binds the nucleus together. The scattering potential from the nucleus can be approximated with a delta function:

$$V(\mathbf{r}) = \frac{2\pi\hbar}{m} b\delta(\mathbf{r}-\mathbf{R})$$

Equation 6.13

where b is the scattering length and m is the mass of the neutron. From this we can define a scattering factor, analogous to *Equation 2.4*.

$$f_n = \frac{m}{2\pi\hbar^2}\int_{Vol} V(\mathbf{r})\exp[2\pi i(\mathbf{q}\cdot\mathbf{r})]\ dr$$

Equation 6.14

The size of the nucleus can range from 1 fm for a single nucleon, up to 7 fm for the heaviest nuclei. This is much smaller than the wavelength of the neutron (~1 Å) and so by assuming the Fermi pseudo-potential is negligible outside the radius of the nucleus, it can be approximated to a point source:

$$f_n = \frac{m}{2\pi\hbar^2} V\frac{4\pi r_o^3}{3}$$

Equation 6.15

Since scattering originates from a point source (unlike X-rays), f_n has no **q** dependence (see *Section 2.2.2)* and so remains constant. f_n is usually tabulated in terms of b, the nuclear scattering length.

At this point the analogy between neutron and X-ray scattering breaks down further when we consider the fact that neutron scattering depends not only on the isotope and atom, but also on the relative coupling between nuclear **I,** and neutron spin σ. Consequently the incident and scattered neutrons are described, as previously mentioned, by its wavevector **k** and spin σ. The differential cross-section dσ/dΩ is found with Fermi's golden rule:

$$\left(\frac{d\sigma}{d\Omega}\right)_{k_0,\sigma_0\to k_1,\sigma_1} = \left(\frac{m}{2\pi\hbar^2}\right)^2 \left|\langle \mathbf{k}_1,\sigma_1|V|\mathbf{k}_0,\sigma_0\rangle\right|^2$$

Equation 6.16

It is often convenient simply to describe the interaction with a scattering amplitude operator, defined as a function of the scattering vector **q**:

$$\frac{d\sigma}{d\Omega}(\mathbf{q})_{\sigma_0\to,\sigma_1} = \left|\langle\sigma_1|a_N(\mathbf{q})|\sigma_0\rangle\right|^2$$

Equation 6.17

where a_N is:

$$a_N(\mathbf{q}) = b_l + A_i\sigma.\mathbf{I}_i$$

Equation 6.18

and A_i is the amplitude of the diffracted beam which can be calculated by summing over all the nuclei in the crystal, see [18].

6.4.2 Scattering from an Ion

The magnetic interactions can be treated independently from the nuclear; they are long range, non-central, and so far more complex. It is between the neutron's magnetic moment μ_n and the magnetic field **H** from any unpaired electrons within the atom.

$$V_M(\mathbf{r}) = -\mu_n.\mathbf{H} = -\mu_n.\left(curl\frac{-\mu_i\times\hat{\mathbf{r}}}{r^2} - \frac{2\mu_B\mathbf{p}_i\times\hat{\mathbf{r}}}{\hbar r^2}\right)$$

Equation 6.19

where the neutron magnetic moment $\mu_n = -\gamma\mu_N\sigma$ ($\gamma = 1.9132$) and the electron magnetic moment $\mu_i = -2\mu_B\mathbf{s}_i$. $\mathbf{s}_i$, $\mathbf{p}_i$ and $\mathbf{r}_i$ are the spin, momentum and position respectively for the ith electron and μ_B and μ_N are the Bohr and nuclear magneton respectively. In terms of the scattering amplitude operator introduced earlier:

$$a_{\mathbf{M}}(\mathbf{q}) = -p\sigma\cdot\sum_i\left[\hat{\mathbf{q}}\times 2\mathbf{s}_i\times\hat{\mathbf{q}} + \frac{2i}{\hbar\mathbf{q}}\left(\mathbf{p}_i\times\hat{\mathbf{q}}\right)\right]e^{i\mathbf{q}.\mathbf{r}_i}$$

Equation 6.20

where $p=\frac{1}{2}\gamma r_o=2.696$ fm. The first term in *Equation 6.20* represents the spin interaction and corresponds to $\mathbf{M}_S(\mathbf{q})$, the Fourier transform of the spin magnetisation density:

$$\sum_i \hat{\mathbf{q}} \times 2\mathbf{s}_i \times \hat{\mathbf{q}} e^{i\mathbf{q}.\mathbf{r}_i} = \hat{\mathbf{q}} \times \mathbf{M}_S(\mathbf{q}) \times \hat{\mathbf{q}}$$

Equation 6.21

Similarly, the second term in *Equation 6.20* represents the interaction due to the orbital motion of the electrons. Although a little more complicated, this can also be written in terms of $\mathbf{M}_L(\mathbf{q})$, the Fourier transform of the orbital magnetization density:

$$\sum_i \frac{2i}{\hbar \mathbf{q}} (p_i \times \hat{\mathbf{q}}) e^{i\mathbf{q}.\mathbf{r}_i} = \hat{\mathbf{q}} \times \mathbf{M}_L(\mathbf{q}) \times \hat{\mathbf{q}}$$

Equation 6.22

It is possible to combine the spin and orbital parts:

$$\mathbf{M}(\mathbf{r}) = \mathbf{M}_S(\mathbf{r}) + \mathbf{M}_L(\mathbf{r})$$

Equation 6.23

such that:

$$\mathbf{M}(\mathbf{Q}) = \int \mathbf{M}(\mathbf{r}) e^{i\mathbf{q}.\mathbf{r}} d^3\mathbf{r}$$

Equation 6.24

The term $\hat{\mathbf{q}} \times \mathbf{M}(\mathbf{q}) \times \hat{\mathbf{q}}$ simply describes the magnetisation perpendicular to the scattering vector $\mathbf{q}$ and so *Equation 6.20* shall be rewritten as:

$$a_M(\mathbf{q}) = p\boldsymbol{\sigma}.\mathbf{M}_\perp(\mathbf{q})$$

Equation 6.25

Due to the dependence of the scattering amplitude operator on the magnetisation component perpendicular to the scattering vector, one can determine the amplitude and orientation of a magnetic moment through performing an inverse Fourier transform. However, the general form presented in *Equation 6.25* is not very useful for atomic calculations without the magnetic form factor, which must be included:

$$a_M(\mathbf{q}) = p\boldsymbol{\sigma}.\boldsymbol{f}(\mathbf{q})\mu_n$$

Equation 6.26

The origin of magnetic scattering (unlike neutron-nuclear) is not from a point source, but rather a spatial distribution of unpaired electrons and so this introduces a scattering form factor which decreases rapidly according to the expanse of the magnetic shell.

From this section and *Section 6.4.1* we can write the total scattering from a magnetic ion as proportional to the sum of the nuclear and magnetic components:

$$\frac{d\sigma}{d\Omega}(\mathbf{q})_{\sigma_0\to\sigma_1} = \left|\langle\sigma_1|a_N(\mathbf{q}) + a_M(\mathbf{q})|\sigma_0\rangle\right|^2$$

Equation 6.27

6.4.3 Polarisation Analysis

For a polarised neutron beam, there is an additional interference term between the nuclear and magnetic contributions. This term is very important when measuring weak magnetic moments and improves the magnetic sensitivity of neutron experiments through allowing an indirect measurement of magnetisation which is not perpendicular to the beam.

If the neutron beam is polarised in the z direction there a four matrix elements for the scattering operator $a(\mathbf{q})$ which are given in the following terms:

$$\begin{aligned}
\langle\uparrow|a(\mathbf{q})|\uparrow\rangle &= f_N(\mathbf{q}) + f_{M\perp z}(\mathbf{q}) \\
\langle\downarrow|a(\mathbf{q})|\downarrow\rangle &= f_N(\mathbf{q}) - f_{M\perp z}(\mathbf{q}) \\
\langle\downarrow|a(\mathbf{q})|\uparrow\rangle &= f_{M\perp x}(\mathbf{q}) + if_{M\perp y}(\mathbf{q}) \\
\langle\uparrow|a(\mathbf{q})|\downarrow\rangle &= f_{M\perp x}(\mathbf{q}) - if_{M\perp y}(\mathbf{q})
\end{aligned}$$

Equation 6.28

The first two matrix elements refer to non-spin flip scattering, whereas the second elements are spin flip; a mechanism which is only possible through magnetic scattering.

6.5 CRISP – ISIS, RAL, U.K.

The CRISP station (one of two reflectometers designed to study a wide variety of samples) is at the ISIS facility, Rutherford Appleton Laboratory, UK. The pulsed (usually 50 Hz) neutron beam is obtained from the ISIS neutron source and gives a

neutron wavelength range of 0.5 – 6.5 Å (or 0.5-13 Å at 25 Hz). A wavelength band is defined by using a rotating variable aperture disk chopper. Unlike X-ray reflectivity, in which **q** is varied by changing the scattering angle, CRISP operates at a fixed angle and allows for a range in **q** through the range in neutron wavelength. The instrument uses a broad band neutron time-of-flight (TOF) method to determine the wavelength. The beam is also collimated by both coarse and adjustable fine slits to give variable beam size and angular divergence.

CRISP can also run in Polarised Neutron Reflectivity (PNR) mode to allow polarisation analysis. This involves the use of polarising mirrors in a static field, spin flippers and a static guide field. A basic schematic illustration of CRISP in PNR mode has been shown in *Figure 6.5:*

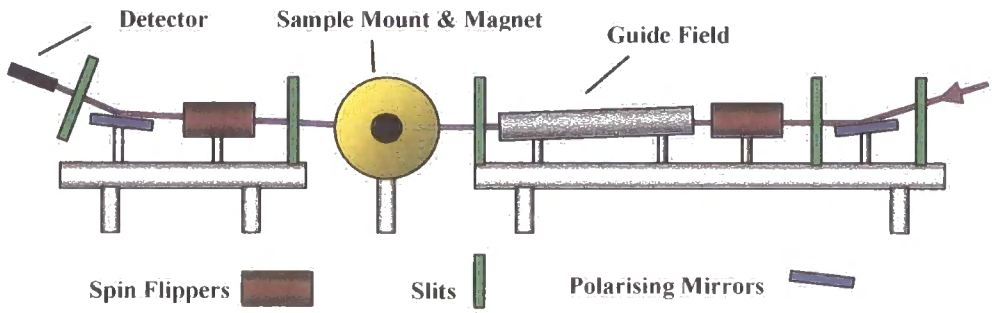

Figure 6.5: *CRISP schematic in PNR mode for PA analysis.*

In this setup we have included a post sample polarising mirror and spin flipper allowing for full polarisation analysis. The guide field simply reduces background scatter and stabilisers the neutron polarisation. The sample mount is located within the magnetic coils allowing an applied field of up 0.4 T. CRISP is equipped with two detectors, a ^{3}He single detector which has been used to record all specular scatter and the 1-D position sensitive multi-detector which has been used in recording 2-D reciprocal space maps to examine the diffuse scatter. Alignment is a relatively simple procedure achieved using an optical laser system set to travel a path identical to that of the neutrons. The sample height and angle are adjusted until the laser beam illuminates the slit at the back of the single detector slits, or in the case of the multi-detector, a mark indicated on the face of the detector.

6.6 Comparing SoXMaS with PNR

PNR experiments provide an average measure of in-plane magnetisation with depth dependent sensitivity and so are ideally suited to the study of magnetic multilayers. It is only recently that disorder measurements have been accessible due to the limited flux available, combined with the low ratios in diffuse to specular scatter. This is not true for X-ray synchrotron sources with resonant enhancement to increase the magnetic signal contribution. The two techniques therefore complement each other in the characterisation of magnetic and chemical structure, their advantages and disadvantages have been summarised below.

6.6.1 Advantages with PNR

- **A Magnetic Probe** – Neutrons directly probe the atomic moment whereas X-rays are sensitive indirectly through changes to the energy band structure.
- **Scattering Cross-sections** – Values that are well known for neutron scattering, but which are not accurately known for resonant X-ray scattering. This limits quantifiable analysis using X-ray data.
- **Atomic and Magnetic Scattering** – PNR allows for both study of ferromagnetic and anti-ferromagnetic structure, however X-rays only measure interference between chemical and magnetic scattering, which is difficult to resolve unless a unique scattering vector can be found.
- **Sample Environment** – Neutron scattering can be performed in a wide range of sample environments in comparison to soft X-ray scattering, which is greatly restricted through the need for a vacuum chamber.
- **Absorption** – Low absorption rate for neutrons, ensuring the multilayer is sampled. A high absorption rate for X-rays at soft energies.
- **Lateral Coherence Length** – Neutrons have a much larger coherence length (~30 μm), allowing one to sample multiple domain structures.

6.6.2 Advantages with SoXMaS

- **Flux** – A much greater flux available from X-ray sources significantly reducing the necessary counting time in comparison to PNR and allowing statistically much more accurate scans, especially in the diffuse regime.
- **Constituent Specificity** – SoXMaS is not only element specific but also shell specific allowing a wide variety of potential experiments.
- **Scattering q – range** – The long wavelength used allows one to probe a large range in q. Neutrons have quite a restricted range of observable scattering vectors, see *Figure 6.17a)* and *Figure 6.19a)*.

6.7 The Samples

In the following sections results from a series of Co/Cu, Fe/Cr and Co/Ru magnetic multilayers are presented. The samples were grown on Si (100) substrates by d.c. magnetron sputtering in a system with a base pressure of less than $2x10^{-8}$ Torr at the Department of Physics, University of Leeds.

The first section introduces SoXMaS via three Co/Cu multilayers; two of which have been grown at the 1st AF coupling peak with 50 and 25 bilayer repeats: $Si/Cu(10Å)/[Co(10Å)/Cu(10Å)]_{xRepeats}$. For the purposes of comparing the out-of-plane magnetic correlation length, results are presented from a third Cu/Co multilayer grown at the 2nd AF coupling peak with a nominal structure: $Si/Cu(10Å)/[Co(10Å)/Cu(21Å)]_{x50}$.

The presentation continues with results obtained from Fe/Cr and Co/Ru multilayers with the thicknesses of the non-magnetic spacer layers set for the 2nd AF coupling peak. By growing these samples at this coupling peak, in preference to the 1st AF coupling peak, we induce a weaker coupling between the magnetic layers thus allowing for the possibility of switching to ferromagnetic alignment in a much lower field. For a direct comparison the **same** Fe/Cr and Co/Ru multilayers have been studied using both SoXMaS and PNR. The nominal structures of these samples are: $Si/Cr(12Å)/[Fe(14Å)/Cr(12Å)]_{x50}$ and $Si/Ru(21Å)/[Co(35Å)/Ru(21Å)]_{x50}$. An additional Co/Ru multilayer was also grown (with slightly thicker magnetic layers) to study the field

dependence in some SoXMaS experiments. This sample, with nominal structure Si/Ru(21Å)/[Co(55Å) / Ru(21Å)]$_{x20}$, was not used in any neutron experiments.

Prior to all experiments these multilayers were magnetised ex-situ with a permanent magnet, providing a field of 1.4 kOe. This ensured AF coupling perpendicular to the beam direction.

6.8 Results

6.8.1 Co/Cu Multilayer

In order to perform magnetic resonant experiments it was necessary to tune very carefully to the appropriate energy, in this case the Co L_{III} or L_{II} edges at 778.1 eV and 793.2 eV respectively. The following figure demonstrates the energy dependence (across the Co edge) to the charge and magnetic scatter:

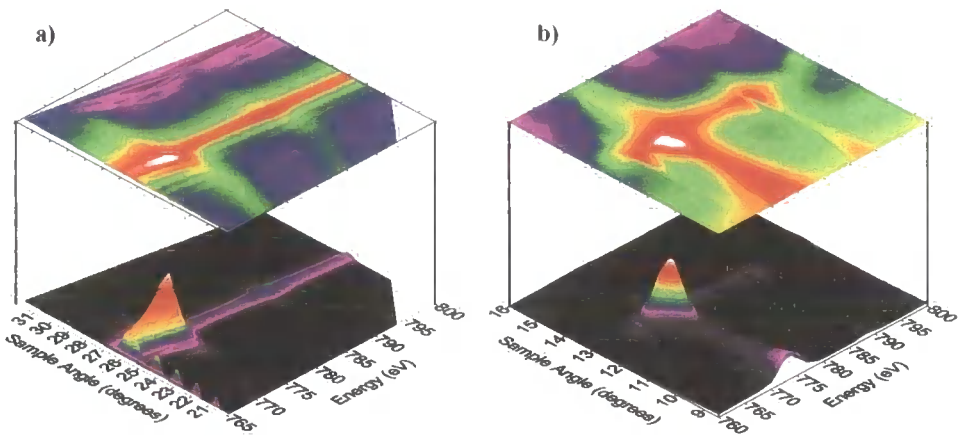

Figure 6.6: *Maps over the* ***a)*** *charge and* ***b)*** *magnetic Bragg peaks as a function of energy over the Co L_{III} and L_{II} edge. The lower z-axis represents the scatter (in arbitrary units) on a linear scale and the top 2D surface map shows it on a log scale.*

The map shown in *a)* is a series of scans made over the charge Bragg peak as a function of energy; it shows the affect of resonance enhancement at the L_{III} edge, and to a lesser extent the L_{II} edge. Map *b)* shows the magnetic Bragg peak over the same energy range; it basically demonstrates the energy-dependence of magnetic sensitivity and the importance of carefully tuning the incident X-rays to the correct wavelength.

The soft X-ray resonance specular reflectivity and off-specular longitudinal diffuse scans for the Co/Cu multilayer have been presented below in *Figure 6.7*. The figure shows two reflectivity profiles for different X-ray energies at the Co L_{III} and Cu L_{III} absorption edges. In the Co L_{III} scans the magnetic Bragg peak is visible, originating from the different periodic spacing present in the magnetic structure.

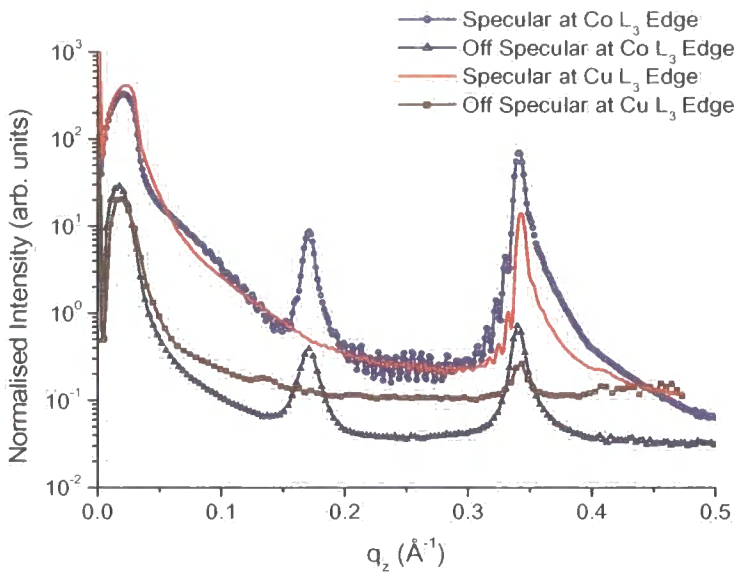

Figure 6.7: *Magnetic and charge scattering from a Cu/Co multilayer, grown at the 1st AF coupling peak, through tuning the incident X-ray energy to the Co and Cu L_{III} edge.*

The magnetic Bragg peak is only visible when we are tuned to the Co L_{III} edge and of course, since Cu is not magnetic (and so not AF coupled), missing at the Cu L_{III} edge. The position of the magnetic Bragg peak is at half that of the chemical Bragg peak; this is due to the AF coupling bringing about a magnetic periodicity twice that of the chemical, see *Figure 6.8*. If the sample was ferromagnetic the magnetic periodicity would match that of the charge structure and so the charge and magnetic Bragg peaks would be located at the same position in reciprocal space. It was for this reason AF coupled samples were chosen, which can provide a peak purely magnetic in origin.

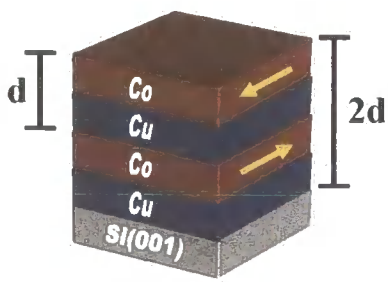

Figure 6.8: *Diagram to illustrate the difference in chemical and magnetic structural periodicity inherent to all AF coupled multilayers.*

The positions of the Bragg peaks, in *Figure 6.7*, are consistent with the nominal structure, with the Kiessig fringes confirming the total stack thickness. The presence of Bragg peaks in the off-specular longitudinal diffuse scan suggests strong correlation through the multilayer, for both the chemical and magnetic structure. Out-of-plane correlation lengths can be determined by fitting the off-specular Bragg peaks. Throughout this work the diffuse scatter has been modelled assuming the standard fractal model, as described in *Section 2.7.2*.

The Co/Cu Bragg peaks were fitted using Lorentzians which, as described in *Appendix D*, mean an equivalent fractal parameter of h=0.5 with a correlation length equal to the inverse half width half maximum (HWHM) in q. The chemical peak revealed an out-of-plane correlation length of ζ_C=104±15 Å. Since the disorder around the AF Bragg peak is magnetic in origin, it is reasonable to assume the length obtained from the HWHM represents a magnetic structural correlation length. In this case calculated at ζ_M=90±15 Å, slightly smaller, but comparable to that of the chemical.

The values obtained for the magnetic out-of-plane correlation length ζ_M, varied from sample to sample and would appear to be related very strongly to the strength of the exchange. For example, samples grown at the 1st AF coupling peak displayed a greater magnetic correlation length in comparison to those grown at the 2nd coupling peak. This has been shown (with the reciprocal lattice units matched) in *Figure 6.9a)* by comparing the Co/Cu multilayer grown at the 1st AF coupling peak with one grown to the 2nd order coupling peak. The vertical magnetic correlation length was ζ_M=90±15 Å and ζ_M=50±10 Å for the 1st and 2nd ordered AF coupled samples respectively. This result should come as no surprise when you consider there should be a greater magnetic interaction with the exchange coupling at the 1st AF coupling peak and thus it is reasonable to assume this will affect the magnetic structure over a greater distance, increasing the correlation length. The chemical structure correlation remained the same between samples at 100±15 Å.

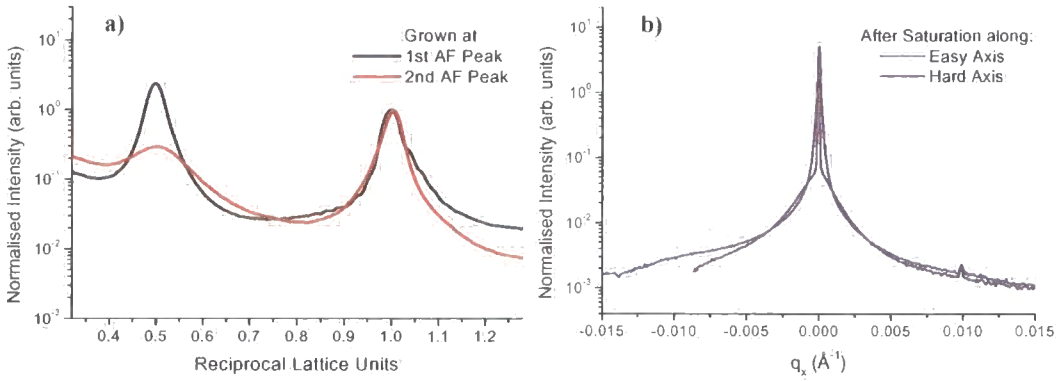

Figure 6.9a): *Longitudinal diffuse scans for Cu/Co layers grown at the 1st (black) and 2nd (red) coupling peaks, where the width of the peak is inversely proportional to the correlation length and* ***b):*** *Transverse diffuse scans across the magnetic Bragg peaks magnetised along the easy (blue) and hard (purple) axis.*

In a similar manner, through fits to the transverse diffuse data, it is possible to measure the average in-plane correlation length. These peaks were also fitted to Lorentzians (h=0.5) to reveal large variations in the in-plane correlation length. The chemical in-plane correlation length was determined as $\xi_C = 50\pm7$ Å. This value is much smaller than the length scales obtained from *Figure 6.9b)* which show two transverse diffuse scans through the AF Bragg peak, providing magnetic correlation lengths of ξ_M=880±20 Å and ξ_M=7000±100 Å for magnetisation along the hard and easy axis respectively. The difference in correlation length with magnetisation orientation is not unexpected since by definition the correlation length defines the length scale over which a structure, statistically speaking, is correlated whether modelling chemical or magnetic structure. When the sample is magnetised along the easy axis, the domain size will, on average, be much larger and so the correlation in magnetic structure will extend over a greater distance, thus increasing ξ_M.

The correlated magnetic roughness could also be estimated by measuring the relative amounts of specular to diffuse scatter and then using the Born approximation (as described in *Section 5.3.1*) to calculate an average σ_M. The Cu/Co system revealed an average magnetic roughness of 9±1 Å, decisively large when compared with the chemical roughness (obtained with the same method at 3±0.4 Å) and in relation to the individual layer thicknesses. However, if the diffuse scatter contains contributions due to domain disorder, the 'roughness' value becomes meaningless in defining magnetic interface morphology. Discussion related to the definition of 'magnetic roughness' will

be considered in much greater detail in the following chapter (*Section 7.3* attempts to separate interface roughness from domain disorder).

Although the field available on the soft diffractometer is limited, it was possible to observe smaller changes in reflectivity as a function of applied field. This has been shown for a similar Co/Cu multilayer (grown at the 1st AF coupling peak) in *Figure 6.10:*

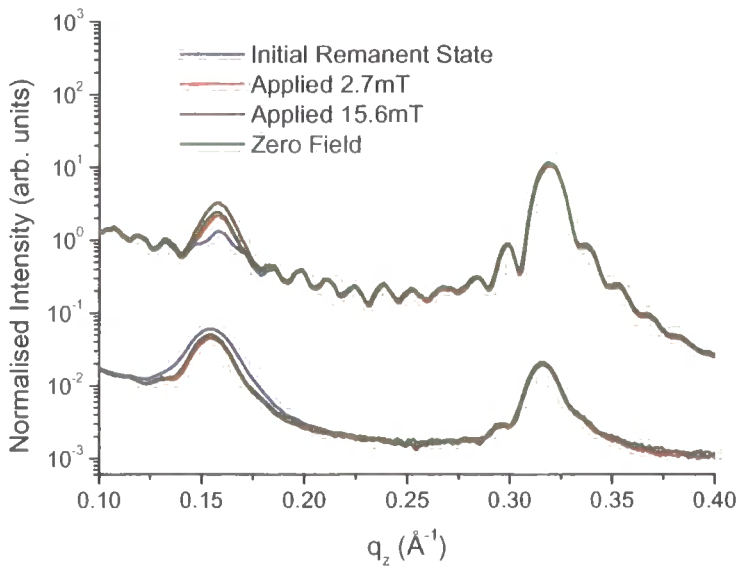

Figure 6.10: *The reflectivity profile for an AF coupled Cu/Co multilayer as a function of applied field.*

Clear changes can be seen in the magnitude of the magnetic Bragg peak with no observable changes to the rest of the reflectivity profile. Although there is still a degree of uncertainty as to the exact mechanics involved in the magnetic moment reorientation, it is strongly believed that some sort of spin flop mechanism is at work [19]. This will be discussed in far great detail in *Section 7.2.1,* where *Figure 7.8* illustrates the most probable moment orientation to explain these results. This does however confirm two observations; the half-order Bragg peak is indeed magnetic in origin, and the rest of the scatter in q_z is not noticeably affected by magnetic effects and therefore must originate from predominantly charge scatter. This suggests the ratio in magnetic to charge signal is much lower than originally thought, an observation which will be discussed in much greater detail in *Section 6.9.*

Another interesting observation highlights the change in magnetic out-of-plane correlation length (ζ_M) apparent from the difference in peak width for the magnetic off-specular Bragg peak. Analysis indicates an increase in correlation length from its initial remnant state with ζ_M = 130±20 Å up to ζ_M = 175±25 Å with an applied magnetic field. With this we observe a small drop in correlated magnetic disorder. These observations are consistent with increased magnetic coupling between the layers as a result of the external applied field.

This section has introduced the reader to SoXMaS and some of its potential characterisation powers for magnetic as well as chemical structure. The next section shall examine the Fe/Cr multilayer using SoXMaS, and as a comparable technique; PNR.

6.8.2 Fe/Cr Multilayer

The M-H loop with the corresponding magnetic data for the Fe/Cr multilayer is shown below in *Figure 6.11*. The loop indicates a small amount of remanence indicative of strong AF coupling between the Fe layers.

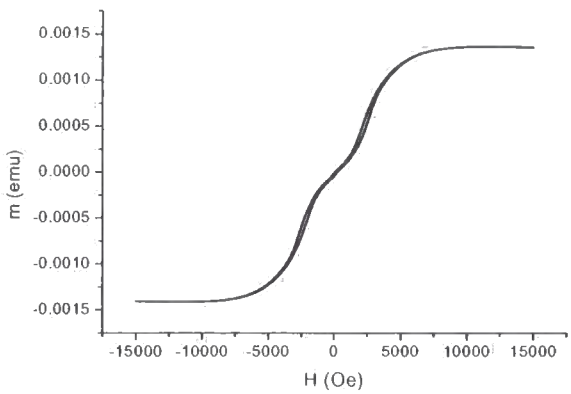

H_c = 150 Oe

$M_r = 4x10^{-5}$ e.m.u.

H_s = 5200 Oe

$M_s = 1.5x10^{-4}$ e.m.u.

Figure 6.11: *The M-H loop with corresponding magnetic data for the Fe/Cr multilayer grown at the 2nd AF coupling maximum. (Courtesy of Dr Chris Marrows)*

In order to examine the chemical roughness and confirm the layer thickness as grown; standard grazing incidence reflectivity measurements were taken at λ = 1.3 Å on station 2.3, Daresbury SRS. The reflectivity profile for the Fe/Cr multilayer has been shown below in *Figure 6.12:*

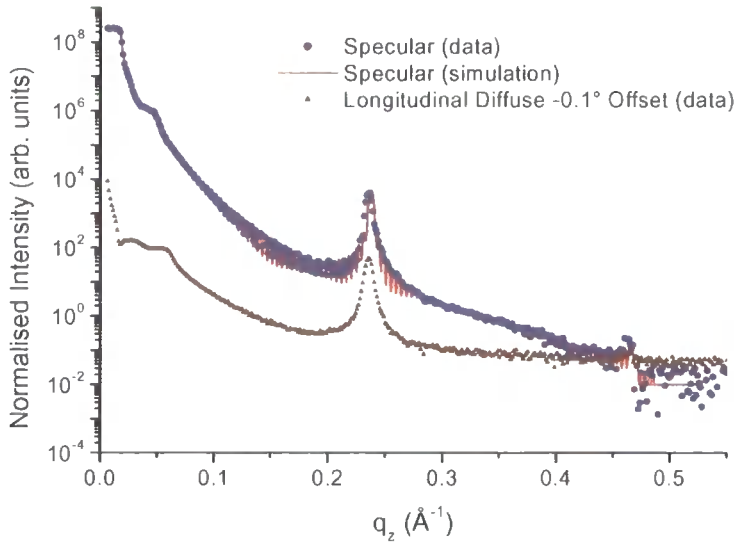

Figure 6.12: *Grazing Incidence X-ray reflectivity profile for the Fe/Cr multilayer with the incident X-ray energy tuned to the Fe K_β edge. The specular scatter (blue) and simulation (red) as well as the (-0.1 °) offset longitudinal diffuse scatter (brown) has been shown.*

Figure 6.12 shows strong Bragg peaks and Kiessig fringes. The high intensity at low scattering angles arises from harmonic contamination in the beam, which proves to be insignificant beyond the fundamental wavelength critical angle due to the fall-off in intensity in excess of q^{-4}. The profile has been fitted using the *Bede Mercury* software, as described in *Section 2.6*, structural parameters gained from this fit have been shown in *Table 6.1:*

Layer	Thickness (Å)	Roughness (Å)	Repeat
Cr_2O_3	4.9±1	12±0.5	-
Cr	12.9±1	9.6±0.5	-
Fe	14.9±1	4.9±0.5	-
Cr	13.3±1	4.6±0.5	-
Fe	14±1	4.5±0.5	-
Cr	11±1	4.7±0.5	-
Fe	14.3±1	4.9±0.5	47
Cr	12.9±1	4.7±0.5	47
Si	N / A	4.5±0.5	-

Table 6.1: *Fitted structural parameters for the Fe/Cr multilayer.*

The simulated modelling parameters indicate a low interface width, which is confirmed from the intense Bragg peak. The simulated fit and position of the Bragg peak correspond to nominal layer thickness values.

To gain information about the in and out-of-plane interface morphology transverse diffuse scans were taken at off-resonance soft energies:

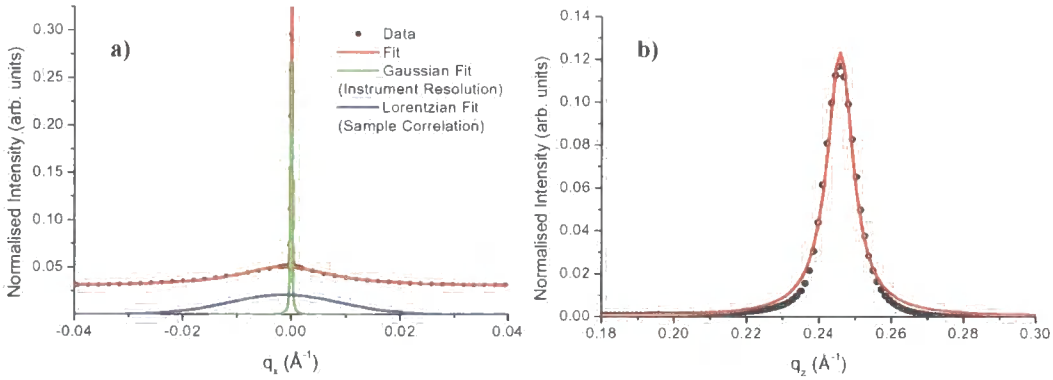

Figure 6.13a): *Transverse diffuse scan in q_x over the Fe/Cr multilayer chemical Bragg peak at an energy of 706 eV, including a fit to obtain the in-plane correlation length and* ***b)*** *the off-specular Bragg peak in q_z (with fit) to determine an out-of-plane correlation length.*

The diffuse scatter has been modelled using the standard fractal model described earlier. Both the transverse diffuse scan (across q_x) and off-specular Bragg peak (across q_z) were fitted to Lorentzians (which is equivalent to a fractal parameter of h=0.5) providing values for the in and out-of-plane correlation lengths of ξ_C=48.7±3 Å and ζ_C=114±9 Å respectively.

6.8.2.1 SoXMaS

As seen previously, it is very important in any resonance experiment to be at the appropriate energy. For the current sample this was at the Fe L_{III} edge, located at 705 eV. *Figure 6.14a)* is an energy scan, across the Fe L_{III} edge, at constant q situated on top of the chemical specular Bragg peak located at q_z=0.24 $Å^{-1}$. The resonance enhancement in scattering is plainly seen at the L_{III} edge with an additional weaker enhancement due to the L_{II} edge. To fine tune to the edge, a series of scans were made across the magnetic Bragg peak found in the off-specular profile, see *Figure 6.14b).* Repeated scans as a function of energy revealed the most defined magnetic Bragg peak and hence the best energy for this SoXMaS experiment.

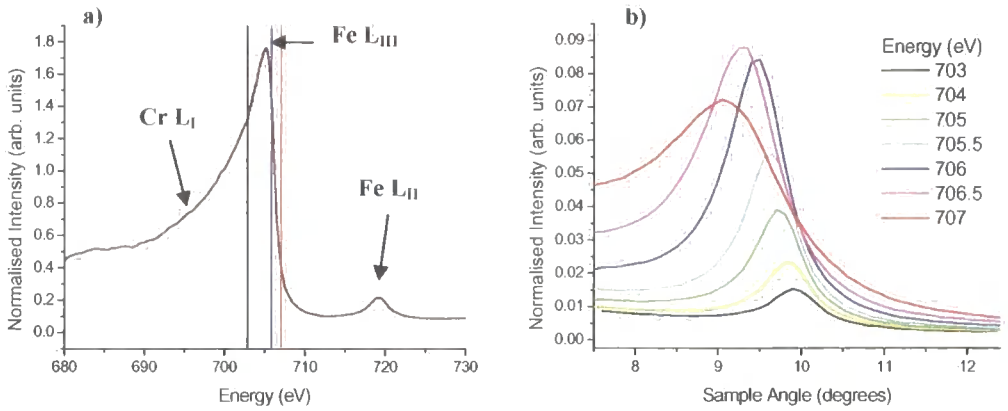

Figure 6.14a): *Energy scan perform at constant q (situated on the Fe/Cr structural Bragg peak) over the Fe L_{III} edge and* ***b)*** *a series of off-specular scans across the magnetic Bragg peak as a function of energy.*

At an energy of 706 eV the standard specular and longitudinal diffuse off-specular scans were performed and have been displayed below in *Figure 6.15:*

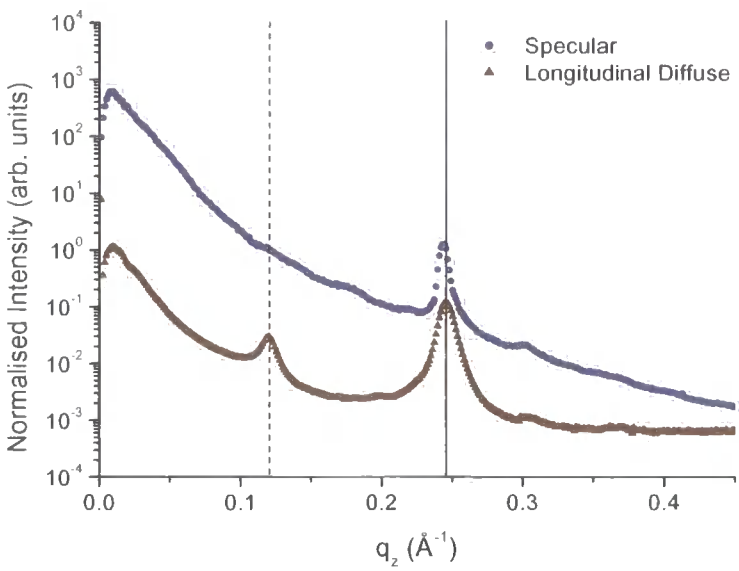

Figure 6.15: *SoXMaS specular and longitudinal diffuse (off-specular) profile for a Fe/Cr multilayer grown at the 2nd AF coupling peak.*

The need for energy alignment from the off-specular magnetic Bragg peak is now clear from *Figure 6.15*. In marked contrast to the Co/Cu multilayer sample presented early, the specular magnetic peak for this sample is not visible. This does not mean the sample is not anti-ferromagnetic since the magnetic VSM data, in addition to the well-

defined magnetic peak at q_z=0.12 Å^{-1} in the off-specular scan, suggest otherwise. This AF off-specular Bragg peak located at half the chemical Bragg peak q_z position (due to the double periodic spacing) indicates a high degree of conformality in magnetic disorder through the stack. However, this does not explain the missing peak in the specular scatter; the most obvious explanation suggests a large amount of magnetic roughness at the multilayer interfaces. If this is the case, all magnetic contributions to the scattering are being scattered into the diffuse. On the other hand, it is also possible to explain the absence of the specular magnetic peak by considering the relative magnetic and charge scattering cross-sections in the scattering factors. Both possibilities relating to the absence of the AF specular Bragg peak will be discussed further in *Section 6.9*. In contrast, the strong chemical peak in the specular demonstrates a low level of chemical disorder, as previously indicated from fits made to reflectivity performed at hard X-ray energies. The strong chemical Bragg peak in the diffuse shows the chemical structural disorder is highly conformal through the stack.

To explore the chemical and magnetic disorder more thoroughly we have again measured the diffuse scatter from both types of interface by recording the scatter distribution in two dimensions of reciprocal space as a function of both in and out-of-plane momentum transfer. To quantify and compare the chemical structure correlation lengths with the magnetic length scales; fits have been made (using Lorentzian peaks) to the longitudinal and transverse diffuse AF Bragg peaks as shown in *Figure 6.16:*

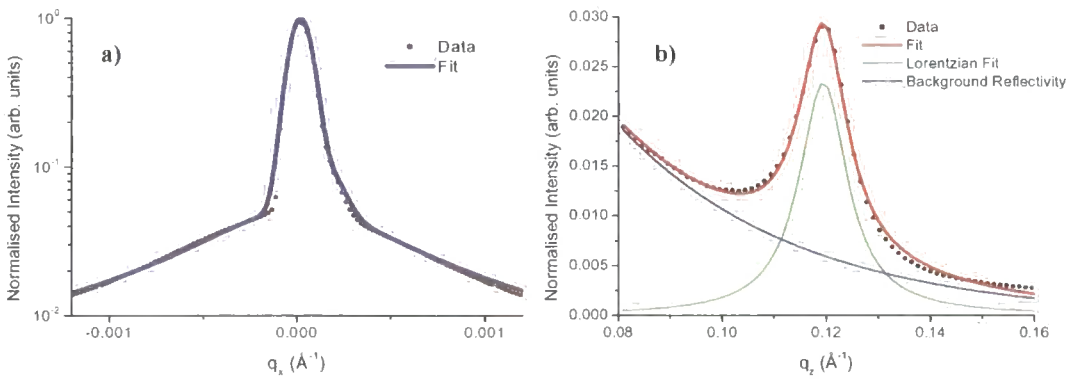

Figure 6.16: *Lorentzian fits to the* ***a)*** *transverse diffuse Bragg peak to reveal the in-plane correlation length and the* ***b)*** *longitudinal diffuse Bragg peak to determine the out-of-plane correlation length.*

Once again the magnetic out-of-plane correlation length is slightly smaller but comparable to that of the chemical structure, fits to the full width half maximum provided an out-of-plane correlation length of ζ_M=90±7 Å. Like the Co/Cu mulilayer, the in-plane magnetic length scales are much larger; ξ_M=800±50 Å. Through rotating the sample 90 ° away from the easy axis, the correlation length reduced to less than half (ξ=390±20 Å). No other differences were observed through the 90 ° rotation.

In addition to the scans presented above, a full reciprocal space map was performed (in the original rotation position) through a series a scans at varying **q** vectors. The smaller scale map in *Figure 6.17a)* demonstrates the wide range in reciprocal space available through using X-rays at soft energies, allowing us to probe length scales down as far as ~50 Å. The cut-off Yoneda wings have been marked in red. The specular ridge is observable at q_x=0 with the chemical Bragg peak located at q_z=0.24 Å^{-1}. The large amount of diffuse scatter around the chemical Bragg peak confirms conformal roughness, with the extent of the scatter in the q_x direction confirming a short in-plane correlation length.

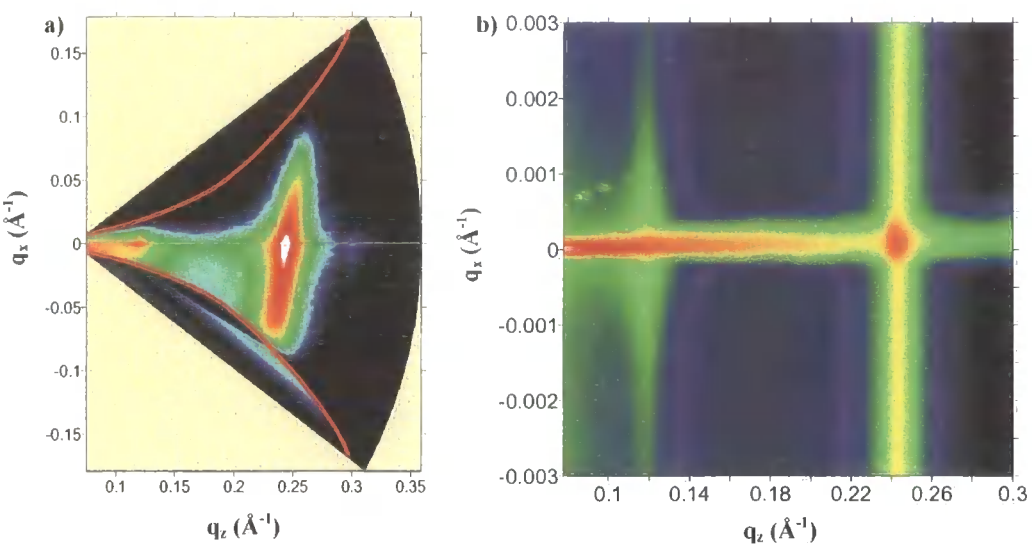

Figure 6.17 a): *2D X-ray diffuse scatter, over the full reciprocal range, under remnant field strength and* ***b)*** *plotted over a much smaller range in reciprocal space.*

The second map is on a much larger scale and shows more clearly the diffuse scatter surrounding the magnetic AF Bragg peak, in addition to the absence of a peak in the specular ridge.

Application of a magnetic field to the Fe/Cr sample made no observable difference to the scans presented above. However this is not surprising due to the limited magnetic field available.

6.8.2.2 PNR

To compare these SoXMaS results with a more established technique; polarised neutron reflectometry has been used. A number of experiments in the specular and diffuse regimes were made to mirror the experiments conducted using SoXMaS. It is important to note that all neutron and soft X-ray experiments were conducted using the same samples.

The neutron specular and off-specular reflectivity has been presented below in *Figure 6.18:*

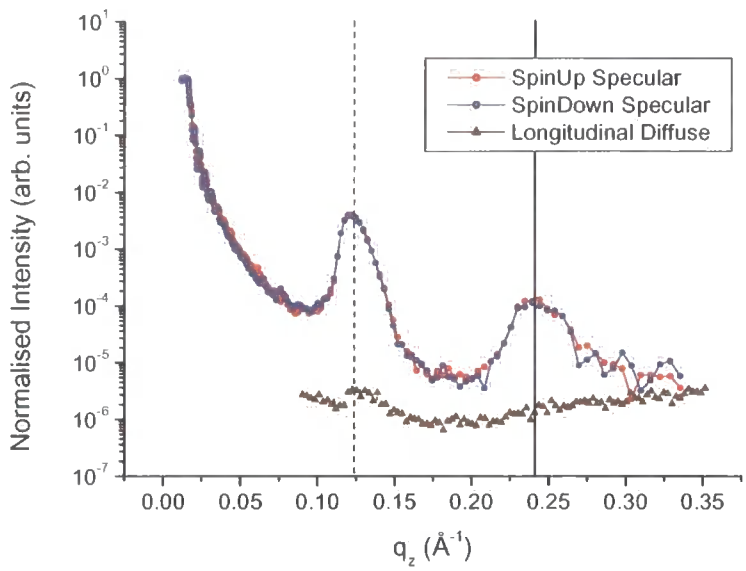

Figure 6.18: *PNR specular and longitudinal diffuse (off-specular) profile for a Fe/Cr multilayer at remanant field.*

The strong Bragg peak at q_z=0.24 Å^{-1} is consistent with the chemical Bragg peak observed with the X-ray experiments. However, a direct comparison with *Figure 6.15* reveals the specular AF Bragg peak at the expected q_z value, which was missing in the X-ray data. This demonstrates good AF coupling as expected, which is confirmed due to

the identical spin up and spin down specular scattering profiles, indicating no net magnetic moment parallel to the applied field (see *Equation 6.28*). The presence of a weak AF peak in the off-specular longitudinal diffuse, again suggests correlation in the magnetic roughness perpendicular to the sample surface. Although, the absence of the chemical structural peak in the off-specular suggests this is not the case for atomic disorder, this again contradicts the observations made from *Figure 6.15*. However, the issue of signal to noise should also be addressed since neutron techniques are inherently noisier due to the low flux.

To compare roughness in more detail (both chemical and magnetic) as 'seen' from the neutrons, diffuse reciprocal space maps were made over a range similar to those probed with the soft X-rays. The combination of the time-of-flight technique combined with the ^{3}He multi-detector, allowed the display of both q_z and q_x components of the neutron wave-vector transfer. A direct comparison with the SoXMaS maps in *Figure 6.17* can be seen below:

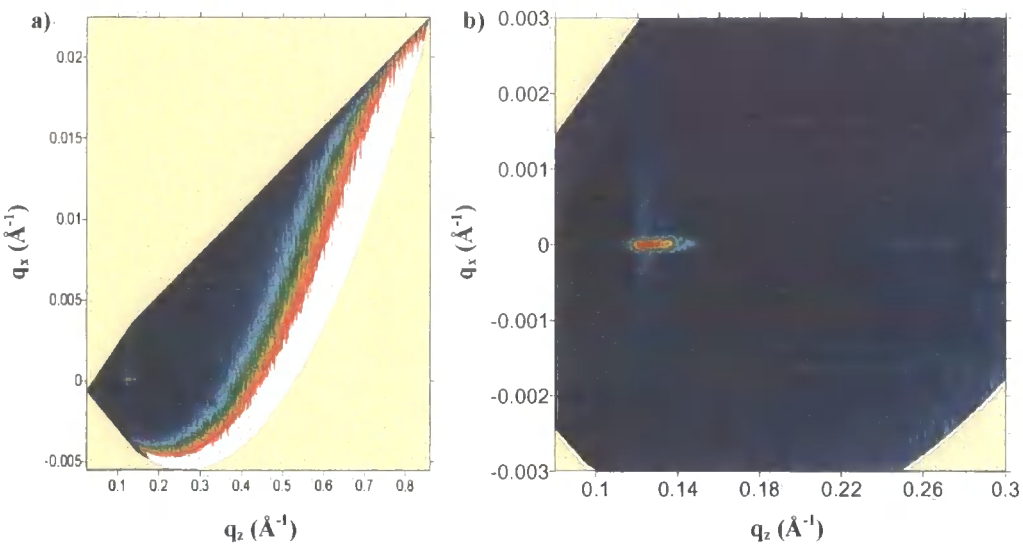

Figure 6.19a): *2D neutron diffuse scatter, over the full reciprocal range, under remnant field strength and b) a large scale plot for direct comparison with Figure 6.17b).*

Figure 6.19a) shows the full range of reciprocal space available with neutron scattering. A quick comparison with *Figure 6.17a)* demonstrates one of the advantages in using the soft X-ray scattering technique, through its ability to probe a much greater area of reciprocal space, an important consideration when measuring short length scales. The high counts observable in the PNR data at high values of q_z is the direct beam.

The section in *Figure 6.19b)* is the region of interest and shown for direct comparison with *Figure 6.17b)*. The diffuse scatter surrounding the AF Bragg peak in q_x indicates a degree of magnetic correlation perpendicular to the sample's surface. In addition, the specular chemical structure Bragg peak can be observed with no surrounding diffuse scatter. This confirms the observations made in the specular and off-specular data shown in *Figure 6.18*. The absence of this diffuse scatter will be discussed further in *Section 6.9*.

Although there was still insufficient field available to saturate the sample, it was possible to induce ferromagnetic alignment. *Figure 6.20* below shows a series of 2D diffuse maps for the Fe/Cr multilayer under an increasing applied field and its correlation with magnetisation according to the M-H loop (also shown).

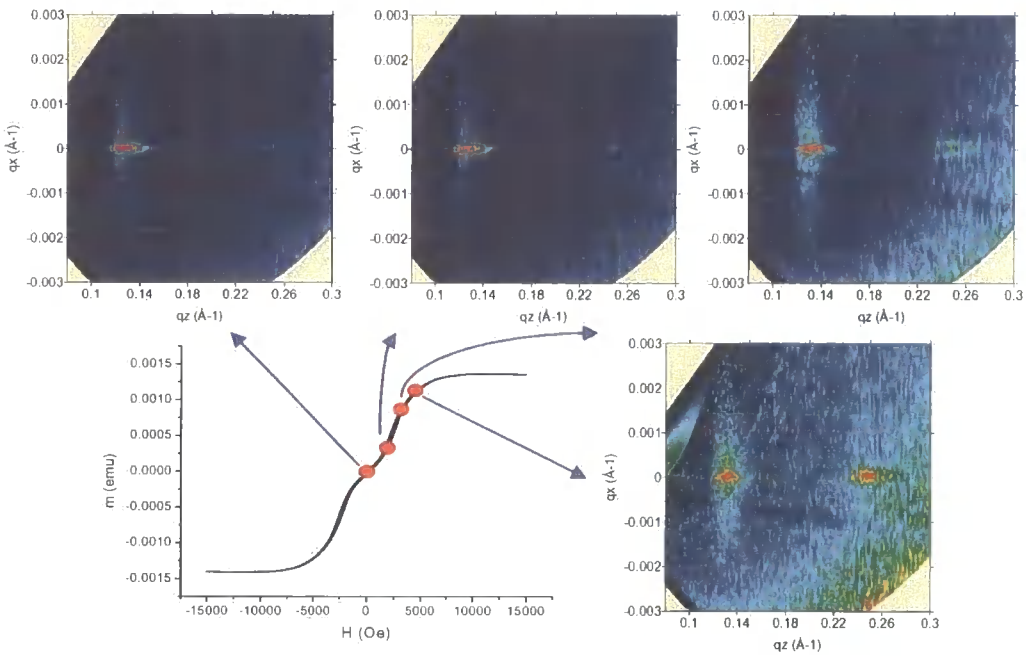

Figure 6.20: *A series of 2D neutron diffuse maps from the Fe/Cr multilayer under increasingly applied field.*

Through inducing ferromagnetic alignment, the magnetic periodicity is doubled to equal that of the chemical, thus Bragg peak intensity is seemingly enhanced (with an accompanying reduction in the AF peak intensity) with the ferromagnetic Bragg peak. The intensity of the magnetic diffuse scatter also reduces. However, it is interesting to note that there is no increase in diffuse scatter around the ferro / chemical Bragg peak. It would appear the magnetic disorder (be it interfacial, domain or both) is reduced

substantially with ferromagnetic alignment. As the sample is saturated the magnetic layers will go from a multi-domain to a single domain state and so this could be cited as evidence to suggest domains are primarily responsible for the roughness contribution to the diffuse scatter. In aligning to a single domain the number of walls responsible for diffuse scatter will reduce. However, a closer look at the magnetic diffuse scatter in *Figure 6.20* shows no change in the diffuse distribution as a function of the in-plane momentum transfer (q_x) and so consequently no change to the in-plane magnetic correlation length. This can be seen more clearly in *Figure 6.21a)*:

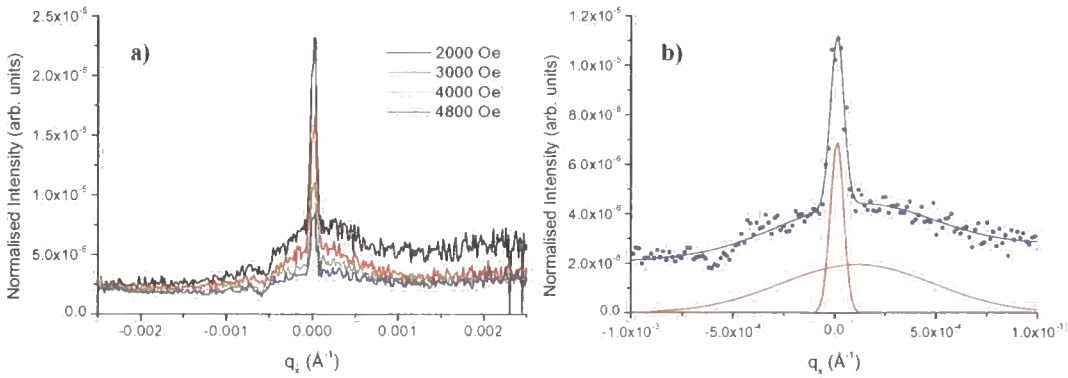

Figure 6.21: *Transverse diffuse in-plane cuts across the AF peak showing the diffuse scatter indicative of magnetic disorder* ***a)*** *as a function of applied field and* ***b)*** *with fit to obtain the corresponding correlation length.*

Due to the experimental setup required for neutrons (see *Section 6.5*) transverse diffuse scans can not be made directly; *Figure 6.21* and the morphological parameters obtained were achieved by extracting one-dimensional slices at fixed q_z values through the maps shown earlier. The data were fitted (as shown in *Figure 6.21b*) with two functions: one, a Gaussian, representing the instrument function, while the broader and weaker Lorentzian arises from the magnetic disorder. The only change recorded as a function of field was in the intensity of the scatter, no change in shape was recorded. This is not consistent with a change to the domain structure, since alignment to a single domain should extend the domain size and magnetic correlation length substantially. An alternative hypothesis examines the possibility that despite the ferromagnetic alignment between the magnetic layers, the field is not sufficient to align the domains within the layers, with no subsequent change to the domain size and correlation length. This theory will be discussed further in *Section 6.9*.

The in-plane correlation length remained constant at ξ_M=2000±400 Å (using a Lorentzian fit), very long in comparison to the value obtained with SoXMaS (ξ_M=800±50 Å) and to the in-plane chemical correlation length only obtainable from the X-rays studies at ξ_C=48.7±3 Å. It should be noted that the correlation length depends strongly on the choice of fitting function; this is a major drawback with neutron diffuse analysis and will be addressed further in the discussion.

Simple estimations of the 'magnetic roughness', within the Born approximation, were made from the relative intensity (integrated over q_x) from the diffuse and specular scatter. The r.m.s. magnetic roughness was determined at σ_M=9.0±1 Å. It is also interesting to note that despite the field, there is no substantial change in magnetic roughness.

There are clearly some significant differences between neutron and X-ray scattering and a number of issues which need to be resolved with respect to the origin of diffuse scatter within the two techniques. The next section presents data from a similar set of experiments conducted using a Co/Ru multilayer.

6.8.3 Co/Ru Multilayer

Figure 6.22 presents the M-H loop for the Co/Ru multilayer, a sample which again shows very little remanence indicative of high AF coupling between the Co layers:

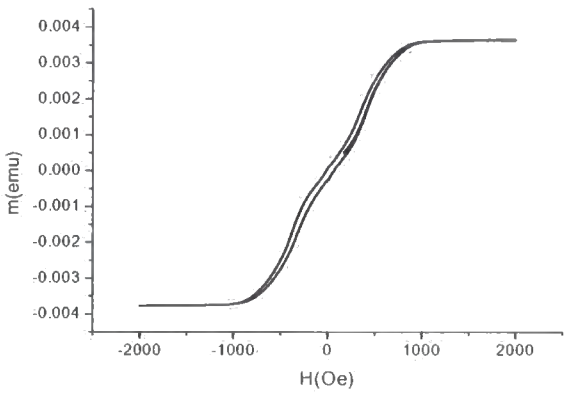

H_c = 70 Oe

M_r = 3x10^{-4} e.m.u.

H_s = 1000 Oe

M_s = 4x10^{-3} e.m.u.

Figure 6.22: *The M-H loop for a Co/Ru multilayer grown at the 2nd AF coupling maximum. (Courtesy of Dr Chris Marrows)*

To confirm the growth parameters and to ascertain something about the chemical roughness, standard hard X-ray energy measurements were performed at station 2.3, Daresbury SRS.

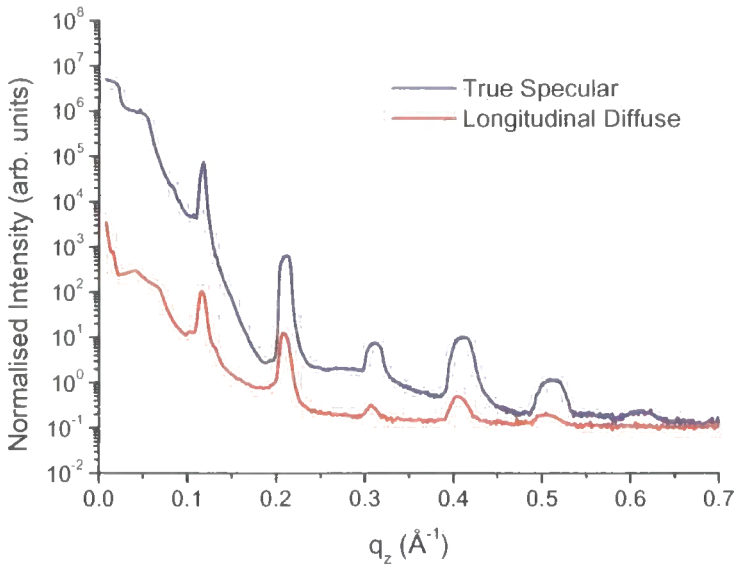

Figure 6.23: *Grazing incidence X-ray reflectivity profile for the Co/Ru sample with an incident wavelength of 1.3 Å.*

Due to an uneven distribution in roughness and bilayer thickness it was not possible to provide an accurate fit to these data. However, from the position of the Bragg peaks it was possible to determine an average bilayer thickness of 56 Å, consistent with the nominal structure. Bragg peaks in the longitudinal diffuse scatter indicate strong out-of-plane correlation, with a length scale of ζ_C=90±15 Å and using the Born approximation a high average chemical roughness value of σ_C=6±1 Å.

6.8.3.1 SoXMaS

In the following SoXMaS experiments two Co/Ru multilayers have been examined, the resonant reflectivity for the first sample is shown below with the energy carefully tuned to the Co L_{III} edge at 778.1 eV:

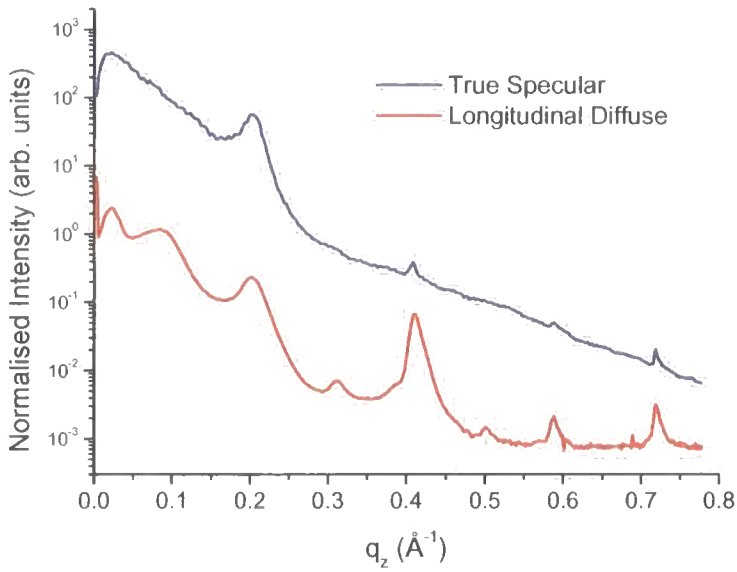

Figure 6.24: *SoXMaS specular and longitudinal diffuse (off-specular) profile for a Co/Ru multilayer grown at the 2nd AF coupling peak.*

The plot confirms the sample has a rough interface structure with the Bragg peaks diminishing very quickly in the specular profile. The high level of roughness is also indicated from the strong longitudinal diffuse scatter where the Bragg peaks are more clearly visible. In addition, no magnetic Bragg peaks were observed (either in the specular or off-specular data), a fact clearly supported through comparing this reflectivity profile with the profile obtained at hard energies (*Figure 6.23*). This is also confirmed through no observable changes with applied magnetic field. This sample will been re-examined using PNR in the following section.

The figure below presents the specular and off-specular profiles for a similar Co/Ru multilayer, grown with 20 bilayer repeats. In this case, the quality of the sample is much higher with prominant chemical structural Bragg peaks (to many orders of magnitude) in the specular profile.

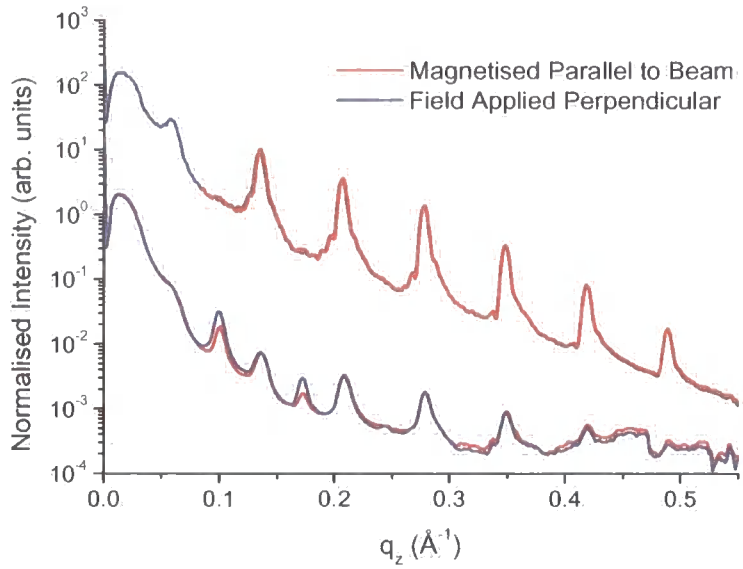

Figure 6.25: *SoXMaS specular and longitudinal diffuse (off-specular) profile for a Co/Ru multilayer grown at the 2nd AF coupling peak; with magnetisation parallel (red) and perpendicular (blue) to the beam.*

Magnetic Bragg peaks are also present in the diffuse scatter, at half the scattering vector (due to AF coupling) to that of the chemical Bragg peaks. Like the Fe/Cr multilayer, there are no magnetic Bragg peaks in the specular scatter and no change with the magnetic field applied perpendicular to the beam direction. There is, however, a significant difference in the off-specular AF Bragg peaks, with the moments aligned parallel to the beam (from an ex-situ field magnetisation) and with the field applied perpendicular, orientating (to a limited degree due to the small field available) the overall moment perpendicular. The increase in AF Bragg peak intensity is discussed in *Chapter 7*.

The off-specular scan has been used to determine a magnetic out-of-plane correlation length of ζ_M=660±35 Å, a length scale much larger compared with the values obtained for the Fe/Cr and Co/Cu multilayer, and much larger than that obtained for the Co/Ru chemical structure out-of-plane correlation length determined at ζ_C=250±20 Å.

The in-plane correlation lengths have been calculated in the same way as before from the transverse diffuse scans taken across the Bragg peaks as shown in *Figure 6.26*:

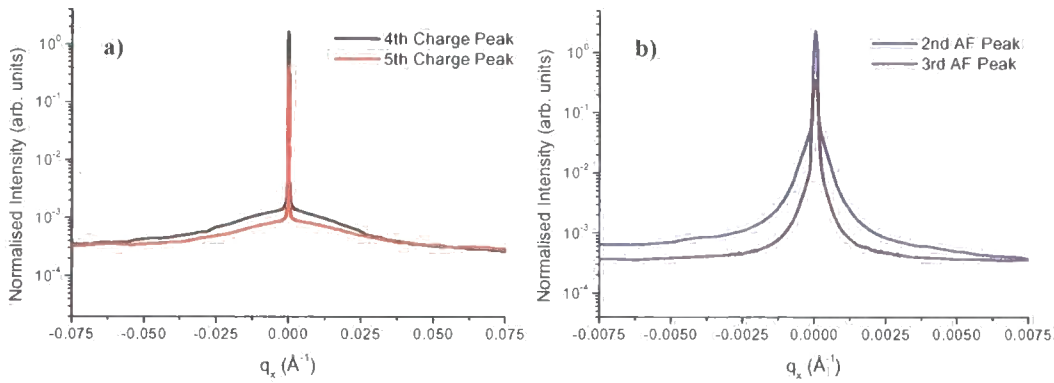

Figure 6.26: *Transverse Diffuse scans across two* ***a)*** *chemical and* ***b)*** *magnetic Bragg peaks from an AF coupled (2nd order) Co/Ru multilayer.*

Although there are minor differences in the in-plane width between Bragg peaks, they remain consistent within error. The in-plane chemical structure correlation length ξ_C, has been determined at 190±30 Å and 170±30 Å for the 4th and 5th Bragg peak respectively. As always the in-plane magnetic correlation length is larger and in this case much larger than the values obtained for the Fe/Cr and Co/Cu multilayers. From the HWHM, ξ_M=18,500±2000 Å and ξ_M=24,000±2100 Å for the 2nd and 3rd Bragg peaks respectively.

6.8.3.2 PNR

To compare the SoXMaS results with PNR (as done for the Fe/Cr multilayer) specular profiles where taken from the 1st Co/Ru multilayer, studied as a function of field. The *figure* below shows the reflectivity profile under a low 20 mT field and at a saturating field of 260 mT. In this case there was sufficient field to saturate the sample completely.

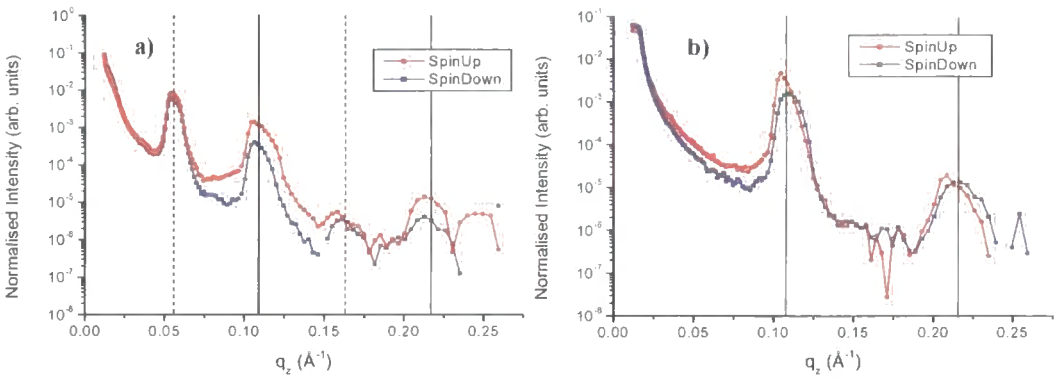

Figure 6.27: *PNR specular profile for the Co/Ru multilayer grown at the 2nd AF coupling peak under* ***a)*** *20 mT and* ***b)*** *260 mT of applied field.*

Figure 6.27a) shows the multilayer in a low remanent field, the strong magnetic Bragg peaks (1st and 2nd order) observable at approximately q_z=0.056 Å^{-1} and q_z=0.16 Å^{-1} correspond to the anti-ferromagnetic magnetic super-structure. The split between the spin up and spin down channels for the chemical structural Bragg peaks at q_z=0.11 Å^{-1} (and q_z=0.22 Å^{-1}) indicate a small ferromagnetic component (despite the low field strength) along the neutron quantisation axis which is caused by a small canting of the spin flip moments. With the saturating field perpendicular to the beam direction, the AF peaks in *Figure 6.27b)* completely disappear under ferromagnetic alignment.

Unfortunately there is no diffuse data available, but this data does compare interestingly with the specular profile of *Figure 6.24* obtained using SoXMaS. The strong magnetic Bragg peaks observable with the neutrons are missing from the SoXMaS data. This again indicates a difference in sensitivity between the two techniques, either in roughness or the relative ratio between nuclear/charge and magnetic scatter.

6.9 Discussion and Conclusion

During this work we have examined different types of Co/Cu, Fe/Cr and Co/Ru multilayers, all AF coupled. As an introduction to the SoXMaS technique, the study began with a look at the Co/Cu multilayers. *Figure 6.7* presented reflectivity data performed at the Co L_{III} absorption edge and showed magnetic scatter in the form of an

AF Bragg peak, at half q_z to that of the chemical peak due to the double periodicity inherent to the AF magnetic structure. The presentation continued, with results obtained from the diffuse scatter, in determining the correlation in chemical and magnetic structure. This introductory section described experimentally the SoXMaS technique and some of the potential offered by this tool in the characterisation of thin magnetic films.

However, the main aim is determine something about the unknown magnetic scattering factors and so this relatively new technique has been compared to neutron reflectivity with the **same** Fe/Cr and Co/Ru multilayers, both grown at the second AF coupling peak. Although these techniques are described by what is, in essence, an identical set of equations, it is evident from these studies that neutrons and X-rays have very different degrees of sensitivity to the individual chemical and magnetic structural components within the sample. In this section we will attempt to highlight and discuss some of the discrepancies between the two techniques.

The first problem arises from an attempt to understand and explain the absence of an AF magnetic Bragg peak in the specular SoXMaS scatter for the Fe/Cr and Co/Ru multilayers. There is insufficient remnant field to produce any significant ferromagnetic alignment and there is ample evidence for AF coupling in the VSM data, as well as the reflectivity data from the longitudinal diffuse scans which show pronounced AF Bragg peaks. The question is compounded further through a direct comparison between the specular profiles seen for both the Fe/Cr (*Figure 6.15* and *Figure 6.18*) and Co/Ru (*Figure 6.24* and *Figure 6.27a*) multilayers using SoXMaS and PNR respectively. With the **same** set of samples, magnetic AF peaks missing from the SoXMaS data are present in the neutron scatter.

The most obvious explanation would be to assume the X-rays 'see' an extremely rough magnetic interface and so the X-rays scatter into the diffuse regime. This would suggest the magnetic roughness is far greater than the chemical roughness and the Fe/Cr and Co/Ru multilayers have significantly rougher magnetic interfaces in comparison with the Co/Cu multilayer. It would also suggest, with respect to the PNR data, that neutrons are less sensitive to magnetic disorder, indicating that the different magnetic interaction mechanisms for X-rays and neutrons are some how responsible for this discrepancy.

Another explanation is centred on the unknown scattering factors which we are attempting to define. It is possible that the relative ratio in scattering cross-sections between the magnetic and chemical components is not big enough to allow us to observe the magnetic Bragg peak from the standard charge scatter. Although PNR has a very similar scattering length for magnetic and atomic nuclear structure, it is possible that SoXMaS, despite being on resonance, still has a magnetic scattering component insufficient to compare with the charge. It must be remembered that the reflectivity profiles are all shown on log scales and so it would not take much distinction from the respective charge and magnetic signals for the larger of the two to dominant the overall scattering. In addition, the samples are relatively smooth, in terms of the chemical interface, which will promote greater charge scatter in the specular profile. This will reduce substantially the amount of diffuse charge scatter to a level comparable to the magnetic diffuse scatter, allowing for the possibility of observing off-specular magnetic AF Bragg peaks, such as those seen in the longitudinal diffuse data for the Fe/Cr (*Figure 6.15*) and Co/Ru (*Figure 6.24*) multilayered samples.

This hypothesis is also supported with the results obtained from the field experiments performed on the Co/Cu (*Figure 6.10*) and Co/Ru (*Figure 6.25*) samples. In both cases, the application of an external magnetic field had no affect on the reflectivity profiles (either specular or off-specular) other than at the magnetic Bragg peak scattering vectors. These peaks occur due to constructive interference from the magnetic super-structure. However, like charge scatter, there should also be a visible contribution (if the scattering factors for charge and magnetic scatter were comparable) to the rest of the specular scatter, with the probable exception of the chemical Bragg peak. In the following chapter a series of multilayer simulations describe the affect of changing the various magnetic parameters. These simulations suggest that a more comparable ratio in charge to magnetic scatter should result in the magnetic structure having a much greater affect on the reflectivity profiles.

To test further this premise, a series of calculations have been made under the Born approximation, to calculate the amount of magnetic roughness required to 'hide' the peak behind the charge scatter. To do this, the in-plane diffuse scans (across the magnetic AF Bragg peak) were integrated, with respect to q_x, to find I_{DIFF}. Using *Equation 5.4* and the assumption that I_{DIFF} remains constant, allowed I_{SPEC} to be calculated as a function of interface roughness. I_{DIFF} is small and so to a first order approximation this approach is valid. The specular FWHM σ (determined by the

instrument resolution) should also be constant and so with the result obtained from integrating a Gaussian (shown below) the height A of the magnetic Bragg peak can be determined.

$$I = A\sigma\sqrt{2\pi}$$

Equation 6.29

Through comparing these results with the charge scatter intensity at the appropriate scattering vector, it is possible to determine whether or not the magnetic peak is visible in the specular scatter. The results for the Fe/Cr multilayer AF Bragg peak analysis have been present below in *Figure 6.28*. Integrating the transverse diffuse data in *Figure 6.16a)* provided the height of the specular peak, which was then compared directly with the specular profile in *Figure 6.15* at q_z=0.12 Å^{-1}.

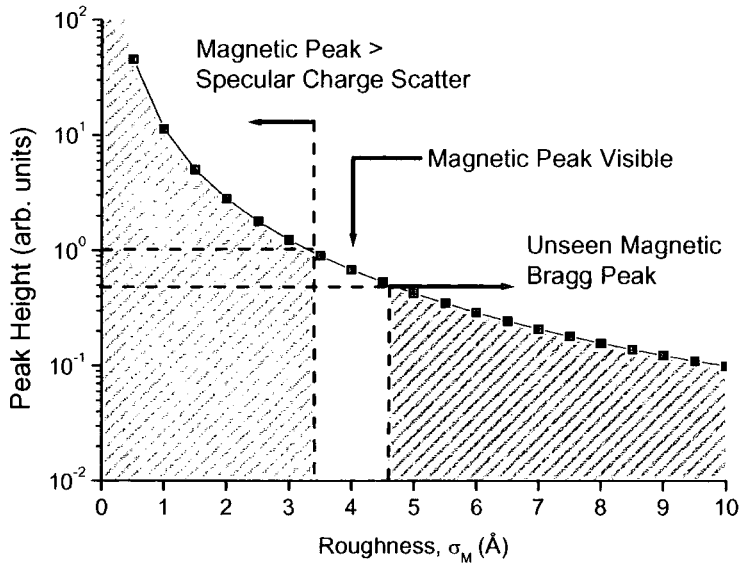

Figure 6.28: *Calculated peak height as a function of roughness using the Born approximation for the Fe/Cr multilayer.*

The AF Bragg peak should be visible with a magnetic roughness lower than 4.6 Å and would dominate the scatter if less than 3.3 Å. The PNR data suggested a roughness of σ_M=9 Å for the Fe/Cr magnetic interface, this level of disorder is much higher than the limit required for a visible AF Bragg peak. The same analysis performed on the Co/Ru multilayer (using *Figure 6.25* and the 3rd Order AF peak in *Figure 6.26b*) revealed a similar story, with the AF Bragg peak becoming visible at 7.8 Å and the magnetic scatter dominating at 6 Å. The Co/Cu multilayer grown at the 1st AF coupling

peak and shown in *Figure 6.9a)* revealed (with magnetisation along the easy axis) that even a roughness greater than 10 Å (the thickness of the layer) would be insufficient to diminish the magnetic Bragg peak from the chemical specular background. This would suggest the Co/Cu multilayer has a magnetic scattering contribution (in comparison to the Fe/Cr and Co/Ru systems) far more comparable to that of the charge.

A similar set of discrepancies is noted in the diffuse scatter through comparing reciprocal space maps for the Fe/Cr multilayer in *Figure 6.17b)* and *Figure 6.19b)* using SoXMaS and PNR respectively. These have been compared directly in *Figure 6.29*. Note that for the purposes of clarity they have been displayed using a different z-scale and colour scale.

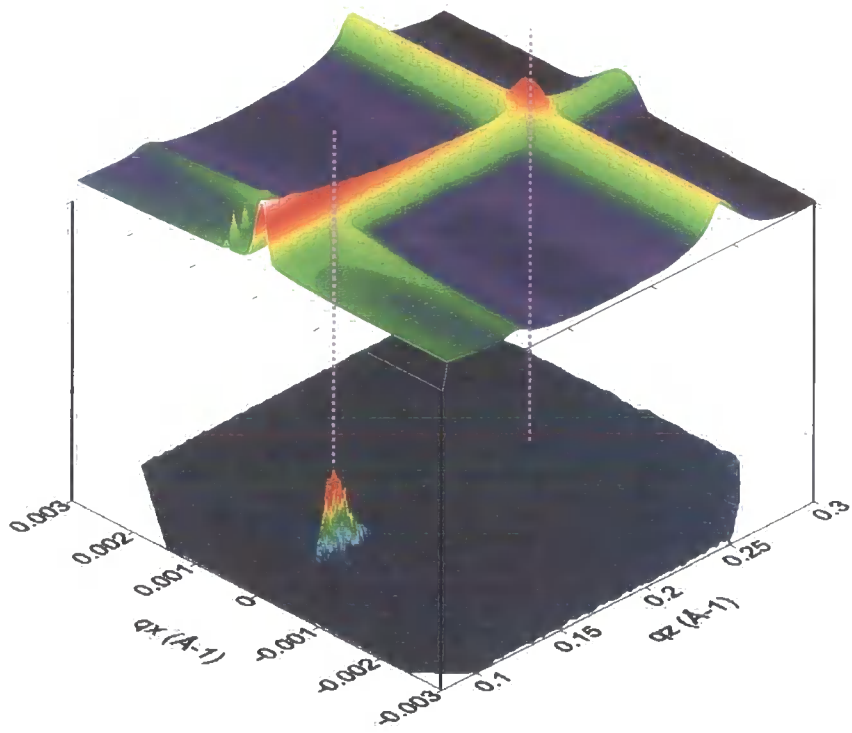

Figure 6.29: *A direct comparison between reciprocal space maps for the Fe/Cr multilayer using SoXMaS (Top - Figure 6.17b) and PNR (Bottom - Figure 6.19b).*

In the X-ray data there is a large amount of diffuse data surrounding the structural Bragg peak indicating conformal roughness, this scatter is absent in the neutron data. This could suggest SoXMaS, in comparison to neutrons, is more sensitive to chemical interface roughness. Born analysis (which is independent of the scattering cross-

sections) conducted on this weak neutron Bragg peak gave a value for the chemical roughness close to zero; this contradicts the average 4.8 Å gained from the fit shown in *Figure 6.12*.

One possible explanation concerning the different interaction mechanisms for X-ray and neutron scattering has been dismissed. X-rays (see *Chapter 2*) provide a measure of the electronic charge density distribution, where as neutrons (see *Section 6.4*) are sensitive to the positions of effectively point-like nuclei. An unrealistic difference between electron distribution and displaced nuclear positions would be required to differentiate between these techniques and this would require a complete breakdown in atomic structure.

The answer to the problem is found in addressing the signal to noise in the instrumental background. To prove this, the Born approximation was once again used to calculate the expected height of the diffuse peak in the PNR data. The chemical roughness obtain from the X-rays studies have provided a value of σ_C=4.8 Å, using this value with the integrated intensity from the neutron structural Bragg peak allowed the diffuse peak intensity to be calculated. The correlation length (and peak width) is known from the X-rays studies and so again using the integration result shown in *Equation 6.29*, the peak height was calculated at 1.6×10^{-9}. A quick comparison with *Figure 6.18* attests the diffuse scatter to be in the background noise, by three orders of magnitude! This analysis does assume we can see the complete specular peak, however, if the specular peak is partially hidden within the noise, then the diffuse peak must also be hidden.

Switching our focus now to the Fe/Cr AF Bragg peak, we note, using both techniques, a bar of strong diffuse scatter running in the q_x direction. This is characteristic of conformal roughness and since this peak arises entirely from magnetic structure, the associated disorder must also be magnetic in origin indicating conformal magnetic disorder at the interface or within the layers. The magnetic roughness, determined from the PNR diffuse map (*Figure 6.21*) with the Born approximation, was found at σ_M=9±1 Å. Of course, the magnetic roughness could only be determined from the neutron analysis since the specular peak is absent from the X-ray data (although from the analysis shown in *Figure 6.28*, suggest σ_M must be greater than 4.6 Å). So according to the PNR results the magnetic roughness is large, almost twice that of the chemical roughness; σ_C=4.8±0.5 Å. However, we must consider carefully what is meant

by magnetic roughness or magnetic disorder and what exactly is being measured during these experiments. The definition of magnetic disorder is considered more carefully in the following chapter, but in these experiments the 'magnetic roughness' is simply a parameter extracted from the relative amounts of diffuse and specular scatter. It is related to a length scale of disorder from within the reflection surfaces, however in the magnetic structure, interface topology, as well as interface anisotropies and domains, will contribute to this disorder. Indeed, the diffuse scatter in PNR is often attributed to magnetic domains and is explained through a vertically coherent domain structure, rather than correlation through magnetic interface structure. The large lateral coherence length of the beam (>30 μm) ensures the experiments will probe multiple magnetic domains.

The field dependence of the AF peak and its corresponding disorder can be seen in *Figure 6.21a)*. With increasing field, the diffuse scatter across the q_z range decreases with no observable increase around the chemical/ferromagnetic Bragg peak. This indicates disorder associated with AF domains and is in contrast to the results obtained by Takeda *et al.* [20] who observed in Fe/Cr multilayers a transfer of diffuse scatter from the AF Bragg peak, to the 1st order chemical/ferromagnetic Bragg peak upon application of a saturating field. Sinha [21] showed this was due to magnetic roughness at the interface and not from the domains.

However, domain structure can not easily explain the consistent peak shape recorded as a function of field around the AF peak, indicating that magnetic correlation lengths also remained constant. Domain alignment to form a single domain should extend the size of the domain and subsequently the correlation length, see *Figure 6.30*:

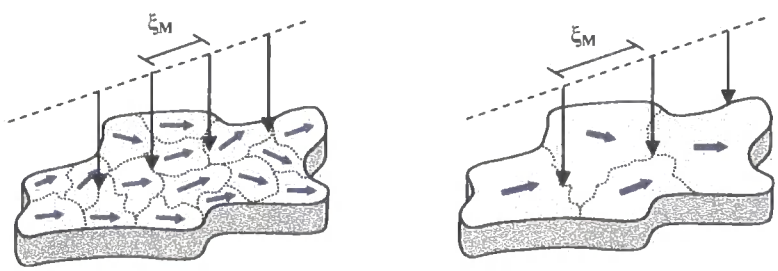

Figure 6.30: *Illustrating the extended correlation length as a function of domain size.*

Since no change in correlation length was recorded, this draws into question the validity of using the domain model to explain neutron diffuse scatter. However the model illustrated above may be a little simplistic. Let us consider the case where a number of domains are strongly pinned to the interface structure. The moments between magnetic layers will close with increasing field towards a parallel state, reducing the AF peak while increasing the chemical Bragg peak with a contribution from the ferromagnetic repeating structure. Once a saturating field is applied the ferromagnetic alignment between the Fe layers destroys the AF correlations and reduces the diffuse scatter around the AF Bragg peak. This idea has been illustrated below in *Figure 6.31*:

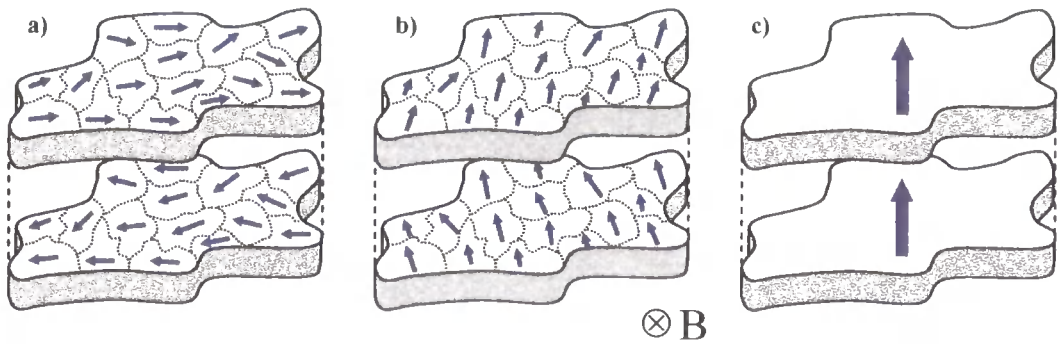

Figure 6.31: *Illustrating the layer switching under a magnetic field from an* ***a)*** *AF state to a* ***b)*** *near ferromagnetic one, with pinned domain structure, to a* ***c)*** *saturated state, as the external magnetic field is applied into the page.*

As demonstrated above, the changing magnetic diffuse scatter and associated correlation length with field can be explained by assuming the diffuse scatter originates from the domain structure. Nevertheless the magnetic interface structure should also be considered for which you would not expect any change in the correlation length as a function of field. You might also expect to find a relationship with the chemical in-plane correlation length but this does not appear to be the case.

In all of the multilayers studied, the in-plane magnetic correlation length is much greater compared with the chemical ($\xi_C << \xi_M$). Freeland *et al.* [22] reasoned this through assuming the in-plane correlation length ξ_C, provided a measure of grain size. If the magnetic coupling was independent of magnetic roughness, then the in-plane magnetic correlation length ξ_M should equal that of the grain size and ξ_C. However since the grains magnetically interact the magnetic in-plane length scales extend over a much greater distance.

For the Co/Cu system, ξ_M=880±20 Å and ξ_M=7000±100 Å depending on the magnetic anisotropy, compared with ξ_C=50±7 Å for the chemical. The Fe/Cr multilayer provided correlation lengths of ξ_C=114±9 Å obtained for the chemical structure and between ξ_M=390±20 Å (hard) and ξ_M=800±50 Å (easy) for the magnetic. It is also interesting to note that the magnetic in-plane length scale determined from the neutrons was much longer; ξ_M=2000±400 Å, an explanation for this difference will be discussed shortly. The Co/Ru multilayer followed a similar pattern providing correlation lengths of ξ_C=190±30 Å and ξ_C=170±30 Å at the 4th and 5th chemical peak. The magnetic correlation lengths were much longer compared to the chemical in-plane correlation lengths and even longer than the magnetic length scales obtained for the Co/Cu and Fe/Cr multilayer; ξ_M=18,500±2000 Å and ξ_M=24,000±2100 Å for 2nd and 3rd AF Bragg peaks respectively. These high in-plane correlation lengths may be related to the greater exchange coupling apparent from the lower remanence and the higher out-of-plane magnetic length scales. The two Co/Cu multilayers grown at the 1st and 2nd AF coupling peaks reveal out-of-plane magnetic correlation lengths of ζ_M=90±15 Å and ζ_M=50±10 Å respectively, the chemical out-of-plane correlation length remained constant at ζ_C=100±15 Å. The out-of-plane correlation lengths for the Fe/Cr multilayer were again comparable; ζ_C=114±9 Å and ζ_M=90±7 Å. The high exchange coupling in the Co/Ru multilayer (as previously mentioned) was apparent in the high out-of-plane magnetic length scales: ζ_M=660±35 Å, a property which may also be related to the increased chemical correlation length ζ_C=250±20 Å.

As discussed in *Appendix D*, the ability to measure correlation lengths depends not only on the FWHM, but perhaps more importantly on the line shape chosen. Diffuse peaks fitted to a Lorentzian with h=0.5 are inversely proportional to the HWHM. However if the peaks were fitted to a Gaussian line shape (h=1) the correlation length would increase by a factor of ~1.66. In fitting it is sometimes difficult to find one line shape in preference to another and for this reason it is sometimes useful to work with inverse length scales. Neutron diffuse studies are inherently difficult due to the low level of flux. The neutron transverse diffuse scan shown in *Figure 6.21* was initially fitted to a Lorentzian line shape to obtain a correlation length of ξ_M=2000±400 Å. However if this is fitted to a Gaussian (which is equally as valid) the correlation length would be ξ_M~3330 Å. Unfortunately due to the low flux there is no clear way in diffuse neutron studies to avoid this problem, this identifies perhaps one of the key advantages with using X-rays in the study of magnetic materials. The high flux available at

synchrotron facilities allows experimentalists to probe the diffuse scatter and the high signal to noise ratios result in clearly defined peaks. This makes any line fitting relatively easy, with the extraction of more accurate correlation length scales.

However, we now turn to the key disadvantage with this technique, a factor which PNR avoids through comparable scattering contributions from magnetic and chemical structure. The original objective of this combined X-ray and neutron study was to use the neutron magnetic scattering, with its well-known scattering cross-sections, to explore the nature of the scattering factors involved in the SoXMaS technique and take us a step further in its development and 'calibration'. AF coupled multilayers were analysed using linear σ-polarised light in order to provide a pure magnetic peak. Unfortunately this approach does not appear to be feasible due to unexpected differences in the relative amount of specular and diffuse scatter recorded using the two techniques, despite the fact that reflectivity was performed using the **same** samples.

The evidence suggests the problem originates due to differences between the charge and magnetic scatter. In the Fe/Cr and Co/Ru multilayers the charge scatter is dominant and thus envelops the magnetic signal from the specular profile making any quantitative analysis extremely difficult. PNR, used to compare the results obtained from the SoXMaS studies, revealed far more comparable magnetic and atomic contributions. This study therefore demonstrates that this is not a suitable strategy in 'calibrating' SoXMaS.

The issue concerning the origin of magnetic diffuse scatter (i.e. magnetic disorder) has not been resolved since the scattering effect of magnetic disorder, be it from domain disorder or roughness at the interface is identical. We note however, a large magnetic roughness in comparison to that of the chemical interface disorder and so speculate the possibility that magnetic roughness recorded in this study is a combination of both domain and interface disorder. The question will be addressed further in the following chapter.

6.10 References for Chapter 6

1. P.M. Platzman and N. Tzoar (1970) "*Magnetic Scattering of X Rays from Electrons in Molecules and Solids*" Phys. Rev. B **2** pg. 3556-3559.

2. F. de Bergevin and B. Brunel (1981) "*Diffraction by Magnetic Materials .I. General Formulas and Measurements on Ferromagnetic and Ferrimagnetic Compounds.*" Acta. Cryst. **A37** pg. 314-324.

3. J.P. Hannon, G.T. Tramwell, M. Blume, and D. Gibbs (1988) "*X-Ray Resonance Exchange Scattering*" Phys. Rev. Lett. **61** (10) pg. 1245-1248.

4. D. Gibbs, D.R. Harshman, E.D. Isaacs, D.B. McWhan, D. Mills, and C. Vettier (1988) "*Polarisation and Resonce Properties of Magnetic X-ray Scattering in Holmium*" Phys. Rev. Lett. **61** (10) pg. 1241-1244.

5. E.D. Isaacs, D.B. McWhan, C. Peters, G.E. Ice, D.P. Siddons, J.B. Hastings, C. Vettier, and O. Vogt (1989) "*X-ray resonance exchange scattering in UAs*" Phys. Rev. Lett. **62** pg. 1671-1674.

6. J.B. Kortright, D.D. Awschalom, J. Stohr, S.D. Bader, Y.U. Idzerda, S.S.P. Parkin, I.K. Schuller, and H.-C. Siegmann (1999) "*Research frontiers in magnetic materials at soft X-ray synchrotron radiation facilities (Topical Review)*" J. Magn. Magn. Mater. **207** pg. 7-44.

7. D. Mannix, A. Stunault, N. Bernhoeft, L. Paolasini, G.H. Lander, C. Vettier, F. de Bergevin, D. Kaczorowski, and A. Czopnik (2001) "*Resonant Enhancement at Nonmagnetic Ions: New Possibilities for Magentic X-ray Scattering*" Phys. Rev. Lett. **86** (18) pg. 4128-4131.

8. G.P. Felcher, R.O. Hilleke, R.K. Crawford, J. Haumann, R. Kleb, and G. Ostrowski (1986) "*Polarised Neutron Reflectometer: A new instrument to measure magnetic depth profiles*" Rev. Sci. Instrum **58** (4) pg. 609.

9. S. Langridge, J. Schmalian, C.H. Marrows, D.T. Dekadjevi, and B.J. Hickey (2000) "*Quantification of Magnetic Domain Disorder and Correlations in Antiferromagnetically Coupled Multilayers by Neutron Reflectometry*" Phys. Rev. Lett. **85** (23) pg. 4964-4967.

10. S.W. Lovesey and S.P. Collins (1996) "*X-ray Scattering and Absorption by Magnetic Materials*" Oxford Science Publications.

11. P. Carra and M. Altarelli (1990) "*Dichroism in the x-ray absorption spectra of magnetically ordered systems*" Phys. Rev. Lett. **64** pg. 1286-1288.

12. M. Blume (1985) "*Magnetic Scattering of X-rays*" J. Appl. Phys. **57** pg. 3615-3618.

13. M. Blume and D. Gibbs (1988) "*Polarization dependence of magnetic x-ray scattering*" Phys. Rev. B **37** pg. 1779-1789.

14. J.P. Hill and D.F. McMorrow (1996) "*X-ray Resonant Exchange Scattering: Polarisation Dependence and Correlation Function*" Acta. Cryst. **A52** pg. 236-244.

15. T.D. Cromer and D.A. Libermann (1981) "*Anomalous dispersion calculations near to and on the long-wavelength side of an absorption edge*" Acta. Cryst. **A37** pg. 267.

16. T.D. Cromer and D.A. Libermann (1970) "*Relativistic Calculation of Anomalous Scattering factors for X-Rays*" J. Chem. Phys. **53** pg. 1891-1898.

17. M.D. Roper and J.A. Purton (2001) "*Recent performance and developments on the Daresbury SRS soft X-ray undulator beamline*" Nucl. Instrum. Methods Phys. Res. Sect. **A467** pg. 516-519.

18. E. Balcar and S.W. Lovesey (1989) "*Theory of Magnetic Neutron and Photon Scattering*" Oxford Science Publications.

19. T.P.A. Hase, I. Pape, B.K. Tanner, H. Durr, E. Dudzik, G. van der Laan, C.H. Marrows, and B.J. Hickey (2000) "*Soft X-ray Resonant Magnetic Diffuse Scattering from Strongly Coupled Cu/Co Multilayers*" Phys. Rev. B **61** (6) pg. 3792-3795.

20. M. Takeda, Y. Endoh, A. Kamijo, and J. Mizuki (1998) "*Surface and interfacial magnetic diffuse scattering*" Physica B **248** pg. 14-24.

21. S.K. Sinha (1995) "*Neutron Scattering in Materials Science II*" Mat. Res. Soc. Symp. Proc. **376** pg. 175.

22. J.W. Freeland, K. Bussmann, Y.U. Idzerda, and C.-C. Kao (1999) "*Understanding correlations between chemical and magnetic interfacial roughness*" Phys. Rev. B **60** (14) pg. R9923-R9926.

Chapter 7

The Influence of Spin Orientation and Magnetic Disorder in SoXMaS Simulations and Measuring the Refractive Index of Co at Resonance

7.1 Introduction

In the previous chapter, Soft X-ray Magnetic Scattering (SoXMaS) reflectivity profiles were taken from a series of anti-ferromagnetic (AF) coupled multilayers. The aim was to determine information about the SoXMaS scattering factors and the relative contributions for charge and magnetic scatter. For comparison, Polarised Neutron Reflectivity (PNR) was therefore employed, with its well-known scattering factors, to attempt to 'calibrate' SoXMaS. Unfortunately vast differences between the techniques and their respective nuclear / charge and magnetic cross-sections made this impossible, with specular X-ray magnetic contributions only being visible through a Cu/Co AF Bragg peak.

In this chapter specular scattering reflectivity profiles from Cu/Co multilayers are examined in greater detail with a number of simulations which investigate how the reflectivity profile in SoXMaS is affected by changes to the magnetic structure. The following section explains the simulation theory, combining elements such as Parratt's formulism introduced in *Section 2.4.2*, with the scattering cross-section described in *Section 6.2*. Simulations are then presented to look at the affect of changing the

magnetic spin moment orientation between the coupled layers. These results are then explained by examining how the refractive index changes as a function of moment angle. Magnetic disorder is then introduced with the Born Approximation. The affect of interface magnetic roughness, dead layer thickness and domain effects are simulated and compared. With the inclusion of a routine employing a genetic algorithm, the simulation software is then used to fit SoXMaS data and the validity of the results are discussed.

The refractive index for Co under differing magnetic orientation is determined experimentally by measuring the Bragg peak as a function of energy across the Co L_{III} and L_{II} magnetic resonance edges. The real and imaginary scattering factors are thus calculated and compared using the Kramers-Kronig transforms. Finally the potential and some of the draw-backs to SoXMaS as a magnetic structural characterisation tool are discussed.

7.2 Simulation Theory

The fitting software presented in this chapter is designed to simulate the specular reflectivity profile for thin films and multilayer structures, both at and away from resonance with an X-ray energy ranging from hard energies greater than 12 keV down to soft energies lower than 100 eV. The simulations are achieved using Parratt's recursive formulism as initially presented in *Section 2.4.2* in combination with the calculated Fresnel coefficients shown in *Section 2.4*.

If we neglect roughness, then layer thickness and refractive index are the only parameters required to calculate the reflectivity. The refractive index is of course related to the scattering factors, see *Equation 2.11* for δ as a function of f_0 and f', and *Equation 2.12* for β as a function of f''. The magnetic resonance terms remain unknown for soft X-ray resonance energies, but their functionality with the magnitude and angle of moment have been determined and are presented in *Section 6.2* in the form of 2×2 matrices in a basis whose components are perpendicular and parallel to the scattering plane. These are labelled, by convention, as the σ and π polarisations respectively. The electric dipole transitions usually dominate the resonant magnetic cross-section and are the only transition to be considered here. The expression below has been derived from *Equation 6.12* and describes the magnetic scattering factor as a function of the incident scattering angle θ and average magnetisation vector. In this case we have also assumed

two dimensional in-plane magnetism in which $\mathbf{z}_3$ has been neglected and $\mathbf{z}_1$ and $\mathbf{z}_2$ have been expressed in terms of the magnitude of the moment M, and its angle θ_M.

$$f_{nE1}^{XRES} = F^{(0)}\begin{pmatrix} 1 & 0 \\ 0 & \cos 2\theta \end{pmatrix} - iF^{(1)}\begin{pmatrix} 0 & M\cos\theta_M \cos\theta \\ -M\cos\theta_M \cos\theta & -M\sin\theta_M \sin 2\theta \end{pmatrix}$$

$$+ F^{(2)}\begin{pmatrix} M^2\sin^2\theta_M & -M^2\sin\theta_M\cos\theta_M\sin\theta \\ M^2\sin\theta_M\cos\theta_M\sin\theta & -M^2\cos^2\theta_M\cos^2\theta\tan^2\theta \end{pmatrix}$$

Equation 7.1

The geometry, with respect to the incident beam has been expressed more explicitly in *Figure 7.1*:

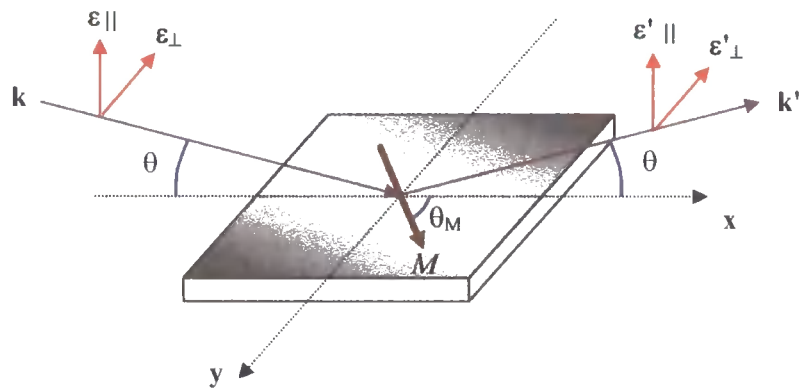

Figure 7.1: *Coordinate system with respect to the sample and magnetic moment.*

Although the refractive index is measurable, see *Section 7.5*, it is very difficult to measure the individual resonant magnetic scattering amplitudes (F_{LM}) which are required (with *Equation 6.9*) for the pre-factors ($F^{(0)}$, $F^{(1)}$ and $F^{(2)}$) in *Equation 7.1* and in the calculation of f_{nE1}^{XRES} as a function of the magnetic moment vector. However, as a starting point, resonance scattering amplitudes used in a series of calculations for magnetic resonance in Co (at the Co L_{III} edge) by Sinha *et al.* [1] are adopted. The normalised values are $F_{10} = 0$, $F_{11} = 12+6i$ and $F_{1-1} = 20-14i$.

The first and second terms of *Equation 7.1* dominate and so, combined with the normalised scattering factors given above, the magnitude of f_{nE1}^{XRES} under σ-polarisation is calculated as a function of the scattering angle θ, and the moment angle θ_M. The magnitude of M is set to unity.

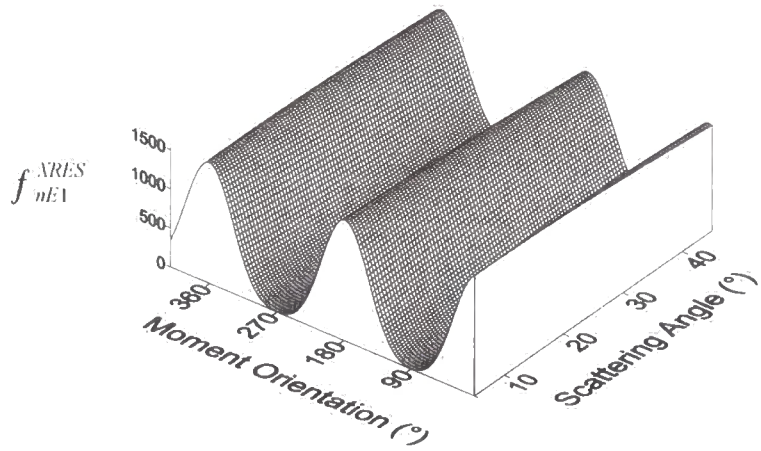

***Figure** 7.2: Magnetic resonance scattering factors (in arbitrary units) as a function of in-plane orientation and incident scattering angle.*

This figure demonstrates the magnetic sensitivity of this technique under σ-polarisation. Although there is little change to f_{nE1}^{XRES} with scattering angle, there is a strong dependence with the moment direction. *Figure 7.2* shows that SoXMaS with linearly σ-polarised light is not sensitive to components of magnetisation perpendicular to the beam.

In the next section SoXMaS simulations have been used to predict the reflectivity profile for a model Co/Cu multilayers (such as those presented in *Section 6.8.1*) using the resonant scattering amplitudes given above. Using *Equation 7.1*, the refractive index of Co (at the Co L_{III} edge) is calculated for all magnetic moment vectors at all scattering angles (due to the anisotropic nature of magnetic resonance scattering). The refractive index of Cu remains constant and has simply been calculated from the scattering factors obtained from the Henke tables. With the refractive index known, Parratt's formulism, as described in *Section 2.4*, is used to calculate the total reflectivity.

7.2.1 Angular Dependent Simulations

In order to study SoXMaS reflectivity and the angular dependence of its moment, a Co/Cu multilayer model has been used in simulating the reflectivity profile at various magnetisation vectors. The model chemical structure used in all simulations is $[Co(10\ Å)/Cu(10\ Å)]_{50}$ grown on SiO_2 with an interface width of 2 Å. A roughness

value of this magnitude is typical of the sputtered multilayers studied in the previous chapter. The magnitude of the moment has been set to unity with all domain and disorder effects neglected.

The first set of simulations present the SoXMaS reflectivity profile with in-plane moment rotation whilst maintaining 180 ° AF coupling. This effectively rotates the sample with respect to the beam as illustrated in the accompanying figure.

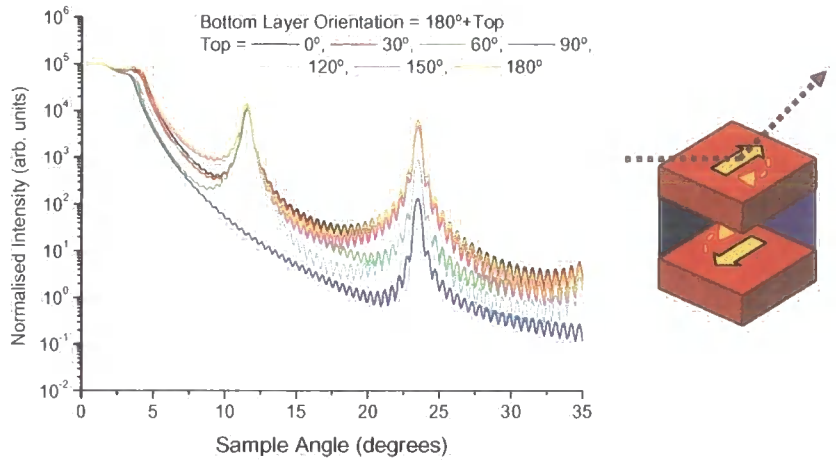

Figure 7.3: *SoXMaS simulations showing the affects of rotation with AF coupling maintained.*

For the most part, the simulations present a profile similar to that obtained experimentally and shown in *Figure 6.7*. Comparable magnetic and chemical Bragg peaks with the former situated at half q_z to that of the chemical peak. High frequency Kiessig fringes are also present from substrate / top surface interference. Our first observation notes very little change in the intensity of the AF Bragg peak as a function of moment orientation. In considering this, it is important to remember the origins of the AF Bragg peak; it is not a direct measurement of the average magnetic moment, or even the difference between the moments, but rather a difference between the complex refractive indices. In each case the moments are pointing in opposite directions producing refractive indices significantly different enough as to produce a clear AF Bragg peak. There is one exception, where moments are orientated at 90 ° and 270 ° to the beam, respectively. In this orientation the scattering factors, to first order approximation, lose all magnetic sensitivity as demonstrated in *Figure 7.2*. The layers are therefore left only with their charge contributions to the refractive indices which are

of course identical, removing any double periodicity in the multilayer structure and therefore the half-order Bragg peak.

Unlike the magnetic AF peak, there are observable changes to the chemical Bragg peak intensity. However it should be realised that this is due to the reflectivity background rather than any direct changes to constructive interference in the chemical structure. Since only the magnetic structure has been changed, the variation must come from changes in magnetic scattering. This makes an interesting observation when compared with *Figure 6.10* where no changes in reflectivity, other than at the AF Bragg peak, were recorded through changing the magnetic structure with applied field. This could indicate the scattering factors used in these simulations have a magnetic contribution much greater compared with the true scattering factors, in which the charge contribution is dominant.

The second set of simulations illustrate the affect of applying a magnetic field perpendicular to the beam direction and strong enough to swing the magnetic moments from their AF coupled state to ferromagnetic (FM) alignment. The simulations are shown below in *Figure 7.4*:

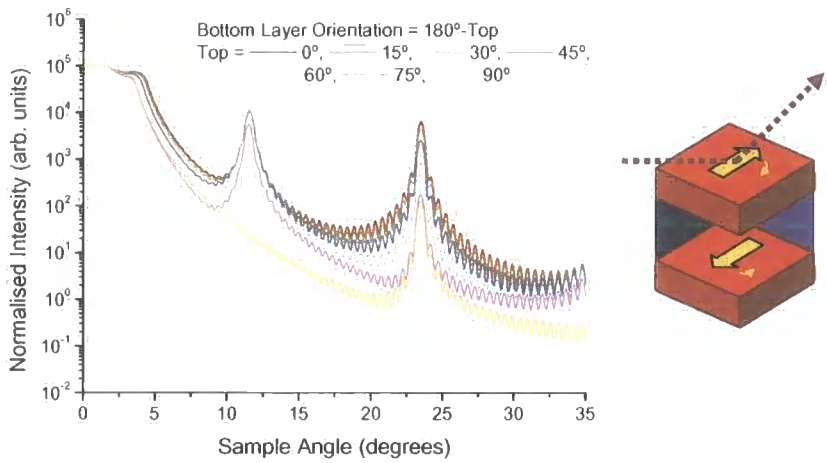

Figure 7.4: *SoXMaS simulations showing the affects of saturation perpendicular to the beam direction.*

Like the previous set of simulations, there is little change to the AF magnetic Bragg peak until the moments are at 75 ° and 105 ° respectively to the beam direction. Only at this point do the refractive indices between adjacent Co layers converge significantly enough to allow for observed changes to the magnetic peak intensity. This suggests

experimentally that the AF Bragg peak will only disappear under a strong saturating field with almost complete FM alignment. It also suggests a lack of sensitivity to moment orientation away from saturation, this is also demonstrated below in which a series of calculations were performed to find the AF peak height (normalised to a linear background and shown on a log scale in arbitrary units) as a function of both moment orientations with respect to each other.

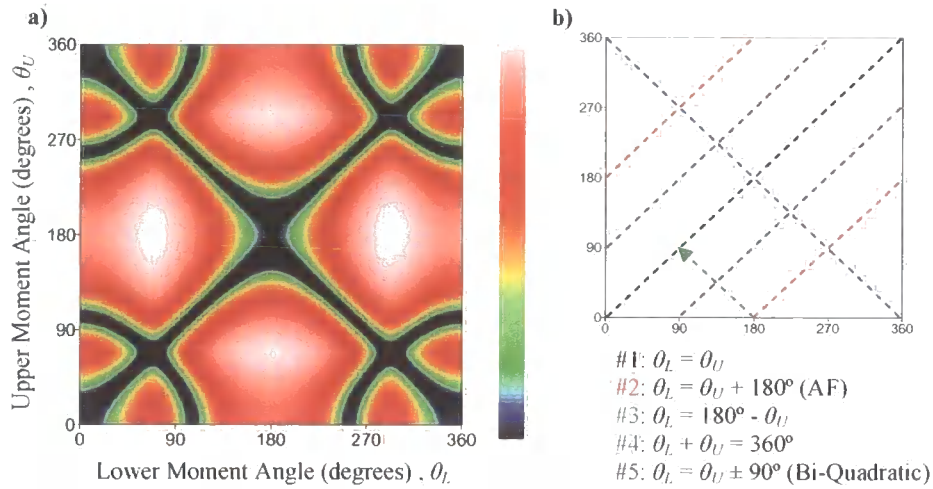

Figure 7.5: ***a)*** *Normalised AF peak height intensity (log scale) as a function of moment orientation with respect to the beam direction from adjacent upper and lower magnetic Co layers, with* ***b)*** *coupled scans of interest.*

Figure 7.5a) shows regions in which the AF Bragg peak intensity is at a maximum (white) and those regions in which the AF peak can not be seen (black), the most obvious of which is when the lower and upper moment orientations are equal (scan #1 FM coupling). Other examples of coupled moment scans are shown in *Figure 7.5b)* including those presented in *Figure 7.3* (scan #2 AF coupling) and *Figure 7.4* (scan #3 AF to FM). The map confirms the earlier observations in which we note a step-like function in AF peak intensity (see colour scale) around the regions where the refractive indices converge.

To a first order approximation, two-fold rotational symmetry exists due to similarities in refractive index where the moments from adjacent layers have equal components parallel to the beam, a fact highlighted from the minimal AF peak intensity found along scan #4. If we assumed perfect symmetry within the Co/Cu multilayer (i.e. ignoring the substrate and air mediums) the pattern would possess a four-fold symmetry with no difference between the upper and lower magnetic layers.

It is also interesting to note the maximum AF peak height, i.e. the greatest difference in refractive indices between the magnetic layers does not in fact occur with perfect AF coupling. This is due to the third term in *Equation 7.1* and understood more clearly by looking at the Argand diagram shown below, depicting the complex refractive index as a function of moment angle and magnitude.

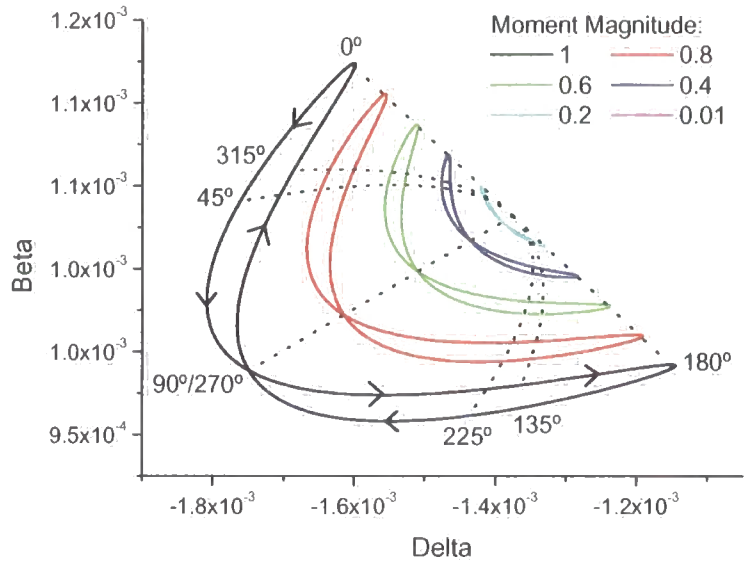

***Figure 7.6**: Calculated complex refractive index for Co as a function of moment orientation and magnitude.*

There is an intercept at 90 ° and 270 ° where the magnetic contribution coincides. If we neglect absorption effects then the difference in refractive index is depicted by the difference in delta i.e. the position along the x-axis, the largest difference therefore corresponds to respective moment orientations at 68 ° and 180 °, consistent with observations in *Figure 7.5*.

The functional variation of the magnetic peak with moment orientation can be used to explain the field dependence observed for the AF coupled Co/Cu multilayer, shown in *Figure 6.10*. The most probable explanation has been depicted below in *Figure 7.7* following the simulations shown in *Figure 7.8*:

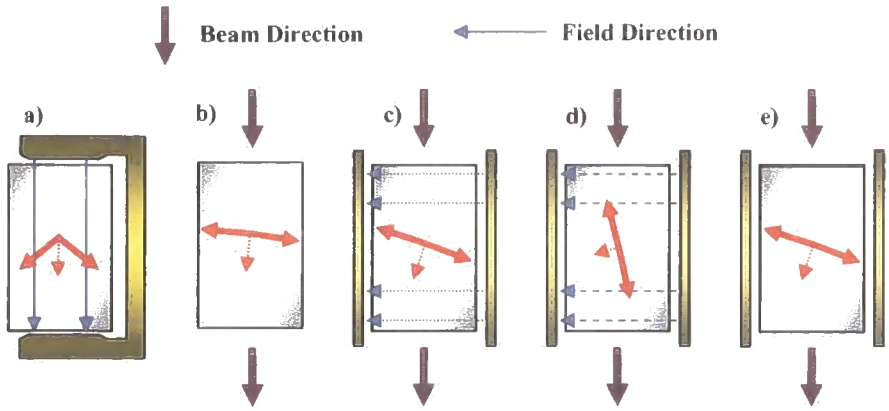

Figure 7.7: *Pictorial representation showing the magnetic moment orientation used to explain the results in Figure 6.10.*

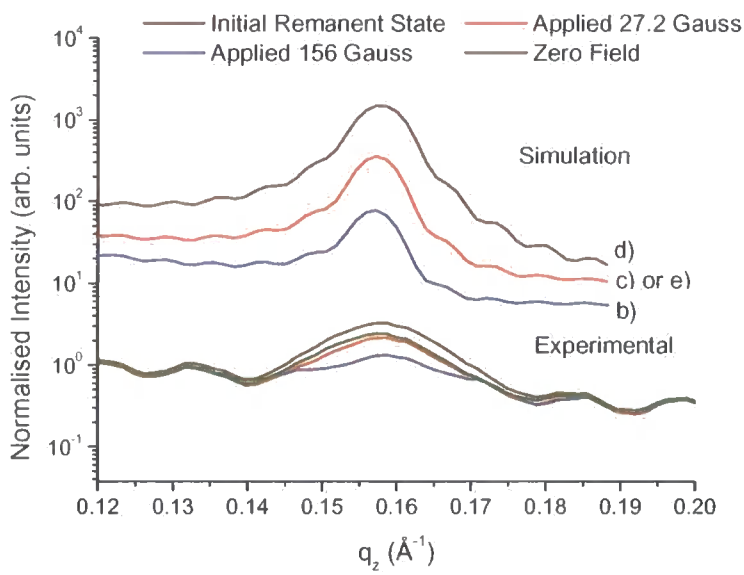

Figure 7.8: *Co/Cu multilayer simulations under different moment orientations (compared with the experimental data shown in Figure 6.10).*

Ex-situ magnetisation (seen in *a*) has sufficient field strength to rotate and partially align the moments ferromagnetically. Once the magnet has been removed the moments go back to AF alignment with a slight canting towards the easy axis. With an applied perpendicular field of increasing strength the moments rotate away from the 90 ° and 270 ° positions seen in *b)* and *c)* where there is little magnetisation sensitivity, towards *d)*, the 0 ° and 180 ° configuration. If the field could be increased further then the moments would begin to align ferromagnetically with a subsequent decrease in

magnetic Bragg peak intensity. Once the field was removed the moments relaxed (see *e*) back to position similar to *c)*.

Although the results can be explained in this way, it was observed in *Chapter 6* that magnetic forces can lead to a reduction in magnetic interface disorder. We have neglected any possible changes to magnetic disorder, such as interface roughness and domain disorder, factors which can heavily influence the reflectivity in the diffuse and specular regime. In the following section magnetic disorder, and the theory required to include its effects, are introduced with a similar range of simulations.

7.3 Magnetic Roughness

In normal X-ray scattering the affect of interface charge / chemical roughness was treated in *Section 2.7.1* using the Born approximation. Roughness was introduced, to the equation for specular scatter (*Equation 2.41*) via the Debye-Waller factor, $\exp(-q_z^2\sigma^2)$, thus reducing the reflected intensity. However, as we observed in the previous chapter, there is still a great deal of uncertainty concerning magnetic disorder. Its origin and variation with applied field are also unclear, since interface anisotropies as well as domain disorder will play crucial roles in determining the magnitude of the magnetic roughness.

Unlike its chemical analogy the magnetic roughness adds new dimensionality to the problem since moments are vector quantities which can introduce additional disorder in terms of magnitude as well as orientation. As seen in *Chapter 6*, there are clear differences between the chemical and magnetic interfaces. Evidence for this was first observed qualitatively with neutron scattering [2, 3] where the reflectivity damping was found to be smaller for the magnetic scatter in comparison to the atomic or chemical drop-off, indicating a smoother magnetic interface. As a consequence, an important issue is how the chemical and magnetic interfaces are correlated. Modelling this correlation can give insight into how the magnetic disorder is related to chemical structure and bulk magnetic properties.

It is important to consider how the magnetic energies affect the magnetic structure. On the one hand there are aligned moments within the bulk of the material whose orientation is determined by the exchange and anisotropy energies, but there are also dipolar energy contributions induced from magnetic disorder at the interface. This can

randomise spin moment directions at the expense of the exchange and anisotropic energies until the competing forces determine the lowest energy configuration. Therefore within this simple model; exchange strength, anisotropy and saturation moment play important roles in determining σ_M.

Freeland *et al.* [4] found a linear relationship between the magnetic and chemical roughness of $\sigma_M \approx 0.73\sigma_C$ in CoFe/Cu interfaces. They reasoned that, since charge disordered roughness at the interface was primarily topological rather than intermixing, very little quenching of the moments at the interface should occur and therefore disorder must originate from moment orientation. With roughness defined in these terms, aligned interfacial spins correspond to less disorder and lower roughness. A constant separation between the two in-plane correlation lengths was also noted, with the magnetic correlation lengths also being greater compared with the charge length scales. This is consistent with the work of Nelson *et al.* [5] and the results obtained in *Chapter 6* for the Co/Cu, Fe/Cr and Co/Ru multilayers.

Kelly *et al.* [6] have also compared the magnetic and chemical roughness in magnetic films and multilayers using a wide variety of different techniques. Their results confirm the above and support the concept of a magnetically dead layer present at the interface separating the chemical and magnetic interface. Magnetic measurements suggest as much as 10 % of the moments are 'lost' in the overall layer magnetisation.

7.3.1 Born Wave Approximation

Let us consider a single interface. Like charge scatter (see *Section 2.7.1*), the magnetic diffuse scattering calculations can also be performed using the Born approximation, following the work of Osgood *et al.* [7, 8]. Within this approximation the sample is treated as a perturbation, thus allowing the chemical and magnetic morphologies to be treated separately. Accordingly the sample can be divided into chemical and magnetic volumes, which are normally split by the presence of a magnetic dead layer. Through neglect of variations in charge and magnetism on an atomic scale we infer the electron number density n_C, and number density of magnetic atoms n_M, to be constant within their respective volumes. The dipole operator, as used in *Equation 6.8*, allows us to deduce the following matrix element for elastic scattering for an initial phonon state $(\mathbf{k}_i,\varepsilon)$ to a final state $(\mathbf{k}_f,\varepsilon')$:

$$\left\langle \mathbf{k}_f, \varepsilon' \middle| T \middle| \mathbf{k}_i, \varepsilon \right\rangle = -4\pi r_o n_C (\varepsilon' \cdot \varepsilon) \int_{V_{Chemical}} e^{-i\mathbf{q}.\mathbf{r}} d^3 r$$

$$-4\pi n_M \left[iA(\varepsilon' \times \varepsilon \cdot \mathbf{M}) \int_{V_{Magnetic}} \rho(\mathbf{r}) e^{-i\mathbf{q}.\mathbf{r}} d^3 r + B(\varepsilon' \cdot \mathbf{M})(\varepsilon \cdot \mathbf{M}) \int_{V_{Magnetic}} e^{-i\mathbf{q}.\mathbf{r}} d^3 r \right]$$

Equation 7.2

where A and B are factors which include the unknown scattering factors, $\mathbf{M}$ is the local magnetisation vector defined within a domain and $\mathbf{q}$ is simply the scattering vector ($=\mathbf{k_f}-\mathbf{k_i}$). Although the chemical and magnetic volumes overlap, their interfaces are generally considered separate due to the presence of a magnetic dead layer, see *Figure 7.9*. As a result, the integral of $e^{-i\mathbf{q}.\mathbf{r}}$ over the chemical and magnetic volumes is also different.

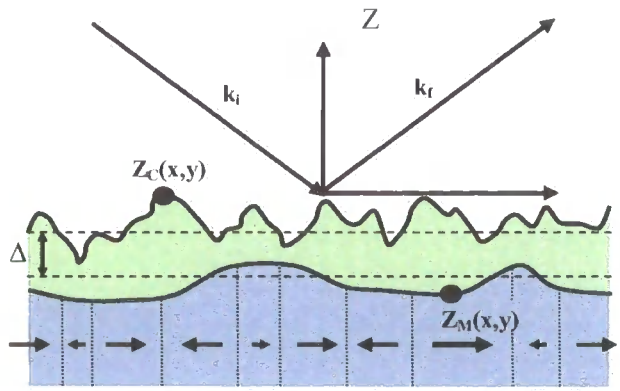

***Figure 7.9**: Diagram to show scattering off the chemical (charge) and magnetic structure across an interface with a magnetic dead layer Δ. Domain walls are shown normal to the average surface (dotted lines).*

Through further assuming domain walls aligned normal to the surface structure we can transform the volume integrals into surface integrals, thus allowing *Equation 7.2* to be expressed in terms of the magnetic domain function $p(x,y)$, defined on the surface, and the chemical $Z_C(x,y)$, and magnetic $Z_M(x,y)$, interface height functions:

$$\left\langle k_f, \varepsilon' \middle| T \middle| k_i, \varepsilon \right\rangle = -4\pi i r_o n_o (\varepsilon' \cdot \varepsilon) \left(\frac{1}{q_z} \right) \iint e^{-iq_z Z_C(x,y)} e^{-i\mathbf{q}\|.\mathbf{p}} dxdy$$

$$+4\pi n_M A(\varepsilon' \times \varepsilon \cdot \mathbf{M}) \left(\frac{1}{q_z} \right) \iint \rho(x,y) e^{-iq_z Z_M(x,y)} e^{-i\mathbf{q}\|.\mathbf{p}} dxdy$$

$$+4\pi i n_M B(\varepsilon' \cdot \mathbf{M})(\varepsilon \cdot \mathbf{M}) \left(\frac{1}{q_z} \right) \iint e^{-iq_z Z_M(x,y)} e^{-i\mathbf{q}\|.\mathbf{p}} dxdy$$

Equation 7.3

where $\mathbf{q}_{||}$, $\mathbf{p}$ are the in-plane components of $\mathbf{q}$ and $\mathbf{r}$. Using the same procedure as described in *Section 2.7.2*, the roughness fluctuations are treated as Gaussian random variables and, as before, we use the same self-affine fractal model as devised by Sinha *et al.* [9] to model both the chemical and magnetic interface:

$$C(X,Y) = \sigma^2 \exp\left(-R/\xi\right)^{2h}$$

Equation 7.4

where σ is the r.m.s roughness, ξ is the correlation length and h is the fractal parameter or roughness exponent. To model both interfaces we need three correlation functions C_{CC}, C_{MM} and C_{CM}, to model the chemical structure (chemical – chemical), magnetic structure (magnetic – magnetic) and a function to describe the correlation between the two (chemical – magnetic). Each has its own r.m.s. roughness parameter, although it can be shown [7] that $\sigma_{CM}^2 = \frac{1}{2}(\sigma_C^2 + \sigma_M^2)$. It has also been further assumed that $\xi_{CM}^2 = \frac{1}{2}(\xi_{CC}^2 + \xi_{MM}^2)$.

Using this approach to describe the height functions allows us to obtain the diffuse scattering cross-section (taking the modulus square of *Equation 7.2* and dividing it by $16\pi^2$):

$$\left.\frac{d\sigma}{d\Omega}\right|_{k_i\varepsilon\to k_f\varepsilon'}^{diffuse} = PS_{CC}(\mathbf{q}) + RS_{MM}^{(1)}(\mathbf{q}) + QS_{MM}(\mathbf{q}) + TS_{CM}(\mathbf{q}) + T^*S_{SM}^*(\mathbf{q})$$

Equation 7.5

S_{CC}, $S_{MM}^{(1)}$, S_{MM} and S_{CM} are defined in *Appendix F* and contain integrals over a surface area D to include information such as roughness and the correlation function. The functions also include the graded nature of the magnetic surface and the surface domain correlation, with $\langle\rho\rangle$ representing the global average of p(X,Y) over all domains. The prefactors P,R,Q and T are complex functions (also defined in *Appendix F*) which include the polarisation states and scattering factors. Since, by definition, the chosen correlation functions approach zero at large $\mathbf{R}$ then S_{CC}, $S_{MM}^{(1)}$, S_{MM} and S_{CM} approach terms proportional to $4\pi^2\delta(q_x)\delta(q_y)$, the delta functions conditional for the specular contribution. We therefore define the specular reflectivity in the Born approximation as:

$$|\mathbf{R}|^2_{\varepsilon\to\varepsilon'} = \frac{16\pi^2}{q_z^4}\left[\begin{array}{l} P\exp(-q_z^2\sigma_C^2)+(Q+R)\exp(-q_z^2\sigma_M^2)+ \\ (T\exp(iq_z\Delta)+T^*\exp(-iq_z\Delta))\exp(-\tfrac{1}{2}q_z^2(\sigma_C^2+\sigma_M^2)) \end{array}\right]$$

Equation 7.6

Like *Equation 2.41* the expression for reflectivity from a chemical and magnetic surface is reduced to that of a smooth surface with the addition of Debye-Waller factors to incorporate the roughness contributions: σ_C, σ_M and the magnetic dead layer Δ. The domains are described by a function $\rho(\mathbf{r})$ which ranges from 1 (for domains aligned parallel) to -1 (for anti-parallel alignment), $<\rho>$ is part of the function for T, simply setting $<\rho>$ and the domain correlation function $\gamma_M(x,y)$, to unity ignores the affect of domains.

Unfortunately with respect to the magnetic interface roughness, this theory only deals with scalar quantities i.e. it only considers spatial magnetic roughness $z_M(x,y)$ rather than orientational disorder from a distribution of spin-moment directions. It should be possible to extend the theory in the distorted wave Born approximation which will enable the interface moments to be modelled as a vectors, however the author is unaware of any such calculations at this time.

7.3.2 Magnetic Disorder Simulations

Previous discussion has realised that magnetic disorder comes in different forms, namely; magnetic roughness, dead layer thickness, domain structure and possible variations in average magnetic moment magnitude. The theoretical arguments relating to how these factors affect scattering have been examined above. This section presents a number of simulations to investigate the affect of different forms of magnetic disorder on SoXMaS specular reflectivity. All simulations are modelled on the Co/Cu multilayer with AF coupling at 0 ° and 180 ° for the bottom and top layer respectively.

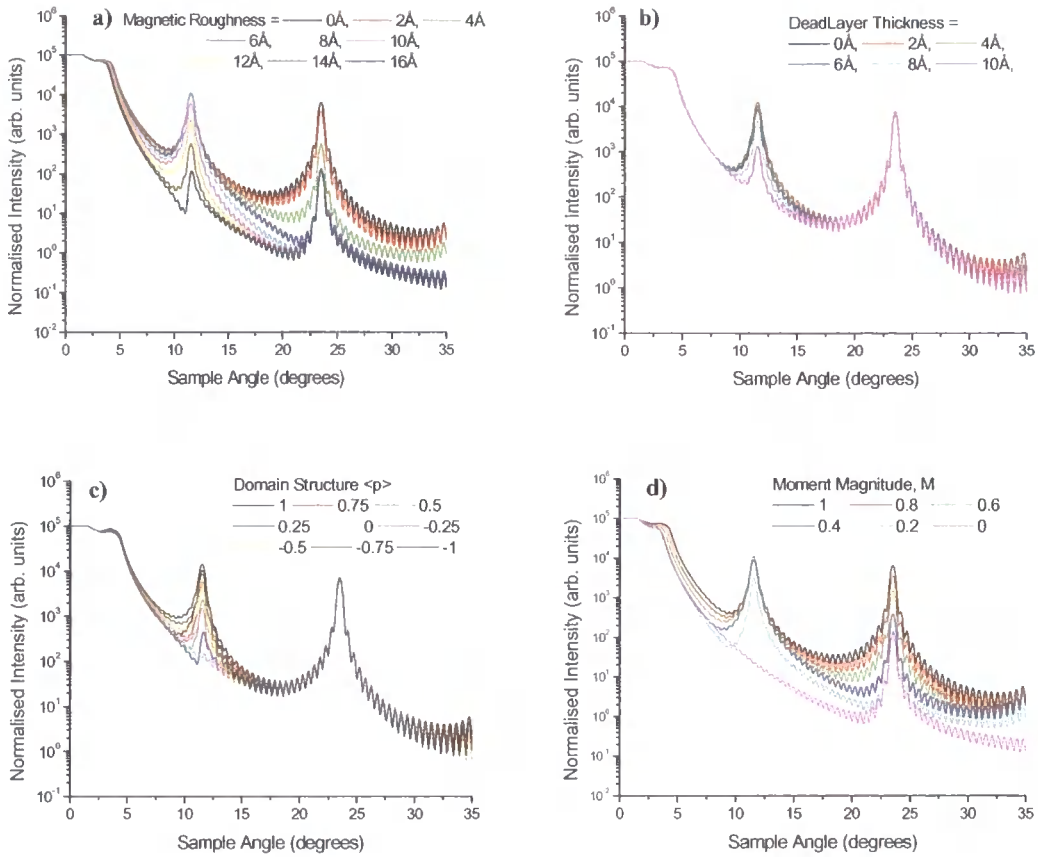

Figure 7.10: *SoXMaS simulations showing the effect on the reflectivity profile of different forms of magnetic disorder:* ***a)*** *interface roughness,* ***b)*** *dead layer thickness,* ***c)*** *domain structure and* ***d)*** *moment magnitude.*

It is clear from *Figure 7.10* that the different forms of magnetic disorder can have different or similar effects on the specular reflectivity. The first observation notes that dead layer thickness and domain disorder only affects the magnetic Bragg peak with little noticeable effects on the rest of the reflectivity profile. In the case of interface roughness and reduced moment magnitude there is not only a reduction in the AF peak, but a significant drop in the background reflectivity.

We have now touched on what is perhaps the biggest problem inherent to SoXMaS specular reflectivity as a characterisation tool for chemical and magnetic structure. Taking first the case of magnetic characterisation, we can see clearly that different forms of magnetic disorder can affect the reflectivity profile in very similar ways and so for example how can we differentiate between the dead layer thickness and domain structure? This also assumes the respective moment orientations are well known. The

chemical structure must also be considered, since this clearly plays a part in defining the specular profile. The following section will attempt to determine the chemical structure first through fitting off-resonance reflectivity and then through fixing those parameters, determine the magnetic structure from SoXMaS reflectivity.

7.4 Fitting Results

In order to fit experimental data, a genetic algorithm (similar to the one used in the *Bede REFS Mercury* code, see *Appendix C*) was written into the SoXMaS simulation software. The section demonstrates the fitting process for a Cu/Co multilayer, bi-quadratically coupled at 90 °. The nominal structure for this sample is $[Co(10\ Å)/Cu(10\ Å)]_{\times 50}$ grown on SiO_2.

The first step in the fitting process should be to fit the specular profile off-resonance and therefore determine the chemical structure. This was performed initially at a hard X-ray energy of 8.9 KeV, as shown in *Figure 7.11*, with the model structure shown in *Table 7.1*. The simulation not only provides a good fit to the data, but the model is also consistent for the reflectivity fit performed at 740 eV (off-resonance at soft energies) as shown. The second step involves fitting the magnetic structure; confident of the chemical structure, these parameters are fixed with only the magnetic parameters free to float. In the fitting routine domain effects have been neglected with $\langle\rho\rangle = 1$.

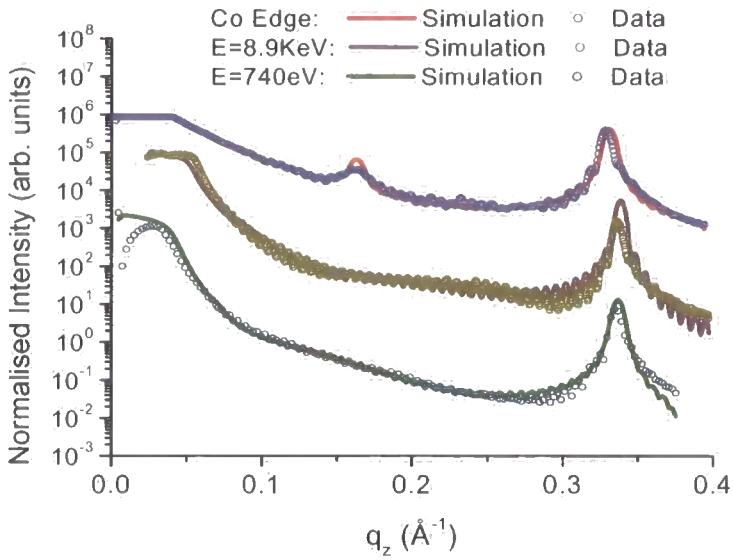

Figure 7.11: *Fits performed to a bi-quadratically coupled Co/Cu multilayer at various energies to determine the chemical and magnetic structure.*

Layer	Thickness (Å)	Roughness(Å)		Dead Layer Thickness (Å)	Spin-Moment		
		Chemical σ_C	Magnetic σ_M		Magnitude |M|	Angle (°)	
CuO	21.9	11.4	7.0	-	-	-	
CoO	**18**	**4.7**	**6.3**	**1.0**	**0.19**	**6.7**	
Cu	8.9	2.1	1.9	6.3	-	-	
Co	**9.9**	**2.5**	**3.9**	**6.3**	**0.1**	**149**	
Cu	8.9	2.1	0.1	1.3	-	-	×24
Co	**9.9**	**2.5**	**0.1**	**1.5**	**0.85**	**100**	
Cu	8.9	2.1	0.2	2.5	-	-	
Co	**9.9**	**2.5**	**0.2**	**2.3**	**0.85**	**6**	
Si	-	2.95	-	-	-		

Table 7.1: *Modelling parameters (chemical and magnetic) used to fit the specular profiles shown in Figure 7.11.*

With identical chemical parameters the simulations provide excellent fits to the experimental data, with magnetic parameters introduced to fit the SoXMaS reflectivity data at the Co L_{III} absorption edge. The layer thickness values are very close to nominal, with a chemical interface roughness of just over to 2 Å, typical for such sputtered

multilayers. The top layers show variation to the multilayer super-structure in both chemical and magnetic structure due to oxidation effects. Magnetic structure within the multilayer seems reasonable, not only do we find sensible values for the average moment magnitude (85 %) but the orientation is also consistent with bi-quadratic coupling. Dead layer thickness values are 1-2 Å, however, the magnitude of magnetic interface roughness is extremely low; 0.1-0.2 Å. Although the literature [4, 5] confirms a low magnetic roughness in comparison to the chemical, this does contradict the findings described in *Chapter 6* which suggest a far higher level of magnetic roughness σ_M~9 Å (correlated roughness) for magnetic disorder. However in these simulations we are neglecting domains which might have a far greater influence on the magnetic disorder.

The validity of these simulations and fits should now be addressed. For the simulations performed off-resonance, with a negligible magnetic contribution, the scattering factors are well known. The simulations shown in *Figure 7.11* provide excellent fits to the experimental data for both non-resonant energies; this indicates accurate fitting parameters for the chemical structure, close to nominal.

On resonance the magnetic structure must be included in the simulation model, with parameters that vary during the fitting routine to obtain the optimum fit. However as we have seen with the simulations shown earlier in *Section 7.3.2*, some magnetic structural variations produce similar or little change to the specular profile. Combined with the large number of magnetic variables, there is substantial uncertainty concerning the accuracy of the model.

Error will also come from the simulation model and the use of the Born approximation to simulate the magnetic disorder. Not only is the Born approximation invalid at low angles (see *Section 2.7.1*) but fails to include directional disorder from the interface moments. Recall that Freeland et al. [4] considered this form of interface disorder to be more prevalent in comparison to the moment's spatial and magnitude variation. Domain structure has also been neglected, a disorder parameter which may be more important than interface disorder [10].

A large contribution to the error comes from the unknown scattering factors with the magnetic contributions appearing to be too strong. In an attempt to compare the simulation scattering factors with experimental data, the follow section determines the

complex refractive index by examining the dependence of the Co/Cu Bragg peak with energy across the Co L_{III} and L_{II} magnetic resonance edge.

7.5 Determining the Optical Constants of Co

The large difference in ratio of magnetic to atomic scattering factors, between soft resonant X-rays and polarised neutrons (*Chapter 6*) has yielded invalid the idea of using PNR to determine the unknown scattering factors needed to develop SoXMaS further. Although the following technique does not actually find the individual scattering factors ($F^{(0)}$, $F^{(1)}$ and $F^{(2)}$) required to quantify the overall resonant magnetic scattering factor f_{nE1}^{XRES} (as a function of M the magnetisation, θ_M the in-plane moment orientation and θ the scattering angle), it can determine the refractive index with the optical parameters δ and β. This experiment will also test whether changes to the magnetic structure, as a result of an applied field, result in any observable changes to δ and β directly.

There are many techniques available which will measure the optical constants; reflectometry measurements [11] and Faraday rotation experiments [12] have been carried out, although few have been performed in the soft X-ray region since no simple crystal [13] provides diffraction data at this wavelength.

Although in principle it is relatively easy to conduct absorption experiments these will only determine the imaginary part β and such experiments are often influenced by saturation effects which strongly depend on the sample thickness [14]. This makes it very difficult to separate the characteristics of the element under investigation from those of the sample being studied. However from β it is then possible, in theory, to calculate the refractive term δ indirectly via the Kramers-Kronig relation (see *Section 7.5.3*), although this can be greatly affected by uncertain assumptions in assigning energy dependence far away from the resonance region.

In the remainder of this chapter the optical constants (both δ and β) of Co are obtained directly across the Co L_{III} and Co L_{II} absorption edges in an energy range between 680 and 880 eV. This is achieved through studying the Bragg peak from a Cu/Co multilayer grown at the Department of Physics at the University of Leeds, by d.c. magnetron sputtering with a base pressure of less than $2x10^{-8}$ Torr, on a standard silicon (100) wafer [15]. The nominal structure of the ferromagnetic multilayer is [Co(11 Å)/Cu(18.9 Å)] with 120 repeats. Such a structure provides an accessible Bragg

peak in the soft X-ray region with a ferromagnetic structure to ensure the refractive index within the magnetic layers remains constant throughout the multilayer, creating a ferromagnetic / chemical structure Bragg peak. The variable characteristics of this Bragg peak across resonance allows for the subsequent determination of both δ and β, or f' and f'', as desired.

In the following section the theory relating to the calculation of δ and β is discussed, followed by the experimental data obtained at the Co L_{III} and Co L_{II} absorption edges. These experiments are performed twice with the moments from the ferromagnetic layer aligned parallel (ex-situ magnetisation) and perpendicular (in-situ magnetisation) to the beam direction. The results obtained for the two orientations are compared directly and with the values obtained from the Henke tables. Finally the success and accuracy of this method is discussed, using the Kramers-Kronig and inverse Kramers-Kronig relations to check consistency between the results obtained.

7.5.1 Theory

7.5.1.1 Relation of δ to Bragg Peak Position

The dispersive part of the refractive index δ, will be discussed first and can be extracted quite simply from the angular position of the Bragg peak. The variation with energy is shown in *Figure 7.12* and its relation to δ found with the modified Bragg equation on accounting for refraction effects [11]:

$$\lambda = 2d((1-\delta)^2 - \cos^2\theta)^{1/2}$$

Equation 7.7

The absorption has been neglected since it appears only in the second order term and therefore *Equation 7.7* is simply rearranged to show the refraction term δ as a function of the position of the Bragg peak θ:

$$\delta = 1 - \sqrt{\left(\frac{\lambda}{2d}\right)^2 + \cos^2\theta}$$

Equation 7.8

This of course provides the average refraction index of the multilayer which is easily decomposed into its individual components of Co and Cu according to their relative concentrations within the sample:

$$\delta = \gamma\, \delta_{Co} + (1-\gamma)\, \delta_{Cu}$$

Equation 7.9

where:

$$\gamma = \frac{d_{Co}}{(d_{Co} + d_{Cu})}$$

Equation 7.10

The experimental results obtained for δ are presented in *Section 7.5.2.1.* f' can in turn be determined from δ using *Equation 2.11.*

7.5.1.2 Relation of β to Bragg Peak Width

In a similar manner the imaginary absorption part β is deduced from the full width at half maximum ω, of the Bragg peak for a given wavelength λ. The variable peak widths (also seen in *Figure 7.12*) follow the variance in average absorption coefficient.

In this case dynamical affects have been ignored since Bartels criterion [16] for dynamical calculations require a reflected intensity stronger than 10 % of the total reflectivity; the Bragg reflection observed here is less than 1 %. The kinematical calculations involved in obtaining the structural factors have been calculated by Séve *et al.* [11] and show the absorption part of the refractive index is simply proportional to the FWHM of the Bragg peak:

$$\beta = C\frac{\lambda\omega}{4\pi}$$

Equation 7.11

The peak width will also depend on a number of addition factors, such as instrument resolution and more importantly, variation in the bilayer repeat thickness. Since the latter is difficult to measure, the value of C has been calculated by rescaling the β profile to fit Henke's Co data at energies below and above the resonance edge where these factors should be accurate. To first order approximation this shift should eliminate

any resolution or variable bilayer thickness effects. Once again f'' can be calculated from β using *Equation 2.12*.

7.5.2 Experiment and Results

Experiments were performed on beamline 5U1 at the Daresbury SRS, as described in *Section 6.3*. A series of specular scans were performed over the Bragg peak as a function of energy over the absorption edges. This procedure was then repeated after magnetising the sample with sufficient field to rotate the moments through 90 °, perpendicular to the beam. *Figure 7.12* below demonstrates the large resonant variations in the Bragg peak parameters for a few different energies with moment magnetisation aligned parallel and perpendicular to the beam direction:

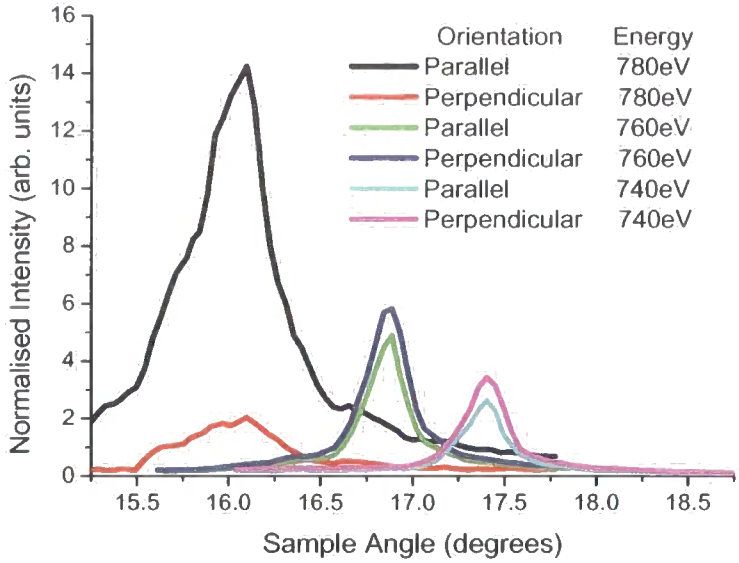

***Figure 7.12**: Bragg peak spectra from the Co/Cu multilayer measured at different incident X-ray energies with different moment orientations.*

After normalising the intensity to the beam monitor, a polynomial background was subtracted to remove the background reflectivity profile. All peaks have been fitted to Lorentzian line shapes.

The energy resolution is of course very important, as discussed in *Section 6.3* and varies with energy. An exiting slit size of 100 μm has been used with an energy FWHM resolution of ~0.4 eV at the resonance edges, small enough to be neglected and so we assume other errors dominate; such as the accuracy in fitting the peaks, as discussed for δ and β in the sections below.

7.5.2.1 Experimental Determination of δ

The theory in *Section 7.5.1.1*, showed clearly that δ is found from the Bragg peak position as a function of energy across resonance. This variation, in comparison to peak position as calculated from Bragg's law, for magnetisation parallel to beam direction is shown below in *Figure 7.13*:

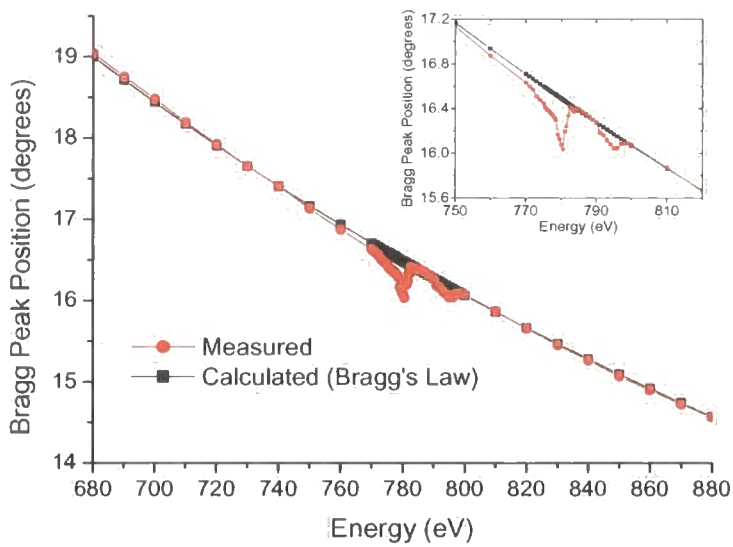

Figure 7.13: *Bragg peak position found experimentally (red) and with the uncorrected version of Bragg's law (black) as a function of energy across the Co L_{III} and L_{II} edges.*

The nominal structure used in calculating the Bragg peak position (black line) shown in *Figure 7.13* fits well off-resonance indicating a bilayer repeat thickness very close to nominal. Using *Equation 7.8*, the average sample value for δ has been calculated and shown below in *Figure 7.14* for the magnetisation orientation aligned *a)* parallel and *b)*

perpendicular to the beam direction. δ_{Co} has been deduced from *Equation 7.9* using the Henke values for δ_{Cu}, and a value of γ=0.37 (*Equation 7.10*).

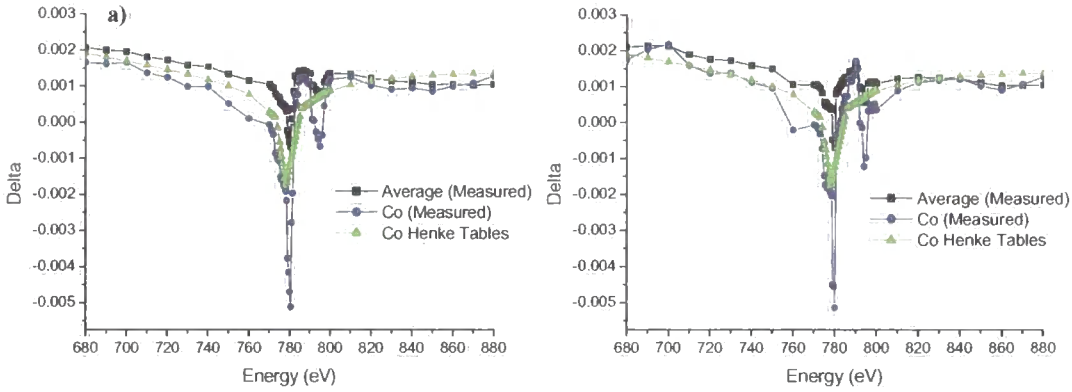

Figure 7.14: *Measured δ and calculated δ_{Co} (from δ_{Cu} obtained from the Henke tables) for the Co ferromagnetic layers aligned* ***a)*** *parallel and* ***b)*** *perpendicular to the beam direction. Henke values for δ_{Co} are also shown for comparison.*

The Henke values for δ are shown in green for Co, showing the affect of resonance. However, the measured values for δ_{Co} (as calculated from the average δ) are far more pronounced across the L_{III} and L_{II} demonstrating the inaccuracy of the Henke tables at resonance.

For a direct comparison, δ_{Co} for magnetisations both parallel and perpendicular to the incident beam have been plotted together in *Figure 7.15* . Error bars have been included, calculated from the uncertainties in Bragg peak position in the fitting procedure.

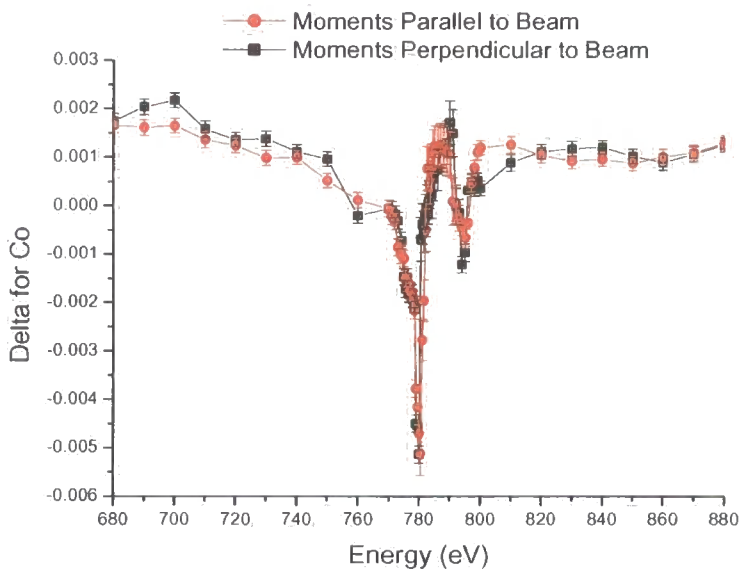

Figure 7.15: *δ_{Co} for moments alignment parallel and perpendicular to the beam direction.*

Within error, there is little difference in δ_{Co} between the two respective magnetisation directions. For comparison, the simulation software presented earlier was used, together with the scattering factors presented in *Section 7.2*, to calculate the form of delta as a function of moment angle with respect to the beam direction, and shown below in *Figure 7.16*.

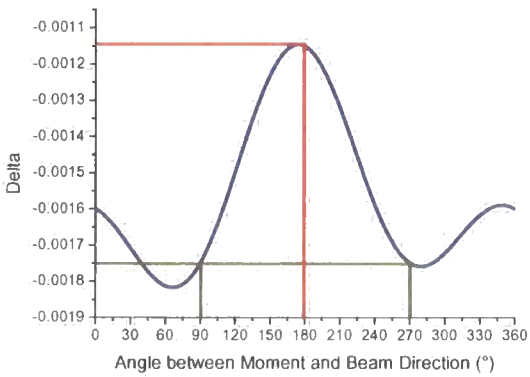

Figure 7.16: *δ_{Co} calculated (using the SoXMaS software) as a function of moment angle with respect to the beam direction.*

This plot also provides a comparison for the delta measured experimentally and the values used in the simulations, showing (although similar in magnitude) a discrepancy between the two values at resonance. *Figure 7.16* also indicates the kind of differences expected through sample rotation. A difference in δ_{Co} of approximately 1.5×10^{-4} is expected, between layers magnetised at 0 ° and 90 °, a value very much comparable to the experimental error in *Figure 7.15*. Therefore assuming the scattering factors used here are correct, it is not surprising that no difference in the δ

energy dependence is observable between magnetisation orientations. *Figure 7.16* also illustrates the identical scattering lengths observable with moments aligned either at 90 ° or 270 °, perpendicular to the beam, discussed in *Section 7.2*.

7.5.2.2 Experimental Determination of β

As explained in *Section 7.5.1.2*, β is proportional to the Bragg peak FWHM. This variation in energy across resonance is evident from the peaks shown in *Figure 7.12*. β measurements have been shown below as a function of energy for both magnetisation orientations:

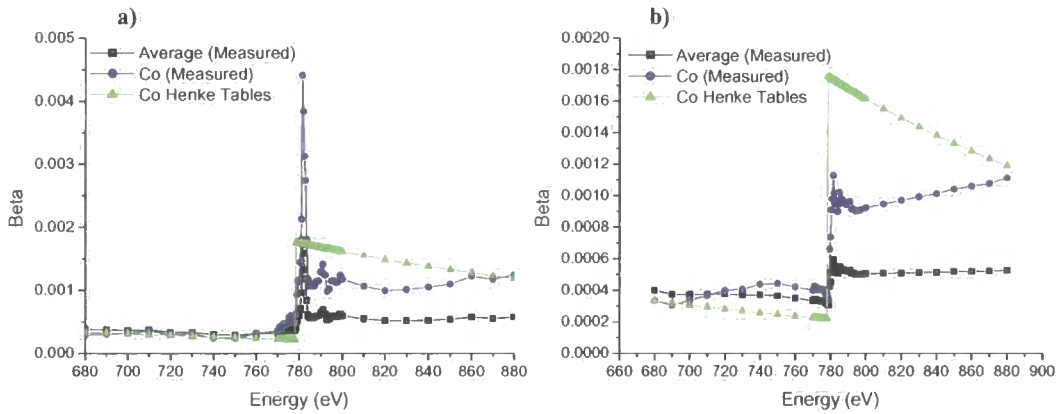

***Figure 7.17**: Measured β and calculated β_{Co} (from β_{Cu} obtained from the Henke tables) for the Co ferromagnetic layers aligned **a)** parallel and **b)** perpendicular to the beam direction. Henke values for β_{Co} are also shown for comparison.*

Once again the values for Co have been calculated from the measured sample average and using the values for Cu, obtained from the Henke tables. Comparison with β_{Co} values obtained from the Henke tables again demonstrate the inaccuracy of the Henke tables around the resonance edge. A direct comparison between the magnetisation orientations has been shown below with errors calculated from the fitting confidence.

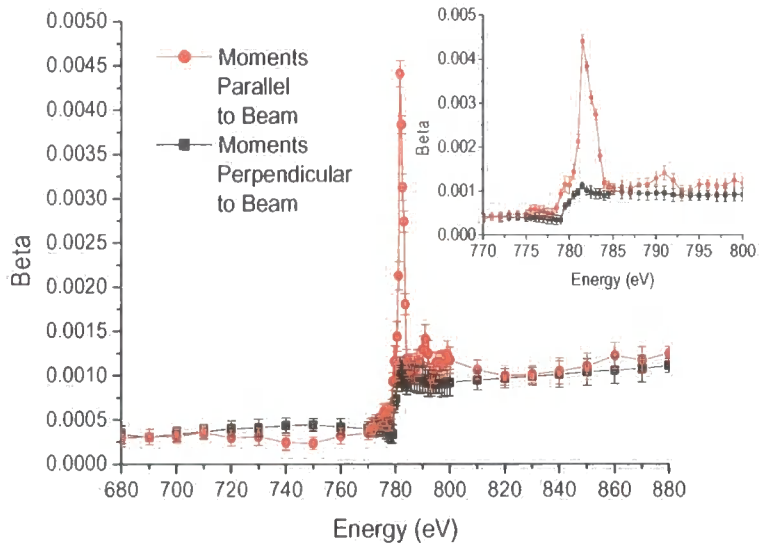

Figure 7.18: *β_{Co} for moments alignment parallel and perpendicular to the beam direction.*

Contrary to the similarity for δ_{Co}, observed between the two magnetisation orientations in *Figure 7.17*, there is a substantial difference observed here. The two absorption edges in β_{Co} are far more sharply defined when the moments are aligned parallel to the beam.

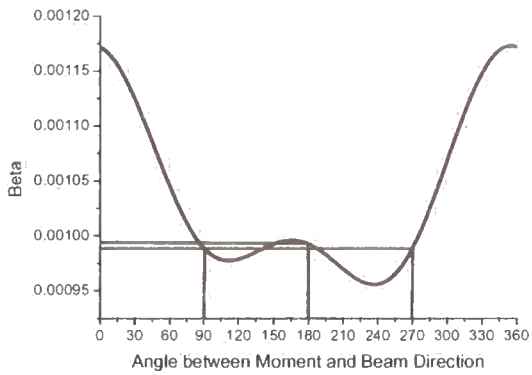

Figure 7.19: *β_{Co} calculated (using the SoXMaS software) as a function of moment angle with respect to the beam direction.*

The figure on the left has again been plotted using the SoXMaS software presented earlier. It shows β, as a function of magnetisation angle with respect to the beam. Unlike δ, as shown in *Figure 7.16*, there is a large change in β between 0 ° and 90 ° with respect to all possible orientations.

Upon 90 ° rotation of the spin moments with applied field, simulations suggest a change in β of approximately $\sim 1.8 \times 10^{-4}$, this value is again comparable to the error and therefore much smaller than the changes observable in *Figure 7.18*. This large discrepancy again draws into question the validity of the scattering factors used in the simulation software.

7.5.3 Comparing δ and β using Kramers-Kronig Transforms

In this section the Kramers-Kronig (KK) transforms are used to test the consistency between the values obtained for δ and β, and the validity of the two independent determinations. The KK and inverse KK transforms link f' and f'' via the following equations:

$$f'(E_o) = \left(\frac{2}{\pi}\right)\int_0^{+\infty} \frac{f''(E)E}{(E_o^2 - E)} dE$$

Equation 7.12

$$f''(E_o) = \left(\frac{2E_o}{\pi}\right)\int_0^{+\infty} \frac{f'(E)E}{(E_o^2 - E)} dE$$

Equation 7.13

These relations allow the real part of the response for a linear passive system to be determined if the imaginary part is already known over all frequencies. The KK transforms are basically Hilbert transforms which assume the system to be a collection of damped harmonic oscillators. For the derivation, the reader is referred to Kittel [17].

f' and f'' were calculated from δ and β using *Equation 2.11* and *Equation 2.12* respectively. The integrations were calculated by Neil Telling at Daresbury Laboratory over the full range of data taken. β was calculated from the inverse KK shown in *Equation 7.13* (for both magnetisations) using δ taken from *Figure 7.15*, and δ from β in *Figure 7.18* using the KK of *Equation 7.12*. Since the KK transforms really require full integration over all energies, the transform results near the edge of the data are meaningless and have therefore been ignored.

The results from all of the transforms are shown in *Figure 7.20* for magnetisation parallel and perpendicular to the incident beam:

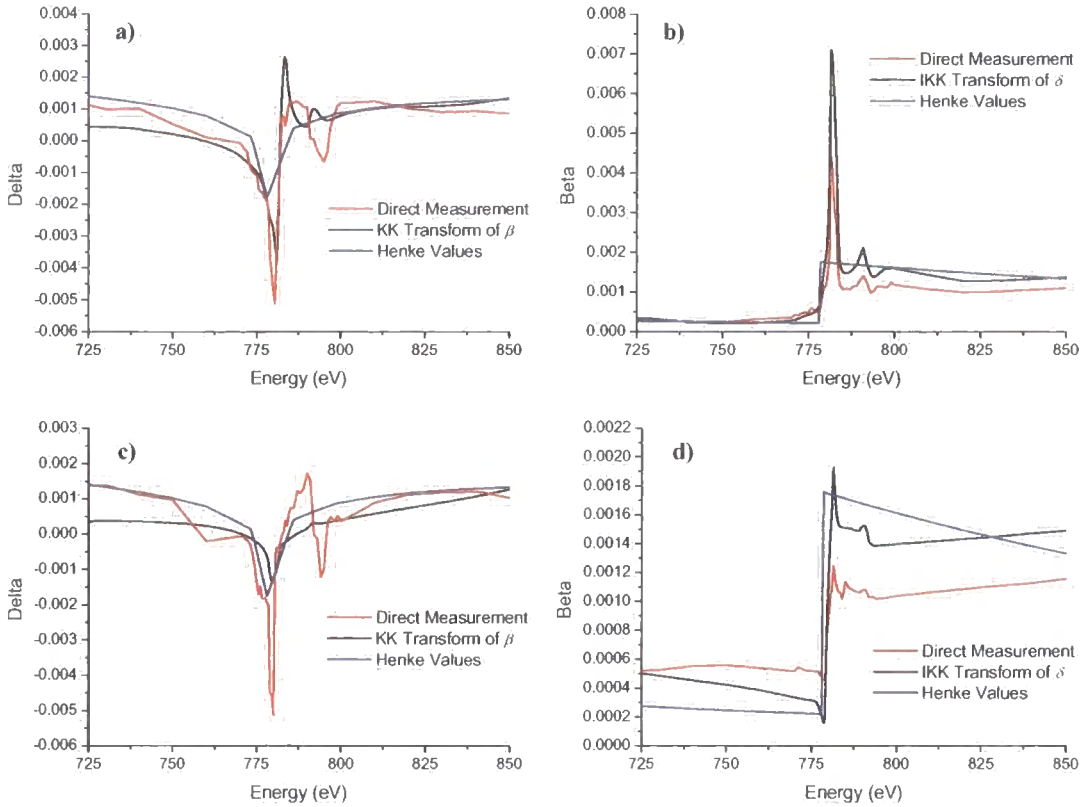

Figure 7.20: *Comparison between δ and ß, and their respective KK transforms for magnetisation parallel δ* ***a)*** *ß* ***b)*** *and perpendicular δ* ***c)*** *ß* ***d)***

Let us examine first the KK transforms (*Figure 7.20a)* and *c)*) to obtained δ and compare it with the direct experimental results gained from the Bragg peak position. Although the amplitudes are comparable, the general shape across the edge does not match. There is virtually no correspondence across the Co L_{II} edge and for the magnetisation aligned perpendicular in *c)* the KK result follows more closely the incorrect Henke values. This is quite surprising when we consider the similarity in line shapes shown for β from the inverse KK transforms shown in *Figure 7.20b)* and *d)*. Both transform and direct experimental data obtained from the peak widths provide similar profiles across both absorption edges; there is however a discrepancy between the amplitudes.

There are a number of errors which can explain the inconsistency between the experimental results and their respective transforms. Of course as already discussed, the largest experimental error is in the precision to which the Bragg peak is fitted. In most

cases this is reasonably satisfactory, although the Bragg peaks do reduce in intensity above the edge due to a loss of contrast between the Co and Cu atoms. This coincides with a rise in the reflectivity background. Both effects lead to a less accurate fit and subsequent determination of the peak position and FWHM. The possibility of growth dispersion (i.e. a variation in the repeater bilayer thickness) within the multilayer is considered since this will effectively broaden the peak. However, this effect is neglected since its energy dependence is linear.

There are also a number of difficulties associated with the integration calculation. The first of which is caused by the limited amount of data of which the integration is performed. In theory the Hilbert transformations should have the integration performed over infinity, this is of course impractical and so errors occur in the transform data edges. KK transforms are also particularly sensitive to noise within the data set, effecting the calculated line shape and magnitude.

7.6 Conclusions

In the chapter we have examined, using a number of simulations based on the Co/Cu multilayer, the affect of spin orientation and magnetic disorder. The theory relating to the SoXMaS simulations has been discussed in detail with respect to calculating the refractive index; a key parameter which varies as a function of moment angle with respect to the beam. Simulations show a step-like function in the magnitude of the magnetic peak since the difference in refractive index is sufficient to produce a strong magnetic Bragg peak unless the moments are almost ferromagnetically coupled. The function of magnetic peak intensity has been used to explain some experimental results concerning magnetic structural changes presented in the previous chapter.

Various forms of magnetic disorder were also a subject of discussion in the previous chapter and these have been discussed here in greater detail. The Born approximation has been used to analyse the affects of magnetic interface roughness, dead layer thickness and domain disorder, their affects on SoXMaS reflectivity shown in *Figure 7.10*. Although fits were made to actual experimental data, the similar effects of magnetic disorder, combined with the large number of variables draw into question the possible validity of using SoXMaS reflectivity in this way. The scattering factors used in these simulations are also questioned when we examine changes to the reflectivity profile as a function of magnetic structure. Experimental data shown in *Chapter 6*, show

only changes to the magnetic Bragg peaks i.e. positions in reciprocal space at which the magnetic scattering is the strongest. This suggests the scattering factors used in these simulations are wrong, with an overestimated value for the magnetic scattering cross-section.

The second part to this chapter determines the refractive index of Co from a ferromagnetically coupled Co/Cu multilayer (similar to that simulated) as a function of moment direction. The real and imaginary components of refractive index were determined by recording the specular Bragg peak across the CoL_{III} and L_{II} edge, and measuring the peak position and width respectively. The results confirm the true scattering factors are significantly different from those found in the Henke tables, which are inaccurate at resonance. We also find a profile similar to that determined for Fe by Mertins *et al.* [18]. Changes in refractive index from different layer magnetisation directions were small and only observed in the imaginary component. Finally the Kramers-Kronig transforms were performed to check for consistency between the values measured for δ and β. Unfortunately due to a number of factors (such as the limited energy range and noise) these transforms showed weak correlation to the counter imaginary or real component.

7.7 References for Chapter 7

1. S.A. Stepanov and S.K. Sinha (2000) "*X-ray resonant reflection from magnetic multilayer: Recurison matrix algorithm*" Phys. Rev. B **61** (22) pg. 15302-15311.

2. M.J. Pechan, J.F. Ankner, C.F. Majkrazk, D.M. Kelly, and I.K. Schuller (1994) "*Magnetic Profile as a function of Structural Disorder in Fe/Cr Superlattices*" J. Appl. Phys. **75** (10) pg. 6178-6180.

3. J.W. Cable, M.R. Khan, G.P. Felcher, and I.K. Schuller (1986) "*Macromagnetism and micromagnetism in Ni-Mo metallic superlattices*" Phys. Rev. B **34** pg. 1643.

4. J.W. Freeland, K. Bussmann, Y.U. Idzerda, and C.-C. Kao (1999) "*Understanding correlations between chemical and magnetic interfacial roughness*" Phys. Rev. B **60** (14) pg. R9923-R9926.

5. C.S. Nelson, G. Srajer, J.C. Lang, C.T. Venkataraman, S.K. Sinha, H. Hashizume, N. Ishimatsu, and N. Hosoito (1999) "*Charge-magnetic roughness correlations in an Fe/Gd multilayer*" Phys. Rev. B **60** (17) pg. 12234-12238.

6. J.J. Kelly, B.M. Barnes, F. Flack, D.P. Lagally, D.E. Savage, M. Friesen, and M.G. Lagally (2002) "*Comparison of magnetic- and chemical-boundary roughness in magnetic films and multilayers*" J. Appl. Phys. **91** (12) pg. 9978-9986.

7. R.M. Osgood, S.K. Sinha, J.W. Freeland, Y.U. Idzerda, and S.D. Bader (1999) "*X-ray scattering from magnetically and structural roughn surfaces*" J. Magn. Magn. Mater. **198-199** pg. 698-702.

8. R.M. Osgood, S.K. Sinha, J.W. Freeland, Y.U. Idzerda, and S.D. Bader (1999) "*X-ray scattering from magnetic, rough surfaces*" J. Appl. Phys. **85** (8) pg. 4619-4621.

9. S.K. Sinha, E.B. Sirota, S. Garoff, and H.B. Stanley (1988) "*X-ray and neutron scattering from rough surfaces*" Phys. Rev. B **38** (4) pg. 2297-2311.

10. S. Langridge, J. Schmalian, C.H. Marrows, D.T. Dekadjevi, and B.J. Hickey (2000) "*Quantification of Magnetic Domain Disorder and Correlations in Antiferromagnetically Coupled Multilayers by Neutron Reflectometry*" Phys. Rev. Lett. **85** (23) pg. 4964-4967.

11. L. Seve, J.M. Tonnerre, and D. Raoux (1998) "*Determination of the Anomalous Scattering Factors in the Soft X-ray Range using Diffraction from a Multilayer.*" J. Appl. Cryst. **31** pg. 700-707.

12. J.B. Kortright, M. Rice, and R. Carr (1995) "*Soft-x-ray Faraday rotation at Fe L2,3 edges*" Phys. Rev. B **51** pg. R10240-10243.

13. S.B. Wilkins, P.D. Hatton, M.D. Roper, D. Prabhakaran, and A.T. Boothroyd (2003) "*Soft X-Ray Resonant Magnetic Diffraction*" Phys. Rev. Lett. **90** pg. 187201.

14. J.B. Knotright and S.-K. Kim (2000) "*Resonant magneto-optical properties of Fe near its 2p levels: Measurement and applications*" Phys. Rev. B. **62** pg. 12216.

15. T.P.A. Hase, I. Pape, D.E. Read, B.K. Tanner, H. Durr, E. Dudzik, G. van der Laan, C.H. Marrows, and B.J. Hickey (2000) "*Soft x-ray magnetic scattering evidence for biquadratic coupling in Co/Cu multilayers*" Phys. Rev. B **61** (22) pg. 15331.

16. W.J. Bartels, J. Hornstra, and D.J.W. Lobeck (1986) "*X-ray Diffraction of Multilayers and Superlattices*" Acta. Cryst. **A42** pg. 539-545.

17. C. Kittel (1986) "*Introduction to Solid State Physics*" 6th Edition, Wiley & Sons.

18. H.-C. Mertins, O. Zaharko, A. Gaupp, F. Schafers, D. Abramsohn, and H. Grimmer (2002) "*Soft X-ray magneto-optical constants at the Fe 2p edge determined by Bragg scattering and Faraday effect.*" J. Magn. Magn. Mater. **240** pg. 451-453.

Chapter 8

Conclusions and Future Work

The impact of magnetic materials in society through technological and economic factors has been extensive, with the magnetic recording and storage industry growing larger each year. Development in growth techniques has led these materials to increasing complexity and therefore the need for more sophisticated experimental probes by which to characterise them. In this thesis, X-ray characterisation has been used not only in defining the chemical structure, but the magnetic as well, relating structural parameters to bulk magnetic and magneto-transport properties. This gains a more accurate definition of the sample, and aids in its development and physical understanding.

In this chapter the important results and conclusions are summarised, with respect to their contribution towards magnetic thin film characterisation and the development of evermore efficient magneto-resistive (MR) sensors. Suggestions for further work will also be proposed.

The first aim was concerned primarily with using X-ray techniques to discern correlation between MR and chemical structure. Grazing incident X-ray reflectivity (GIXR) studies, in both specular and diffuse regimes allowed parameters such as layer thickness, topological roughness and intermixing to be extracted.

This was demonstrated in *Chapter 3*, where a series of nominally identical spin valves were characterised. It was observed that MR varied as a function of NiO thickness, along with an increased interface width between the NiO layer and the Si substrate. Any change to the magnetic or chemical structure of the NiO pinning layer will affect its exchange coupling with the pinned magnetic layer, and subsequently the magnitude of MR. All other structural parameters showed no correlation with MR. The power of fluorescence was also demonstrated as a simple method by which to determine the relative concentrations of elements within the sample. By assuming Castaing's

approximation the thickness of the Cu spacer layer within the Co/Cu/Co trilayer was determined.

Magnetic Tunnel Junctions (MTJs) were the focus of *Chapter 4*, in which a series was studied as a function of barrier oxidation time. For an initial Al thickness of ~15 Å, an oxidation period of 3 minutes produced MTJs with the highest MR value. Under-oxidation can result in conductive regimes within the barrier with the possibility of pin-holes, and over-oxidation causes the lower magnetic layer to oxidise, affecting both chemical and magnetic structure. GIXR also indicates a substantial increase (almost a factor of 2) in barrier thickness with oxidation. This is inconsistent with the barrier thickness as derived from I(V) fits to the Simmons' model, due to localised tunnelling across the barrier. These regions of localised tunnelling occur due to defects and other fluctuations due to non-conformal roughness across the barrier.

An important area of study concerns the barrier oxidation, a process which is not fully understood. Further study is required in order to build a more accurate model of oxidation and the affect it has on the chemical and magnetic structural properties. The mechanism behind the increase in average barrier thickness should be addressed, as well as any affect on the interface. The affects of over-oxidation should also be investigated, unwanted oxidation of the lower magnetic layer can create an unwanted pseudo pinning-layer affecting magnetic structure and the magneto-transport properties.

MTJs are a rapidly progressive field of study, with their potential not restricted to simple magnetic sensors. Their use as Magnetic Tunnel Transistors (MTTs), used to inject a highly spin-polarised current into a semi-conductor with control over the spin-polarisation, is a key part of many spintronic devices.

One disadvantage of MTJs within industrial applications are their dramatic decrease in MR with bias voltage. A possible solution to this problem lies in the development of double tunnel junctions with the added advantage of increased spin polarisation. The increase in the number of layers means that growing pinhole-free barriers is more difficult and so accurate characterisation of the structure is needed to improve the accuracy and control of the growth procedure. The author in collaboration with colleagues at Exeter University intends to examine a series of double tunnel junctions with particular emphasis on the barrier structure.

The initial Al deposition process of MTJs was examined in *Chapter 5*, using specular and diffuse scattering methods to determine the level of intermixing at Al-transition metal interfaces. These were conducted for Al on X and X on Al, where X represents the transition metal from groups 4, 5 and 6 of the periodic table. Studies indicate a surprisingly large amount of intermixing which can not be explained or correlated through bulk diffusion parameters. In-plane diffraction data suggests grain boundary diffusion as a possible mechanism for such a large degree of mixing.

This investigation would benefit further with a more extensive study of in-plane grain size and its correlation with intermixing length. It might also be useful to examine this in a series of trilayer samples, possible buffers (prior to Al deposition) and their subsequent affect on Al grain size and the interdiffusion of X on Al. Again the affects of oxidation should also be explored, examining ways in which it affects interface structure, a key parameter in tunnel junctions. These samples are currently been examined using Transmission Electron Microscopy (TEM).

The second aim of the thesis was centred on the continued development of Soft X-ray Magnetic Scattering (SoXMaS) as a technique by which to measure the magnetic structure, in analogy to the chemical characterisation studies discussed earlier. SoXMaS techniques have received an increasing amount of attention over recent years with increasing development being made to the beamline facilities. The soft X-ray measurements made in this thesis were taken on station 5U1 at the Daresbury SRS. During the last few years the author has been involved in the upgrading of this facility, increasing the magnetic field available in-situ and the provision of liquid nitrogen cooling. Due to spatial constraints (with the diffractometer being under vacuum) further development is difficult. An obvious part of future work involves the development of a more adaptable in-vacuum diffractometer. A larger chamber could include additional motors such as a χ rotation to study parameters like in-plane magnetic anisotropy, and an increased magnetic field to study a wider range of magnetic materials.

The main disadvantage with SoXMaS comes with the fact that the scattering factors at magnetic resonance remain unknown. *Chapter 6* offered a comparison between SoXMaS and polarised neutron reflectivity (PNR) with the hope of using PNR (with its well known scattering factors) to affectively 'calibrate' SoXMaS. Unfortunately this

proved impossible due to vast differences between magnetic and chemical scattering contributions from the two techniques.

Further SoXMaS studies of the diffuse scatter did allow magnetic and chemical correlation length scales to be determined both in- and out-of-plane. This revealed magnetic length scales (in both geometries) large in comparison to the chemical length scales. Variations in out-of-plane magnetic length scales were also observed according to the magnitude of the exchange coupling. Similarly, a dependence on in-plane length scale (according to magnetic anisotropy) was observed with length scales being much larger for magnetisation along the easy axis. This type of measurement is very difficult to make using PNR due to limited flux in the diffuse scatter and the subsequent choice of correlation function.

The study of magnetic length scales (as well as chemical) is an important feature for many magnetic materials. There are a large number of potential experiments which would benefit from using SoXMaS in this way. Current and future experiments are particularly interested in correlating the magnetic to chemical correlation length scales within different materials. Changes in magnetic length scales can also be studied as a function of temperature, examining changes to in- and out-of-plane length correlation through ordering transition temperatures of AF coupled multilayers.

Chapter 7 presented a number of simulations to demonstrate the moment angular dependence on the magnetic Bragg peak intensity from the SoXMaS reflectivity. The Born approximation was also employed to look at the affect of various forms of magnetic disorder i.e. interface roughness, domain disorder, dead layer thickness and moment quenching. Similar affects on reflectivity due to different changes in magnetic structure indicate the impracticalities of SoXMaS to characterise, with great accuracy, the magnetic structure with magnetic multilayers.

Future theoretical work should include a fuller description concerning the affect of magnetic structure (and its different forms of disorder) on resonant X-ray scattering. The Born approximation is inaccurate around high levels of scattering at low angles and high intensity Bragg peaks. It also fails to account for directional inhomogeneity of moments at the interface, an important factor at the interface where moments are potentially disturbed due to interactions with chemical interface disorder. Further work should include an extension to the distorted wave Born approximation which will allow

interface moments to be modelled as vectors rather than scalar quantities. Simulation code to predict diffuse measurements would also be beneficial in determining magnetic and chemical structure.

The later half of the *Chapter 7* concerned the determination of the complex refractive index of Co across the Co L_{III} and L_{II} edges, in which relatively small variations were found under different magnetisation directions. Although there are a number of methods by which to determine the refractive index, a different approach is required if the individual factors within the dipole operator are to be found.

Appendix A: Thomson Scattering from an Electric Dipole

In this section the derivation of *Equation 2.2* is discussed in more detail under the dipole approximation. The aim is to evaluate the radiated electric field (from a dipole) at an observation point defined by **r**, see *Figure A.1*.

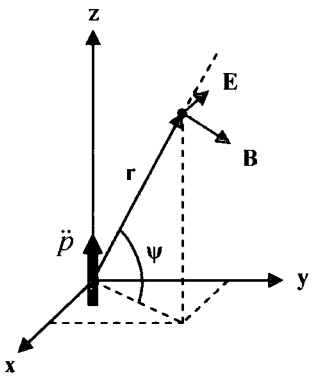

Figure A.1: *Electromagnetic wave (under the far-field limit) from a forced dipole oscillation at the origin.*

Under the dipole approximation we assume **r** >> dV, the spatial extent of the charge distribution. We further assume **r** >> λ, and the electrons are free.

The magnetic and electric fields can be derived from their vector potential:

$$\mathbf{B} = \nabla \times \mathbf{A} \qquad \textit{Equation A.1}$$

with the vector potential at **r** given by [i]:

$$A(\mathbf{r},t) = \frac{1}{c^2}\int_V \frac{J(\mathbf{r}',t-|\mathbf{r}-\mathbf{r}'|/c)}{|\mathbf{r}-\mathbf{r}'|}d\mathbf{r}'$$

Equation A.2

where $J(\mathbf{r}',t)$ is the current density of the source. Since, under the dipole approximation we assume **r** >> **r**':

$$A(\mathbf{r},t) = \frac{1}{c^2}\int_V \frac{J(\mathbf{r}',t-\mathbf{r}/c)}{\mathbf{r}}d\mathbf{r}'$$

Equation A.3

Given that $J=\rho v$, where ρ is the charge density and v the velocity, the current density can be re-written in terms of discrete charges q_i such that:

$$\int_V J d\mathbf{r}' = \int_V \rho v d\mathbf{r}' = \sum_i q_i v_i = \frac{d}{dt'}\sum_i q_i r_i' = \dot{\mathbf{p}}(t')$$

Equation A.4

where $\dot{\mathbf{p}}$ is the electric dipole moment. Assuming the beam is polarised along the z-axis:

$$A_z = \frac{\dot{\mathbf{p}}(t')}{c^2 r} \qquad A_x = A_y = 0 \qquad \textit{Equation A.5}$$

and therefore from *Equation A.1:*

---

[i] J. Als-Nielson and D. McMorrow (2001) "*Elements of Modern X-Ray Physics*." Wiley.

$$B_x = \frac{\partial \mathbf{A}_z}{\partial y} \qquad B_y = -\frac{\partial \mathbf{A}_z}{\partial y} \qquad B_z = 0$$

Equation A.6

For B_x we need to evaluate:

$$\frac{\partial A_z}{\partial y} = \frac{1}{c^2}\frac{\partial}{\partial y}\left(\frac{\dot{\mathbf{p}}(t')}{r}\right) = \frac{1}{c^2}\left[\frac{1}{r}\frac{\partial \dot{\mathbf{p}}(t')}{\partial y} - \frac{\dot{\mathbf{p}}(t')}{r^2}\frac{\partial r}{\partial y}\right]$$

Equation A.7

Since we are in the far-field limit we can ignore the second term from this derivative and using the fact:

$$\frac{\partial}{\partial y} = \frac{\partial}{\partial t'}\frac{\partial t'}{\partial y} = \frac{\partial}{\partial t'}\frac{\partial}{\partial y}\left(t - \frac{1}{c}\sqrt{x^2 + y^2 + z^2}\right) = -\frac{1}{c}\left(\frac{y}{r}\right)\frac{\partial}{\partial t'}$$

Equation A.8

we get:

$$B_x \approx -\frac{1}{c^3 r}\ddot{\mathbf{p}}_z(t')\left(\frac{y}{r}\right)$$

Equation A.9

By including B_y and B_z, *Equation A.9* is generalised to any direction of $\ddot{\mathbf{p}}(t')$:

$$B \approx \frac{1}{c^3 r}\ddot{\mathbf{p}}(t') \times \hat{\mathbf{r}} = \frac{1}{c^3 r}\ddot{\mathbf{p}}(t')\cos\psi$$

Equation A.10

where $\hat{\mathbf{r}}$ is the unit vector and ψ is the angle defined in *Figure A.1*. By solving the wave equations for **E** and **B**, we find $|\mathbf{E}| = c|\mathbf{B}|$ and therefore:

$$\mathbf{E}(\mathbf{r},t) = -\frac{1}{c^2 r}\ddot{\mathbf{p}}(t')\cos\psi$$

Equation A.11

$\ddot{\mathbf{p}}(t')$ must now be calculated in terms of the incident electric field which drives the dipole into oscillations. Assuming the polarisation is such that the maximum acceleration is observed, ψ=0°:

$$\ddot{\mathbf{p}}(t')\cos\psi = \ddot{\mathbf{p}} = q\ddot{\mathbf{z}} = q\frac{Force}{m} = q\frac{qE_{IN}}{m} = \frac{q^2}{m}E_o e^{-2\pi i(\omega t - \mathbf{k}\cdot\mathbf{r})}$$

Equation A.12

Inserting this into *Equation A.11* with q=-e provides the elastically (Thomson scattering) radiated field introduced in *Equation 2.2*:

$$E(\mathbf{r},t) = -\frac{e^2}{mc^2}\frac{E_o}{r}e^{2\pi i(\mathbf{k}\cdot\mathbf{r} - \omega t)} \qquad \textit{Equation A.13}$$

Appendix B: 3-Dimensional Scattering Vector

This section determines the 3D scattering vector, used in horizontal scattering. The incident wavevector $\mathbf{k}_{IN}$ is defined in the x-z plane with the exiting wavevector $\mathbf{k}_{OUT}$ scattering in x-z and y. The 3D matrix expressions are then reformulated back into the 2D equations presented in *Section 2.3*.

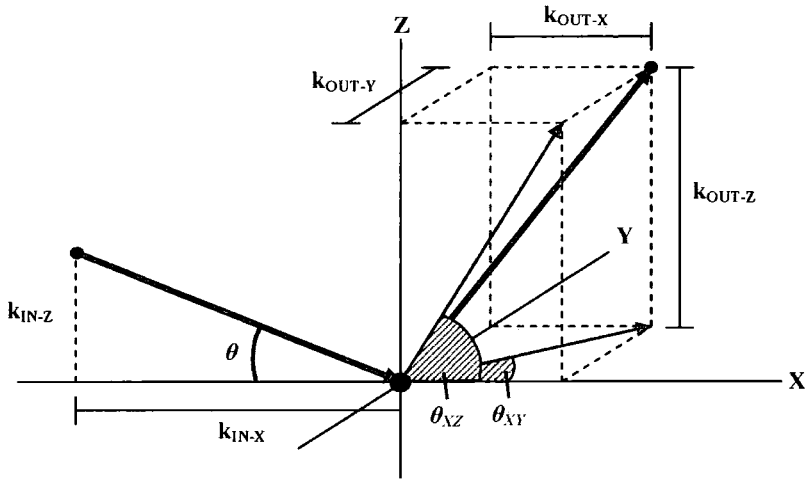

***Figure B.1**: 3D scattering vector coordinate system.*

The incident ($\mathbf{k}_{IN}$) and exiting ($\mathbf{k}_{OUT}$) wavevectors are defined from *Figure B.1* as follows:

$$\mathbf{k}_{IN} = \begin{vmatrix} k_{IN\text{-}X} \\ k_{IN\text{-}Y} \\ k_{IN\text{-}Z} \end{vmatrix} = |\mathbf{k}_{IN}| \begin{vmatrix} \cos\theta \\ 0 \\ -\sin\theta \end{vmatrix} \qquad \mathbf{k}_{OUT} = |\mathbf{k}_{OUT}| \begin{vmatrix} \cos\theta_{XZ}\cos\theta_{XY} \\ \cos\theta_{XZ}\sin\theta_{XY} \\ \sin\theta_{XZ}\cos\theta_{XY} \end{vmatrix}$$

Equation B.1

Assuming elastic scattering, the scattering vector is defined as:

$$\mathbf{q} = \mathbf{k}_{OUT} - \mathbf{k}_{IN} = \frac{2\pi}{\lambda} \begin{vmatrix} \cos\theta_{XZ}\cos\theta_{XY} - \cos\theta \\ \cos\theta_{XZ}\sin\theta_{XY} \\ \sin\theta_{XZ}\cos\theta_{XY} + \sin\theta \end{vmatrix}$$

Equation B.2

To return to the 2D formulism, we set $\theta_{XY} = 0$ and thus:

$$q_x = \frac{2\pi}{\lambda}(\cos\theta_{XZ} - \cos\theta) \qquad q_z = \frac{2\pi}{\lambda}(\sin\theta_{XZ} + \sin\theta)$$

Equation B.3

The equations are now re-written in terms of ϕ and γ, as defined in *Figure 2.2*. Using $\phi + 2(90-\theta) = 180$ as deduced from *Figure 2.2* and $\theta_{XZ} + \theta = \phi$ from *Figure B.1*:

$$\theta = \frac{\phi}{2} + \gamma \qquad \theta_{XZ} = \frac{\phi}{2} - \gamma \qquad \textit{Equation B.4}$$

Therefore:

$$q_x = \frac{2\pi}{\lambda}\left[\cos\left(\frac{\phi}{2} - \gamma\right) - \cos\left(\frac{\phi}{2} + \gamma\right)\right] \qquad \textit{Equation B.5}$$

Using the following trigonometric identity:

$$\cos(A\text{-}B) - \cos(A+B) = 2\sin A \sin B \qquad \textit{Equation B.6}$$

$$q_x = \frac{4\pi}{\lambda}\sin\frac{\phi}{2}\sin\gamma \qquad \textit{Equation B.7}$$

As seen in *Equation 2.29* and similarly for q_z:

$$q_z = \frac{2\pi}{\lambda}\left[\sin\left(\frac{\phi}{2} - \gamma\right) + \sin\left(\frac{\phi}{2} + \gamma\right)\right] \qquad \textit{Equation B.8}$$

$$\sin(A\text{–}B) + \sin(A+B) = 2\sin A\cos B \qquad \textit{Equation B.9}$$

$$q_z = \frac{4\pi}{\lambda}\sin\frac{\phi}{2}\cos\gamma \qquad \textit{Equation B.10}$$

For completeness $q^2 = q_x^2 + q_z^2$, and therefore we return to *Equation 2.9*:

$$q = \frac{4\pi}{\lambda}\sin\frac{\phi}{2}(\sin^2\gamma + \cos^2\gamma) = \frac{4\pi}{\lambda}\sin\frac{\phi}{2} \qquad \textit{Equation B.11}$$

Appendix C: Genetic Algorithms

There are usually multiple solutions to a single problem, the hard part is finding the best solution from among the others. The variable range of suitable solutions is called search (or state) space and each point within this space is defined by a cost or fitness according to the problem. The objective is to find that point in search space which provides the best solution. Such a task is relatively easy for few variables, but as the number of variables increases so does the complexity of search space. It is clear from *Figure C.1* that a fitting routine such as *downhill complex* could potentially (as shown) get 'stuck' in a *local minimum* resulting in a poor solution.

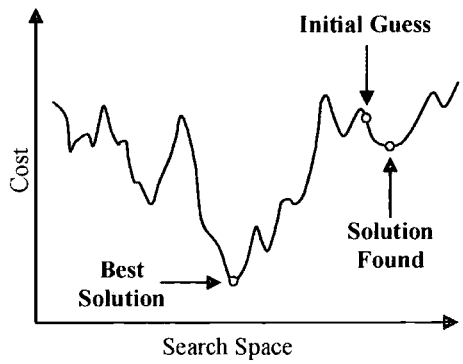

***Figure C.1**: Example of search space*

Genetic algorithms (GAs) were inspired by Darwin's theory of evolution with the solutions to the problem evolving! The algorithm will start with a set of solutions called a population, with each solution usually represented by a binary code (chromosomes). Solutions are then selected according to their suitability (fitness) to form a new generation.

The mating cross-over and mutation are the two most important parts of the GA, its performance is mainly influenced by these operations. After the 'parents' have been selected their binary codes are crossed-over at a random point, thus creating two new binary sequences and two new 'children' for the next generation. After the cross-over, mutation can take place changing 1 to 0 or 0 to 1. The probability of mutation should remain low, but it is important in preventing solutions from falling into local minima.

The basic procedure is outlined as follows:

1. **Start** – generate a random population of solutions.
2. Evaluate the **Fitness** of each solution (convert binary code to variables).
3. **Select** parents with probability according to fitness.
4. **Cross-over** chromosomes to produce children.
5. Allow the possibility of **Mutation** to occur at each position in the chromosome.
6. Repeat steps 3 to 5 until the next generation population is complete.
7. Go back to step 2.

Appendix D: Correlation Lengths

In *Section 2.7.2* correlation functions were introduced to describe the probability of position x being correlated with the origin at x=0. *Equation 2.38* was introduced to describe this function in terms of the exponent h and a correlation length ξ:

$$C(X,Y) = \sigma^2 \exp\left[-\left(\frac{(X,Y)}{\xi}\right)^{2h}\right] \qquad \textit{Equation D.1}$$

The correlation function can be measured directly in reciprocal space with its function related to the Fourier transform of *Equation D.1*. This section demonstrates the transform from real to reciprocal space and how the line shape and FWHM are directly related to the exponent h and correlation length ξ respectively.

Let us work on a simple 1D example, assuming the correlation length is an exponential decay and therefore we set h=0.5:

$$C(x) = \sigma^2 \exp\left[-x\xi^{-1}\right] \qquad \textit{Equation D.2}$$

By applying the Fourier transform:

$$C(q) = \int_{-\infty}^{\infty} C(x)\exp(iqx)dx = \sigma^2 \int_{-\infty}^{\infty} \exp\left[-x\xi^{-1}\right]\exp(iqx)dx \qquad \textit{Equation D.3}$$

Since the function is symmetrical:

$$C(q) = \sigma^2 \int_{-\infty}^{\infty} \exp\left[-x\xi^{-1}\right]\cos(qx)dx \qquad \textit{Equation D.4}$$

$$C(q) = \sigma^2 \,\mathrm{Re} \int_{0}^{\infty} \exp\left[\left(-\xi^{-1} + iq\right)x\right]dx \qquad \textit{Equation D.5}$$

Evaluation of the integral gives:

$$C(q) = \sigma^2 \,\mathrm{Re}\left[\frac{1}{(iq-\xi^{-1})}\left[\exp(iq-\xi^{-1})x\right]_0^{\infty}\right] \qquad \textit{Equation D.6}$$

$$C(q) = \sigma^2 \,\mathrm{Re}\left[\frac{\xi^{-1} + iq}{\xi^{-2} + q^2}\right] = \frac{\sigma^2 \xi^{-1}}{\xi^{-2} + q^2} \qquad \textit{Equation D.7}$$

The function shown in *Equation D.7* is a Lorentzian, centred at q=0 with a peak height of $\sigma^2\xi$. A simple calculation reveals the FWHM is inversely proportional to the correlation length:

$$\Delta q_{FWHM} = \frac{2}{\xi} \qquad \textit{Equation D.8}$$

This demonstrates the reciprocal nature between real and reciprocal space, and the relationship which allows correlation length scales to be calculated from scattering. In a very similar manner it can be shown the Fourier transforms of *Equation D.1* with h=1, results in a Gaussian line-shape with:

$$\Delta q_{FWHM} = \frac{4\sqrt{\ln 2}}{\xi} \qquad \textit{Equation D.9}$$

For other correlation functions, the Fourier transform functions are far more complex, with different values relating Δq_{FHWM} to the inverse correlation length ξ^{-1}. For more information see [ii,iii].

[ii] J. Als-Nielson and D. McMorrow (2001) "*Elements of Modern X-Ray Physics.*" Wiley.

[iii] T.P.A. Hase, S.B. Wilkins and I.G. Hughes (2003) *To be Submitted.*

Appendix E: Al/X and X/Al Specular Profiles

This section presents the remaining specular profiles (with fit) for bilayers presented in the intermixing study made in *Chapter 5* and displayed in *Table 5.9*.

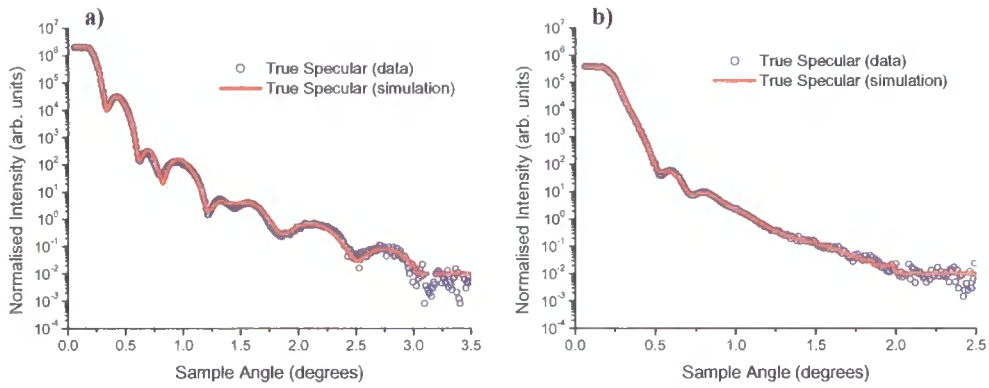

Figure D.1: *Specular profile for bilayers with nominal structure* ***a)*** *SiO_2/Ti(50Å)/Al(50Å) and* ***b)*** *SiO_2/Al(50Å)/Ti(50Å).*

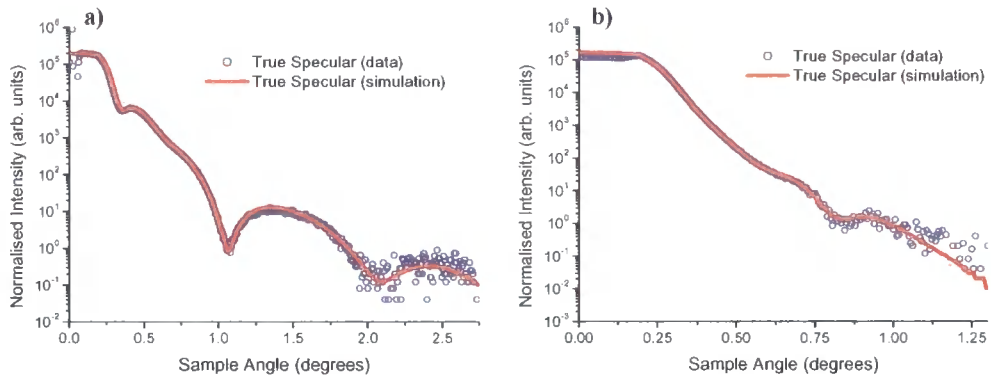

Figure D.2: *Specular profile for bilayers with nominal structure* ***a)*** *SiO_2/V(50Å)/Al(50Å) and* ***b)*** *SiO_2/Al(50Å)/V(50Å).*

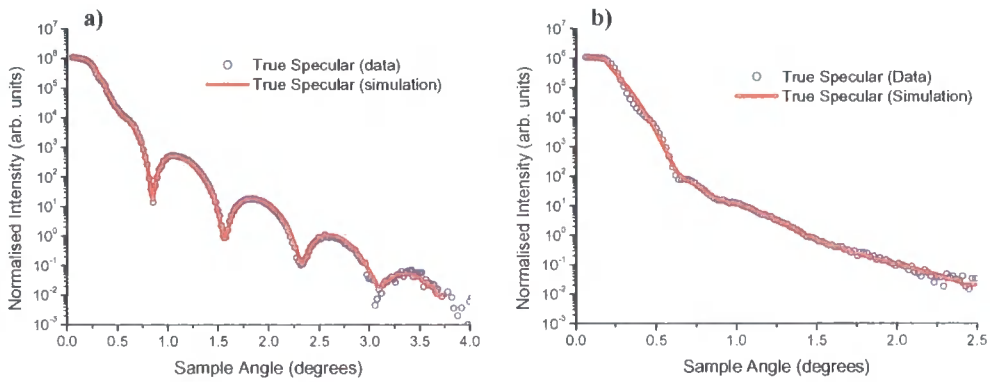

Figure D.3: *Specular profile for bilayers with nominal structure* ***a)*** *SiO_2/Cr(50Å)/Al(50Å) and* ***b)*** *SiO_2/Al(50Å)/Cr(50Å).*

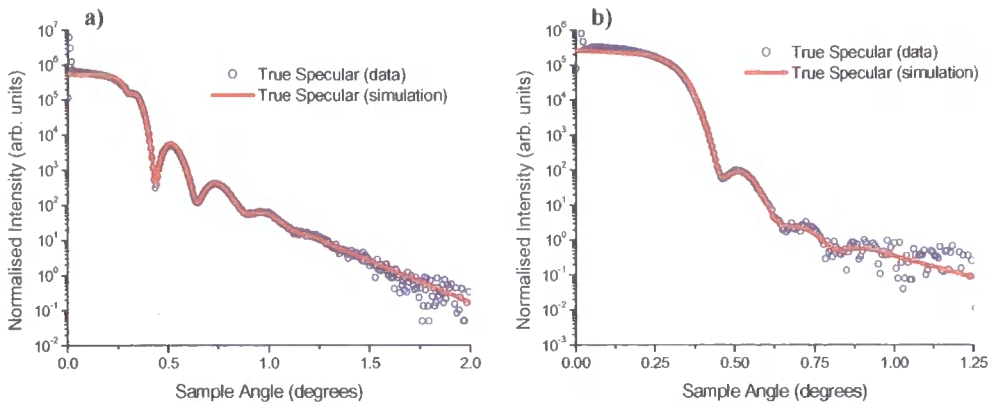

Figure D.4: *Specular profile for bilayers with nominal structure* ***a)*** *SiO_2/Mn(50Å)/Al(50Å) and* ***b)*** *SiO_2/Al(50Å)/Mn(50Å).*

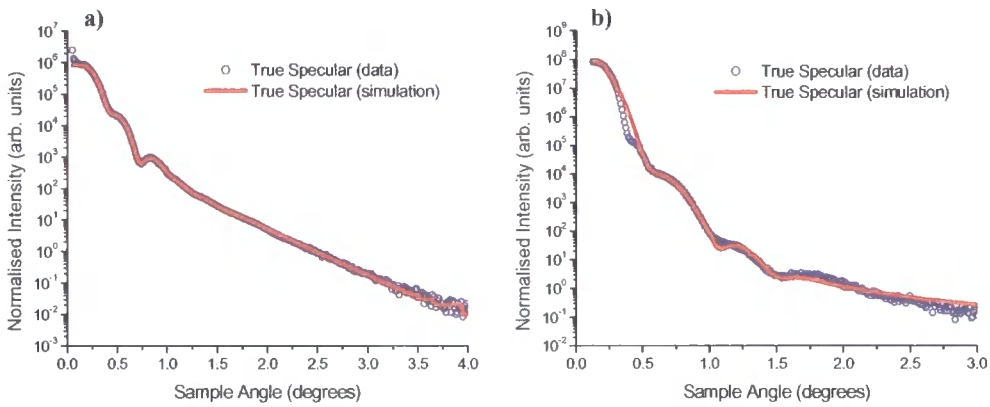

Figure D.5: *Specular profile for bilayers with nominal structure* ***a)*** *SiO_2/Cu(50Å)/Al(50Å) and* ***b)*** *SiO_2/Al(50Å)/Cu(50Å).*

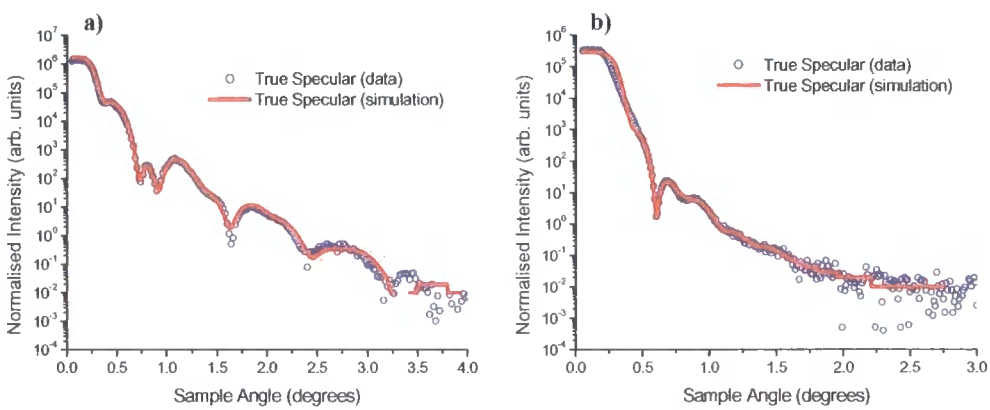

Figure D.6: *Specular profile for bilayers with nominal structure* ***a)*** *SiO_2/Zr(50Å)/Al(50Å) and* ***b)*** *SiO_2/Al(50Å)/Zr(50Å).*

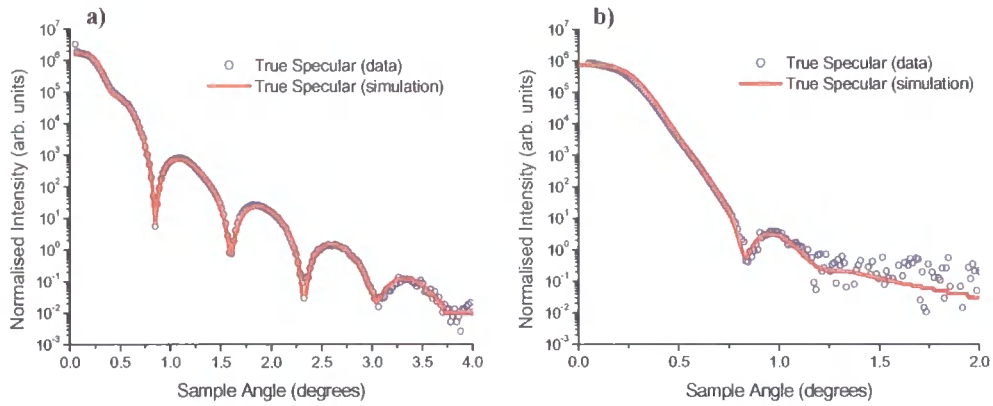

Figure D.7: *Specular profile for bilayers with nominal structure* ***a)*** *SiO_2/Nb(50Å)/Al(50Å) and* ***b)*** *SiO_2/Al(50Å)/Nb(50Å).*

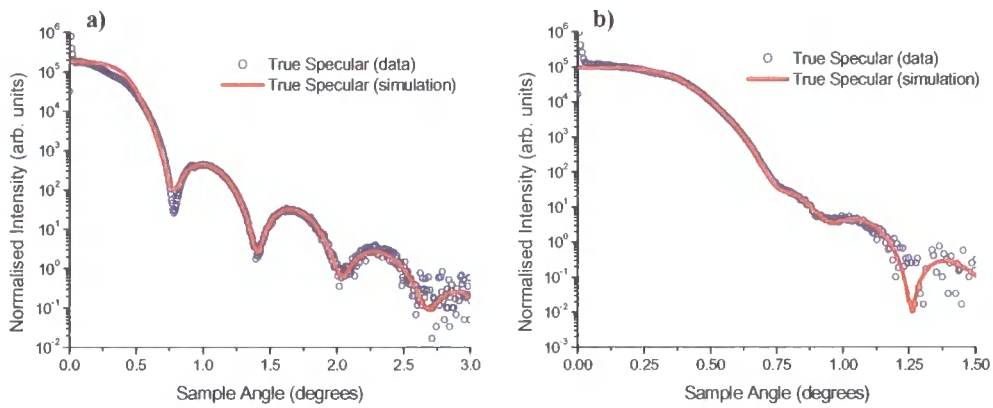

Figure D.8: *Specular profile for bilayers with nominal structure* ***a)*** *SiO_2/Ru(50Å)/Al(50Å) and* ***b)*** *SiO_2/Al(50Å)/Ru(50Å).*

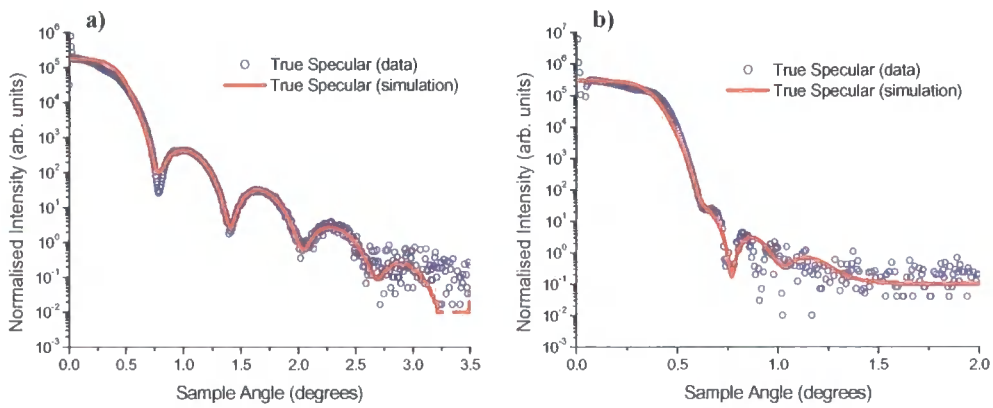

Figure D.9: *Specular profile for bilayers with nominal structure* ***a)*** *SiO_2/Rh(100Å)/Al(100Å) and* ***b)*** *SiO_2/Al(100Å)/Rh(100Å).*

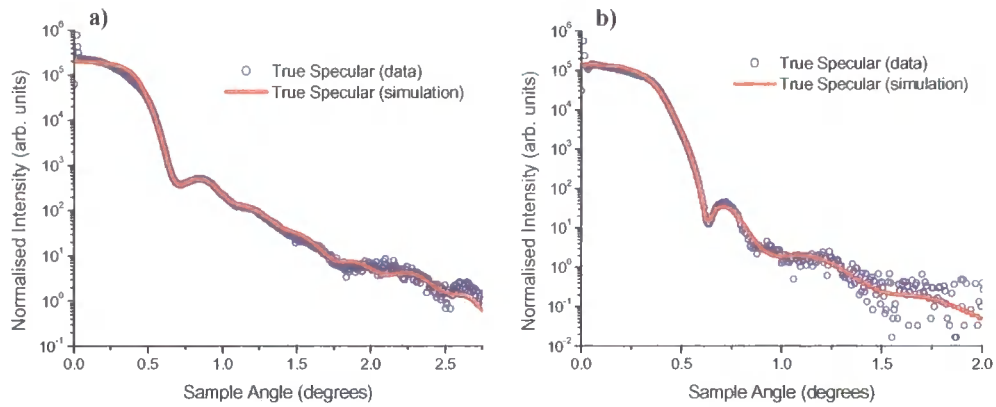

Figure D.10: *Specular profile for bilayers with nominal structure* ***a)*** *SiO_2/Pd(50Å)/Al(50Å) and* ***b)*** *SiO_2/Al(50Å)/Pd(50Å).*

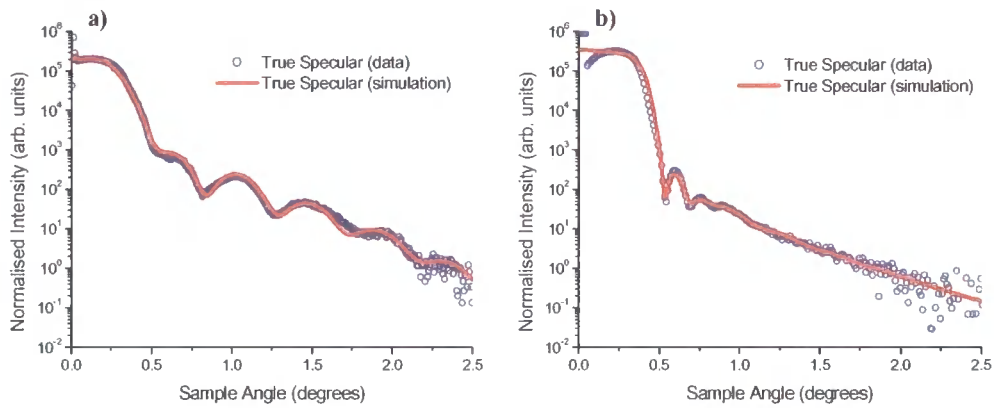

Figure D.11: *Specular profile for bilayers with nominal structure* ***a)*** *SiO_2/Ru(10Å)/Ag(50Å)/Al(50Å) and* ***b)*** *SiO_2/Al(50Å)/Ag(50Å).*

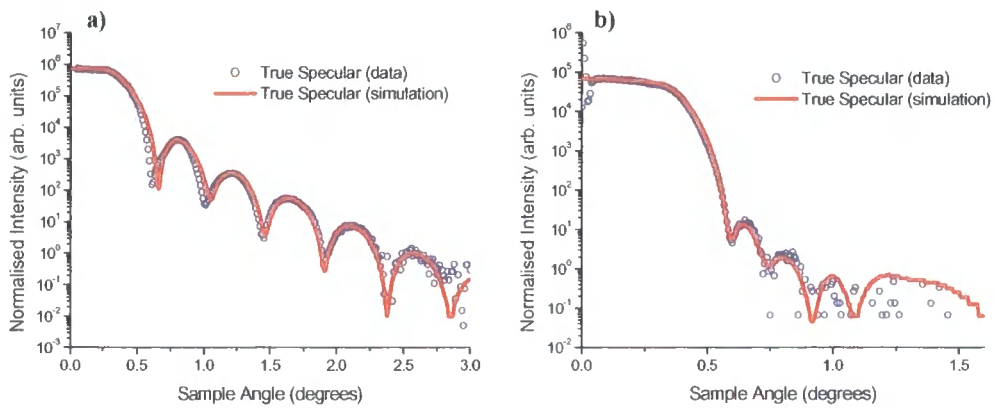

Figure D.12: *Specular profile for bilayers with nominal structure* ***a)*** *SiO_2/Hf(50Å)/Al(50Å) and* ***b)*** *SiO_2/Al(50Å)/Hf(50Å).*

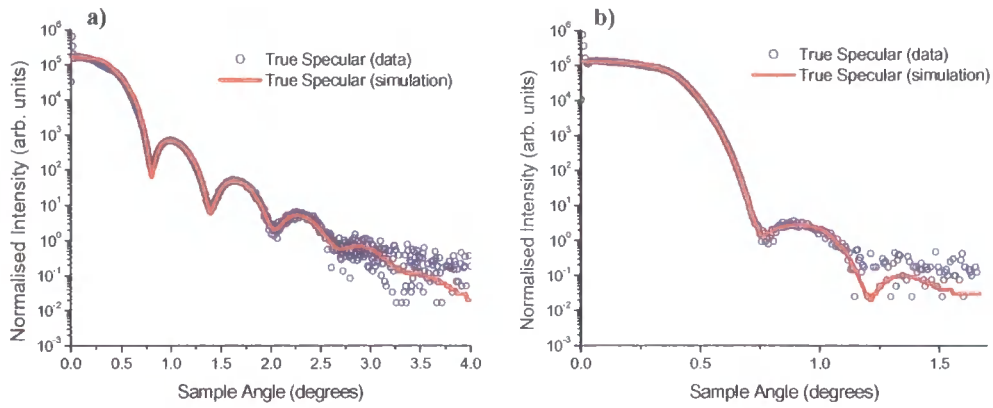

Figure D.13: *Specular profile for bilayers with nominal structure* ***a)*** *SiO_2/Ta(50Å)/Al(50Å) and* ***b)*** *SiO_2/Al(50Å)/Ta(50Å).*

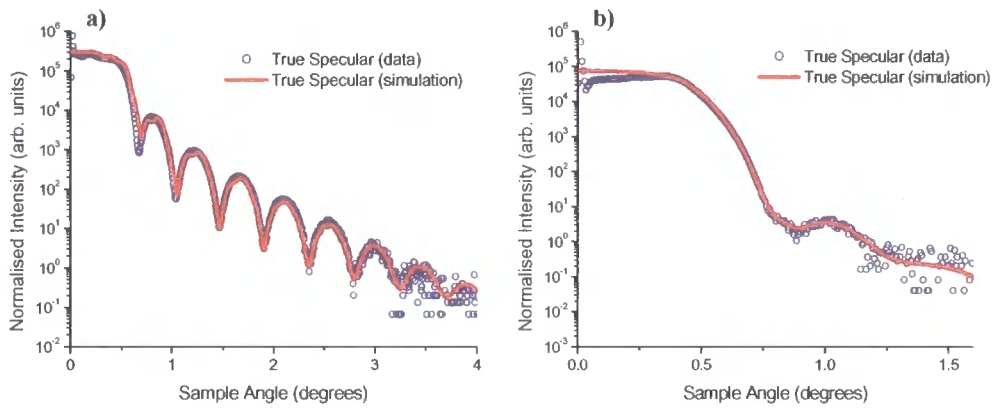

Figure D.14: *Specular profile for bilayers with nominal structure* ***a)*** *SiO_2/W(50Å)/Al(50Å) and* ***b)*** *SiO_2/Al(50Å)/W(50Å).*

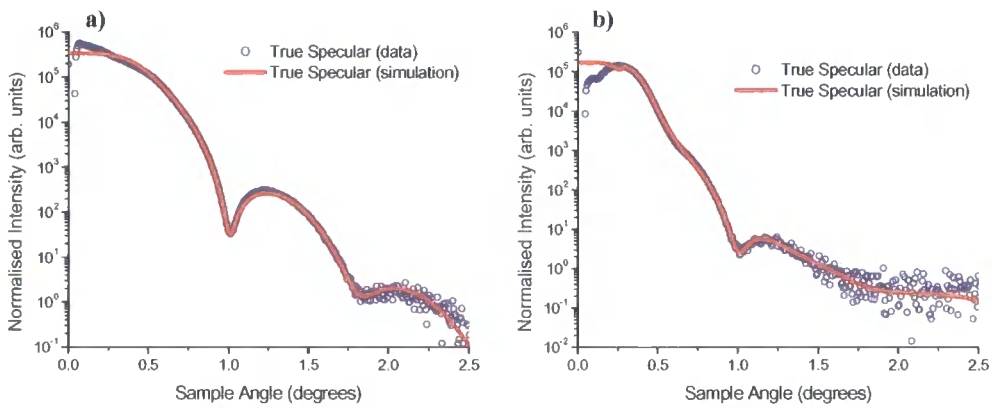

Figure D.15: *Specular profile for bilayers with nominal structure* ***a)*** *SiO_2/Re(50Å)/Al(50Å) and* ***b)*** *SiO_2/Al(50Å)/Re(50Å).*

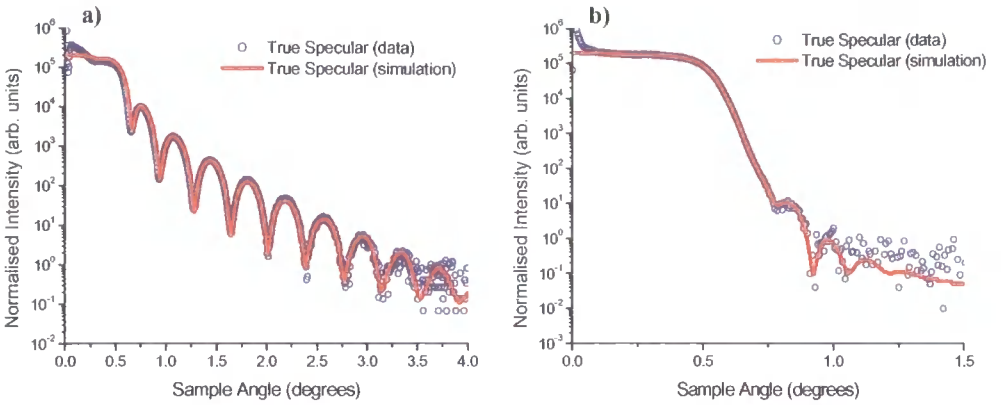

***Figure D.16**: Specular profile for bilayers with nominal structure **a)** SiO_2/Os(100Å)/Al(100Å) and **b)** SiO_2/Al(100Å)/Os(100Å).*

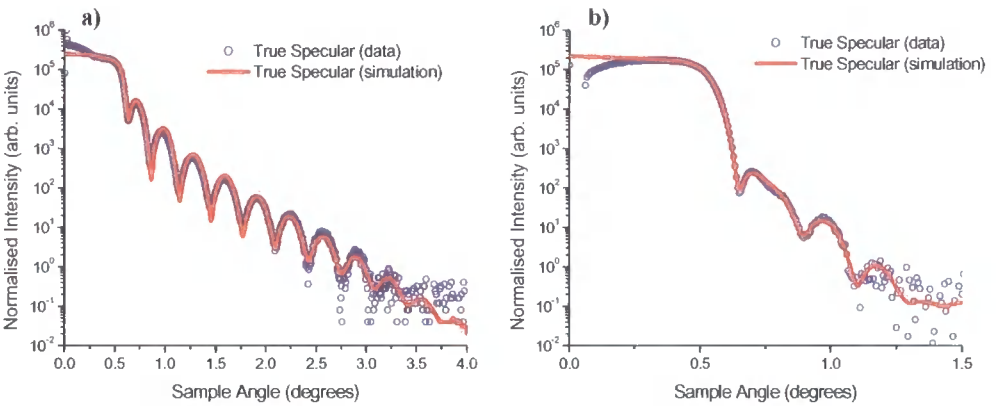

***Figure D.17**: Specular profile for bilayers with nominal structure **a)** SiO_2/Ir(50Å)/Al(50Å) and **b)** SiO_2/Al(50Å)/Ir(50Å).*

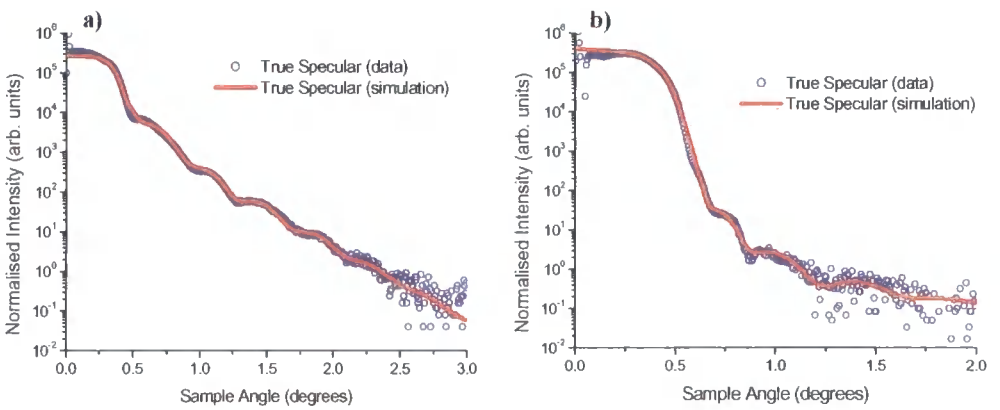

***FigureD.18**: Specular profile for bilayers with nominal structure **a)** SiO_2/Au(100Å)/Al(100Å) and **b)** SiO_2/Al(100Å)/Au(100Å).*

Appendix F: Magnetic Roughness under the Born Approximation

The following equation describes the diffuse scattering cross-section for elastic scattering over a chemical and magnetic volume, as shown in *Equation 7.5*:

$$\left.\frac{d\sigma}{d\Omega}\right|_{k_i\varepsilon\to k_f\varepsilon'}^{diffuse} = PS_{SS}(\mathbf{q}) + RS_{MM}^{(1)}(\mathbf{q}) + QS_{MM}(\mathbf{q}) + TS_{SM}(\mathbf{q}) + T^*S_{SM}^*(\mathbf{q})$$

Equation F.1

where:

$$P = r_o^2 n_o^2 |\varepsilon'\cdot\varepsilon|^2$$

Equation F.2

$$Q = n_M^2([|B|^2 |(\varepsilon'\cdot M)(\varepsilon\cdot M)|^2)] - 2Re\{iAB^*<p>[\varepsilon'\times\varepsilon\cdot M][(\varepsilon'\cdot M)(\varepsilon\cdot M)]\})$$

Equation F.3

$$R = n_M^2 |B|^2 |\varepsilon'\times\varepsilon\cdot M|^2$$

Equation F.4

$$T = r_o n_o n_M ([\varepsilon'\cdot\varepsilon][B(\varepsilon'\cdot M)(\varepsilon\cdot M)] + iA^*<p>[\varepsilon'\times\varepsilon\cdot M])$$

Equation F.5

n_o is the electron number density, n_m is the number density of magnetic atoms and r_o is the Thomson scattering length. $<p>$ is the global average of p(x,y), a functional vector which defines domains, assumed to be independent of magnetic and chemical roughness fluctuations.

The terms S_{ss}, S_{SM}, $S^{(1)}{}_{MM}$ and S_{MM} are as follows:

$$S_{SS}(\mathbf{q}) = \frac{D}{q_z^2} e^{-q_z^2\sigma_C^2} \iint dXdY (e^{q_z^2 C_{CC}(X,Y)} - 1) e^{-i\mathbf{q}\|\cdot\mathbf{p}}$$

Equation F.6

$$S_{SM}(\mathbf{q}) = \frac{D}{q_z^2} <\rho> e^{-\frac{1}{2}q_z^2(\sigma_C^2+\sigma_M^2)} e^{-iq_z\Delta} f_M(q_z) \iint dXdY (e^{q_z^2 C_{CM}(X,Y)} - 1) e^{-i\mathbf{q}\|\cdot\mathbf{p}}$$

Equation F.7

$$S_{MM}^{(1)}(\mathbf{q}) = \frac{D}{q_z^2} e^{-q_z^2\sigma_M^2} |f_M(q_z)|^2 \iint dXdY (e^{q_z^2 C_{MM}(X,Y)} - 1) e^{-i\mathbf{q}\|\cdot\mathbf{p}} \gamma_M(X,Y)$$

Equation F.8

$$S_{MM}(\mathbf{q}) = \frac{D}{q_z^2} e^{-q_z^2\sigma_M^2} |f_M(q_z)|^2 \iint dXdY (e^{q_z^2 C_{MM}(X,Y)} - 1) e^{-i\mathbf{q}\|\cdot\mathbf{p}}$$

Equation F.9

The integrals are not included in the simulation code, but are required to describe diffuse scatter, including the C_{CC}, C_{MM} and C_{CM} to model the chemical-chemical, magnetic-magnetic and chemical-magnetic correlation functions, as well as γ_M, the domain correlation function. The function f_M is a form factor which can be included to take into account the graded nature of the magnetic surface .

For more information the reader is referred to Osgood *et al.* [iv, v].

[iv] R.M. Osgood, S.K. Sinha, J.W. Freeland, Y.U. Idzerda and S.D. Bader (1999) "*X-ray scattering from magnetic, rough surfaces.*" J. Appl. Phys. **85**(8) pg. 4619-4621.

[v] R.M. Osgood, S.K. Sinha, J.W. Freeland, Y.U. Idzerda and S.D. Bader (1999) "*X-ray scattering from magnetically and structural rough surfaces.*" J. Magn. Magn. Mater. **198-199** pg. 698-702.